Mapping tissue magnetic susceptibility and its biological correlates in the human brain



Chaoyue Wang

St Peter's College

University of Oxford

A thesis submitted for the degree of

Doctor of Philosophy

Michaelmas Term 2021

Abstract

Magnetic resonance imaging (MRI) of the brain visualises anatomical structures on the scale of millimetres, but is nevertheless sensitive to microscopic tissue features. One of the features that is intrinsically important to MRI is magnetic susceptibility (χ). In brain imaging, χ contrast between structures primarily arises from tissue iron, calcium and myelin content, all of which are important tissue constituents related to a variety of brain functions and diseases.

Interest in quantification of tissue χ distribution has thus led to quantitative susceptibility mapping (QSM), a technique that quantifies tissue χ distributions through sophisticated postprocessing of phase images. The past decade has witnessed great progress in QSM. The histological correlates of χ estimates have been established including an approximately linear relationship with iron concentration validated using post-mortem brain tissue, and *in vivo* studies have demonstrated QSM's ability to detect disease-relevant changes, particularly iron accumulation in neurodegeneration.

The work presented in this thesis seeks to further investigate the biological correlates of tissue χ measures in previously unexplored settings. The first experimental chapter discusses the development of a QSM processing pipeline for fixed post-mortem, whole-brain data. Using this pipeline, we compared the resulting χ maps in brains from patients with amyotrophic lateral sclerosis and controls, with validation against iron and myelin histology.

The second and third research chapters discuss implementing QSM in a large-cohort study. We developed a robust QSM processing pipeline to produce χ estimates in 35,885 subjects from the UK Biobank imaging study. We carried out phenotypic association studies and the first genome-wide association studies of χ estimates in the brain, identifying a broad range of associated phenotypes and genetic variants.

The results presented in this thesis demonstrate the richness of information provided by QSM and hopefully promote greater clinical take-up of QSM in the future.

Acknowledgements

There are many people who have contributed to the work presented in this thesis, I would like to thank everyone involved for their help and support.

Firstly, I would like to express my deepest appreciation to my supervisors, Professor Karla Miller and Dr Benjamin Tendler for their continuous guidance and support throughout my DPhil. Karla and Ben gave me the best DPhil training I could ever ask for. Outside research, they gave me advices and feedbacks on each of my presentations, which made me a much better speaker.

I am very grateful for the funding from the China Scholarship Council-University of Oxford Scholarship that supported my DPhil study. I would like to thank Karla for the financial support in the last year of my DPhil.

I would like to thank my colleagues and friends in FMRIB for giving me valuable advices on my research projects, it has been a great pleasure working with them. I am particularly grateful to Dr Aurea Martins-Bach, Dr Fidel Alfaro-Almagro and Prof Stephen Smith for their help with the UK Biobank project; and Dr Weikang Gong, Ying-Qiu Zheng, Xi Chen and Dr Yan Tong for sharing their knowledge on programming, FSL, cluster, MRI physics, etc.

Finally, I wish to thank my family: my parents, Qi Wang and Suping Wang for the endless love and support they gave me throughout my life; my wife, Dr Yaxuan Meng, whose company has been the best thing in my life. Without her love, support and encouragement, I could not have finished this thesis in this challenging time.

Contents

Chapter 1 Introduction ····· **1**

1.1 Motivation ····· **1**

1.2 Thesis outline ····· **3**

Chapter 2 Background ····· **5**

2.1 The formation of MR signal ····· **6**
2.1.1 Excitation ····· 6
2.1.2 Spatial encoding ····· 7
2.1.3 Signal reception ····· 7
2.1.4 Relaxation ····· 8

2.2 Gradient echo imaging ····· **9**

2.3 Complex representation of MR signal ····· **11**

2.4 T2* quantification ····· **13**

2.5 Magnetic susceptibility ····· **14**

2.6 Quantitative susceptibility mapping ····· **17**
2.6.1 Combination of multi-channel phase data ····· 19
2.6.2 Phase unwrapping ····· 22
2.6.3 Generation of masks ····· 25
2.6.4 Background field removal ····· 26
2.6.5 Dipole inversion ····· 30
2.6.6 Performance of phase processing algorithms ····· 34

Chapter 3 Methods for quantitative susceptibility and R2* mapping in whole post-mortem brains at 7T ····· **35**

3.1 Introduction ····· **35**

3.2 Methods ····· **37**
3.2.1 Post-mortem brain samples ····· 37
3.2.2 Sample preparation and MRI data acquisition ····· 38
3.2.3 Post-mortem brain susceptibility model simulation and QSM pipeline evaluations ····· 41
3.2.4 Experimental QSM post-processing pipeline ····· 47
3.2.5 R2* post-processing pipeline ····· 56
3.2.6 MR image analysis ····· 57
3.2.7 Histological analysis ····· 60
3.2.8 Statistical analysis ····· 63

3.3 Results ····· **63**
3.3.1 Quantitative χ and R2* maps ····· 63
3.3.2 Histological results and their relation to MRI-derived measures ····· 65

3.4 Discussion ····· **67**
3.4.1 QSM pipeline considerations ····· 67
3.4.2 Histology analysis considerations ····· 69

3.4.3 Correlations between χ/R2* measures and ferritin/PLP SAFs ····· 69
3.4.4 ALS pathology associated changes in χ and R2* ····· 71
3.4.5 Study limitations ····· 72
3.4.6 Conclusions ····· 74

Chapter 4 Development of an optimal QSM processing pipeline for UK Biobank brain swMRI data ····· 76

4.1 Introduction ····· 76

4.2 QSM pipeline evaluation and development, QSM and T2* IDP generations 79
4.2.1 MRI Data acquisition and participant information ····· 79
4.2.2 Evaluation and development of QSM processing pipeline for UK Biobank swMRI data ····· 80
4.2.3 Evaluations of reference region for χ maps ····· 90
4.2.4 Generation of QSM-based image-derived phenotypes ····· 94
4.2.5 Generation of T2*-based image-derived phenotypes ····· 97
4.2.6 Phenotypic association of T2* IDPs before and after deconfounding of macroscopic field gradients ····· 101

4.3 Discussion ····· 104

Chapter 5 Phenotypic and genetic associations of MR susceptibility in UK Biobank brain imaging ····· 104

5.1 Introduction ····· 104

5.2 Methods ····· 106
5.2.1 IDP generations, outliers and confounds removal ····· 106
5.2.2 Associations between IDPs and non-imaging measures ····· 107
5.2.3 Associations between IDPs and genetic variants ····· 108
5.2.4 Voxel-wise associations with phenotypes and genetic variants ····· 111

5.3 Results ····· 112
5.3.1 Associations between IDPs and phenotypes ····· 112
5.3.2 Associations between IDPs and genetic variants ····· 121

5.4 Discussion ····· 135
5.4.1 Phenotypic and genetic associations with QSM ····· 135
5.4.2 Iron and calcium in quantitative swMRI ····· 136

Chapter 6 Summary and Future Work ····· 138

6.1 Summary ····· 138
6.1.1 QSM pipeline considerations ····· 138
6.1.2 Biological correlates of magnetic susceptibility in the brain ····· 140
6.1.3 QSM vs T2* ····· 142

6.2 Future Work ····· 143
6.2.1 Post-mortem dataset: combining QSM and R2* data with other imaging modalities and histology ····· 143
6.2.2 Voxel-wise correction for UK Biobank T2* maps ····· 144
6.2.3 Future work enabled by the UK Biobank QSM resource ····· 147

Appendices ····· 154

Chapter 1

Introduction

1.1 Motivation

The majority of magnetic resonance imaging (MRI) techniques create images based on the magnitude of the MRI signal; a small but important set of methods are based on the signal phase [1]. One of the most common phase-based methods is susceptibility-weighted MRI. Phase information in susceptibility-weighted MRI was first exploited in the non-quantitative susceptibility-weighted imaging (SWI) method [2], and later in quantitative susceptibility mapping (QSM) [3], which is the topic of this thesis. Here, 'susceptibility' refers to magnetic susceptibility, χ, a property intrinsic to all materials. In brain imaging, χ contrast primarily arises from tissue iron, calcium and myelin content, all of which are important tissue constituents related to a variety of brain functions and diseases [4]. Therefore, SWI has been widely used clinically for venography and detection of microbleeds [5]. One limitation of SWI is that it does not provide a quantitative measure of the underlying χ distribution. This limitation arises in part because the phase in a given voxel reflects not only the local χ value, but also the χ distribution of nearby structures [3]. This 'blooming' effect is well-defined but complicated, with phase of different structures depending on their χ distributions, the shape of structures, and their orientations to the static magnetic field [3].

Interest in quantification of tissue χ distribution has thus led to QSM, a technique that quantifies tissue χ distributions through sophisticated postprocessing of phase images. The past decade has witnessed great progress in QSM. Numerous algorithms have been developed for QSM, aiming to produce robust χ maps with minimum artefacts. The histological correlates of estimated χ have been established including an approximately linear relationship with iron concentration validated using post-mortem brain tissue [6], and χ in calcified lesions have been validated using CT attenuation values [7]. Furthermore, *in vivo* studies have demonstrated QSM's ability to detect disease-relevant changes, such as iron accumulation in neurodegenerative disorders [4], and to provide an index of microstructural changes to tissue in normal ageing [8].

In this thesis, I will present implementations of QSM in two unique datasets: (i) whole, post-mortem brains with a neurodegenerative disease and (ii) a population-level neuroimaging resource. To date, *ex vivo* QSM studies have been using either unfixed (*in situ*) post-mortem brains [6] or sliced sections of fixed brain samples [9]. The use of fixed, whole post-mortem brains offers both flexibility in sample storage and whole brain coverage which is particularly advantageous in studies of neurodegenerative diseases, as most neurodegenerative diseases develop with stereotyped patterns of progression over the entire brain [10]. QSM in whole post-mortem brains thus creates a unique opportunity for direct comparison between χ and histology measures in multiple regions of interest (ROIs).

Furthermore, *in vivo* QSM has been largely conducted in the traditional framework of small cohorts (tens to hundreds of subjects) that are optimised for homogeneity and aiming to study a specific group or effect of interest. They are effective in detection of pathological changes of χ, but cannot capture the variance that exists across populations, limiting the opportunities for non-hypothesis-driven discovery. A powerful alternative is

to prospectively image healthy individuals at large scale and track subsequent health outcomes. One of such large prospective studies is UK Biobank, which is collecting brain susceptibility-weighted MRI (swMRI) data in 100,000 participants who are largely healthy when scanned [11]. These participants have been deeply phenotyped and genotyped and consent to long-term access to health records [11]. The UK Biobank swMRI protocol was designed to enable QSM [11,12], which creates an unprecedented opportunity to explore the potential of QSM at the population level.

The ambition of this thesis is to further explore the biological correlates of tissue magnetic susceptibility measures in the brain both *ex vivo* (using the fixed, whole post-mortem ALS brains) and *in vivo* (using the UK Biobank swMRI data). The main aims are to: i) develop a pipeline for QSM reconstructions for whole, post-mortem brains and investigate the histopathological correlates of χ measures in brains with ALS pathology; and ii) develop a pipeline for QSM reconstructions specifically optimized for the UK Biobank swMRI data and investigate the phenotypic and genetic associations of χ in the brain.

1.2 Thesis outline

This thesis is structured as follows:

Chapter 2 gives a brief background on MRI signal formation, gradient echo imaging, magnetic susceptibility, quantitative susceptibility mapping and a variety of algorithms developed for QSM.

Chapter 3, the first research chapter, describes a QSM study of fixed, whole post-mortem ALS brains. This chapter presents the details on the development of a QSM and R2* pipeline for whole post-mortem brains. χ and R2* estimates in multiple ROIs are compared between ALS brains and controls. Histological measures related to iron and myelin content are compared with χ and R2* estimates in multiple ROIs.

Chapter 4 describes the development of a QSM pipeline specifically optimized for the UK Biobank swMRI data. In this chapter, an extensive evaluation of a variety of existing algorithms is presented. This chapter also presents the approach to generate summary measures of χ in a few ROIs including deep grey structures and white matter hyperintensity lesions.

Chapter 5 presents the phenotypic and genetic associations of the summary measures of χ produced from the UK Biobank data using the pipeline developed in Chapter 4. Chapter 5 also presents the comparison of phenotypic and genetic association patterns between χ and T2* measures.

Chapter 6 summarises the research work presented in this thesis and discusses possible future research directions.

Chapter 3 is based on a peer-reviewed journal paper published in NeuroImage [13]. Chapters 4 and 5 are based on a journal paper [14] that has been submitted to a journal and is under peer review, at the time of writing this thesis.

Chapter 2

Background

This chapter outlines the underlying physics of magnetic resonance imaging techniques of direct relevance to quantitative susceptibility mapping. These topics are sufficient to put this thesis into context and provide background of the work presented in this thesis. To avoid unnecessary repetition of well-established physics that has been recapitulated in thousands of theses, many topics that are core to other MRI techniques are not described in this chapter. A significant portion of the theory presented in this chapter has been obtained from textbooks [1], [15]. Other sources not contained within these books are listed within the text.

2.1 The formation of MR signal

Magnetic resonance imaging (MRI) is a non-invasive imaging technique that provides rich information related to tissue structure and function. The MR signal arises through the interaction of an object's nuclear spins with the static magnetic field, $\vec{B}_0$, leading to precession about $\vec{B}_0$. The frequency of this precession (referred to as the Larmor frequency) is defined as:

$$\omega_0 = \gamma \cdot B_0 \tag{2.1}$$

where γ is the gyromagnetic ratio (for a hydrogen proton, $\gamma = 2.68 \times 10^8\ rad/s/tesla$). MRI of human tissue generally detects hydrogen protons in water molecules, which are present in great abundance in the human body. MR image formation is achieved through manipulation of the precessing spins using MRI hardware that manipulates electromagnetic fields over space and time. In addition to the magnet that generates the static magnetic field, there are three major components that are essential to image formation: (1) transmit radio frequency (RF) coils; (2) magnetic field gradient coils; and (3) receive RF coils. This section briefly overviews the formation of MR images, including excitation, spatial encoding, signal reception and relaxation.

2.1.1 Excitation

In the presence of the static magnetic field, the net magnetization of the spins is oriented in the direction of $\vec{B}_0$ which is its equilibrium state. In this thesis, the direction of $\vec{B}_0$ is defined as along the z-axis, also referred to as the longitudinal axis. Orthogonal to this axis, the x-y plane is referred to as the transverse plane. The transmit radio frequency (RF) coils produce a time-varying magnetic field perpendicular to $\vec{B}_0$, which is referred to as a RF pulse. RF pulses are generally designed to contain significant energy at a RF frequency equal to the Larmor frequency. RF pulses are used to 'tip' the magnetization

away from its equilibrium state (to the transverse plane), this step is known as excitation. The duration and intensity of the RF pulse determines the angle of rotation away from the longitudinal axis, which is called the flip angle (FA). After application of the RF pulse, spins slowly return to their equilibrium orientation aligned to $\vec{B}_0$, in a process called relaxation.

2.1.2 Spatial encoding

During the relaxation process, a spatially-varying magnetic field (known as the gradient field $G(\vec{r})$) is generated by the three gradient coils. The gradient field is along the $\vec{B}_0$ direction, but its amplitude varies linearly in space. $G(\vec{r})$ can be described as $[G_x, G_y, G_z]$ which represents the gradients along three orthogonal axes. The spins at location (x, y, z) thus experience a total magnetic field given by:

$$B(x, y, z) = B_0 + G_x \cdot x + G_y \cdot y + G_z \cdot z \tag{2.2}$$

this leads to spatially-varying precession frequency $\omega(x, y, z)$:

$$\omega(x, y, z) = \omega_0 + \gamma\big(G_x \cdot x + G_y \cdot y + G_z \cdot z\big) \tag{2.3}$$

which is a linear mapping between spatial location and Larmor frequency. The accumulated phase, up to time t, due to the spatially-varying frequencies is:

$$\phi_G(x, y, z, t) = -\gamma \left[\int_0^t G_x(t')x\, dt' + \int_0^t G_y(t')y\, dt' + \int_0^t G_z(t')z\, dt'\right] \tag{2.4}$$

2.1.3 Signal reception

RF receive coils are used to detect the signal that arises from the time-varying magnetic field. The signal recorded at a specific time t is given by:

$$s(t) \propto \iiint \rho(x, y, z)\, e^{i\phi_G(x,y,z,t)} dxdydz \tag{2.5}$$

where $\rho(x, y, z)$ is the effective proton density. By defining:

$$k_x(t) = \frac{\gamma}{2\pi}\int_0^t G_x(t')dt',\ k_y(t) = \frac{\gamma}{2\pi}\int_0^t G_y(t')dt',\ k_z(t) = \frac{\gamma}{2\pi}\int_0^t G_z(t')dt' \tag{2.6}$$

Eq. 2.5 can be rewritten as:

$$s(k_x, k_y, k_z) = \iiint \rho(x, y, z)\, e^{-2\pi i(k_x x + k_y y + k_z z)} dx dy dz \quad (2.7)$$

Equation 2.7 defines the measured signal as the Fourier transform of the effective proton density $\rho(x, y, z)$. Conventionally, the MRI signal space defined by Eq. 2.7 is referred to as 'k-space'. Reconstruction of the effective proton density (in the spatial domain) using Eq. 2.5 requires sufficient coverage of k-space. This is normally achieved by varying the amplitude or duration of the gradients G_x, G_y, G_z. The three orthogonal gradients can also be referred to as the readout, phase encoding, and slice selection gradients.

2.1.4 Relaxation

This description of MRI as yielding an image of proton density is incomplete. One of the most important determinants of the properties of MR images is relaxation. Depending on the timings of an MRI acquisition, relaxation causes tissues to have different signal levels, or 'contrast', even if they have identical proton density. The excitation process (through application of an RF pulse) effectively reduces the longitudinal magnetization M_z and creates transverse magnetization M_{xy}. After excitation, the magnetization recovers to its equilibrium state M_0. The first type of relaxation, known as spin-lattice relaxation, describes the regrowth of longitudinal magnetization to its equilibrium state due to the process of the excited spins transferring energy to the surroundings (lattice). This recovery process is exponential, characterized by a time constant T1 (i.e., after a 90° excitation, at time *t*, $M_z(t) = M_0(1 - e^{-t/T_1})$). The second type of relaxation is known as spin-spin relaxation which describes the decay of transverse magnetization, characterized by a time constant T2 (i.e., at time *t*, $M_{xy}(t) = M_0 e^{-t/T_2}$). This type of relaxation occurs due to interactions between the magnetic fields of neighbouring nuclei which leads to a loss of phase coherence ('dephasing') among the exited spins and an effective 'cancelling' of net transverse magnetisation. Furthermore, the decay of M_{xy} is

also influenced by additional factors such as $\vec{B}_0$ inhomogeneity. In the presence of these field inhomogeneities, the decay of M_{xy} is faster than the T2 decay and is characterized by another time constant T2*:

$$\frac{1}{T_2^*} = \frac{1}{T_2} + \frac{1}{T_2'} \tag{2.8}$$

where T_2' describes the additional decay induced by field inhomogeneities. With T2* decay, $M_{xy}(t) = M_0 e^{-t/T_2^*}$. Even if a scanner's magnet produces a perfectly homogeneous $\vec{B}_0$ in isolation, the local field inhomogeneity still arises due to the phenomenon that the object placed in the magnet can induce magnetisation that perturbs the local magnetic field. This phenomenon is characterised by a property known as magnetic susceptibility, which is the key focus of this thesis and will be discussed in detail in the following sections. In practice, T2* provides interesting information about the underlying structure of tissue. Images with contrast that predominantly reflects the T2* of different tissue types can be captured using a technique known as gradient echo imaging.

2.2 Gradient echo imaging

The sequence of different RF pulses and gradients form what is referred to as an MRI 'pulse sequence'. Many pulse sequences have been developed over the past decades. One of the most important and widely used sequences is the gradient echo (GRE) sequence. GRE sequences use both positive and negative gradients to sample over positive and negative k-space locations. GRE sequences typically apply one RF pulse with small flip angle (< 90°) for excitation, after which the dephasing of transverse magnetisation leads to an intrinsic T2* weighting of GRE signal. Thus, GRE sequences are thus uniquely sensitive to magnetic susceptibility properties of tissue. Note that GRE is just one category of MRI acquisition methods. Other methods use additional RF pulses to achieve

contrast that is predominantly weighted by T2 (e.g., spin echoes) or T1 (e.g., inversion-recovery experiments). However, these methods are not described there as they are not useful for quantitative susceptibility mapping.

In the diagram of a typical 3D GRE sequence shown in **Fig. 2.1**, the readout gradient G_x consists of both negative and positive gradients with the same amplitude (in practice, they can have different amplitudes, as long as their zeroth moments match at $t = t_3$), and the timing of G_x is set as $t_3 - t_2 = t_2 - t_1$. This negative G_x gradient from t_1 to t_2 induces additional dephasing of the magnetisation, then the positive G_x gradient from t_2 to t_3 induces rephasing of the magnetisation which removes the additional signal decay induced by the negative G_x gradient. The second half of positive G_x gradient (after t_3) again induces additional dephasing of the magnetisation.

Therefore, at $t = t_3$, from Eq. 2.6, $k_x(t_3) = \frac{\gamma}{2\pi} G_x[-(t_2 - t_1) + (t_3 - t_2)] = 0$, which indicates that an 'echo' is formed. As shown in **Fig. 2.1**, the duration from the RF pulse to t_3 is defined as the echo time (TE) and the duration between two RF excitations is defined as the repetition time (TR).

Note, the sequence shown in **Fig. 2.1** has only one echo (i.e., one TE) which is called a single echo GRE sequence. It can be configured to a multi-echo GRE sequence by repeating the G_x gradients with the same settings after each RF excitation (within one TR), which enables acquiring signal at different TEs during one excitation.

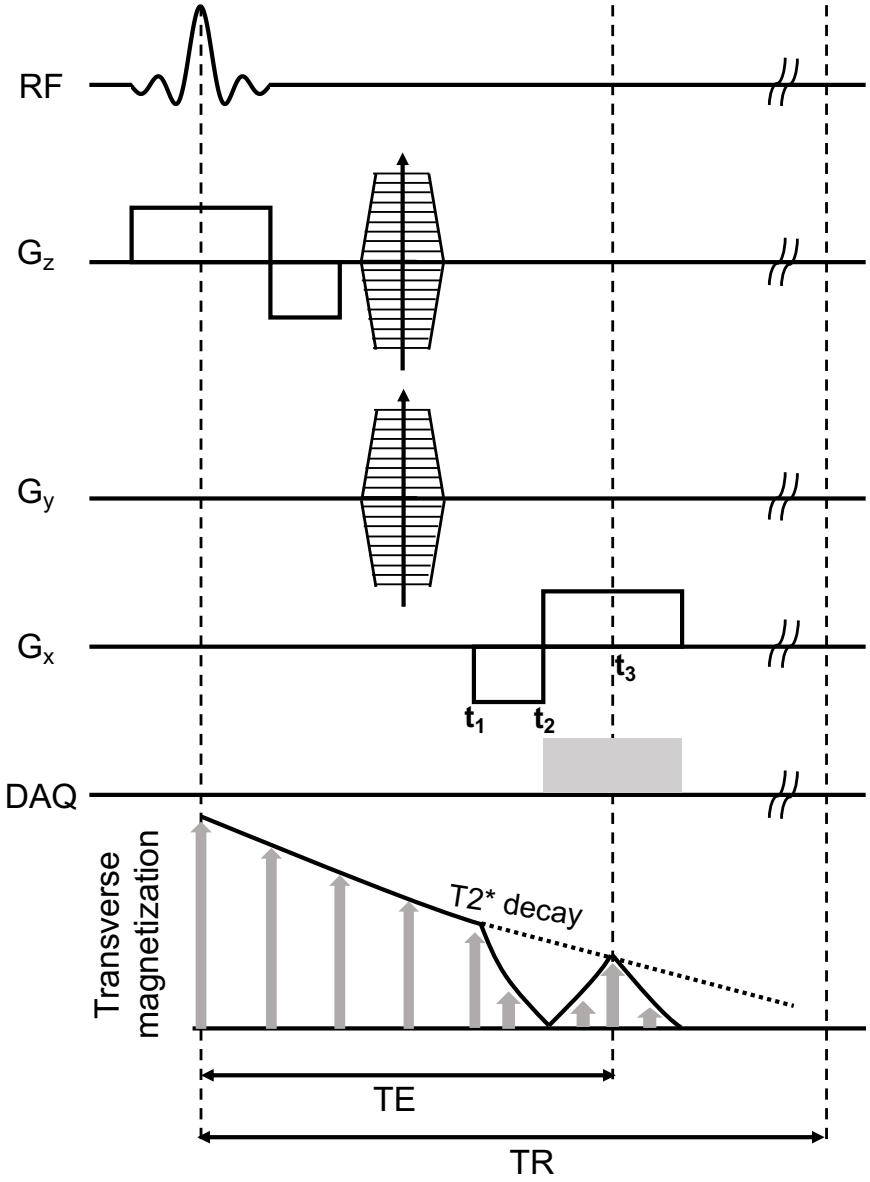


Figure 2.1 Sequence diagram of a 3D single-echo GRE sequence. G_z, G_y, G_x correspond to slice selection, phase encoding and readout gradient. DAQ represents data acquisition during the grey-shade area. TR (repetition time) is the length of time between two RF excitation pulses. TE (echo time) is the duration from the RF excitation pulse to centre of the readout echo. Note that, G_z and G_y gradients also induce additional signal decay, which is neglected here for simplicity.

2.3 Complex representation of MR signal

The precession of the spin in the transverse plane can be represented by complex notation. In MRI, the signal is commonly detected and demodulated using two (orthogonal) channels, representing real and imaginary components of a complex signal:

$$S(t) = S_{real}(t) + i \cdot S_{imag}(t) \tag{2.9}$$

For a GRE sequence, this complex signal can also be represented as magnitude and phase components (**Fig. 2.2**), defined as:

$$Mag(t) = |S(t)| = |S_0|e^{-\frac{t}{T2^*}}$$

$$Phase(t) = \phi(t) = \arctan\left(\frac{S_{imag}(t)}{S_{real}(t)}\right) \quad (2.10)$$

where S_0 is signal amplitude at t=0. Thus, Eq. 2.6 can be rewritten as:

$$S(t) = S_0 e^{-\frac{t}{T2^*}} e^{i\phi(t)} \quad (2.11)$$

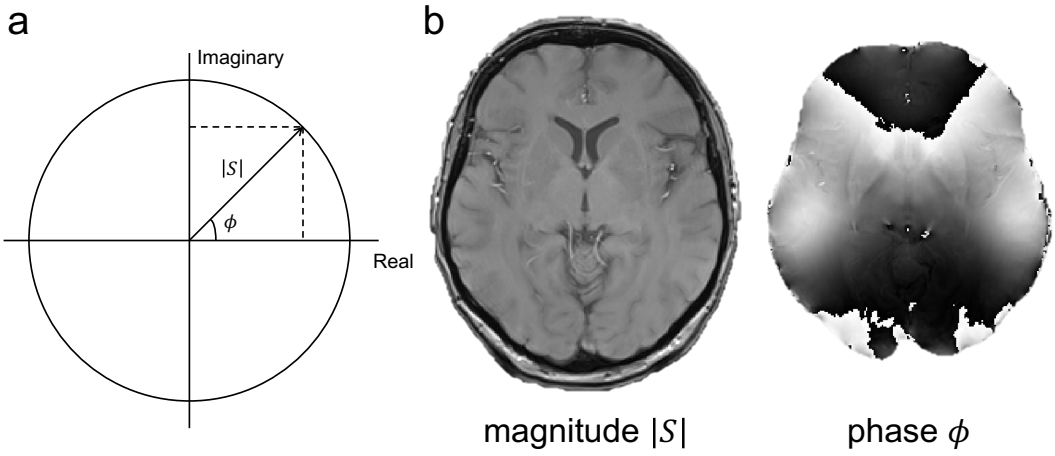


Figure 2.2 (a) Complex representation of an MRI signal *S* through 'Real' and 'Imaginary' channels. φ represents the phase component of the signal. **(b)** Example magnitude and raw phase (after brain extraction) images from a GRE acquisition.

From Eq. 2.1, in the presence of local field variations $B(\vec{r})$ induced by inhomogeneities in the magnetic field, for a right-handed system, the phase accumulated at time t can be written as:

$$\phi(\vec{r}, t) = -\omega_0 \cdot t + \gamma B(\vec{r}) \cdot t = -\gamma\big(B_0 - B(\vec{r})\big) \cdot t$$

or,
$$\phi(\vec{r}, t) = -\gamma \Delta B(\vec{r}) \cdot t \quad (2.12)$$

For the remainder of this thesis, $\Delta B(\vec{r})$ will be used to define local field perturbations. Here, $\Delta B(\vec{r})$ is defined as $(B_0 - B(\vec{r}))$, which is to keep the negative sign of the frequency term $(\gamma \Delta B(\vec{r}) \cdot t)$.

For a GRE acquisition, the accumulated phase at echo time TE (for a right-handed system) can be written as:

$$\phi(\vec{r}, TE) = -\gamma \cdot \Delta B(\vec{r}) \cdot TE + \phi_0(\vec{r}) \tag{2.13}$$

where $\phi_0(\vec{r})$ is a time-independent phase offset related to coil sensitivity profiles, local conductivity, permittivity, and inhomogeneities of transmit RF ($B1^+$) field, etc. When multi-channel receive coils are used, combination of phase data from multiple channels normally aims to remove the $\phi_0(\vec{r})$ term.

2.4 T2* quantification

T2* relaxation time provides one of the most important basic, intrinsic contrast mechanisms in MRI. Quantification of T2* is of interest as different constituents in tissue can lead to different T2* values. Therefore, quantification of T2* can provide an insight into tissue composition, often distinguishing between healthy and diseased tissue. As described in previous sections, the signal evolution in a GRE acquisition experiences T2* decay, which makes GRE acquisitions ideal for T2* quantifications.

A simple approach to estimate T2* from multi-echo GRE data is to take the natural logarithm on both side of Eq. 2.7, yielding:

$$\ln[Mag(TE)] = \ln|S_0| - \frac{TE}{T2^*} \tag{2.14}$$

As there are two unknowns here ($|S_0|$ and $T2^*$), at least two TEs are required to estimate T2*. Estimation is typically achieved using a voxel-wise linear least-squares fit. The fit to the slope of signal magnitude evolution over multiple TEs yields the quantity $-\frac{1}{T2^*}$ and the fit to the intercept yields $|S_0|$. In Chapter 3, we introduce a method that accounts for the impact of noise on the T2* estimation [13].

2.5 Magnetic susceptibility

Magnetic susceptibility is an intrinsic property of all materials. It describes the degree of magnetisation induced when a material is exposed to an external magnetic field, and what form of interaction takes place. When an object with magnetic susceptibility χ is placed in an external magnetic field $\vec{H}$ (in A/m), its induced magnetization $\vec{M}$ (in A/m) is related to $\vec{H}$ through:

$$\vec{M} = \chi \cdot \vec{H} \tag{2.15}$$

Magnetic susceptibility χ is typically defined as a dimensionless constant with units parts per million (ppm) or parts per billion (ppb), also known as the volume magnetic susceptibility. Although alternative definitions of magnetic susceptibility (e.g., mass susceptibility) exist, in this thesis we only refer to the volume magnetic susceptibility.

In a vacuum, the relationship between static magnetic field $\vec{B}_0$ (in tesla) and $\vec{H}$ can be written as:

$$\vec{B}_0 = \mu_0 \cdot \vec{H} \tag{2.16}$$

where $\mu_0 = 4\pi \times 10^{-7} TmA^{-1}$ is the permeability of a vacuum. When an object with susceptibility χ is placed in the vacuum, the total magnetic field $\vec{B}$ is perturbed due to the magnetization $\vec{M}$ induced by this object, as follows:

$$\vec{B} = \mu_0 \cdot (\vec{H} + \vec{M}) \tag{2.17}$$

Combining Eq. 2.14 and 2.16 gives:

$$\vec{B} = \mu_0 \cdot (1 + \chi)\vec{H} = \mu_0 \cdot \left(1 + \frac{1}{\chi}\right)\vec{M} \tag{2.18}$$

Based on the magnetization they induced, biological materials can be roughly classified into two types: diamagnetic and paramagnetic. Paramagnetic materials are characterised by a positive χ and increase $\vec{B}$, whereas diamagnetic materials are

characterised by a negative χ and decrease $\vec{B}$. In studies of biological tissues, susceptibility values are approximately referenced, most commonly to water, which is approximately -9.04 ppm relative to vacuum [16]. Thus, the terms "paramagnetic" or "diamagnetic" used in this thesis refers to tissue being more paramagnetic or more diamagnetic than water. For example, hydroxyapatite (Ca^{2+}) with χ = -14.8 ppm relative to vacuum [17] is considered to be 'diamagnetic'; deoxygenated blood (χ = -7.9 ppm relative to vacuum) and ferritin (χ = 520 ppm relative to vacuum) [16] are both considered to be 'paramagnetic'.

Given that human tissue has susceptibilities on the order of 10^{-6}, under the assumption of $\chi \ll 1$, Eq. 2.17 can be further simplified as:

$$\vec{B} = \mu_0 \cdot \left(1 + \frac{1}{\chi}\right) \vec{M} \approx \mu_0 \cdot \vec{M}/\chi \tag{2.19}$$

In practice, the introduction of an object with susceptibility distribution $\chi(\vec{r})$ into a magnetic field gives rise to a complicated distribution of field perturbations within and surrounding the object. These field perturbations depend strongly on the shape of the susceptibility distribution, in addition to the magnitude and sign of χ. For susceptibility distributions corresponding to a simple geometric shape (e.g., cylinders, spheres, ellipsoids), analytical solutions describing the field distributions exist. However, for the susceptibility distributions encountered in experimental MRI (e.g., arising from the human brain), the field perturbations must be predicated directly. In practice, this is achieved via the convolution of the susceptibility distribution with the field perturbations predicted from a point source, known as the dipole kernel. Here we provide a brief overview of how to achieve this. Defining that the external field is along the z-direction, the z-component of field perturbations can be written as:

$$\Delta B_Z(\vec{r}) = \frac{\mu_0}{4\pi} \int_{V'} d^3r' \left\{ \frac{3M_z(\vec{r'})(z-z')^2}{|\vec{r}-\vec{r'}|^5} - \frac{3M_z(\vec{r'})}{|\vec{r}-\vec{r'}|^3} \right\} \tag{2.20}$$

This equation can be expressed in terms of a convolution:

$$\Delta B_Z(\vec{r}) = \mu_0 M_z(\vec{r}) * d(\vec{r}) \tag{2.21}$$

where $d(\vec{r})$ is the dipole field (kernel), equal to:

$$d(\vec{r}) = \frac{1}{4\pi}\frac{3cos^2\theta - 1}{r^3} \tag{2.22}$$

and θ is the angle between $\vec{r}$ and $\vec{z}$, notably $cos^2\theta = \frac{z^2}{r^2}$. When $\chi \ll 1$, the induced magnetic field perturbation can be defined as:

$$\Delta B_Z(\vec{r}) = \mu_0 M_z(\vec{r}) * d(\vec{r}) \approx B_0 \chi(\vec{r}) * d(\vec{r}) \tag{2.23}$$

Convolutions in image space can be expressed as a product in Fourier space, leading to:

$$\Delta B_Z(\vec{r}) = B_0 \cdot FT^{-1}\{\chi(\vec{k}) \cdot d(\vec{k})\} \tag{2.24}$$

where FT^{-1} represents inverse Fourier transform, $\chi(\vec{k})$ and $d(\vec{k})$ are the Fourier transforms of $\chi(\vec{r})$ and $d(\vec{r})$. $d(\vec{k})$ can be written as:

$$d(\vec{k}) = FT[d(\vec{r})] = \begin{cases} \frac{1}{3} - \frac{k_z^2}{k^2}, & for\ k \neq 0 \\ 0, & for\ k = 0 \end{cases} \tag{2.25}$$

where $k^2 = k_x^2 + k_y^2 + k_z^2$ (k_x, k_y and k_z are the coordinates in k-space). Dipole field $d(\vec{r})$ and $d(\vec{k})$ are visualized in **Fig. 2.3a,b**.

Using Eqs. 2.22 to 2.24, the induced field perturbations of an object (with a given susceptibility distribution) can be predicted from the underlying magnetic susceptibility distribution, which is referred to as 'forward modelling'. More importantly, the susceptibility distribution $\chi(\vec{r})$, which is directly related to the property of underlying tissue constituents, can be calculated from the field perturbation $\Delta B_Z(\vec{r})$, which can be calculated from the measured phase $\phi(\vec{r})$ using Eq. 2.10. However, in practice, susceptibility quantification cannot be done through a simple inversion (i.e., division by the dipole field in k-space). This is due to the presence of zeros and near-zero values in $d(\vec{k})$ as shown in **Fig. 2.3c**. Division by zero is not possible and division by near-zero

values amplifies noise present in the estimated $\Delta B_Z(\vec{r})$. Thus, the inversion from field perturbation $\Delta B_Z(\vec{r})$ to susceptibility distribution $\chi(\vec{r})$ is an 'ill-posed' inverse problem.

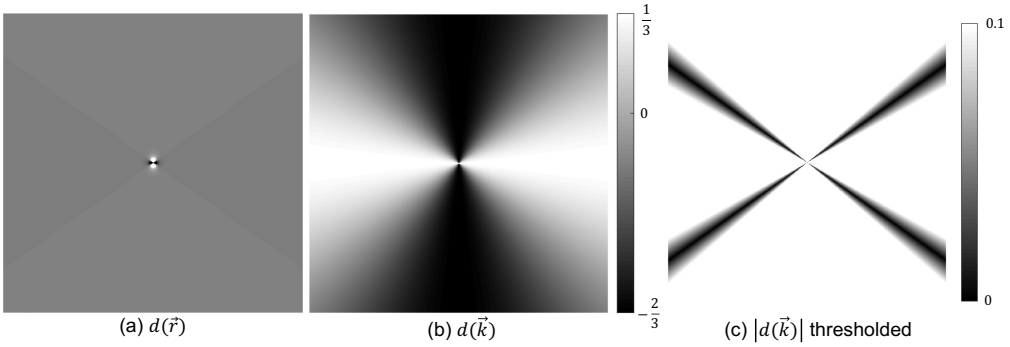


Figure 2.3 The dipole field visualized in image space (a), k-space (b) and the modulus of the dipole field in k-space $\left|d\left(\vec{k}\right)\right|$ thresholded between 0 to 0.1 to emphasize the zero and near-zero values.

An additional challenge is that raw phase, $\phi(\vec{r})$, is not directly usable, as it is normally overwhelmed with different types of 'artefacts' (**Fig. 2.2b**). In practice, susceptibility quantification from GRE phase data is composed of several steps to address these challenges.

2.6 Quantitative susceptibility mapping

A typical phase image processing pipeline is illustrated in **Fig. 2.4** and will be discussed in detail in the following sections.

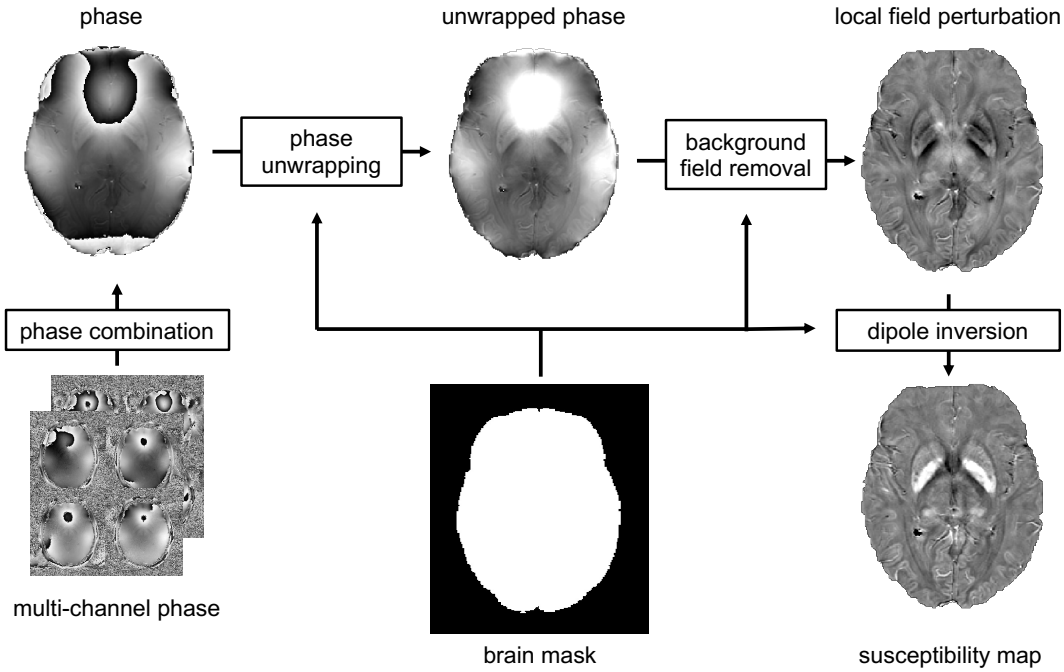


Figure 2.4 Illustration of a typical phase image processing pipeline, consisting of (1) coil combination, (2) phase unwrapping, (3) background field removal and (4) dipole inversion.

In the brain, the strongest magnetic susceptibility sources include iron content (e.g., ferritin or deoxygenated heme), calcium (e.g., mineralization or calcification), and myelin content. Susceptibility contrast can provide a marker of tissue composition of these constituents, which are all relevant to brain function and disease. For example, iron, an essential transition metal, is involved in many fundamental biological processes in the brain including neurotransmitter production, myelin synthesis and many metabolic processes [18]. Iron homoeostasis is essential to maintain normal physiological brain function, whereas elevated iron level can cause oxidative stress and cellular damage [18]. It is now clear that progressive accumulation of iron occurs in several brain regions during healthy aging [18]. However, abnormal iron accumulation is associated with many neurodegenerative diseases that are prevalent in aging population including Alzheimer's disease, Parkinson's disease, and multiple sclerosis [18]. Therefore, quantification of tissue susceptibility distribution may enable the discrimination of healthy and diseased

tissue, in addition to providing insights into mechanisms of disease and healthy brain functions.

After removal of artefacts, GRE phase images provide contrast between different tissue constituents (e.g., iron vs calcium) through their differences in χ properties. However, as discussed in section 2.5, χ creates non-local phase effects (through convolution with the dipole field), that is, biologically interesting variations in tissue χ propagate far outside the regional sources of these variations on phase images. Therefore, phase in a given voxel or region is not directly indicative of χ, as it is confounded by the distribution of χ in the vicinity. Removal of these non-local effects requires deconvolution of the dipole kernel which led to the development of quantitative susceptibility mapping (QSM) [19]. As shown in **Fig. 2.4**, QSM is a multi-step processing of the phase images from GRE acquisition that enables the quantification of the underlying χ distribution. Here, I will provide details on each of these steps.

2.6.1 Combination of multi-channel phase data

Multi-channel receive coils are widely used in MRI, providing images with a higher signal-to-noise ratio (SNR) and parallel imaging to accelerate MR acquisitions [20]. In GRE acquisitions, phase images collected from each channel are characterised by different phase offsets $\phi_0(\vec{r})$ associated with the individual coil's coil-sensitivity profile [20]. If not properly handled, these phase offset will lead to signal cancelation and subsequent artefacts in channel-combined phase data (**Fig. 2.5**). A proper combination of phase data from multi-channel coils is therefore crucial for any studies using phase images. A few established multi-channel phase combination methods are described here.

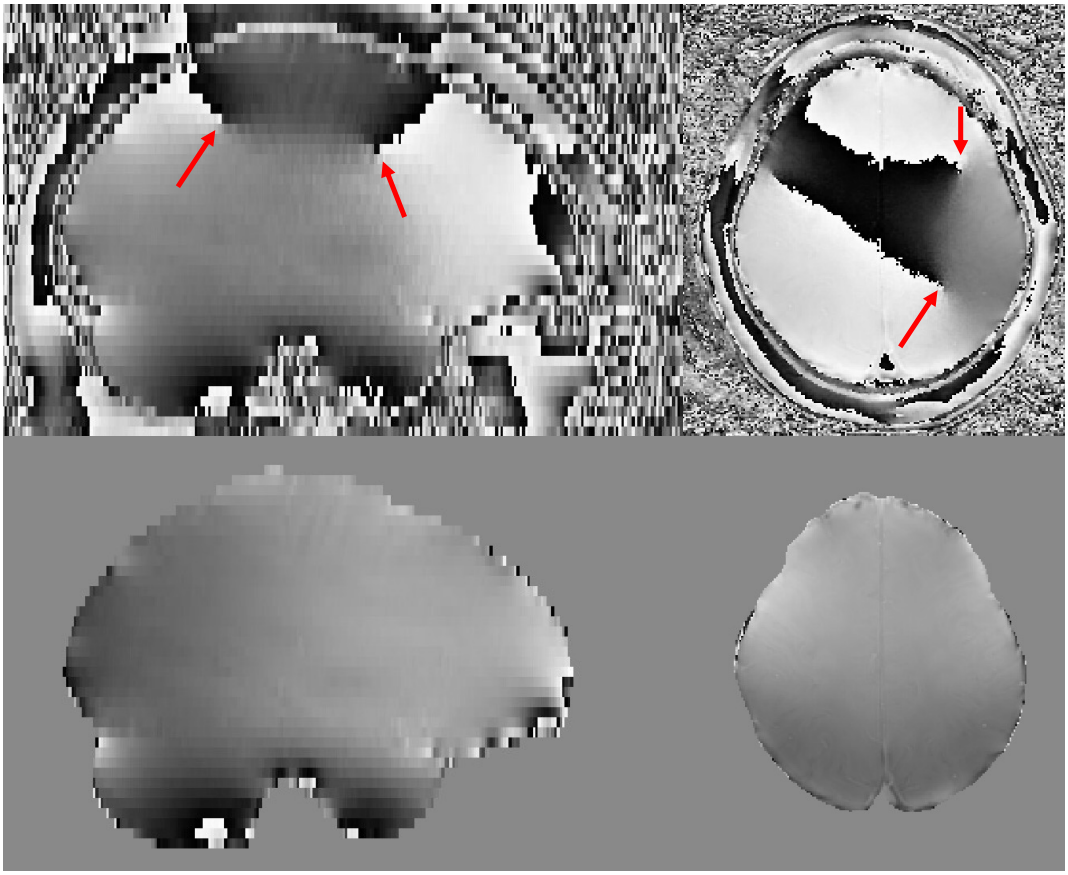


Figure 2.5 Example phase image (TE=9.4ms) combined on the Siemens scanner (top row) and off-line using MCPC-3D-S approach (bottom row) from the same set of individual-channel phase data. Red arrows are indicating the open-ended fringe lines (artefacts). These open-ended fringe lines will lead to artefacts for any analysis using the phase information.

From Eq. 2.13, phase at two echo times, TE_1 and TE_2, from the jth channel can be written as:

$$\phi^j(\vec{r}, TE_1) = -\gamma \cdot \Delta B(\vec{r}) \cdot TE_1 + \phi_0^j(\vec{r})$$

$$\phi^j(\vec{r}, TE_2) = -\gamma \cdot \Delta B(\vec{r}) \cdot TE_2 + \phi_0^j(\vec{r}) \quad (2.26)$$

Naturally, a challenge in multi-channel phase combination is removing $\phi_0^j(\vec{r})$ in order to obtain combined outputs with no phase cancellation.

Phase difference method

One simple approach to remove the channel-dependent phase offset $\phi_0^j(\vec{r})$ is to calculate the phase difference for each channel between two TEs [20], [21]. This produces a phase

map with equivalent TE = $TE_2 - TE_1$. Complex signals $S^j(\vec{r}, TE) = Mag^j(\vec{r}, TE)e^{i\phi^j(\vec{r},TE)}$ are normally used:

$$\phi_{diff,comb}(\vec{r}) = angle\left[\sum_j S^j(\vec{r}, TE_2)/S^j(\vec{r}, TE_1)\right] \quad (2.27)$$

Multi-Channel Phase Combination using 3D phase offsets simplified (MCPC-3D-S)

MCPC-3D-S [22] is a recently proposed algorithm that uses a scaled channel-combined phase difference map to estimate the phase offset in each coil, defining:

$$\phi^j_{0,est}(\vec{r}) = \phi^j(\vec{r}, TE_1) - \Psi(\phi_{diff,comb}(\vec{r})) \cdot \frac{TE_1}{TE_2 - TE_1} \quad (2.28)$$

where Ψ represents an unwrapping operator (which is required when the scaling factor $\frac{TE_1}{TE_2 - TE_1}$ is not an integer, to avoid incorrect scaling due to the presence of wraps in $\phi_{diff,comb}(\vec{r})$); and $\phi^j_{0,est}(\vec{r})$ is the estimated phase offset for jth channel. $\phi^j_{0,est}(\vec{r})$ estimates are spatially-smoothed and subtracted from $\phi^j(\vec{r}, TE_1)$ and $\phi^j(\vec{r}, TE_2)$ to generate individual channel phase data without offsets. These phase maps can be subsequently coil-combined, resulting in a single phase map for each echo. A similar method, known as 'ASPIRE' [22], uses two echoes at a specific echo time ratio (scaling factor $\frac{TE_1}{TE_2 - TE_1}$ equals to an integer) which negates the requirement of unwrapping $\phi_{diff,comb}(\vec{r})$ in Eq. 2.28.

COMbining Phase data using a Short Echo time Reference scan (COMPOSER)

COMPOSER [23] utilizes phase data acquired at a very short TE which could be collected in a separate acquisition or as the first echo of a multi-echo acquisition. This method exploits the observation that field perturbation $\gamma \cdot \Delta B(\vec{r}) \cdot TE$ tends to zero when $TE \approx 0$ such that $\phi^j(\vec{r}, TE) \approx \phi^j_0(\vec{r})$. Hence, COMPOSER uses the phase acquired at short TE as an approximation to the phase offsets, which enables a direct combination via subtraction of the reference phase $\phi^j_{ref}(\vec{r}, TE_{short})$ from phase at longer TEs $\phi^j(\vec{r}, TE)$.

In general, phase images combined using the phase difference method has the lowest SNR, compared to phase combined using other aforementioned methods. This is due to the subtraction of phase images that causes signal loss. More detailed comparisons of these methods using experimental data are presented in the following chapters.

2.6.2 Phase unwrapping

The operation of arctangent function in Eq. 2.7 is only able to produce a phase value within the range of $-\pi$ to $+\pi$. However, the true value of $\phi(\vec{r}, TE)$ may exceed these bounds and hence will be wrapped back into this range. This is called phase aliasing (or wrapping) and can be described as:

$$\phi_{wrap}(\vec{r}) = \phi_{true}(\vec{r}) + 2\pi \cdot N(\vec{r}) \tag{2.29}$$

where $N(\vec{r})$ indicates the number of 2π wraps and is always an integer. To utilize true phase images without any wraps, $\phi_{true}(\vec{r})$ is usually obtained through phase unwrapping. In practice, to calculate the number of 2π wraps (to solve Eq. 2.29), assumptions about phase continuities have to be made. Existing phase unwrapping algorithms can be categorized into two types:

Spatial domain unwrapping algorithms

Phase unwrapping in the spatial domain works under the assumption of spatial continuity of phase; that is, that phase generally changes smoothly between spatially adjacent voxels unless a wrap has occurred. To date, numerous spatial domain algorithms have been proposed, here, two of the most widely-used methods, 'PRELUDE' [24] and 'Laplacian-based unwrapping' [20], [25] will be discussed.

Phase Region Expanding Labeler for Unwrapping Discrete Estimates (PRELUDE)

PRELUDE [24] creates labels for different regions, then it uses a region-merging approach to optimize a cost function that penalizes phase differences across boundaries. It is fully automated and can be implemented on both 2D and 3D data. Essentially,

PRELUDE identifies distinct wrapped voxels and adding $\pm 2\pi N(\vec{r})$ to reveal the true phase value.

Laplacian-based unwrapping

The Laplacian unwrapping [20], [25] is based on the following relation:

$$e^{i\phi_{wrap}(\vec{r})} = e^{i\phi_{wrap}(\vec{r})\pm 2\pi N(\vec{r})}$$

and with a proper integer $N(\vec{r})$, $$= e^{i\phi_{true}(\vec{r})} \quad (2.30)$$

Based on Eq. 2.30, we can derive a relation between the Laplacians $\nabla^2\phi_{true}(\vec{r})$ and $\nabla^2\phi_{wrap}(\vec{r})$:

$$\nabla^2\phi_{true}(\vec{r}) = cos\phi_{wrap}(\vec{r})\nabla^2 sin\phi_{wrap}(\vec{r}) - sin\phi_{wrap}(\vec{r})\nabla^2 cos\phi_{wrap}(\vec{r}) \quad (2.31)$$

where $\nabla^2 sin\phi_{wrap}(\vec{r})$ and $\nabla^2 cos\phi_{wrap}(\vec{r})$ can be calculated using the properties of Fourier transforms. However, the Laplacian operation effectively performs an additional 'filtering' of the phase, due to the Laplacian of 'external field perturbations' (induced by sources outside the defined ROI) being equivalent to zero (discussed further in Section 2.6.3) [20], [26]. For QSM, this 'filtering' effect is negligible as external field perturbations are not of interest and will be removed in the 'background field removal' step (discussed in Section 2.6.3).

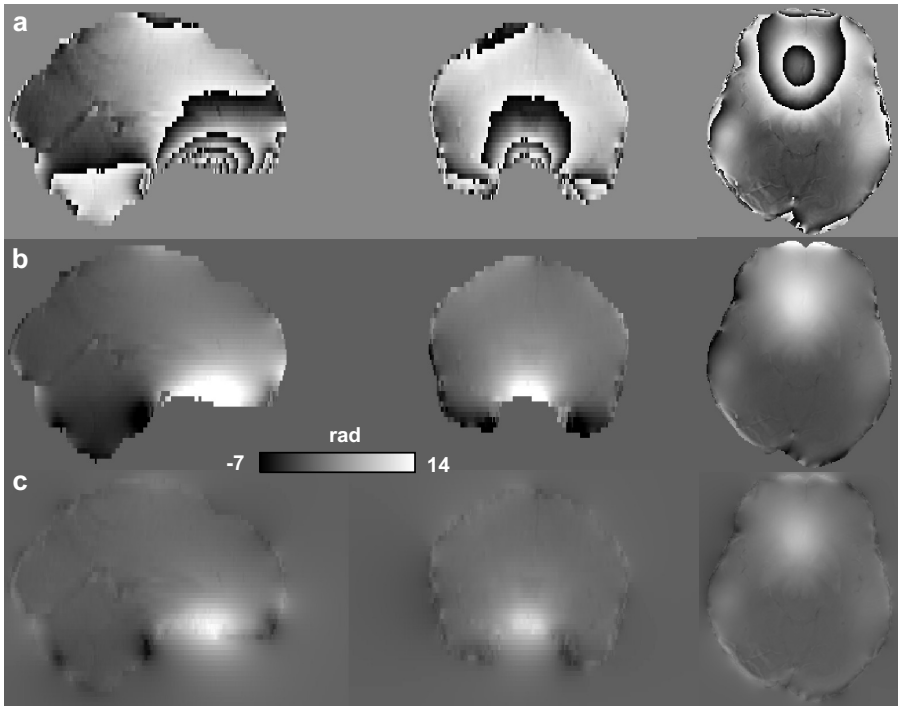


Figure 2.6 Example of phase unwrapping using two spatial domain algorithms. **(a)** Wrapped phase image. **(b)** Unwrapped phase image using PRELUDE. **(c)** Unwrapped phase image using a Laplacian-based algorithm. Both algorithms are able to produce wrap-free phase images, however, Laplacian based methods perform an additional filtering of the phase image, as highlighted by the smoothness of the resulting image (c).

Temporal domain unwrapping algorithms

Temporal domain phase unwrapping requires phase data collected at multiple echo times. Acquisitions with short echo spacing (ΔTE, effective TE between echoes) is preferred, in which phase increments between adjacent echoes are generally small. Temporal methods offer voxel-wise phase unwrapping with fast processing speed. Furthermore, when the true phase difference between two spatially adjacent voxels is greater than π (which does happen e.g., at the boundary of an iron-laden lesions), spatial domain unwrapping methods may fail due to the violation of the smoothness assumption. In such cases, temporal domain phase unwrapping may still provide reliable results as it only uses phase evolution information across TEs in a given voxel and the phase difference between two adjacent echoes may be smaller than π. The range of phase increment between two TEs can be roughly pre-estimated *in vivo*, and thus can be controlled when designing the

scanning protocol. For example, a shorter echo spacing may be appropriate when imaging patients with potential large iron-laden lesions or haemorrhage.

Phase unwrapping by fitting to the complex phase

As field perturbation $\Delta B(\vec{r})$ is of interest in QSM, not unwrapped phase itself, an alternate approach is to estimate $\Delta B(\vec{r})$ directly by fitting the complex temporal signal evolution $S(\vec{r}, TE)$ at each voxel location over echoes:

$$argmin_{\phi_0(\vec{r}),\Delta B(\vec{r})} \left\| (S(\vec{r}, TE) - |S(\vec{r}, TE)| \cdot e^{i(\phi_0(\vec{r}) + \gamma \cdot \Delta B(\vec{r}) \cdot TE)}) \right\|_2^2 \quad (2.32)$$

This method is essentially temporal-based as it only uses phase information across echoes. Note that this method does not unwrap the phase, thus, resulting $\Delta B(\vec{r})$ maps may still have wraps. To overcome this limitation, we propose an initialization of $\phi_0(\vec{r})$ and $\Delta B(\vec{r})$ terms for the fitting, which is applied experimentally in the work presented in Chapter 3. The detailed implementation of this method is discussed in Section 3.2.4.

2.6.3 Generation of masks

In QSM, an important step is to generate a binary mask defining the ROI (e.g., brain tissue without skull), which is essential for the boundary value problem in background field removal (described in Section 2.6.4). This mask may be required from the earliest stage of QSM processing (e.g., multi-channel phase combination) to the final dipole inversion. Apart from unrelated structures, noisy regions with unreliable phase values (e.g., regions near the air/tissue interfaces) should be excluded from the mask as well, as they will induce errors and artefacts to the susceptibility estimation. For in vivo brain imaging, the Brain Extraction Tool (BET) in FSL (FMRIB Software Library) [27] is widely used to generate brain masks. Alternatively, thresholding the magnitude image could also be used. Custom algorithms may be developed for specific datasets to better remove regions with unreliable phase values, for example, we developed custom algorithms to generate brain masks for each of the datasets used in Chapters 3 and 4.

2.6.4 Background field removal

As can be observed on successfully unwrapped phase images in **Fig. 2.6b,c** and **Fig. 2.7a**, slowly-varying but strong phase variations are superimposed on the phase contrast from local anatomical structures. This is because the field variation $\Delta B(\vec{r})$ extracted from phase images can be considered as a combination of a macroscopic background field $\Delta B_b(\vec{r})$ and a local field $\Delta B_l(\vec{r})$ [26]:

$$\Delta B(\vec{r}) = \Delta B_b(\vec{r}) + \Delta B_l(\vec{r}) \tag{2.33}$$

The background field $\Delta B_b(\vec{r})$ is induced by all sources outside the defined ROI, which normally includes air/tissue interfaces, field inhomogeneities and ROI geometry. In QSM, we are interested in isolating the local field, $\Delta B_l(\vec{r})$ that is generated by the susceptibility distributions inside the defined ROI. The background field is dominated by the susceptibility difference between air and tissue, which is approximately 9.04 ppm [16], much greater than the susceptibility differences between tissue inside the brain (<1 ppm) [26]. $\Delta B_b(\vec{r})$ is thus typically one to two orders of magnitude larger than $\Delta B_l(\vec{r})$ and it dominates the contrast in phase images (**Fig. 2.7a**). Hence, $\Delta B_b(\vec{r})$ needs to be removed prior to dipole inversion. To date, many algorithms have been proposed for removal of the background field.

Sophisticated Harmonic Artifact Reduction for Phase (SHARP) and its extensions

SHARP [28] is based on the principal that $\Delta B_b(\vec{r})$ is a harmonic function inside the ROI. The spherical mean value property of harmonic functions implies that:

$$\Delta B_b(\vec{r}) = \Delta B_b(\vec{r}) * s \tag{2.34}$$

where s is a normalized spherical kernel and $*$ represents a convolution operation. From Eqs. 2.33 and 2.34:

$$\Delta B'(\vec{r}) \triangleq \Delta B(\vec{r}) - \Delta B(\vec{r}) * s = \Delta B_l(\vec{r}) - \Delta B_l(\vec{r}) * s \tag{2.35}$$

$\Delta B_l(\vec{r})$ may be partially removed by the spherical filtering (convolution with the spherical kernel), hence, as a final step, the loss can be compensated by a deconvolution process:

$$\Delta B_l(\vec{r}) = \Delta B'(\vec{r}) * (\delta - s)^{-1} \tag{2.36}$$

where $(\delta - s)^{-1}$ is a regularized inverse kernel. Note that it is necessary to erode the ROI mask by the radius of the spherical kernel to remove the unreliable convolution results close to the boundary.

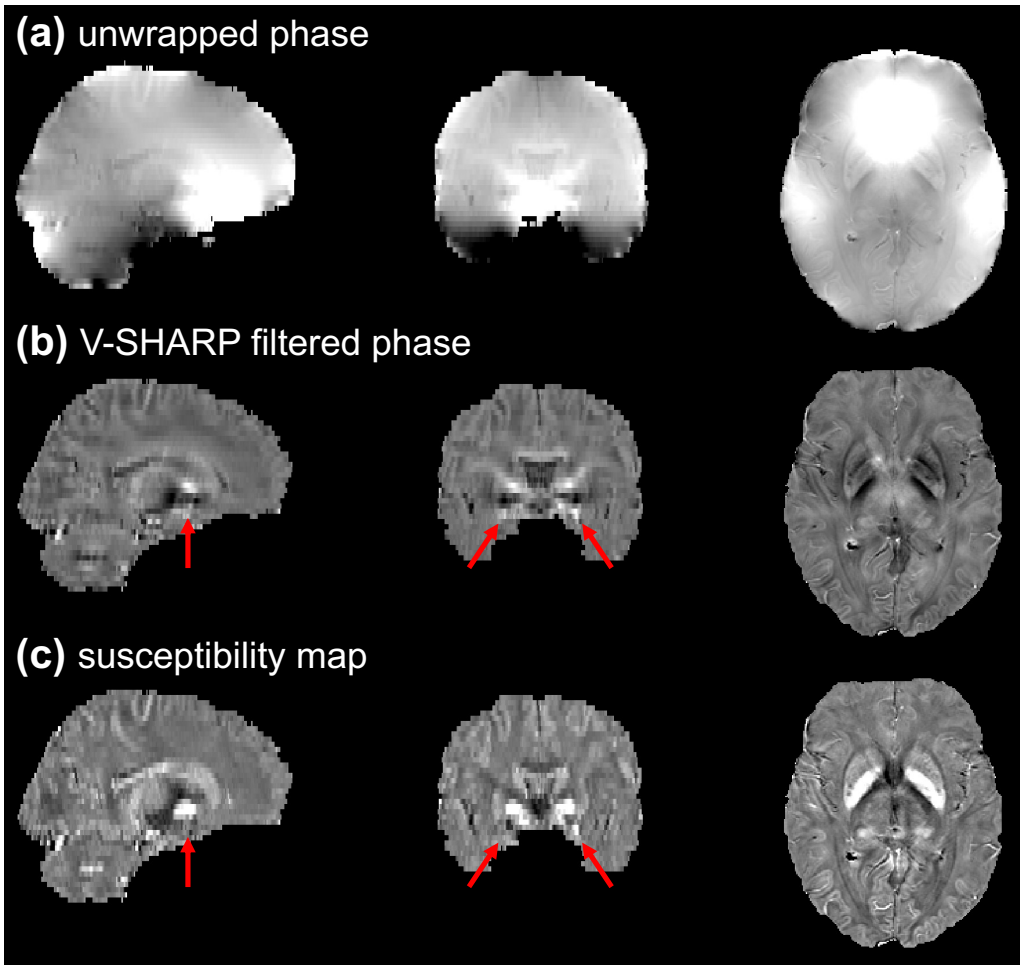


Figure 2.7 Example images of **(a)** unwrapped phase, **(b)** V-SHARP filtered phase and **(c)** susceptibility map. The contrast on unwrapped phase image (a) is dominated by strong background field $\Delta B_b(\vec{r})$. The local field, $\Delta B_l(\vec{r})$, is revealed after removal of $\Delta B_b(\vec{r})$, however, $\Delta B_l(\vec{r})$ still suffers from non-local effects as indicated by red arrows in (b), which clearly shows a dipole pattern. After dipole inversion, the underlying susceptibility distribution can be quantified. As shown in (c), dipole pattern observed in (b) arises from deep grey matter structures with high iron concentrations.

Variable-radius SHARP (V-SHARP)

The selection of the radius of the spherical kernel in SHARP is a trade-off, in which larger radius results in higher accuracy in the spherical filtering process but incurs greater loss of voxels at the ROI boundary due to the erosion step. To achieve a better compromise for this problem, Wu et al. [29] proposed to use a sphere kernel with variable radius for the convolution in Eq. 2.34, hence, V-SHARP. In V-SHARP, a large radius is used for voxels in the centre of the ROI and gradually reduced radii are used closer to the boundary. The radius of the deconvolution kernel is equal to the largest radius used in the convolution step. Therefore, the accuracy of V-SHARP processed phase gradually decreases towards the boundary due to the mismatch between radii used in convolution (used to calculate ΔB') and deconvolution kernels (used to calculate $\Delta B_l(\vec{r})$).

Regularization-enabled SHARP (RESHARP)

The accuracy of SHARP processed phase also depends on the regularization in the deconvolution process in SHARP. Sun et al. [30] proposed to use Tikhonov regularization at the deconvolution stage, by minimizing:

$$argmin_{\Delta B_l(\vec{r})} \left\| Mask \cdot [(\Delta B(\vec{r}) - \Delta B_l(\vec{r})) * (\delta - s)^{-1}] \right\|_2^2 + \lambda \|\Delta B_l(\vec{r})\|_2^2 \qquad (2.37)$$

where λ is the Tikhonov regularization parameter for the minimum-norm procedure.

Projection onto Dipole Fields (PDF)

Another popular background field removal algorithm is projection onto dipole fields (PDF) [31], which exploits the orthogonality of dipole fields generated inside and outside an ROI. In PDF, $\Delta B_b(\vec{r})$ inside the ROI is assumed to be induced purely by dipolar point sources outside the ROI, representing a susceptibility distribution $\chi_{out}(\vec{r})$ outside the ROI that induces $\Delta B_b(\vec{r})$ inside the ROI. $\chi_{out}(\vec{r})$ is estimated by minimizing:

$$argmin_{\chi_{out}(\vec{r})} \| Mask \cdot [\Delta B(\vec{r}) - B_0 \chi_{out}(\vec{r}) * d(\vec{r})] \|_2^2 \qquad (2.38)$$

where $Mask$ is the ROI mask. Once $\chi_{out}(\vec{r})$ is estimated, $\Delta B_b(\vec{r})$ can be estimated from the susceptibility distribution (Eqs. 2.23 to 2.25) and removed from $\Delta B(\vec{r})$. Note that the estimated $\chi_{out}(\vec{r})$ is not necessarily the actual susceptibility distribution outside the ROI, and should only be used for the purpose of background field removal.

Laplacian boundary value (LBV)

The aforementioned algorithms directly or indirectly exploit the observation that $\Delta B_b(\vec{r})$ is a harmonic function; that is, $\Delta B_b(\vec{r})$ is the solution of Laplace's equation. Therefore, mathematically, $\Delta B_b(\vec{r})$ can be calculated by solving $\nabla^2 \Delta B_b(\vec{r}) = 0$ inside the ROI, which effectively is a boundary value problem [32]. Although the boundary values are unknown, given the fact that $\Delta B_b(\vec{r})$ is normally one or two orders of magnitude greater than $\Delta B_l(\vec{r})$, we assume that $\Delta B(\vec{r}) = \Delta B_b(\vec{r})$ in the boundary region. Under these assumptions, the boundary value problem can be solved and thus $\Delta B_b(\vec{r})$ can be estimated. LBV uses an efficient solver (full multigrid) for this boundary value problem [32].

improved HARmonic (background) PhasE REmovaL using the LAplacian operator (iHARPERELLA)

The iHARPERELLA algorithm [33] is a Laplacian-based technique based on the same equation (Eq. 2.31) used in Laplacian phase unwrapping, thus it works with either wrapped or unwrapped phase images. It first transforms the phase image to Laplacian space $\nabla^2 \phi(\vec{r})$. The Laplacian of the phase outside the ROI $\nabla^2 \phi_{out}(\vec{r})$ is then estimated by minimizing:

$$argmin_{\nabla^2 \phi_{out}(\vec{r})} \left\| W_{ROI}(\vec{r}) \cdot FT^{-1} \left\{ \frac{1}{k^2} \cdot FT[\nabla^2 \phi(\vec{r}) \cdot Mask + \nabla^2 \phi_{out}(\vec{r})(1 - Mask)] \right\} \right\|_2^2 \quad (2.39)$$

where $W_{ROI}(\vec{r})$ is a weighting function and $Mask$ is the ROI mask. Once $\nabla^2 \phi_{out}(\vec{r})$ is estimated, $\Delta B_l(\vec{r})$ can be calculated as:

$$\Delta B_l(\vec{r}) = Mask \cdot FT^{-1}\left\{\frac{1}{k^2} \cdot FT[\nabla^2\phi(\vec{r}) \cdot Mask + \nabla^2\phi_{out}(\vec{r})(1 - Mask)]\right\} \quad (2.40)$$

2.6.5 Dipole inversion

After removal of the background field, contrast from anatomical structures is revealed on $\Delta B_l(\vec{r})$ map, however, $\Delta B_l(\vec{r})$ still reflects non-local effects rather than the local susceptibility (**Fig. 2.7b**). Therefore, it is necessary to obtain the true susceptibility distribution $\chi(\vec{r})$ from $\Delta B_l(\vec{r})$. As discussed in Section 2.5, the dipole field $d(\vec{k})$ has zeros and near-zero values which makes a direct inversion impossible. Many algorithms have been proposed to overcome the ill-posed nature of this inversion from $\Delta B_l(\vec{r})$ to $\chi(\vec{r})$. Existing algorithms can be classified into two major types:

Single orientation methods

Thresholded k-space division (TKD).

The simplest way to solve the inverse problem is setting thresholds $\alpha_{\pm}$ to construct a truncated dipole field in k-space $d(\vec{k})$ as:

$$d(\vec{k}) = \begin{cases} \alpha_- \,, if\ d(\vec{k}) > \alpha_- \ and\ d(\vec{k}) < 0 \\ \alpha_+ \,, if\ d(\vec{k}) \geq 0\ and\ d(\vec{k}) < \alpha_+ \\ \left(\frac{1}{3} - \frac{k_z^2}{k^2}\right), \qquad otherwise \end{cases} \quad (2.41)$$

This method is referred to as 'thresholded k-space division' (TKD) [19], [34]. The TKD method is time-efficient and effective, but it leads to streaking artefacts in the reconstructed $\chi(\vec{r})$ maps and is known to under-estimate $\chi(\vec{r})$.

Least Squares Minimisation with Regularisation

More sophisticated algorithms have been proposed to improve the quality and accuracy of $\chi(\vec{r})$ maps. Many novel algorithms solve the inversion problem as an optimization process:

$$argmin_{\chi(\vec{r})} \|W \cdot [\Delta B(\vec{r}) - \chi(\vec{r}) * d(\vec{r})]\|_2^2 + \lambda \cdot a \quad (2.42)$$

where W is a weighting function and $\lambda \cdot a$ is a regularisation term. Different combinations of W and $\lambda \cdot a$ are utilized in a variety of algorithms.

Morphology enabled dipole inversion (MEDI)

MEDI [35] imposes an anatomical prior that assumes edges in the $\chi(\vec{r})$ map coincide with edges in the corresponding magnitude images. In MEDI, the weighting function W is proportional to the image magnitude to compensate for the noise variation in $\Delta B(\vec{r})$ measurement. The regularisation term is $\|M\nabla\chi(\vec{r})\|_1$, where M is derived from the gradient of the magnitude image and ∇ represents the gradient operator. Thus, Eq. 2.42 becomes:

$$argmin_{\chi(\vec{r})}\|W \cdot [\Delta B(\vec{r}) - \chi(\vec{r}) * d(\vec{r})]\|_2^2 + \|M\nabla\chi(\vec{r})\|_1 \quad (2.43)$$

Total Field Inversion (TFI)

A derivative of MEDI is the total field inversion (TFI) method [36]. As the name suggests, TFI utilizes total field $\Delta B(\vec{r})$ for the dipole inversion; therefore, background field removal is not required prior to TFI. TFI can jointly estimate susceptibility sources outside and inside the ROI, $\chi_{out}(\vec{r})$ and $\chi_{in}(\vec{r})$ respectively, by minimizing:

$$argmin_{\chi_{total}(\vec{r})}\frac{1}{2}\|W \cdot [\Delta B(\vec{r}) - \chi_{total}(\vec{r}) * d(\vec{r})]\|_2^2 + \lambda \cdot \|M\nabla\chi_{total}(\vec{r})\|_1 \quad (2.44)$$

where $\chi_{total}(\vec{r}) = \chi_{in}(\vec{r}) + \chi_{out}(\vec{r})$. Like MEDI, W is a weighting function proportional to the image magnitude to compensate for the noise variation in $\Delta B(\vec{r})$ measurement, M is derived from the gradient of the magnitude image and ∇ represents the gradient operator. This iterative optimization process can lead to slow convergence, so Li et al. [36] proposed using a prior-enhanced preconditioning to improve convergence speed.

Streaking artifact reduction for QSM (STAR-QSM)

STAR-QSM [37] carries out a 'two-level' susceptibility estimation by varying the regularisation λ, to better suppress streaking artifacts induced by strong susceptibility sources. In STAR-QSM, the algorithm minimises:

$$argmin_{\chi(\vec{r})}\|\Delta B(\vec{r}) - \chi(\vec{r}) * d(\vec{r})\|_2^2 + \lambda \cdot \left\|W_\chi \nabla\chi(\vec{r})\right\|_1 \quad (2.45)$$

Where λ is the regularization parameter that determines the smoothness of the reconstructed $\chi(\vec{r})$ map. W_χ is a weighting factor derived from susceptibility map estimated initially using Fast-QSM method [38]. Fast-QSM is a method that measures $\chi(\vec{r})$ using a filtered direct inversion to provide an accurate estimate of susceptibility boundaries. ∇ represents the gradient operator.

In first level, a large λ is used to estimate strong susceptibility sources $\chi_{strong}(\vec{r})$. The field perturbation induced by the strong susceptibility sources is reconstructed and subsequently subtracted from the total field map $\Delta B(\vec{r})$ yielding $\Delta B_{residual}(\vec{r})$. $\chi_{residual}(\vec{r})$ is estimated from $\Delta B_{residual}(\vec{r})$ and finally, $\chi_{STAR}(\vec{r}) = \chi_{strong}(\vec{r}) + \chi_{residual}(\vec{r})$.

iLSQR

The iLSQR method [38] builds on the original LSQR [29] method by incorporating a 'three-level' estimation to further suppress the streaking artefacts. The LSQR method exploits the fact that at locations where $d(\vec{k}) = 0$, its first-order derivative, $d'(\vec{k}) \neq 0$. The first step in iLSQR is to estimate χ using the LSQR method where $\chi_{LSQR}(\vec{r})$ is estimated by solving:

$$FT^{-1}\{d(\vec{k}) \cdot FT(W \cdot \Delta B(\vec{r}))\} = FT^{-1}\{d(\vec{k}) \cdot FT[W \cdot FT^{-1}\{d(\vec{k}) \cdot FT(\chi_{LSQR}(\vec{r}))\}]\} \quad (2.46)$$

where W is an image-domain weighting term which is used to reduce artifacts caused by strong susceptibility sources that lead to inaccurate phase unwrapping. In the (separate)

second step, the susceptibility artefact (in k-space) $\chi_{SA}(\vec{k})$ in a direct dipole inversion is estimated by minimizing:

$$argmin_{\chi_{SA}(\vec{k})} \left\| W_\chi \cdot \nabla\{\chi_0 - FT^{-1}[\chi_{SA}(\vec{k}) \cdot Mask_{ill}]\} \right\|_2^2 \quad (2.47)$$

where W_χ is a weighting factor derived from susceptibility map estimated initially using Fast-QSM method. ∇ represents the gradient operator. $\chi_0(\vec{r})$ is the susceptibility estimation by directly solving Eq. 2.24. $Mask_{ill}$ is a binary mask of the k-space regions of dipole field where $|d(\vec{k})| < th$, which corresponds to regions with zeros and near-zero values in dipole field. The final susceptibility $\chi_{iLSQR}(\vec{r})$ can be calculated as:

$$\chi_{iLSQR}(r) = \chi_{LSQR}(\vec{r}) - FT^{-1}[\chi_{SA}(\vec{k}) \cdot Mask_{ill}] \quad (2.48)$$

Multiple orientation methods

An alternative approach to solve the ill-posed inversion problem is acquiring data with multiple orientations with respect to the $\vec{B}_0$ field. As this orientation varies, the ill-conditioned region of a dipole field (i.e., regions with zeros and near-zero values) rotates accordingly, due to a basic Fourier relationship that a rotation in image domain is also a rotation in its Fourier domain. Combining data at different orientation can effectively produce a dipole field without ill-conditioned regions. Thus, this can almost perfectly solve the inversion problem. This method is known as Calculation of Susceptibility Through Multiple Orientation Sampling (COSMOS) [39] . As the resulting χ maps exhibit good quality with little or no streaking artifacts, COSMOS is often considered to be the gold standard of dipole inversion. However, COSMOS requires data collected at a minimum of three orientations which prolongs the scan time and is impractical in clinical settings. In addition, as COSMOS assumes isotropic susceptibility, it is confounded by anisotropic susceptibility, particularly in regions contain white matter fibre bundles.

In light of the recent advances in deep learning techniques, several learning-based algorithms have been proposed for dipole inversion. Some of these algorithms trained their models with χ maps reconstructed using COSMOS, which offers the potential of generating COSMOS-quality χ maps from single orientation data [40].

2.6.6 Performance of phase processing algorithms

The performance of aforementioned algorithms has been extensively evaluated in literature, but there is not necessarily a single 'best' algorithm for each processing step. The potential artefacts from one stage of processing can be more or less problematic for different algorithms at later stages. The performance of these algorithms depends to a non-trivial degree on the properties of the data, which will be driven by hardware and protocol details.

Therefore, in the work presented in this thesis, evaluations of these algorithms were performed for the purpose of finding the optimal combination of algorithms for our specific datasets. The details of these evaluations are discussed in Chapter 3 and 4.

Chapter 3

Methods for quantitative susceptibility and R2* mapping in whole post-mortem brains at 7T

3.1 Introduction

In this chapter, methods for quantifying magnetic susceptibility (χ) and R2* (1/T2*) in whole, fixed post-mortem brains are presented, with direct comparisons to histology in the same tissue. This chapter is based on a peer-reviewed journal paper we published in NeuroImage [1].

As discussed in Chapter 2, susceptibility-weighted MRI is sensitive to the para- and diamagnetic properties of tissue. This sensitivity forms the foundation of contrast in images derived from both QSM and R2* mapping [2]. A fundamental difference between QSM and R2* mapping is that para- and diamagnetic inclusions have opposite effects on χ, but the same effect on R2*. In neurodegenerative diseases, changes in tissue myelin and iron content may co-occur. As myelin and iron have opposing signs of χ, the combination of QSM and R2* mapping has the potential to shed light on the overall pathology, provided their histopathological correlates can be clearly defined.

To date, several studies have reported the correlation of R2* and χ with brain iron and myelin content using either whole, unfixed post-mortem brains (in situ) or small, fixed brain tissue samples [3–7]; however, no studies have applied QSM in whole, fixed post-mortem brains. Imaging whole fixed brains presents additional challenges including the presence of air bubbles, which induce rapid focal field variations; and the influence of brain shape on the macroscopic magnetic field homogeneity. To directly compare whole-brain QSM to histology in the same tissue, we therefore need to develop bespoke imaging approaches and processing pipelines for whole, fixed post-mortem brains. Here, we demonstrate this approach in an exemplar neurodegenerative disease, amyotrophic lateral sclerosis (ALS).

ALS is a terminal neurodegenerative disease of the motor system, characterized by rapidly progressive and irreversible loss of motor function [8]. In the brain, ALS pathology is hypothesized to follow a standard progression within the cerebral cortex, starting in the primary motor cortex (M1) and gradually progressing into other brain regions [9,10]. By the end-stage of the disease (corresponding to the situation encountered post-mortem), different brain regions are anticipated to have different degrees of neuropathology, dependent on their stage of involvement (**Fig. 3.1**).

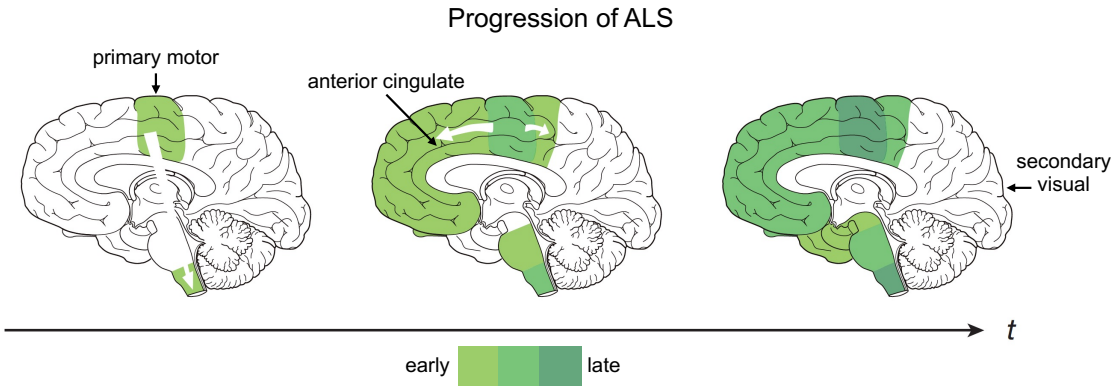


Figure 3.1 Illustration of a typical progression of ALS pathology. M1 is involved from the beginning of the disease (Stage 1, anticipated significant pathology), the anterior cingulate cortex (ACC) is involved at a later disease stage (Stage 2/3, anticipated intermediate pathology), and the secondary visual cortex (V2) is uninvolved (no involvement, anticipated no pathology) [15]. Diagrams of brain were adapted from [11].

Our motivation for scanning whole brains (as opposed to small tissue samples) is to study the relationship between MRI and histopathology across different brain regions anticipated to be involved at different timepoints in ALS [12] (**Fig. 3.1**). Importantly, estimates of χ and R2* have demonstrated sensitivity to changes in tissue composition associated with ALS pathology. A previous study comparing R2* with iron histology in a single ALS brain demonstrated elevated R2* in the deep layers of M1 that corresponded to iron accumulation shown with iron histological staining [13]. Recent in vivo QSM studies of ALS have shown elevated χ in the motor cortex and a range of subcortical nuclei [14-16], hypothesized to be driven by an increased concentration of iron.

To perform our investigation, susceptibility-weighted MR data were acquired using a multi-echo gradient echo (GRE) acquisition in whole, fixed post-mortem brains from nine ALS patients and three control subjects. Based on both realistic simulations and experimental post-mortem data, we developed a custom analysis pipeline to generate quantitative χ and R2* maps in each post-mortem brain. Brains were subsequently sectioned and stained using immunohistochemistry targeting myelin proteolipid protein (PLP) and ferritin in three brain regions associated with different disease stages of ALS (M1, ACC and V2, anticipated to have a different neuropathological profile) and correlated with χ/R2* estimates in the same regions. Our results provide proof-of-principle for using MRI-histology comparisons to study the histopathological correlates of neurodegeneration at the whole brain level.

3.2 Methods

3.2.1 Post-mortem brain samples

Twelve whole, formalin fixed post-mortem brains were obtained from the Oxford Brain Bank (based at the John Radcliffe Hospital, Oxford), under its generic Research Ethics

Committee approval (15/SC/0639). The cohort consisted of nine donors with a clinical diagnosis of ALS, and three control donors with no known neurological disorder. Diagnosis was confirmed by a neuropathologist. Patient demographics, post-mortem information, and relevant tissue handling properties are listed in **Table 3.1**.

Table 3.1 Patient demographics and post-mortem information.

Case	Age	Sex	PM delay (days)	Fixative	Time in fixative before scan (days)	Neuropathological diagnosis
1	66	M	7	10% Formalin	137	ALS
2	65	M	4	10% Formalin	94	ALS
3	76	M	3	10% Formalin	158	ALS
4	68	M	1	10% NBF	35	ALS
5	54	M	N/A	10% Formalin	77	ALS
6	65	M	N/A	10% Formalin	96	ALS
7	68	M	2	10% NBF	87	ALS
8	71	M	3	10% NBF	94	ALS
9	79	F	2	10% NBF	139	ALS
10	61	M	3	10% NBF	115	Control
11	74	M	3	10% NBF	45	Control
12	61	M	3	10% NBF	396	Control

PM delay = post-mortem delays, indicating the time between death and tissue dissection;N/A = Not Available; NBF = Neutral Buffered Formalin

3.2.2 Sample preparation and MRI data acquisition

Brains were imaged using a 7T whole-body human scanner (Siemens Healthcare, Erlangen, Germany) using a 32-channel head coil and a multi-echo GRE sequence. To prepare each brain for scanning, the brain was first removed from storage in formalin.

Excess formalin remaining within the ventricles was removed by mildly compressing the brain whilst being held with the cerebellum pointing downwards. Excess formalin on the brain surface was removed using paper towels. The brain was then placed in a plastic bag filled with a susceptibility-matched perfluorocarbon liquid (3M™ Fluorinert™ FC-3283) and gently compressed/rotated to fill the ventricles with Fluorinert and remove any excess air-bubbles. This process also removed any remaining formalin within the ventricles, which has a lower density than Fluorinert (and hence floats to the top of the bag). This process continued until no new air-bubbles/formalin were observed. The brain was subsequently transferred and sealed in a 3D printed brain-shaped container (**Fig. 3.2**), keeping the fourth ventricle pointing upwards to prevent loss of Fluorinert during the transition. The 3D printed shell was subsequently filled with Fluorinert and gently manipulated to remove any new air bubbles that may have formed during the transfer.

This brain-shaped container was then placed in an external brain holder with a dome-shape chamber (**Fig. 3.2**) that was again filled with Fluorinert. This external holder achieves two aims: first, ensuring that brains are consistently positioned in the main magnetic field; and second, providing a spherical shape that minimizes field distortions in the brain. Both of these aims will benefit reproducibility and data quality. As shown in **Fig. 3.3**, the phase images acquired with the spherical holder showed substantially less phase aliasing, reflecting improved B0 homogeneity.

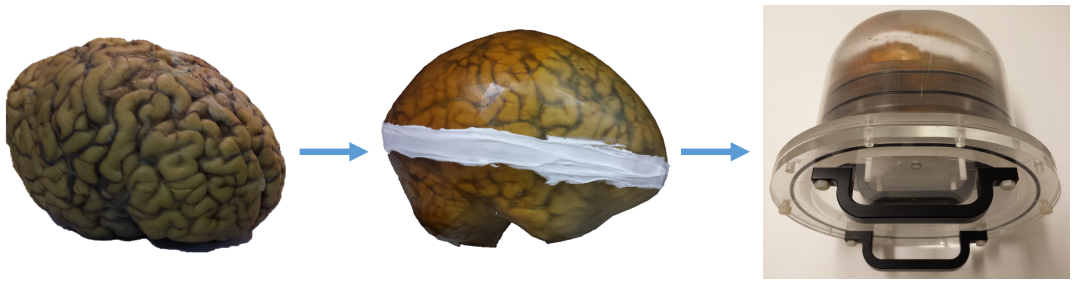


Figure 3.2 Illustration of the 3D printed shell and external holder for scan preparation. The 3D printed shell was provided by Dr Alard Roebroeck, Maastricht University. The custom holder was provided by Dr Sean Foxley.

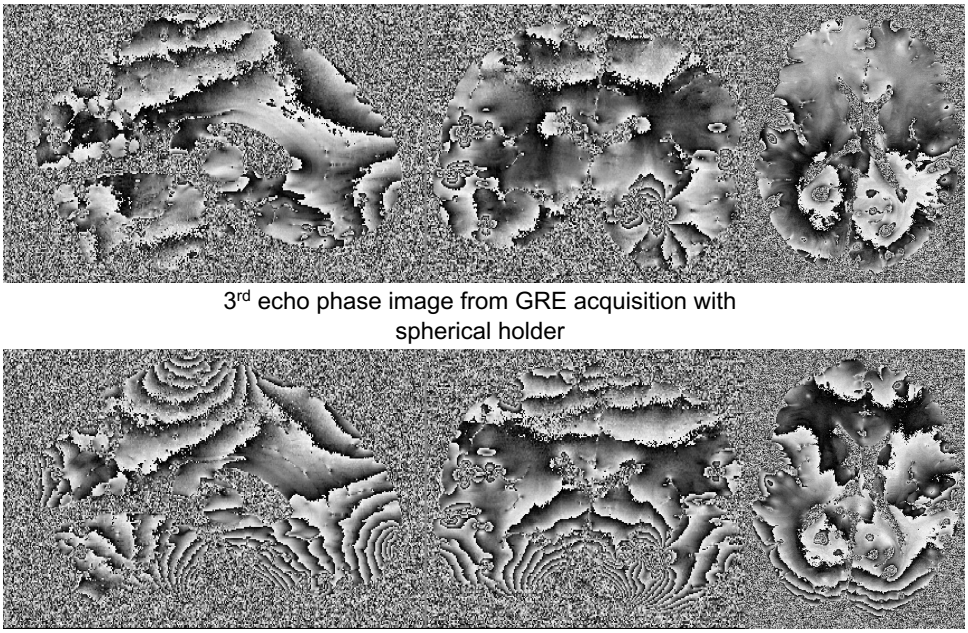


Figure 3.3 Comparison of the measured GRE phase in a post-mortem brain with (top) and without (bottom) the custom holder. The phase images acquired with the spherical holder (top) show substantially less phase aliasing, reflecting improved B0 homogeneity. Phase images displayed here were generated using the manufacturer-supplied reconstruction, rather than the custom reconstruction pipeline from the k-space data described in Section 3.2.4.

Susceptibility-weighted data were collected each brain using a 3D multi-echo GRE sequence with following parameters: TEs = 2, 8.6, 15.2, 21.8, 28.4, 35 ms with monopolar readout (i.e., readout gradients for all echoes had the same polarity) and non-selective RF pulse, TR = 38 ms, flip angle = 15°, bandwidth = 650 Hz/pixel, GRAPPA factor = 2, in-plane resolution = 0.5x0.5 mm^2, and number of repeats = 4.

Over the course of our experiment, the acquisition was modified to increase the resolution along the slice direction. Here, cases 1-3 were scanned with slice thickness = 1.3 mm (cases 4-7 with 1.2 mm), cases 1-7 were scanned with matrix size = 384x310x104, total scan time = 11 min); Cases 9-12 were scanned with slice thickness = 0.6 mm (Case 8 with 0.55 mm), Cases 8-12 were scanned with matrix size = 384x310x208, total scan time = 22 min). The GRE acquisition was repeated four times for each brain with raw multi-channel k-space data collected.

To perform our comparative analysis at a similar voxel size, the raw k-space data from Cases 8-12 was truncated along the slice direction to down-sample the data to closely match the slice thickness of Cases 1-7 (1.1 mm for Case 8 and 1.2 mm for Case 9-12). As part of a larger study, structural, relaxometry and diffusion data were also acquired (full details of the multi-modal MRI acquisition are described in [12]).

3.2.3 Post-mortem brain susceptibility model simulation and QSM pipeline evaluations

To select the optimal combination of QSM algorithms for our post-mortem setup, an evaluation of the robustness of different algorithms for background field removal and dipole inversion in post-mortem data processing was performed using both simulated and experimental data.

Brain susceptibility model simulation

To simulate the postmortem brain acquisition, a 3D post-mortem brain susceptibility model was generated based on a model proposed by Haacke et al. [19], as shown in **Fig. 3.3a,b**. This model was designed to closely match our post-mortem acquisition: no skull or CSF was present in the simulation, and the brain model was surrounded by a susceptibility-matched medium (equivalent to our custom-built holder filled with the susceptibility-matched fluid Fluorinert shown in **Fig. 3.2**). We assigned typical χ values to the tissue (brain tissue: -0.02 to 0.06 ppm, Fluorinert: 0 ppm, air: 9.4 ppm) [19]. Based on to Eq. 2.23 in Chapter 2, the brain susceptibility model was convolved with a dipole kernel to generate the field perturbation map and subsequently multiplied by gyromagnetic ratio and echo time to simulate the phase images acquired from a 3D GRE acquisition. Here, the ground truth phase (without background field, **Fig. 3.3c**) was calculated using only the brain tissue (without simulating the air compartments, **Fig. 3.3a**). The simulated post-mortem phase (**Fig. 3.3d**) was calculated using the simulation setup

where brain was placed inside a spherical holder (filled with Fluorinert) along with outside air compartments (**Fig. 3.3b**).

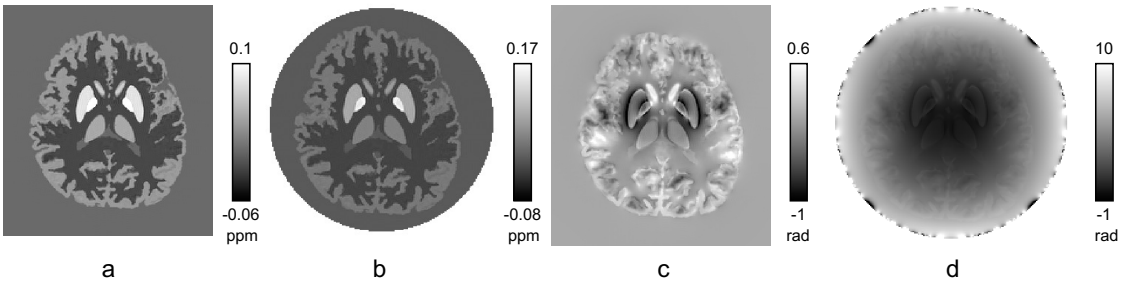


Figure 3.3 Brain model simulation. **(a)** Axial slice of the 3D susceptibility model with brain tissue only, the susceptibility outside the brain is set to 0 ppm. **(b)** Axial slice of the 3D susceptibility model with brain tissue and Fluorinert inside a spherical holder, the susceptibility outside the holder is set to 9.4ppm (air). **(c)** Same slice showing phase ground truth image (phase induced by local field only) **(d)** Same slice showing simulated post-mortem phase images including the Fluorinert and air compartments.

Evaluation of algorithms for background field removal and dipole inversion

Three existing algorithms for background field removal were evaluated: variable kernel SHARP (V-SHARP) [19,20], projection onto dipole fields [21] and Laplacian boundary value (LBV) [22]. We also evaluated three algorithms for dipole inversion: thresholded k-space division (TKD) [23], morphology enabled dipole inversion (MEDI) [24] and streaking artifact reduction for QSM (STAR-QSM) [25]. The detailed description of these algorithms is presented in Chapter 2, section 2.6.

Brain simulations

The accuracy of the three background field removal algorithms was evaluated through error maps calculated as background-field removed post-mortem phase subtracted by the ground truth phase (**Fig. 3.3c**). The estimated χ maps from the three dipole inversion algorithms were also compared with the ground truth χ distribution (**Fig. 3.3a**) with error maps (via subtraction) were generated to assess the accuracy of the algorithms.

As shown in **Fig. 3.4**, LBV was able to remove background field from simulated phase images with the best accuracy compared to V-SHARP and PDF. Therefore, three dipole

inversion algorithms were performed to the LBV processed phase. As shown in **Fig. 3.5**, χ maps generated by MEDI clearly demonstrate the lowest error compared to the ground truth, and in particular more homogeneous χ values. Note that due to the lack of 'real' magnitude data associated with this simulation, the 'magnitude' data fed into MEDI were derived from the ground truth susceptibility model (i.e., this 'magnitude' data had the same edge information as the susceptibility model, which would not happen in experimental data). This could explain the superior performance of MEDI in this simulation, as MEDI imposes structural consistency between magnitude and susceptibility images. χ maps generated by TKD and STAR-QSM demonstrated similar quality.

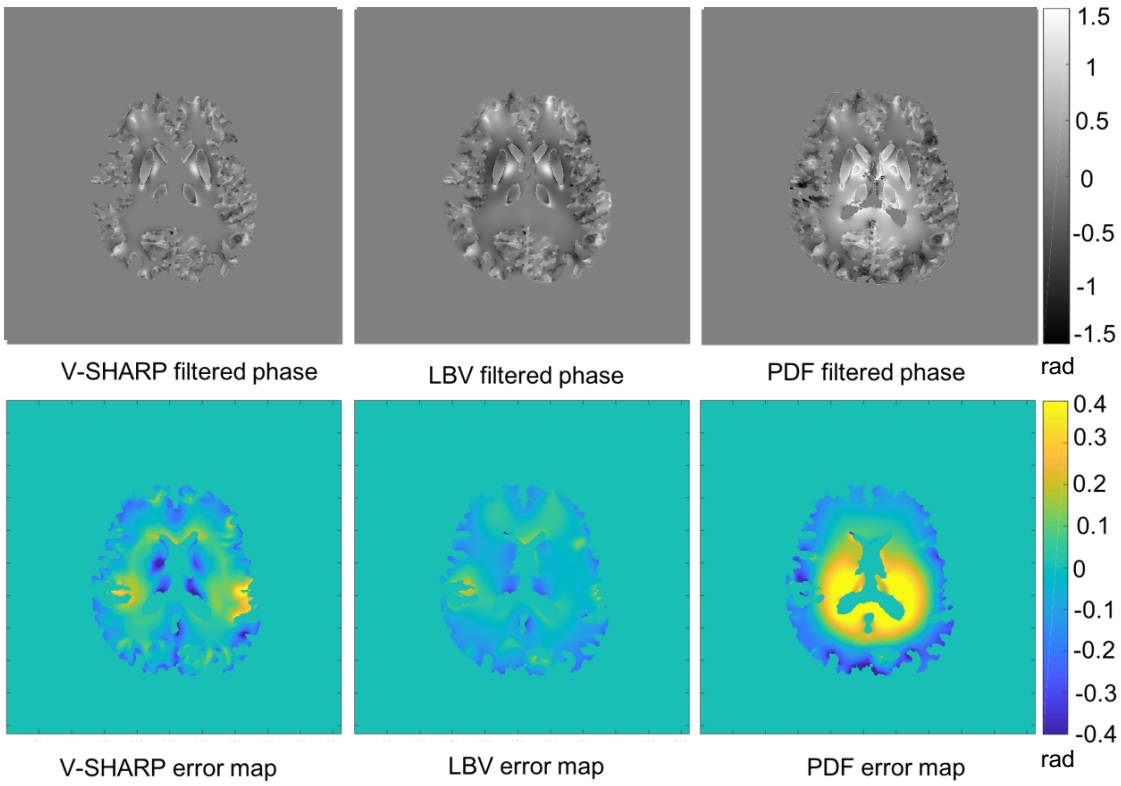


Figure 3.4 Simulated phase maps (in rad) processed using the three background field removal algorithms (top) and their corresponding error maps (bottom) defined as their differences with respect to the ground truth phase. Here, codes for LBV and PDF were from the MEDI toolbox, and the V-SHARP code was written in-house.

Experimental post-mortem data

For experimental post-mortem data where there is no ground truth, the performance of different combinations of algorithms was evaluated by visual inspection of the quality of the final χ maps. Representative χ maps from these comparisons are shown in **Fig. 3.6**. Overall, we found that the combination of V-SHARP and STAR-QSM was the most robust for our given post-mortem datasets, yielding χ maps which did not contain large scale inhomogeneities (consistent with incomplete background field removal), had fewer steaking artefacts and did not appear over-smoothed.

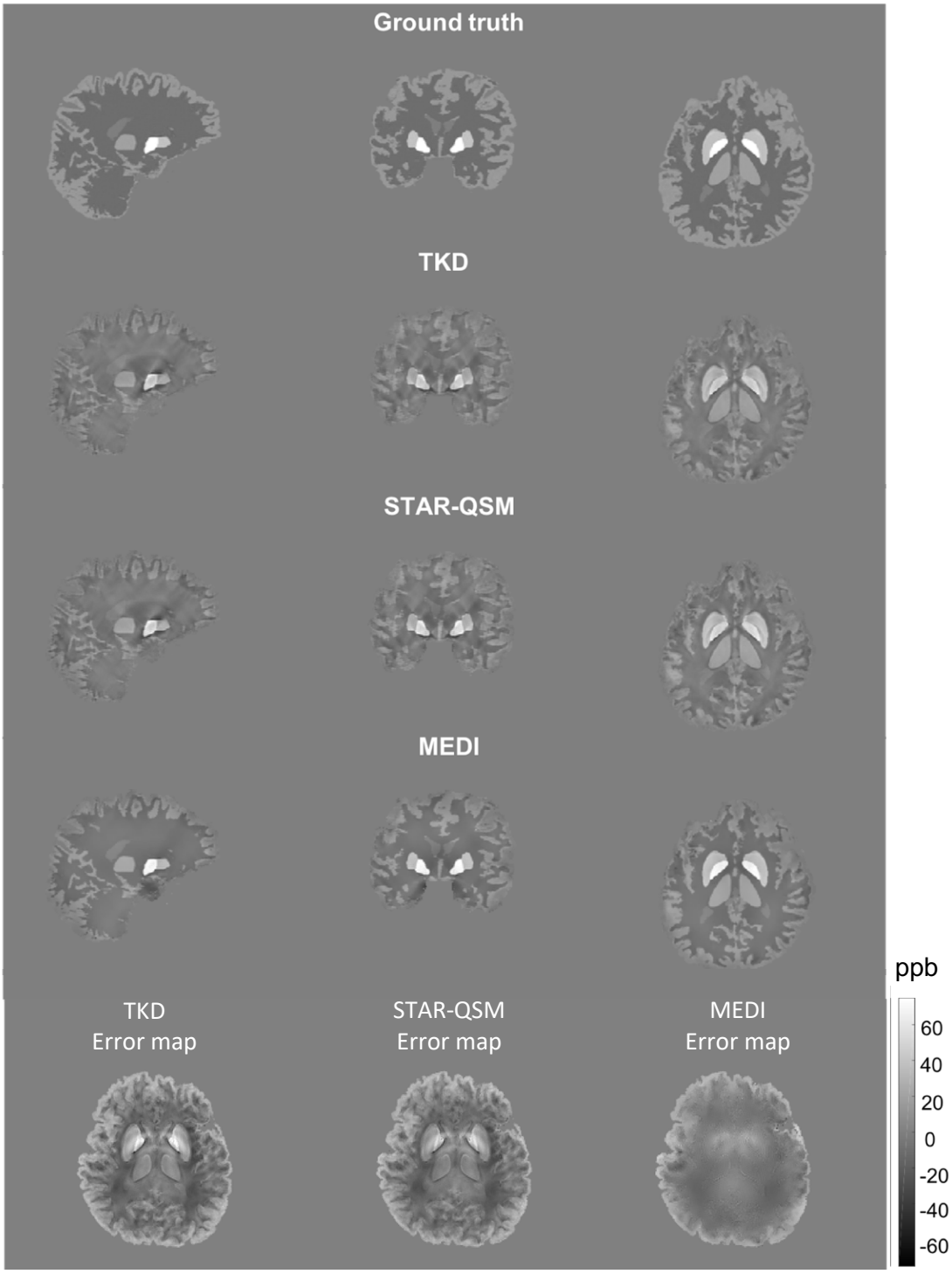


Figure 3.5 Resulting χ maps using TKD, MEDI and STAR-QSM dipole-inversion algorithms (from LBV processed phase), with corresponding error maps (last row) defined as their differences with respect to the ground truth χ distribution.

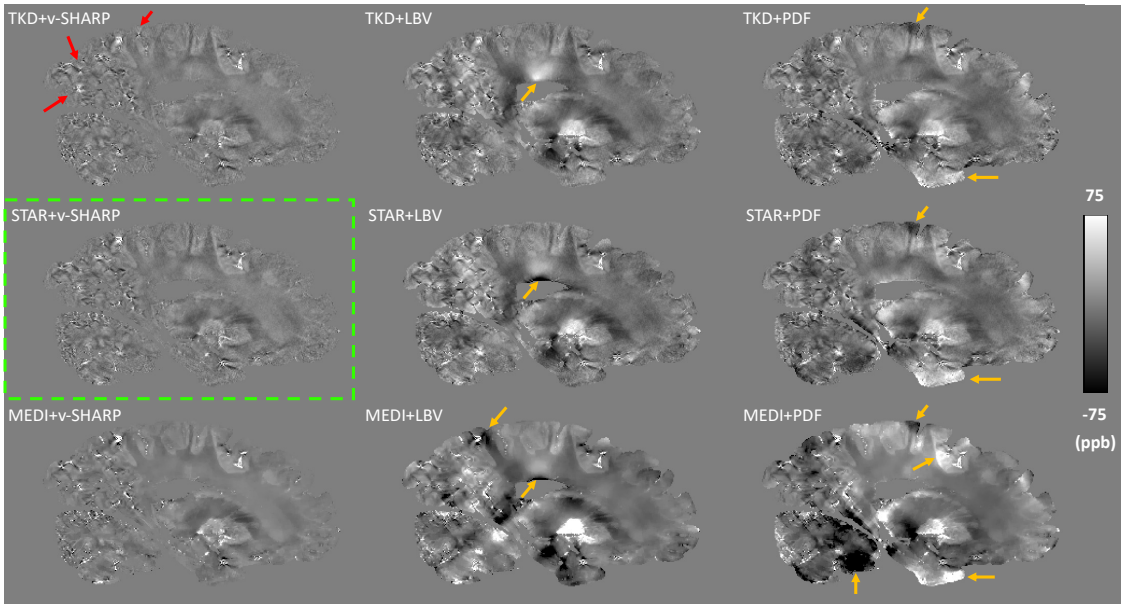


Figure 3.6 χ maps from combinations of three background field removal methods and three dipole inversion methods. Red arrows indicate streaking artefacts and orange arrows indicate remaining large scale inhomogeneities on other χ maps compared to maps generated using STAR-QSM and v-SHARP. χ maps generated with MEDI showed slightly different contrast compared to χ maps generated using other methods, for instance, there was less contrast within white matter regions but very sharp edges at the grey and white matter boundary. Although there was no ground truth χ maps to validate, given that MEDI imposes regularization based on magnitude gradients, this 'smooth' contrast was deemed unrealistic for χ distributions in the brain. Implementation of PDF, LBV and MEDI were from the MEDI toolbox. Implementation of STAR-QSM was from STI suite (https://people.eecs.berkeley.edu/~chunlei.liu/software.html).

The comparisons using simulated and experimental postmortem data yielded inconsistent results. One potential explanation for this is that MEDI imposes L1 regularization based on prior magnitude information (spatial gradients of magnitude images) [24], as discussed in Chapter 2. Preliminary tests were performed to evaluate various regularization parameters for MEDI, and the results showed that the χ maps generally showed similar contrast with small differences. In the simulated data, magnitude images had the same gradients as the ground truth χ distribution. However, this will not be the case in real experimental data: magnitude images do not necessarily have the same tissue contrast as χ maps and therefore will not have an identical gradient profile. Given the discrepancy between simulated and experimental data for evaluating MEDI, we based our evaluations on the experimental analysis. Here, it was found that

STAR-QSM generated χ maps with reduced streaking artefacts and inhomogeneities compared to the other dipole inversion algorithms (**Fig. 3.6**). Notably, STAR-QSM was initially anticipated to yield improved χ maps from post-mortem imaging, given its accommodation of large χ variations in tissue (e.g., air-bubbles) as discussed in Chapter 2.

3.2.4 Experimental QSM post-processing pipeline

Based on the aforementioned evaluation, an image processing pipeline for generating QSM and R2* maps was developed for our post-mortem data. The overall pipeline is displayed in **Fig. 3.7**. the details of each processing step are described in the following sections.

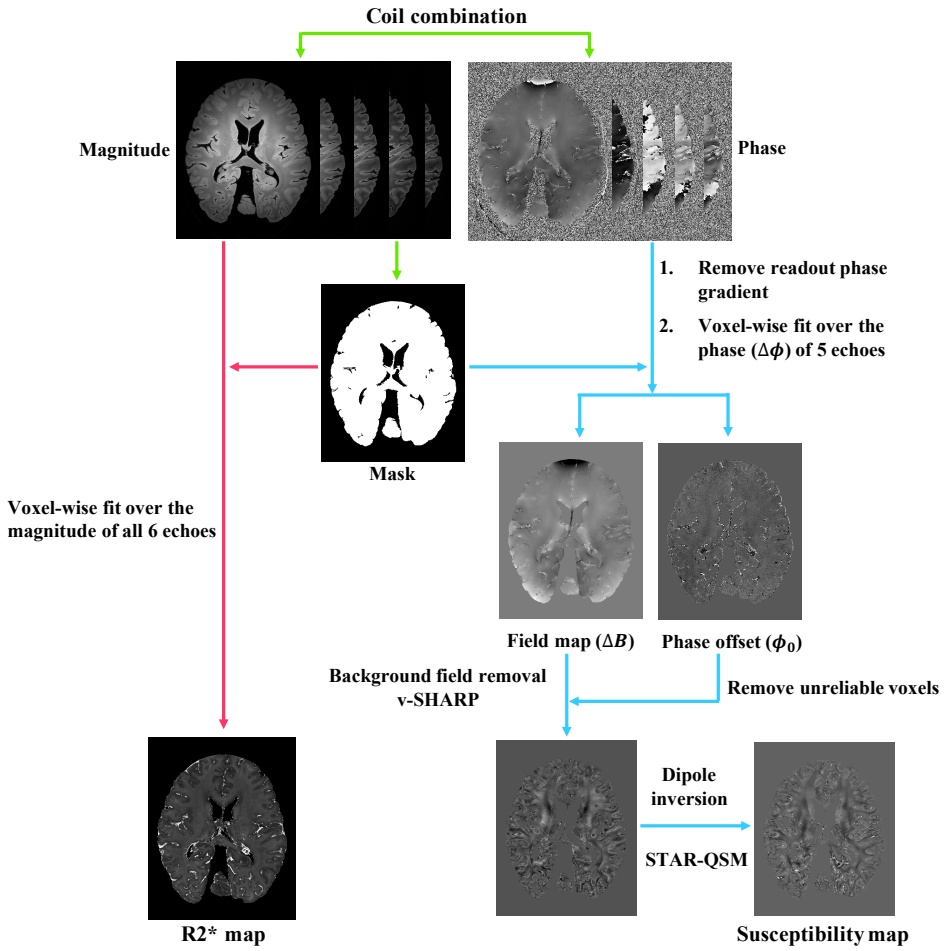


Figure 3.7 Illustration of the post-processing pipeline. Green arrows indicate the pre-processing steps including coil combination and mask generation, red arrows indicate the R2* mapping processing steps, and blue arrows indicate the QSM processing steps.

Image reconstruction and alignment

Non-physical phase singularities (open-ended fringe lines) were observed in the coil-combined phase maps provided by the manufacturer-supplied reconstruction (**Fig. 3.8**). These fringe lines were also observed in single RF channels originating in regions of highly focal signal loss induced by the coil sensitivity profiles. Open ended fringe lines in coil-combined phase maps will lead to artefacts in resulting χ maps. To address this, we developed a custom reconstruction pipeline for the raw k-space data designed to remove these fringe lines described in detail below. Briefly, the stages of our pipeline consist of: (i) parallel imaging (GRAPPA) reconstruction; (ii) removing coil-specific phase offsets; (iii) combining phase images across coils; and (iv) aligning repeat scans. This reconstruction produces a phase image for each echo that is free of open-ended fringe lines.

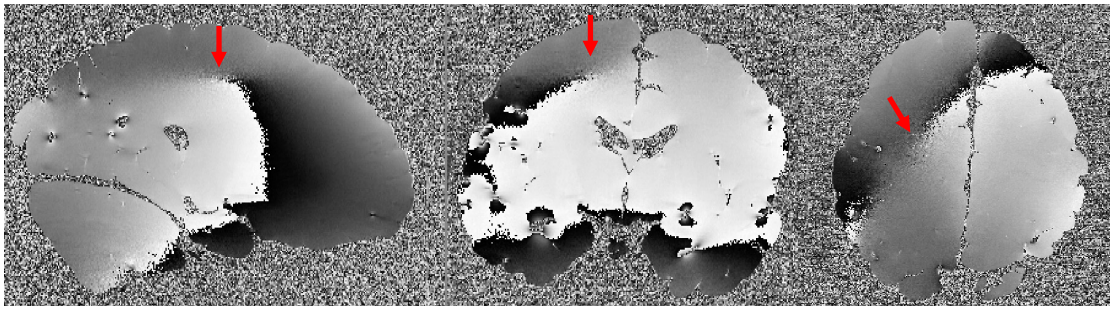


Figure 3.8 Example phase images from a post-mortem brain demonstrating the open-ended fringe lines (red arrows).

As discussed in Chapter 2, section 2.6.1 and Eq. 2.13, phase images collected from each channel have different phase offsets $\phi_0(\vec{r})$ associated with the individual coil's coil-sensitivity profile. Coil-specific $\phi_0(\vec{r})$ needs to be removed prior to channel combination of phase. To achieve this, for the post-mortem data, $\phi_0(\vec{r})$ was first removed by subtracting the phase of the first short TE echo $\phi(TE_1)$ ($TE_1 = 2\,ms$) from all subsequent echoes. This produces five phase images $\Delta\phi(TE_n{}')$ for each channel with

equivalent echo times $TE_n' = TE_n - TE_1$ (specifically, 6.6, 13.2, 19.8, 26.4 and 33 ms). This phase difference method is analogous to the "COMPOSER" technique [26]. Crucially, this step removes the $\phi_0(\vec{r})$ component in all of the phase images. For each equivalent echo time, TE_n', a coil-combined phase image was subsequently generated using a complex sum over all the coils. Magnitude images were combined using a simple "sum-of-squares" method for all 6 echoes.

Before we could perform the correction to remove $\phi_0(\vec{r})$, we first had to remove an observed image misalignment between different echoes along the phase encoding direction. The amount of misalignment increased with echo time, with the largest misalignment found between the first and sixth echo in Case 12, as shown in **Fig. 3.9**. This misalignment was hypothesised to be induced by B_0 drift caused by temperature changes of the passive shim material [27], as has been reported previously for long-duration post-mortem scans [54]. Before removing the coil-specific phase offsets, we therefore coregistered the first echo to each subsequent echo. By co-registering the first echo (which is only used for the $\phi_0(\vec{r})$ correction), we avoid interpolating the later echoes at this stage. Although there was another co-registration of all echoes performed at a later stage of the pipeline, we nevertheless minimized the total number of interpolations performed in the pipeline. This linear image registration was constrained to translation along the phase encoding axis using FLIRT (FMRIB's Linear Image Registration Tool) with a custom schedule file [55], [56]. This was done separately for the four repeats.

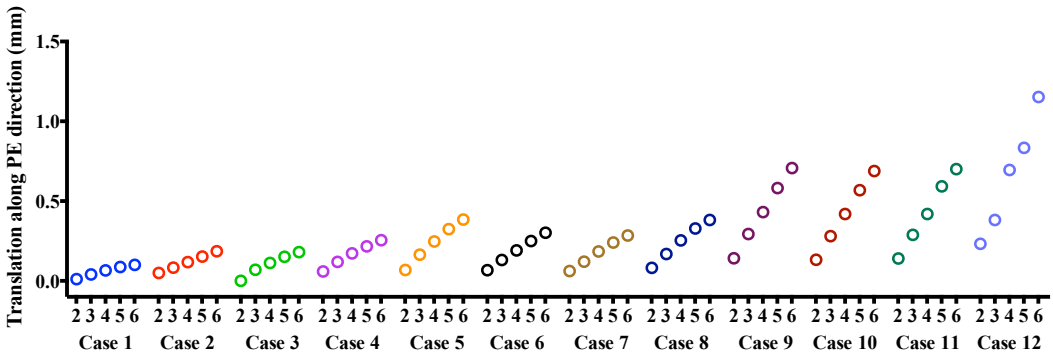


Figure 3.9 Translations along the phase encoding direction estimated to register the 1st echo to the 2nd - 6th echoes for repeat 1 using FLIRT for all cases. The slice thickness was reduced for Cases 1-7 versus Cases 8-12, leading to longer scan time per GRE repeat for Cases 8-12 and hence larger misalignments along the phase encoding direction.

Finally, image misalignments between the different acquisition repeats were observed, again consistent with B_0 drift caused by temperature changes of the passive shim material. Thus, a further registration step was performed to align all coil-combined phase images $\Delta\phi(TE')$ across repeats. This alignment used FLIRT with a specific schedule file constrained to translations along x, y and z axes (the largest misalignment was found along the phase encoding direction, but small misalignments along the other two directions were also observed). The alignment used the second echo from repeat 1 as the reference, and registered all other echoes from the 4 repeats to this reference.

Field map estimation

The field map $\Delta B_z(\vec{r})$ was estimated using a voxel-wise fit of the complex data, $S(\vec{r}, TE')$, over the co-registered coil-combined echoes [57], [58] by minimizing:

$$argmin_{\phi_0(\vec{r}),\Delta B_z(\vec{r})} \left\| \left(S(\vec{r}, TE') - |S(\vec{r}, TE')| \cdot e^{i\left(\phi_0(\vec{r}) + \gamma \cdot \Delta B_z(\vec{r}) \cdot TE'\right)}\right) \right\|_2^2 \text{ for } \vec{r} \in mask, \quad (3.1)$$

where γ is the gyromagnetic ratio. The cost function is evaluated only for voxels in a mask that was generated by thresholding the magnitude image from the first echo. Assuming linear phase evolution, ϕ_0 will have been removed by our coil combination approach. We included $\phi_0(\vec{r})$ in the $\Delta B_z(\vec{r})$ fitting process as an indication of the goodness of the fit. Small remaining estimates of ϕ_0 may correspond to a slightly non-linear phase evolution due to tissue microstructure, while large, focal estimates of ϕ_0 would be indicative of noisy voxels with unreliable phase that can corrupt the entire χ estimation in their vicinity (leading to streaking artefacts) [19], which should not be included in the later steps of QSM processing. Fitting was performed using the *lsqnonlin* function in MATLAB (R2016a).

Fitting was initialized with estimates of $\phi_0(\vec{r})$ and $\Delta B_z(\vec{r})$ obtained from the first two echoes of our coil combined data. To achieve this, a phase difference map between the first two echoes was generated:

$$\Delta\phi_{diff}(\vec{r}) = \text{angle}\left[\frac{e^{i\cdot\Delta\phi(\vec{r},TE_2')}}{e^{i\cdot\Delta\phi(\vec{r},TE_1')}}\right], \tag{3.2}$$

and spatially unwrapped using PRELUDE [24]. The phase map at the first echo was also spatially unwrapped, with initializations estimated as follows:

$$\Delta B_{z_{est}}(\vec{r}) = \frac{\Delta\phi_{diff,uw}(\vec{r})}{(TE_2'-TE_1')\cdot\gamma}, \tag{3.3}$$

$$\phi_{0_{est}}(\vec{r}) = \Delta\phi_{uw}(\vec{r},TE_1') - \gamma\cdot\Delta B_{z_{est}}(\vec{r})\cdot TE_1', \tag{3.4}$$

This initialization offers some advantages. Firstly, without initialization of the fitting, phase aliasing may remain in the estimated $\Delta B_z(\vec{r})$ map due to rapid temporal phase evolution in tissue that exceeds the Nyquist limit. By providing an initialization consisting of a wrap-free $\Delta B_{z_{est}}(\vec{r})$ map on the order of the true $\Delta B_z(\vec{r})$, we can produce $\Delta B_z(\vec{r})$ maps (without aliasing) that are estimated from all the echoes in our offset-corrected phase data. Secondly, spatial phase unwrapping is only performed on the first echo and the phase difference between the first two echoes to generate $\phi_{0_{est}}(\vec{r})$ and $\Delta B_{z_{est}}(\vec{r})$. These images will contain few phase wraps compared to the phase images acquired at higher echo times, enabling robust unwrapping performance and initialization estimates with minimal artefacts.

As shown in **Fig. 3.10**, voxels with very large and focal $\phi_0(\vec{r})$ values occurred at the edges of the brain and were found to be due to the presence of blood vessels or air bubbles. These voxels are sources of artefacts of no interest in QSM. Therefore, the brain mask was refined by thresholding the $abs(\phi_0(\vec{r}))$ map to remove these focal field outliers. The field perturbations induced to voxels in the vicinity of the blood vessels or air bubbles would be removed in the following background field removal step.

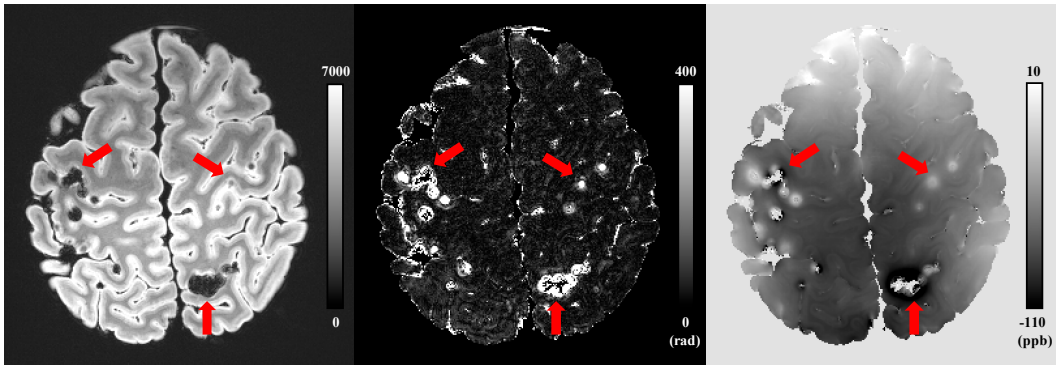


Figure 3.10 Illustration of detecting noisy voxels with unreliable phase (corresponding to air bubbles or blood vessels) from the $\phi_0(\vec{r})$ map estimated from fitting. Air bubbles and blood vessels correspond to large, focal voxels on the $abs[\phi_0(\vec{r})]$ maps (red arrows).

When comparing the predicted phase evolution from TE'_1 to the observed phase evolution in later echoes, we consistently observed a linear phase gradient along the readout direction (**Fig. 3.11**, similar to the effect found by Tendler et al. [59]). This was hypothesised to be due to eddy currents or an accumulative mistiming of the centre of the readout gradient (resulting a shift of k-space centre). These phase gradients would lead to apparent gradients in field offset along the readout direction and need to be removed. These shifts were estimated by a 1D linear fit along the readout direction over the phase increments of $\Delta\phi(TE'_2)$ to $\Delta\phi(TE'_5)$ with reference to $\Delta\phi(TE'_1)$, and subsequently removed from $\Delta\phi(TE'_2)$ to $\Delta\phi(TE'_5)$ using the approach described in [40].

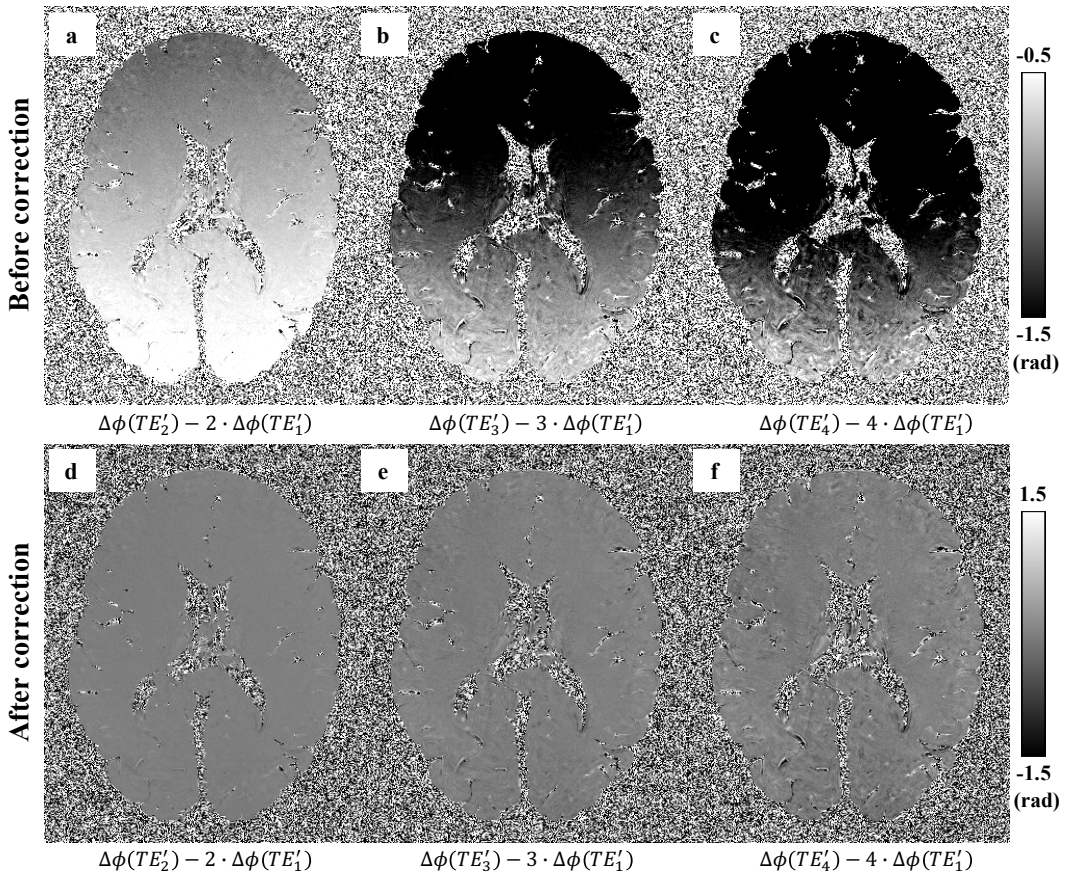


Figure 3.11 Difference between the observed phase and predicted phase based on the first effective echo TE'_1 assuming linear phase evolution ($\Delta\phi(TE_n') = n \cdot \Delta\phi(TE_1')$). If phase evolution was purely linear, these difference maps would be flat and close to zero. In practice, these phase difference maps consistently exhibit a linear phase gradient along the readout direction (a-c). A 1D linear phase was estimated and removed along the readout direction using the methodology described in [59], resulting in homogenous phase difference maps (d-f).

Averaging, background field removal and dipole inversion

Four repeats of the GRE sequence were performed for each post-mortem brain sample (note that in Case 2, only data from two repeats were available for the QSM reconstruction). Prior to each repeat, the scanner performs a whole-brain center frequency calibration, such that the phase over the whole brain should average to zero for each echo. However, investigation of the mean temporal phase evolution over the four repeats revealed a non-zero, variable slope of phase evolution that consistently increased from the first to last repeat (quantified as the mean frequency offset Δf of the $\Delta B_z(\vec{r})$ map, **Fig. 3.12A**). This is also likely due to B_0 drift induced by temperature changes of the passive

shim material inside the scanner bore during acquisition [54]. Notably, the GRE data used in this investigation were obtained as part of a larger study [12] acquiring multi-modal MRI data within each brain. Over the course of the protocol, the gradient duty cycle ranges from an intensive 24-hour diffusion-weighted protocol to a moderate T1/T2 weighted protocol, making it likely that the scanner temperature was unstable during the GRE acquisition. Even with an accurate frequency calibration at the beginning of each GRE repeat, this could lead to frequency drift during each repeat (duration of each repeat could take as long as 22 min, as mentioned in section 3.2.2).

Figure 3.12B plots the change in Δf between adjacent repeats (red boxes). Comparing this to the translations along the phase encoding direction between repeats (blue circles), we see a very similar pattern. These results are consistent with the hypothesis that both the between-repeat image misalignments and mean Δf differences are caused by B_0 drift induced by temperature changes of the scanner's passive shim material. If this is true, these results indicate that scanner temperature stabilized during the course of GRE acquisitions, demonstrated by the decreasing change in Δf and decreasing translations over the course of multiple repeats.

Averaging the phase data from 4 repeats prior to fitting for $\Delta B_z(\vec{r})$ would require a correction for this B_0 drift to avoid phase cancellation. Instead, the estimated $\Delta B_z(\vec{r})$ maps from 4 repeats were estimated and averaged to obtain the final $\Delta B_z(\vec{r})$ map. We found the latter approach to be more robust than the former to certain artefacts in the data. In particular, one brain showed evidence of Fluorinert leakage during the course of the scan, leading to local changes in $\Delta B_z(\vec{r})$ due to the difference in χ between Fluorinert and air.

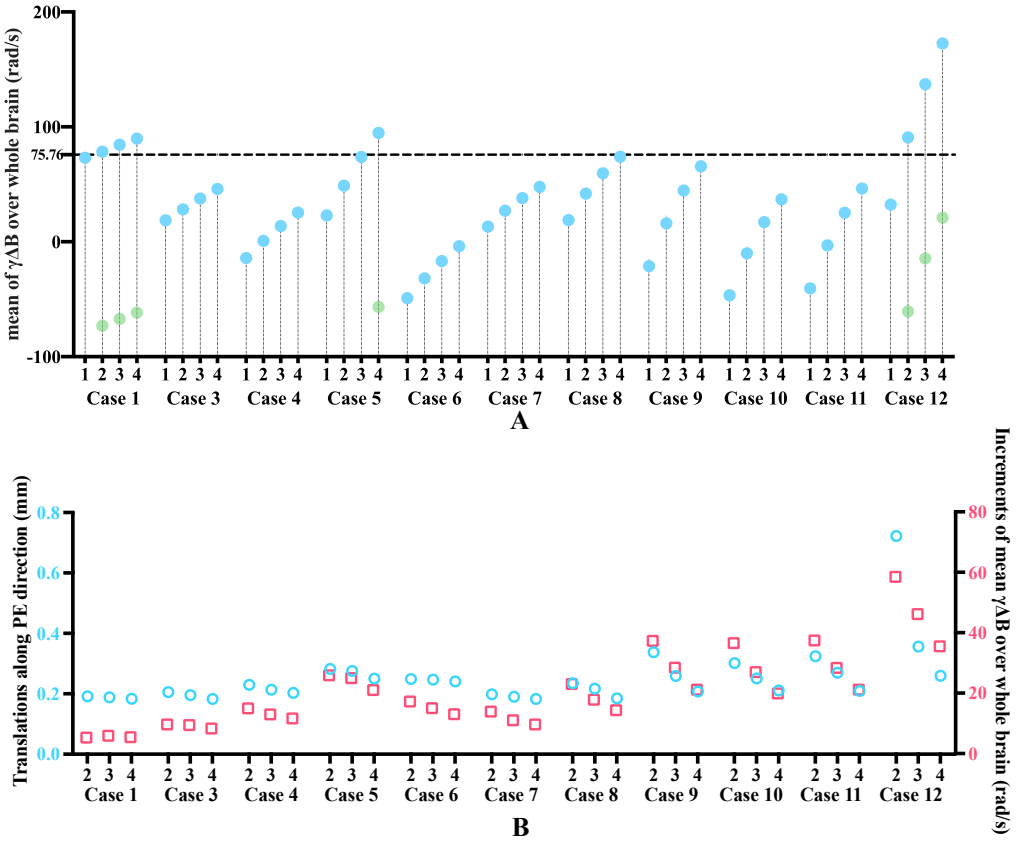


Figure 3.12 (A) Mean values of the frequency evolution ($\Delta f = \gamma \Delta B$) over the whole brain for each of the 4 repeats (only two repeats were available for Case 2 which is not presented here). The dashed horizontal line corresponds to the Δf value that accumulates phase of π with echo spacing of 6.6 ms ($\frac{\pi}{2\pi \times 6.6 \times 10^{-3}} = 75.76$ rad/s), leading to aliasing when Δf is above this value (as indicated by the green dots). This aliasing was observed in Cases 1, 5 and 12. **(B)** Blue circles: Translations along the phase encoding direction needed to align echo six of repeats 2-4 to echo two of repeat 1. Red squares: Increments of mean Δf over the whole brain between the labelled repeat and the preceding repeat. The correspondence of patterns between blue and red squares is consistent with our hypothesis that both effects are driven by a common source, hypothesised to be due to B_0 drift induced by temperature change of the passive shim material.

Background fields in the estimated $\Delta B(\vec{r})$ maps were removed using the V-SHARP algorithm [19,20] with our refined mask, a maximal kernel size of 12 mm and regularisation parameter of 0.02 mm^{-1}. Finally, the χ maps were generated using the STAR-QSM algorithm [25].

In QSM, the centre of k-space of the estimated χ map cannot be accurately obtained [60], making resulting χ estimates a measure of tissue's relative χ. In this study, χ

estimates were referenced to the whole brain by setting the mean χ value across the whole brain to zero.

3.2.5 R2* post-processing pipeline

The multi-echo GRE dataset was also used to generate R2* estimates from the magnitude images. R2* maps were estimated assuming mono-exponential evolution using a voxel-wise fitting of the magnitude images of all 6 echoes, achieved by minimizing:

$$argmin_{M_0(\vec{r}),R2^*(\vec{r}),noise(\vec{r})} \left\| \left(M(TE,\vec{r}) - [M_0(\vec{r}) \cdot e^{-TE \cdot R2^*(\vec{r})} + noise(\vec{r})]\right\|_2^2, \quad (3.5)$$

where $M(TE,\vec{r})$ is the measured magnitude data, $M_0(\vec{r})$ is the extrapolated signal magnitude at TE = 0 ms, and $noise(\vec{r})$ represents the noise floor. Retrospectively, we found that the model used for R2* fitting could be further improved which is discussed in Section 3.4.5.

As described above, B_0 drift induced effects were observed and corrected during the processing of phase data. Previous work has reported a linear dependence of T2* measurements on sample temperature [61]. To test for such effects in our data, the T2* maps from individual repeats of each brain were estimated, and the mean T2* values over whole brain were calculated. Our results found a small change ($0.41\% \pm 0.29\%$) in the mean T2* values from repeats 4 relative to repeat 1 over the 11 brains (change in ms for each brain and repeat shown in **Fig. 3.13**). As the mean T2* value drifts over 4 repeats were small, no correction of the temperature effect was performed. The final R2* maps were generated using averaged magnitude images over the four repeats for each brain.

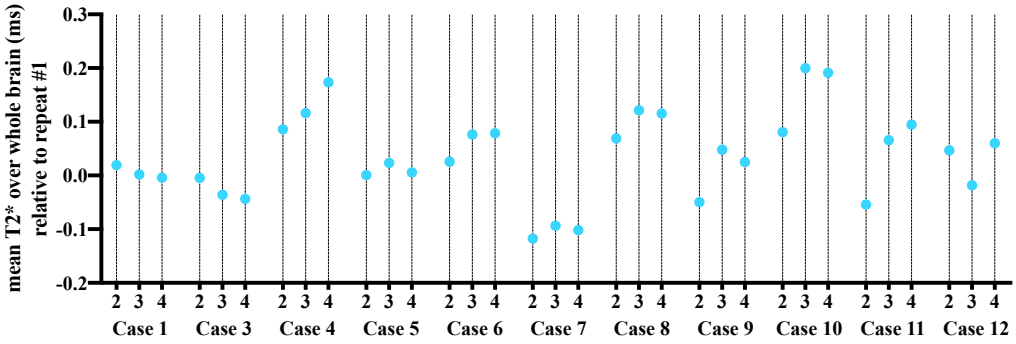


Figure 3.13 Change in T2* over the whole brain for repeats 2-4 relative to repeat 1 in 11 brains. Only two repeats were available for case 2, which was not included here.

3.2.6 MR image analysis

To investigate variations in R2* and χ, three brain regions of interest (ROIs) were analyzed (**Fig. 3.14**). These regions were chosen to represent three different stages of ALS disease progression as shown in **Fig. 3.1**: M1 (Stage 1, anticipated significant pathology), ACC (Stage 2/3, anticipated intermediate pathology) and V2 (no pathology, defined as an internal control). M1 was further separated into face, hand and leg areas to represent variability in patients, who may initially experience weakness in a particular limb or the face. M1 regional masks were created in MNI space and subsequently co-registered to the diffusion data also available for each brain (for full details of the multi-modal MRI protocol, see Pallebage-Gamarallage et al. [12]). Masks were manually refined in each hemisphere by an experienced researcher familiar with M1 anatomy using the diffusion MRI mean diffusivity maps as a reference, chosen due to their excellent grey-white matter contrast. The resulting ROI masks were subsequently registered to the GRE data using FLIRT [55], [56]. Masks of ACC and V2 were hand-drawn by a researcher with anatomical expertise, based on the location of the tissue block stained for histology available in these regions. Briefly, the histological stained slides were carefully mapped to the corresponding location in the 3D structural images by visually comparing photographs of the coronal sampled brain slices to the MR image. Masks of ACC and V2 were manually drawn in space of the structural MRI data (chosen due to its high

resolution to facilitate MRI-histology comparisons) to match the cortical region on the stained slides, and finally co-registered to GRE data using FLIRT [55], [56].

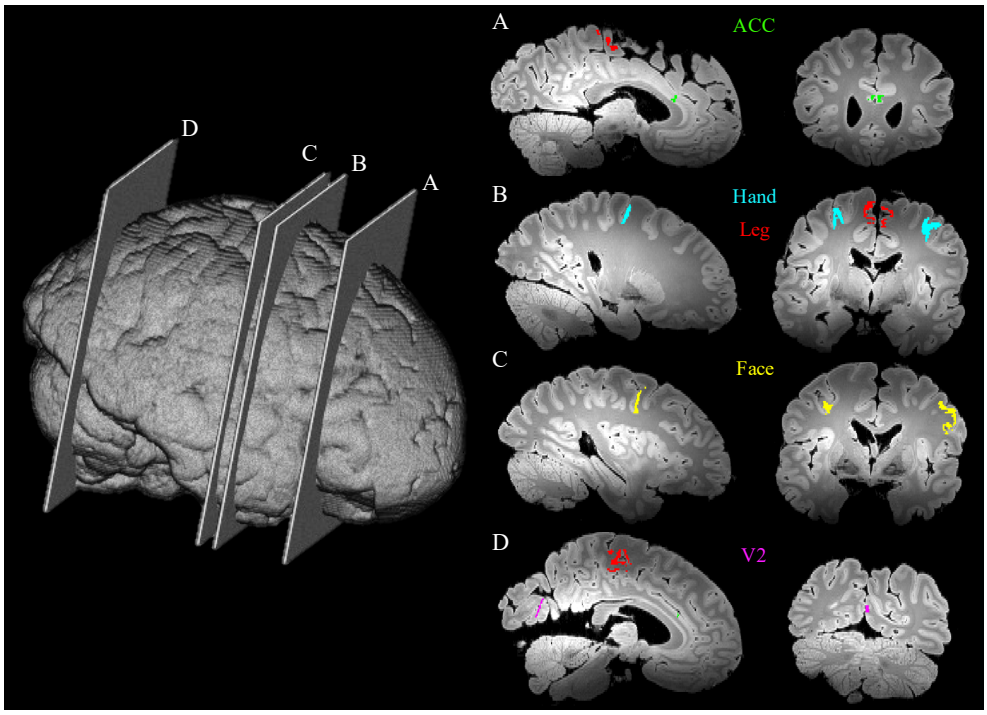


Figure 3.14 Illustration of slide sample locations across a whole brain from a single subject to highlight the ROIs used in our analysis. The yellow, blue, red, green and purple regions correspond to the M1 face area, M1 hand area, M1 leg area, anterior cingulate cortex (ACC) and secondary visual cortex (V2), respectively.

Due to a change in the Oxford Brain Bank tissue protocol, two types of fixative (10% neutral buffered formalin (NBF) and 10% formalin) were used for fixation of the brains. The impact of the type of fixative on R2* and χ estimates were investigated. As shown in **Fig. 3.15A,B**, differences were found in mean R2* between two fixative groups over the whole brain (29.7% difference between the group means) and M1 (29.4% difference between the group means). The choice of fixative (characterized as an indicator variable) was therefore regressed out from mean R2* value over the whole brain. As the mean χ value across the whole brain set to zero (whole brain referencing), only the group difference in averaged χ value in the M1 region between the two fixative groups was investigated (**Fig. 3.15C**). This group difference was found to be not significant (7.5%

difference between the group means). Note that due to the time it takes for fixative to penetrate into the tissue combined with leakage of the fixative from the tissue surface, the effect of fixation on R2* might vary across the brain. This is discussed in Section 3.4.5 and a plot of R2* of voxels with different distances to the nearest brain surface is shown in Fig. 3.24.

Effects of post-mortem delay and time in fixative before scanning on the χ and R2* maps were also investigated: no significant associations were found.

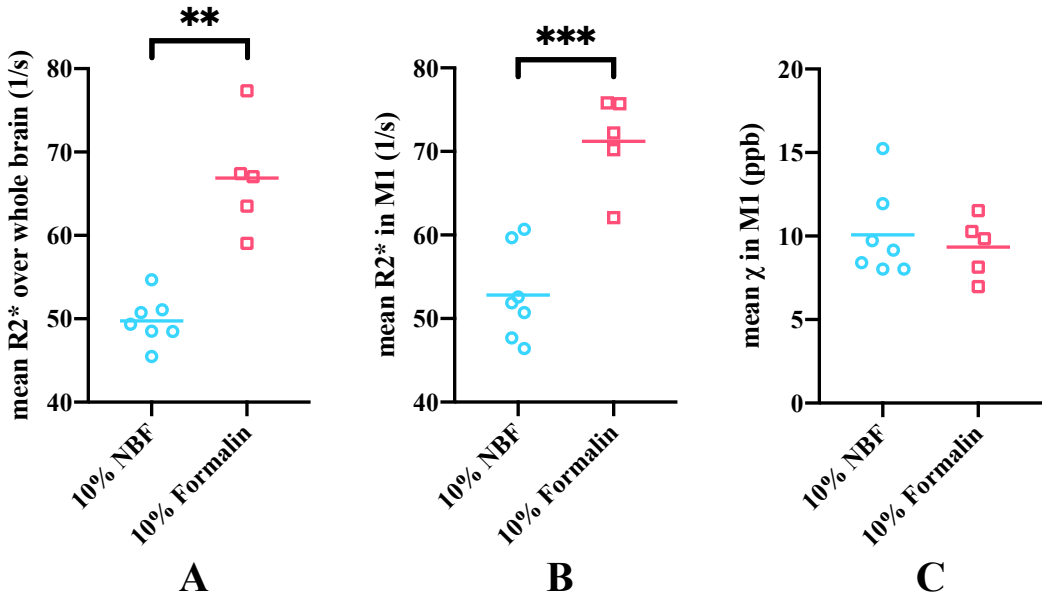


Figure 3.15 Comparison of the influence of the two types of fixative on χ and R2* estimates. Mean R2* values over the whole brain are plotted for the two types of fixative **(A)**, in addition to mean R2* **(B)** and χ **(C)** values in the primary motor cortex (M1). Mean R2* values for brains fixed with 10% NBF were significantly lower than those for brains fixed with 10% formalin over whole brain (p=0.0031, Hedges's g=-3.287) and in M1 (p=0.0004, Hedges's g=-3.059). No significant difference was found for the mean χ values in two fixative groups (p=0.58, Hedges's g= 0.286).
** *p<0.01;* *** *p<0.001*

Although care was taken to detect and remove the voxels corresponding to air bubbles as described in section 3.2.2, some large positive or negative χ values induced by remaining air bubbles still existed in the final χ maps. An outlier detection process was performed on χ and R2* values within our anatomically defined ROIs prior to measuring

the mean value. Outliers were defined as values more than three scaled median absolute deviations away from the median and excluded from the ROI analysis. Following outlier rejection, mean χ and R2* values within each ROI mask were calculated.

3.2.7 Histological analysis

Following MRI, tissue blocks were systematically extracted by an experienced histopathologist according to the anatomically-defined protocol described by Pallebage-Gamarallage et al. [12]. Briefly, the M1 leg region was represented on the medial surface of the paracentral lobule at the banks of the interhemispheric fissure. The M1 hand area (hand knob) was recognised by the inverted omega on the precentral gyrus at the anterior bank of the central sulcus. Similarly, the M1 face region was identified on the precentral gyrus, at the anterior bank of the central sulcus, lateral to the intersection of inferior frontal sulcus and precentral sulcus. Brains were subsequently sliced in a coronal plane for the ACC and V2 to be sampled. The ACC was extracted from the coronal slice represented with the striatum (caudate and putamen) and the anterior limb of the internal capsule rostral to the anterior commissure and posterior to the head of the caudate nucleus. V2 was sampled adjacent to the primary visual cortex (V1), identified by the stria of Gennari at the banks of the calcarine fissure.

Full tissue block processing protocol is described in Pallebage-Gamarallage et al. [12]. Briefly, tissue blocks were cut to 6 μm thick sections and mounted on 75 x 26 mm slides for immunohistochemistry. Sections were incubated with primary antibodies against ferritin (for iron) and PLP (for myelin), with 3,3'-diaminobenzidine (DAB) being used to impart a brown stain to the target protein, and haematoxylin being used as a counterstain that imparts a purple stain to cell bodies. Whole slides were digitised at x20 objective magnification. A colour deconvolution algorithm was used to separate the brown stain of

interest (targeted protein) from the counter-stain (cell bodies), and generate a binary segmentation mask of the stain of interest. The thresholds used for the colour deconvolution algorithm were previously validated [12] and unique to each stain. The ratio of stained area (with pixels exceeding the threshold) to the total area within a ROI was calculated as the stained area fraction (SAF). The SAF is a standard semi-quantitative measure of DAB-stained tissue with no units. Cortical ROIs were defined by an experienced histologist based on histological and neuroanatomical landmarks on each slide. Example annotations of cortical ROIs on histology slides are shown in **Fig. 3.16**. Representative digital histology images and segmentation of the targeted protein for ferritin and PLP stains are shown in **Fig. 3.17**. The SAF calculations were validated by a neuropathologist.

Ferritin staining was performed in the left hemisphere for M1 (leg and face areas, in two separate experiments), ACC and V2. We conducted ferritin staining in two batches, with each batch including one M1 region, ACC and V2. As a result of cross-batch variability, the ferritin SAF calculated from two batches had substantial differences in the range of SAF values. To combine the ferritin results across experiments, SAFs were standardized within each batch (demean then divide by the standard deviation) prior to combined analysis of both batches. Thus, ferritin SAFs reported have zero mean, and therefore will include negative "fractions". PLP staining was also performed in both hemispheres for M1 (leg, face and hand areas), ACC and V2. Standardization was not required for PLP SAFs as the PLP staining protocols are different to the ferritin protocol and are more reproducible/stable.

No significant effects in the histology data were found when comparing fixative type, post-mortem delay, or time in fixative before MRI scanning.

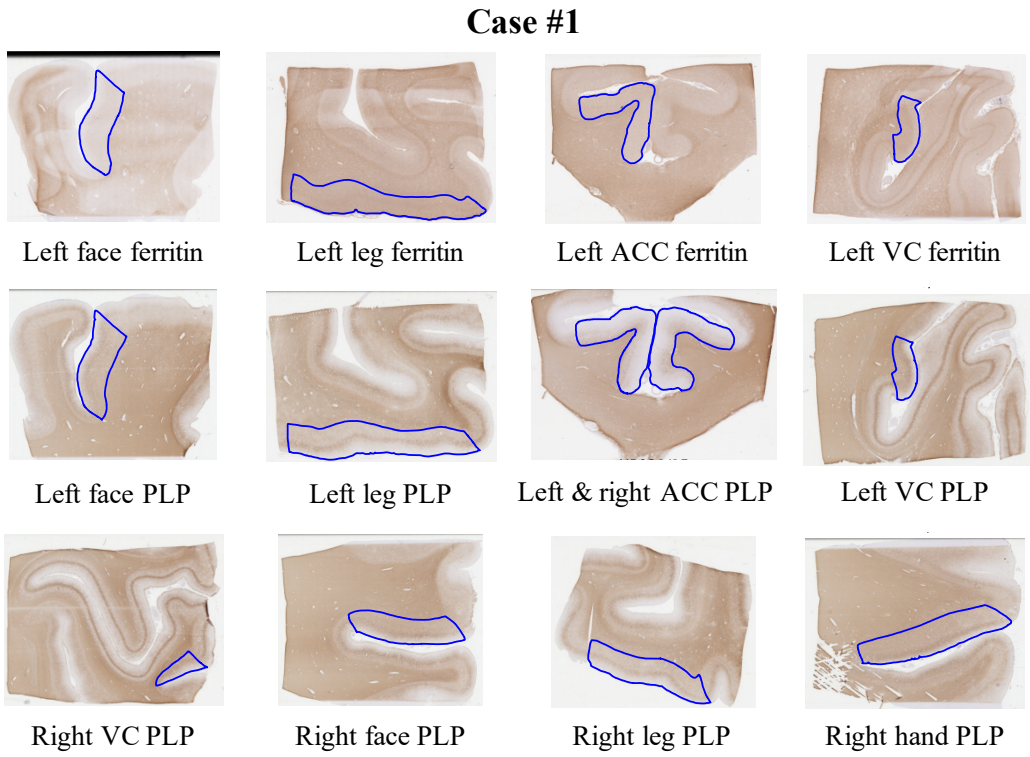


Figure 3.16 Digital stained histology images with cortical annotations for Case 1.

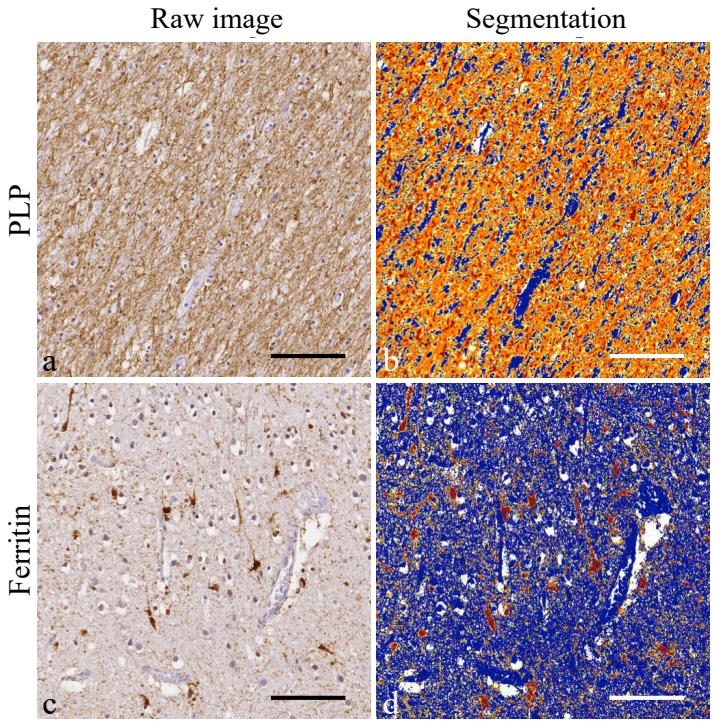


Figure 3.17 Digital histology images from motor cortex subcortical white matter stained for PLP (**a**) and grey matter stained for ferritin (**c**) in ALS. Colour deconvolution for positive staining (brown) generates segmentation images (**b** and **d**) showing unstained pixels as white, negative stained pixels as blue, weak positive pixels as yellow, medium positive pixels as orange and strong positive pixels as red. *Scale bar = 100 μm*

3.2.8 Statistical analysis

All statistical analyses were performed using SPSS version 25.0 (IBM, Armonk, NY). Pearson correlation analyses were used to assess (i) the relation between χ and R2* values, (ii) the relation between ferritin and PLP, and (iii) the relation between pairs of MRI and histological stains.

Welch's t-tests were used to compare (i) the group differences (ALS vs controls) in mean χ and R2* and (ii) the group differences (ALS vs controls) in ferritin and PLP stains in available M1 areas. Hedges's g was calculated for each t-test as effect size, which has a similar interpretation to Cohen's d but is generally considered more accurate for small sample sizes.

All p-values presented are for two-tailed tests. A p-value less than 0.05 was considered significant.

3.3 Results

3.3.1 Quantitative χ and R2* maps

Figure 3.18 depicts four ALS cases that exhibited visually apparent hyperintensities in χ and R2* within the cortical grey matter of M1 compared to the surrounding tissue, including the adjacent primary sensory cortex. For example, this is clearly visible around the 'hand knob' in Case 6 and 9, but also extending towards face and leg areas. The remaining brains did not exhibit obvious visible hyperintensities in M1. χ and R2* maps from all brains are shown in Appendix A.

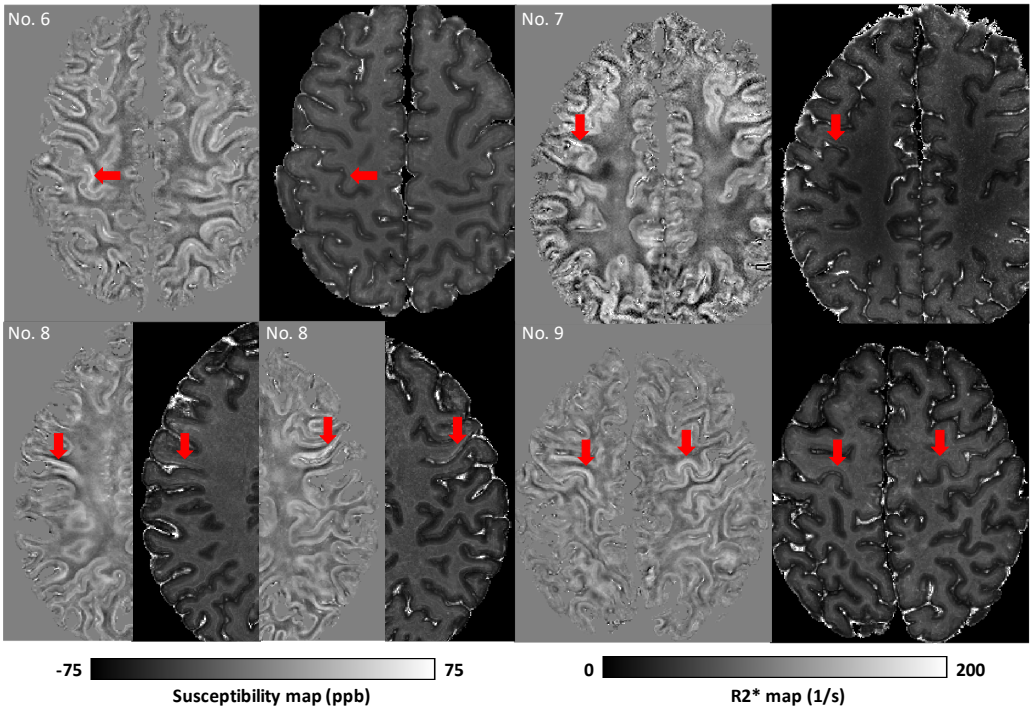


Figure 3.18 χ and R2* images from the four ALS brains that exhibited visually apparent hyperintensities in χ and R2* within the cortical grey matter of M1, as indicated by the red arrows. Specifically, hyperintensities were found in the left M1 hand area in brain No. 6, left M1 face area in brain No. 7, both right and left M1 face area in brain No. 8, and both right and left M1 hand areas in brain No. 9.

ALS brains were found to have greater mean χ and R2* values in M1 when compared to controls (**Fig. 3.19**).

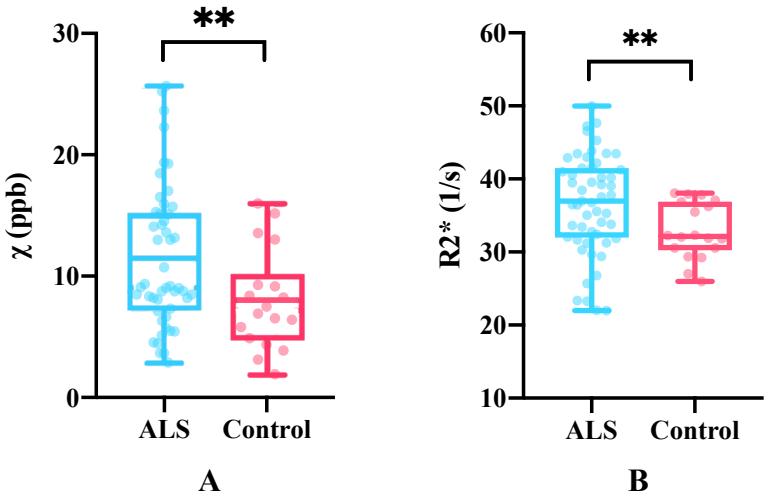


Figure 3.19 Mean χ (A) and R2* values (B) in all M1 sub-areas in both hemispheres between ALS and control brains. Group differences were significant, with p=0.0098 (Hedges's g=0.63) and p=0.0065 (Hedges's g=0.59) for χ and R2* respectively. Each plot in these plots represents one χ/R2* measure from one sub-region.
** *p<0.01*

The mean χ and R2* values were compared across all regions (M1, ACC and V2) and showed a strong positive linear correlation with a slope of 0.93 $ppb^{-1}s^{-1}$ (**Fig. 3.20**). In comparison, a previous in vivo study by Deistung et al. [2] found no significant correlation between χ and R2* values for various cortical grey matter structures including motor, sensory, occipital, prefrontal and temporal cortices. The linear correlation presented here is largely driven by the regional differences between the three regions that were found to have different levels of ferritin and myelin content based on histology. The observed consistency between the χ and R2* values reflects the common factors driving both QSM and R2* mapping, which relate to relative χ offsets in different tissue compartments.

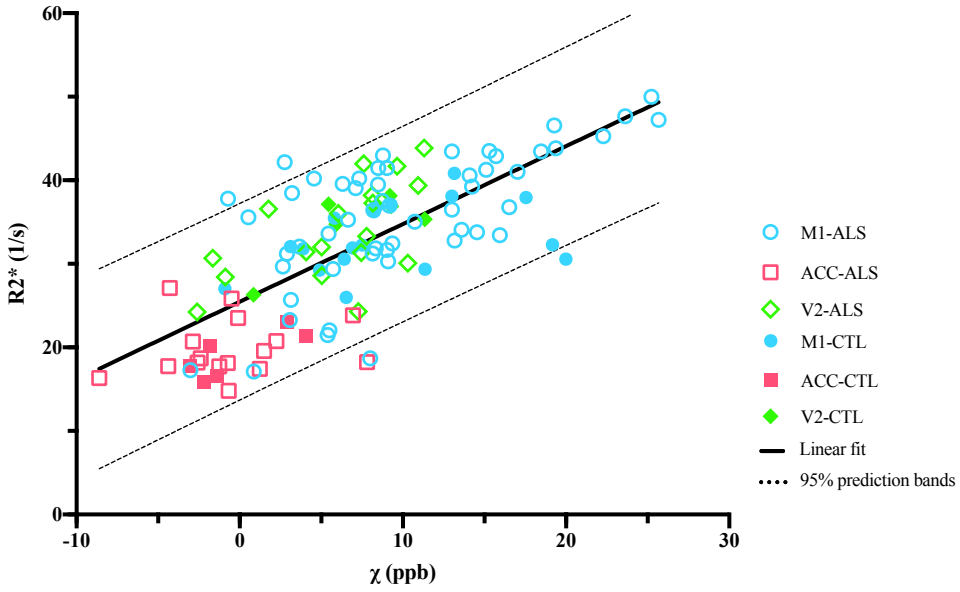


Figure 3.20 Correlation between mean R2* and χ values within all the ROIs (R=0.73, p<0.0001). The regression line is given by $R2^*(\chi) = 0.93\ ppb^{-1}s^{-1} \cdot \chi + 25.45\ s^{-1}$.

3.3.2 Histological results and their relation to MRI-derived measures

As shown in **Fig. 3.21**, the cortical grey matter of M1 in ALS brains exhibited higher average ferritin and PLP stained area fractions compared to control brains, although the group differences were not significant. Both χ and R2* showed positive correlations with

both ferritin and PLP when analysing the leg and face area of M1, ACC and V2 regions together (**Fig. 3.22** and **2.23**). We also performed partial correlation in order to assess the unique variance in each MRI measure that is explained by each histological stain, as a positive correlation between ferritin and PLP SAFs was found (r=0.35, p=0.011).

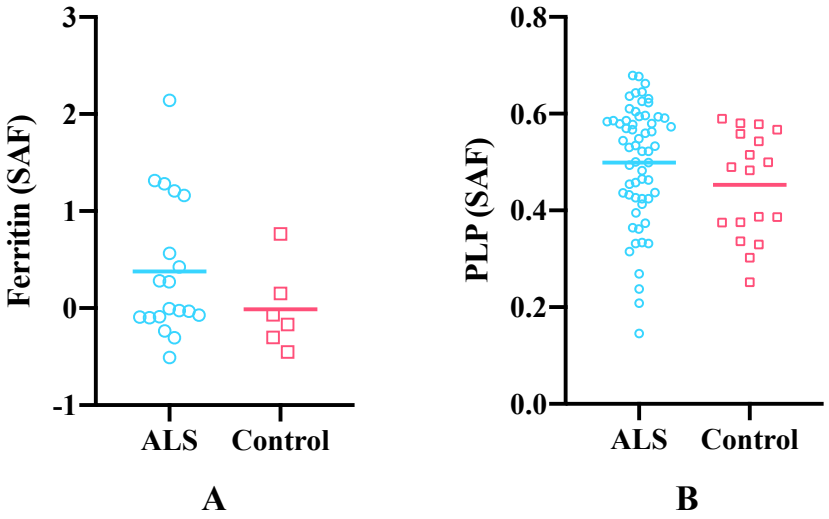


Figure 3.21 Group mean differences in ferritin (A) and PLP (B) stained area fractions (SAF) between ALS and control brains in M1. Ferritin results are drawn from M1 face and leg areas in the left hemisphere, while PLP results consists of all M1 sub-areas in both hemispheres (reflecting the more manually-intensive nature of the ferritin staining procedure). ALS brains exhibited greater ferritin and PLP SAFs compared to control brains, but group differences for both stains were not significant (p=0.125 and p=0.135, respectively).

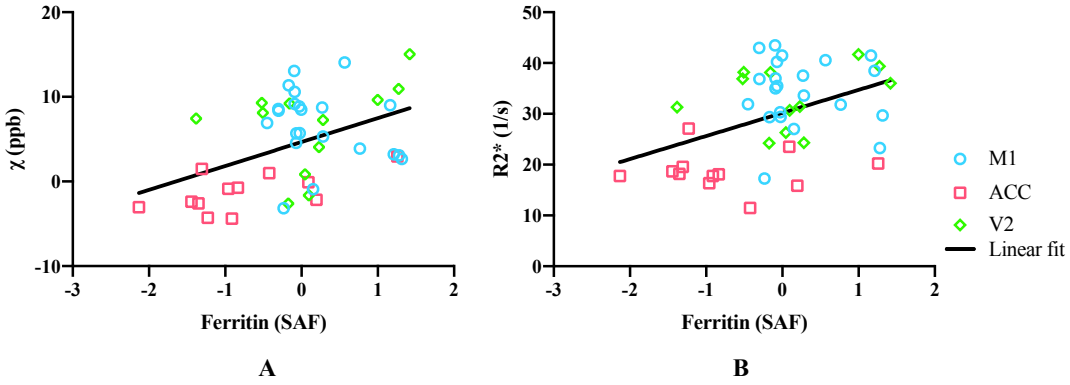


Figure 3.22 (A) χ values correlate with ferritin (r=0.43, p=0.0027), including after partial correlation controlling for PLP (r=0.34, p=0.023) when analysing over the three ROIs. When analysing individual regions separately, a correlation between χ and ferritin was only found in the ACC (r=0.59, p=0.043), no significant correlation was found in M1 or V2 (r=-0.22, p=0.32 and r=0.14, p=0.67, respectively). (B) R2* values correlate with ferritin (r=0.42, p=0.0035), including after partial correlation controlling for PLP (r=0.31, p=0.039) when analysing over the three ROIs. When analysing individual regions separately, no significant correlation between R2* and ferritin was found in M1, ACC or V2 (r=-0.056, p=0.80; r=-0.0031, p=0.99

and r=0.30, p=0.35, respectively). M1 includes face and leg areas. All data were from the left hemisphere. Note that Ferritin SAF values were standardised, hence have negative values.

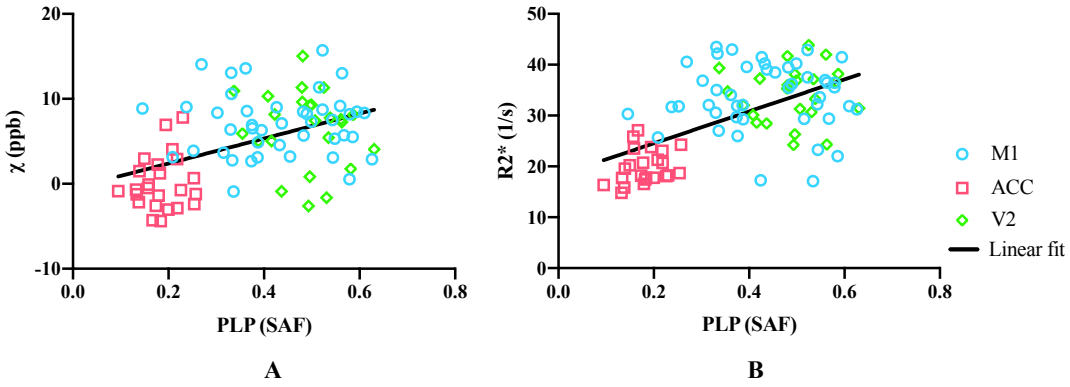


Figure 3.23 (A) χ values correlate with PLP (r=0.47, p<0.0001), including after partial correlation in the left hemisphere controlling for ferritin (r=0.37, p=0.015) when analysing over the three ROIs. When analysing individual regions separately, no significant correlation between χ and PLP was found in M1, ACC or V2 (r=0.0076, p=0.96; r=0.14, p=0.50 and r=-0.16, p=0.47, respectively). (B) R2* values correlate with PLP (r=0.40, p<0.0001), including after partial correlation in the left hemisphere controlling for ferritin (r=0.48, p=0.00097) when analysing over the three ROIs. When analysing individual regions separately, no significant correlation between R2* and PLP was found in M1, ACC or V2 (r=-0.0041, p=0.98; r=0.26, p=0.22 and r=0.039, p=0.86, respectively). M1 includes face and leg areas. Data presented here are from both hemispheres.

3.4 Discussion

3.4.1 QSM pipeline considerations

Acquisition of high-quality quantitative χ maps in whole, formalin fixed post-mortem brains has both challenges and opportunities that are not present in vivo. Long scan times enables us to increase signal-to-noise ratio (SNR) and spatial resolution. Post-mortem tissue provides an opportunity to compare against histology drawn from a broad range of brain regions. The proposed experimental setup and image processing pipeline for quantitative susceptibility and R2* mapping was developed to address the specific challenges associated with post-mortem acquisition. First, the absence of skull will in general alter the macroscopic background field compared to in vivo. By embedding the brain within a spherical cavity (**Fig. 3.2**), we can improve the overall shim quality (**Fig.**

3.3). Second, reliable positioning of the brain is important for achieving consistent QSM results, particularly in white matter where susceptibility anisotropy causes the estimated χ value to depend on orientation to the B_0 field. This challenge was overcome through the use of an internal brain-shaped holder that could be reliably positioned within the outer sphere (**Fig. 3.2**). Third, the presence of air bubbles causes severe signal dropout and phase aliasing (**Fig. 3.10**), while small air bubbles induce strong dipole-shaped fields around the region that may lead to streaking artefacts during the dipole inversion step. We addressed this by identifying and removing voxels with unreliable phase information (**Fig. 3.10**), alongside outlier detection when performing the ROI analysis.

Finally, post-mortem scans tend to be associated with long scan times, during which gradient-intensive sequences can cause significant heating of the gradient hardware. If this heating is transferred to the passive shim material inside the scanner bore, it can lead to significant B_0 drift during the course of acquisitions [53]. In our study, image misalignments along the phase encoding direction and differences in the slope of phase evolution between different GRE repeats were observed that would be consistent with such a B_0 drift. In addition, T2* values have previously been demonstrated to be sensitive to temperature. Changes in temperature inside the scanner bore could be transferred to the sample, depending on air circulation and heat capacity of the sample while embedded in the susceptibility-matching fluid. In our study, very small differences in mean T2* values over whole brain between the four GRE repeats were found for all brain samples. This suggests that the sample temperature was relatively stable during the course of GRE acquisitions. Importantly, although changes in passive shim temperature and sample temperature could both be caused by gradient heating, they need not be coupled, since the two effects depend on details of heat transfer between different physical systems. The

above-mentioned issues were addressed by appropriately constrained post-processing corrections in our study.

3.4.2 Histology analysis considerations

Similarly, histology data requires optimisation. The quality of immunohistochemistry was assessed during protocol development by an experienced histologist, and validated by a clinical neuropathologist. We now describe for each stain the cellular specificity that was observed for DAB and prior literature reporting similar results. PLP staining was observed to be specific to axonal fibres of the cortical grey matter and no staining was observed in neurons or oligodendrocytes. Myelin PLP staining was most dense in M1 and V2 and less dense in ACC. This agrees with previous reports that ACC is substantially less myelinated than the M1 and V2 [62], [63]. Ferritin staining was apparent in myelin, glial cells and oligodendrocytes. Previous work showed that myelinated fibres colocalised with ferritin staining in both grey and white matter [64]. Furthermore, microglial ferritin staining has been demonstrated in the frontal cortex of Alzheimer's disease [65] and in the deep layers of the motor cortex of ALS [49]. Since the majority of iron is bound to ferritin, studies have validated intracellular ferritin as a surrogate marker for iron content in tissue [65], [66]. Shortcomings of immunostaining with respect to quantification are described below.

3.4.3 Correlations between χ/R2* measures and ferritin/PLP SAFs

R2* and χ and both showed a positive correlation with the ferritin SAF (**Fig. 3.22**). This is as expected, due to the paramagnetic properties of iron. However, what was not expected is that both χ and R2* values additionally showed positive correlations with PLP. Positive correlation is expected for R2* estimates [67], but a negative correlation would be predicted for χ due to the diamagnetic properties of myelin. A similar result to ours has been previously reported [43], which has been attributed to a correlation between iron

and myelin content in grey matter, which was also observed in our data. To explore whether this explanation is consistent with our data (i.e., that the apparent correlation was in effect an indirect relationship mediated by cortical iron content), we performed a partial correlation analysis. Regressing the ferritin SAF out of both PLP SAF and χ estimates prior to correlation reduced the positive correlation, but did not produce the expected negative correlation. To the extent that ferritin SAF accounts for iron (caveats on this point are discussed below), the partial correlation analysis was unable to explain this finding. This positive partial correlation of PLP with χ is not in agreement with the diamagnetic nature of myelin and remains unexplained.

More generally, it is worth noting that the correlations presented here are driven primarily by regional differences rather than variation within region, reflected as a clustering of regions in **Fig. 3.23**. In this situation, correlations are prone to identifying apparent relationships between any properties exhibiting regionally-specific differences. In general, we did not observe meaningful correlations within individual regions, with the only significant correlation being between ferritin SAFs and χ in the ACC, although this does agree well with the overall inter-regional correlations. The lack of significant correlations in individual regions could reflect low statistical power in the presence of small effect size (differences between brains) and a small sample size (n=12). Furthermore, the ROIs used in this work were all grey matter regions where iron is likely the primary source of susceptibility variations, while white matter has richer deposits of myelin content. Therefore, extending our ROIs to white matter might help shed light on the correlation between myelin and susceptibility measures.

This unexpected correlation between PLP SAF and χ could reflect some limitations in the immunohistochemistry methods used within our study. First, DAB staining does not follow the Beer-Lambert law (the optical density is not representative of the protein

concentration). This is the primary motivation for semi-quantitative analysis based on SAF rather than optical density. One drawback of measuring SAF is the need to use thresholding to determine positively stained area. In this work, a single threshold for each stain was manually chosen by a histologist which could potentially fail to account for slide-to-slide variability. A pipeline that enables automated thresholding of digital histology images is currently under development [68]. Second, ferritin staining is not directly quantitative of iron load. Each ferritin complex can carry a variable number of iron atoms, meaning that ferritin-associated iron is not necessarily proportionate to the protein content measured here. Third, although ferritin is the principal iron storage protein, non-ferritin iron would also contribute to MR susceptibility signal. This would lead to both an underestimate in the apparent correlation with iron load and, potentially, an imperfect deconfounding of iron from PLP stains. Other techniques that more directly measure iron concentration, such as the mass spectrometry technique used in Langkammer et al. [6], could offer a more accurate quantification of iron in tissue. However, such techniques require heating the sample which may damage the tissue chemical structure and preventing further use of the histology sample.

3.4.4 ALS pathology associated changes in χ and R2*

Previous studies have reported χ and R2* hyperintensities in M1 of ALS patients [50]–[52]. We observed similar effects in cortical grey matter of M1 in four out of nine ALS brains, corresponding to different sub-regions. This variability might relate to disease heterogeneity. Furthermore, in our study ALS brains were found to have greater mean χ and R2* values in M1 compared with control brains, while ALS brains also exhibited greater ferritin and PLP stained area fractions compared with control brains, although group differences were not statistically significant. The result of higher PLP SAFs in the M1 region in ALS brains compared to control brains (**Fig. 3.21B**) is potentially surprising

as neurodegeneration is more often associated with demyelination. A related result has been previously reported by Meadowcroft et al. [69], where an increased staining and optical density of subcortical white matter in the primary motor cortex was found in ALS tissue compared to controls using a different myelin stain (Luxol fast blue). Disease-related iron and myelin changes in M1 and their contributions to the MRI susceptibility signal need further investigation.

3.4.5 Study limitations

This study had several limitations. First, the GRE acquisition protocol could have been better optimised, as the readout train included unnecessary dead time. To give a feel for the potential gains, if one wished to leave the exact TEs and TR unchanged (e.g., if the first echo required a particularly short TE=2ms), a bandwidth of 210 Hz/pixel could be achieved for echoes 2-5, increasing the SNR by 1.76x for these echoes. Second, we retrospectively found that the model (Eq. 3.5) used for R2* fitting could be further improved by replacing the noise term $noise(\vec{r})$ with $[M(TE,\vec{r})^2 + noise(\vec{r})^2]^{0.5}$, here, $M(TE,\vec{r})$ represents magnitude data. Furthermore, a noise term would not be required, if a different coil-combination method is used that keeps phase data from all 6 echoes with their original TEs, we could combine field ($\Delta B_z(\vec{r})$) and R2* estimations into one single complex model fit that uses magnitude and phase data from all 6 echoes to estimate $\Delta B_z(\vec{r})$ and R2* simultaneously. This would more accurately account for the presence of noise, particularly in voxels with very low signal. Third, registration between histology slides and MRI data was not performed, requiring us to correlate at the level of region-of-interest rather than pixel-wise. A pipeline that enables automated registration of histology slides to 3D MRI images using dissection photos as an intermediary is currently under development [70]. This registration pipeline aims to enable pixel-wise comparisons between MRI and histology acquired within the same sample. Forth, we were only able

to obtain ferritin histology in limited regions of interest over two separate experiments. This limitation reflects challenges in ferritin staining, with quality of stain being operator dependent such that direct comparison requires that all slides are processed as a single batch. To enable combination of stained area fractions measured from two batches, ferritin SAFs were standardized statistically within batch to account for technician-related bias. Fifth, QSM is a measure of tissue's relative χ, which is generally made in comparison to an internal reference region (e.g., cerebrospinal fluid). In our study, we lack a reliable reference region that can be confidently considered to be free of pathology (indeed, even the region chosen to represent very low pathology, V2, may be affected). As such, χ values were referenced to the whole brain by setting the mean χ of the whole brain to zero. Sixth, only three control brains are included, which limits statistical power in this current cohort. Seventh, we observed a variation of R2* values with distance to the tissue surface in post-mortem brains (**Fig. 3.24**). This may be due to the time it takes for fixative to penetrate into the tissue [71] combined with leakage of the fixative from the tissue surface. A correction for this effect can be applied based on forward simulation of the diffusion of fixative over time [72].

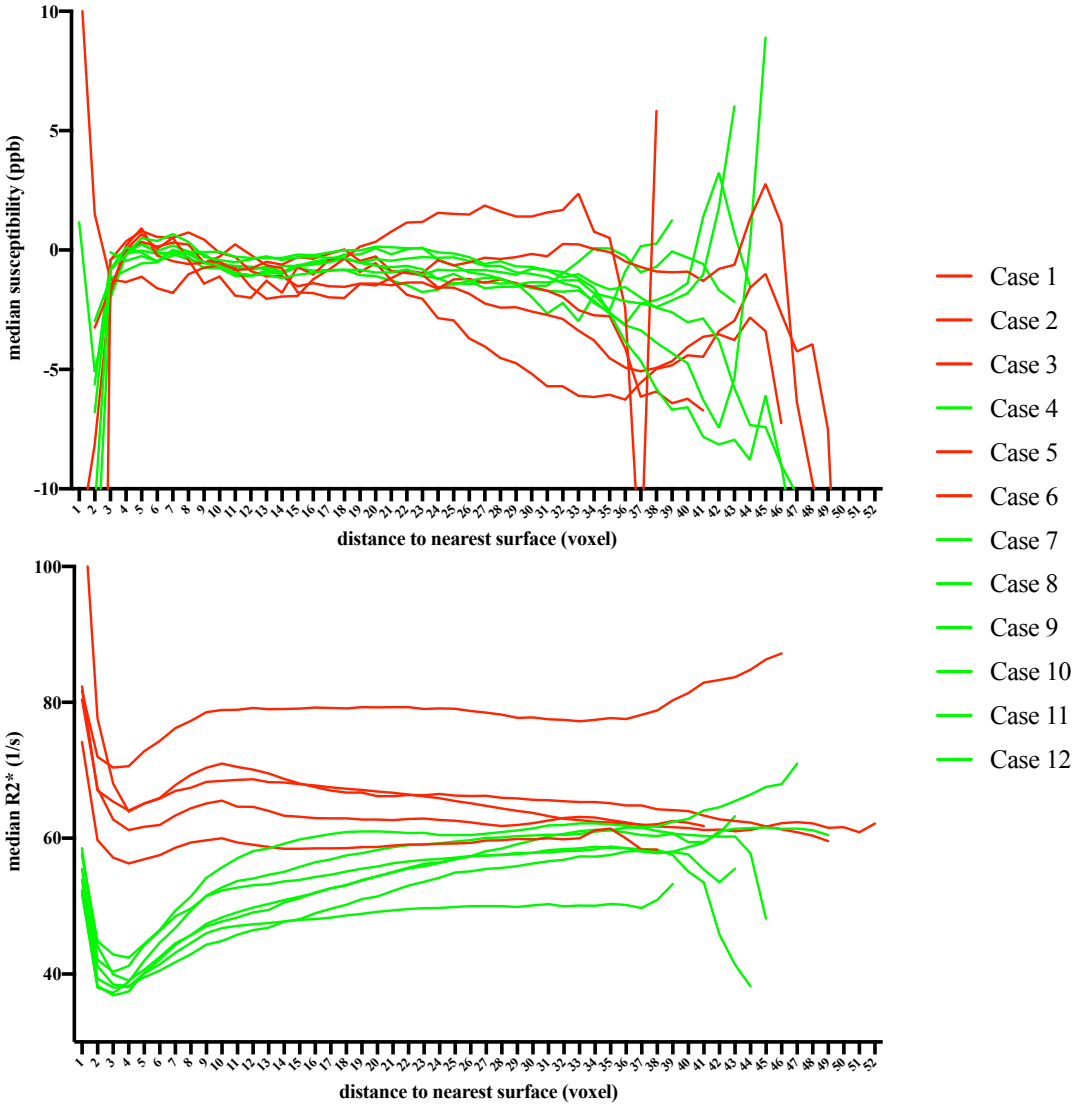


Figure 3.24 Median χ and R2* of voxels with different distances to the nearest brain surface for all thirteen brains. Here the red and green lines correspond to the two different fixatives used within our project (red - 10% formalin and green - 10% neutral buffered formalin). For the R2* maps, a difference is observed for the R2* estimates which depends on the type of fixative used. A similar trend was not observed for the χ estimates.

3.4.6 Conclusions

In conclusion, we have developed a QSM and R2* processing pipeline for whole, fixed post-mortem brain acquisition. Comparison with semi-quantitative ferritin and myelin histology demonstrates the potential for χ and R2* maps to serve as a quantitative imaging marker for the diagnosis of ALS or other neurodegenerative diseases. Translation of quantitative susceptibility techniques to clinical use is associated with several challenges

including requirements of complicated multi-step postprocessing (or the lack of a ‘click of a button’ style pipeline), and variations of results due to the use of different algorithms.

Chapter 4

Development of an optimal QSM processing pipeline for UK Biobank brain swMRI data

4.1 Introduction

In this chapter, a QSM pipeline specifically optimized for the UK Biobank susceptibility-weighted MRI data is presented. This chapter is based on a journal paper we submitted to a journal and is under peer review, at the time of writing this thesis [14].

As outlined in previous chapters, QSM provides a quantitative measure of tissue χ distribution that is sensitive to tissue iron, myelin and calcium content in the brain. Our work presented in Chapter 2 along with numerous literatures have demonstrated the histological correlates of χ, and its association with neurological pathology, particularly the potential to investigate iron accumulation in aging and neurodegeneration. To date, QSM has been largely conducted in the traditional framework of small cohorts (tens to hundreds of subjects) that are optimised for homogeneity and aiming to study a specific group or effect of interest. They are effective in detection of pathological changes of χ, but cannot capture the variance that exists across populations, limiting the opportunities for non-hypothesis-driven discovery.

A powerful alternative is to prospectively image healthy individuals at large scale and track subsequent health outcomes. Participants in this kind of studies are typically intensively phenotyped and even deeply genotyped. The past decade has witnessed a number of studies aiming to image large-scale cohorts such as the ENIGMA Consortium [73] and German National Cohort [74]. Although such study can be expensive, it is also efficient in capturing early biomarkers and risk factors for a broad range of diseases. It can further discover unexpected interactions between risk factors (such as lifestyle and genetics). However, QSM, as a relatively novel technique, has not been implemented in prospective large-cohort studies, until the UK Biobank imaging study which is collecting susceptibility-weighted MRI data.

UK Biobank is a prospective epidemiological resource gathering extensive questionnaires, physical and cognitive measures, and biological samples (including genotyping) in a cohort of 500,000 participants (40–69 years of age at baseline recruitment) [75]. Participants consent to allow access to their full health records from the UK National Health Service. An imaging extension to the existing UK Biobank study was funded in 2016 to scan 100,000 subjects from the existing cohort using multi-modal, multi-organ imaging [11]. Importantly, UK Biobank participants are predominantly healthy when scanned. The brain imaging protocol included susceptibility-weighted MRI (swMRI) using a dual-echo GRE sequence [11]. The combination of the number of subjects, the breadth of linked data (to be discussed in depth in Chapter 5) and access to long-term health outcomes results in an unprecedented swMRI resource that is particularly appropriate for the study of diseases associated with ageing.

However, UK Biobank is not yet fully exploiting the available brain imaging data, particularly the susceptibility-weighted MRI (swMRI) scan. As described in previous chapters, swMRI signals in the brain are primarily influenced by iron, myelin and calcium

content due to the shifted magnetic susceptibility (χ) of these constituents relative to tissue water [76], [77]. The signal magnitude from swMRI has been analysed to provide estimates of T2* [11], [12], but the signal phase has not previously been analysed for QSM. The UK Biobank brain imaging thus creates unique opportunities to investigate QSM in previously unexplored territory, including as an early disease marker.

To ensure the robustness of our QSM pipeline and to select the optimal pipeline for the UK Biobank protocol, development and optimisation of QSM pipeline will be revisited. As outlined in previous chapters, one important feature of QSM, which differs from other MRI modalities, is that the optimised processing pipeline depends to a non-trivial degree on the imaging protocol and data properties. The optimal QSM pipeline for UK Biobank swMRI data may differ significantly from the pipeline proposed for post-mortem data in Chapter 3. Therefore, we carried out extensive evaluations of established algorithms (from widely-used and publicly-available toolboxes) for each step. In addition, QSM provides a measure of relative, rather than absolute χ [78]. The presence of an unknown offset in the estimated map for any individual is problematic for comparison of χ values across subjects. To address this, χ values are commonly reported as offset with respect to an internal reference region [79]. In this work, we compared the use of three widely-used reference regions: mean χ across (i) the whole brain, (ii) cerebrospinal fluid (CSF) and (iii) a white matter region (forceps minor).

In this chapter, we describe the results of our extensive evaluations, as well as the production of imaging-derived phenotypes (IDPs), which are scalar summary measures of χ in a range of brain structures for inclusion in the wider UK Biobank imaging resource.

4.2 QSM pipeline evaluation and development, QSM and T2* IDP generations

4.2.1 MRI Data acquisition and participant information

We used data from 35,885 participants in the UK Biobank early-2020 release who had susceptibility-weighted MRI (swMRI) data collected. Participants were 53.1% female and aged 45-82yo (64.04±7.5yo) at time of imaging. Of these participants, 1,447 returned for a repeat scan approximately 2 years (2.25±0.12y) after the first imaging session. A detailed overview of the neuroimaging acquisition protocols used in UK Biobank brain imaging has been described previously [11].

Susceptibility-weighted MRI scans were acquired on 3T Siemens Skyra MRI scanners (software platform VD13) with 32-channel head receive coils. swMRI data were acquired using a three-dimensional (3D) dual-echo gradient echo (GRE) sequence with the following parameters: voxel size = 0.8 × 0.8 × 3 mm^3, matrix size = 256 × 288 × 48 (whole-brain coverage), TE1/TE2 = 9.4/20 ms, TR = 27 ms and in-plane acceleration = 2, total scan time = 2:34 min. Magnitude and phase data from each receive channel were saved for off-line coil combination, described below.

The UK Biobank brain imaging protocol includes T1- and T2-weighted structural acquisitions, and they have been processed using the UK Biobank image processing pipeline [12]. In our work, brain masks and image registration references were derived from the T1-weighted structural scans acquired using a 3D MPRAGE protocol (voxel size = 1×1 × 1 mm^3, matrix size = 208 × 256 × 256, inversion time (TI)/TR = 880/2000 ms, in-plane acceleration = 2, total scan time = 4:54 min) [12]. Ventricle and white matter hyperintensity masks were derived from T2-weighted fluid attenuated inversion recovery

(FLAIR) scans (3D SPACE, voxel size = 1.05 × 1 × 1 mm^3, matrix size = 192 × 256 × 256, TI/TR = 1800/5000 ms, in-plane acceleration = 2, total scan time = 5:52 min) [12].

The quality control (QC) pipeline developed for UK Biobank brain imaging [12] was applied to all subjects included in this study. Several QC measures related to T1-, T2-weighted and swMRI data were used here. For example, subjects were excluded if registration from T1 space to standard space failed or their T2 FLAIR images were unusable (hence, no ventricle masks), for example due to excessive head motion, atypical structure and/or anatomical abnormalities. Full details of the quality control pipeline have been previously described [12]. Finally, 35,273 participants were selected in this study whose data were deemed suitable for quantitative susceptibility mapping analysis.

4.2.2 Evaluation and development of QSM processing pipeline for UK Biobank swMRI data

The proposed QSM processing pipeline for UK Biobank swMRI data is shown in **Fig. 4.1**. The evaluations and rationale of selecting these specific algorithms are discussed in the following sections.

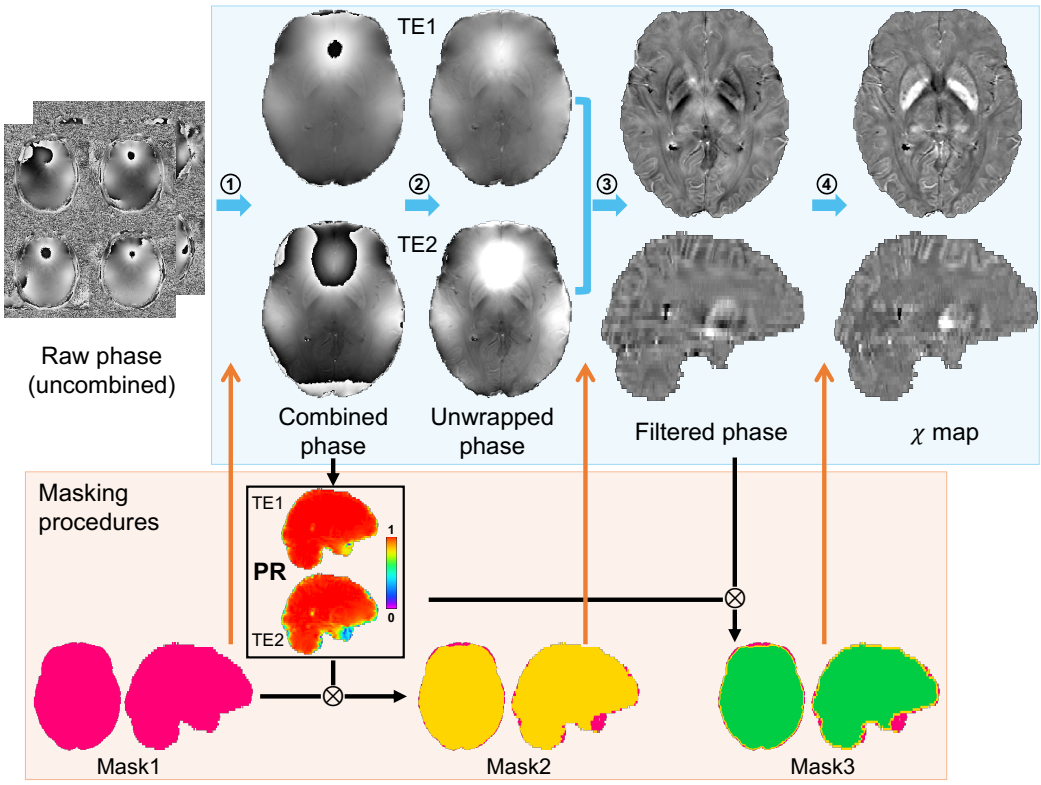


Figure 4.1 QSM processing pipeline for UK Biobank swMRI data. Blue arrows indicate the main processing steps. Step 1: Channel combination using MCPC-3D-S. Step 2: Phase unwrapping using a Laplacian-based algorithm. Step 3: Background field removal using V-SHARP. Step 4: Dipole inversion using iLSQR. Black arrows indicate the brain mask evolution, and orange arrows indicate the brain mask applied at each step. Briefly, the brain mask provided by UK Biobank (Mask1, pink) was first used for the channel combination step. To exclude unreliable voxels in the vicinity of sinus cavities, the mask was subsequently refined using a 'phase reliability' map (PR, black box) (Mask2, yellow). After background field removal, the output mask from V-SHARP was further refined using the phase reliability map, with the resulting mask (Mask3, green) used for dipole inversion.

Combination of multi-channel phase data

As discussed in Chapter 2, robust combination of multi-channel phase data is crucial for performing QSM. The UK Biobank swMRI protocol collects two echoes (TEs = 9.4 and 20 ms), only a handful of algorithms can be used for coil combination. In this work, we compared two different coil combination methods: phase difference method [21] and MCPC-3D-S [22]. The underlying mechanisms of these two methods are discussed in detail in Chapter 2, section 2.6.1.

Although MCPC-3D-S is slower than the phase difference method due to multiple additional steps including phase unwrapping, here performed using PRELUDE [24], it generates coil-combined phase data with higher SNR verses the phase difference method, as shown in **Fig. 4.2**.

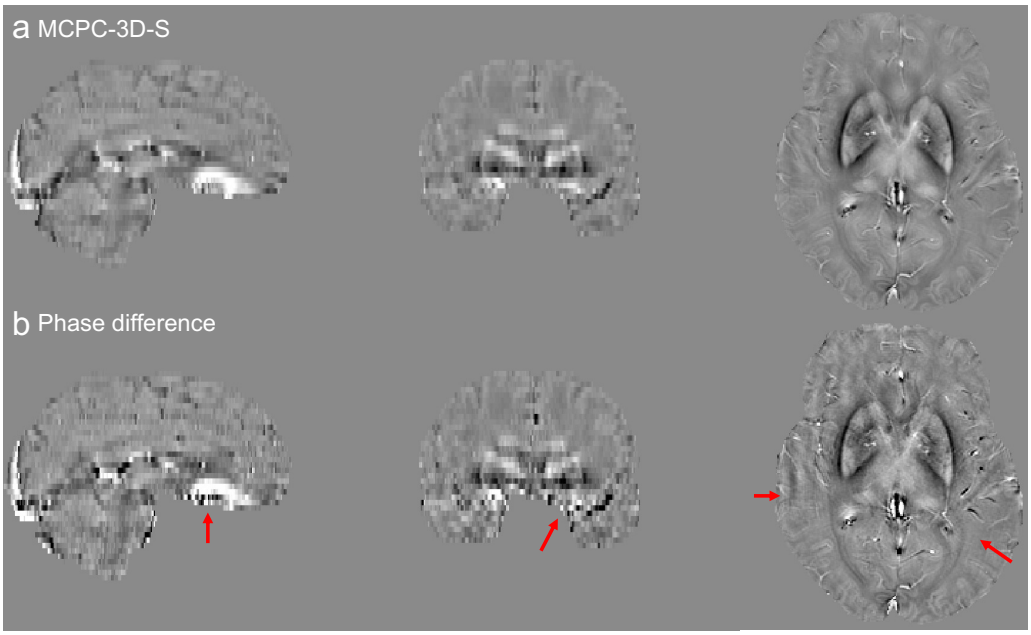


Figure 4.2 Example filtered phase data from a single UK Biobank subject using MCPC-3D-S **(a)** and phase difference **(b)** channel combination. Overall, MCPC-3D-S (a) generated images with higher SNR and fewer imaging artefacts (red arrows) than phase difference (b).

Unwrapping of channel-combined phase

As presented in Chapter 2, section 2.6.2, there are a number of algorithms that have been developed for phase unwrapping. In this study, we compared a path-based (FSL's PRELUDE [24]) and a Laplacian-based [25] (from the STI suite toolbox https://people.eecs.berkeley.edu/~chunlei.liu/software.html) algorithm. Overall, the Laplacian-based algorithm demonstrated rapid phase unwrapping with smoother phase variance in (noisier) regions with large phase jumps verses PRELUDE, as shown in **Fig. 4.3**. Laplacian-based algorithms perform a degree of background field removal when unwrapping phase maps, which restricts their use when quantitative phase values are required (e.g., the coil-combination step). However, because unwrapped phase data are

subsequently filtered in QSM to remove background field contributions, this does not restrict their use for generating χ maps.

The unwrapped phase images were subsequently (prior to background field removal) combined into a single phase image via a weighted sum [80] over the two echoes to increase signal-to-noise ratio of the phase data that will be filtered in the following step. The weighting factor, W, is defined as [80]:

$$W = \frac{TE_{1/2} \cdot e^{-TE_{1/2}/T2^*}}{\sum_{n=1}^{2} TE_n \cdot e^{-TE_n/T2^*}} \quad (4.1)$$

Here, $T2^*$ was set as a constant (40 ms). This effectively weights each echo by its predicted signal-to-noise ratio.

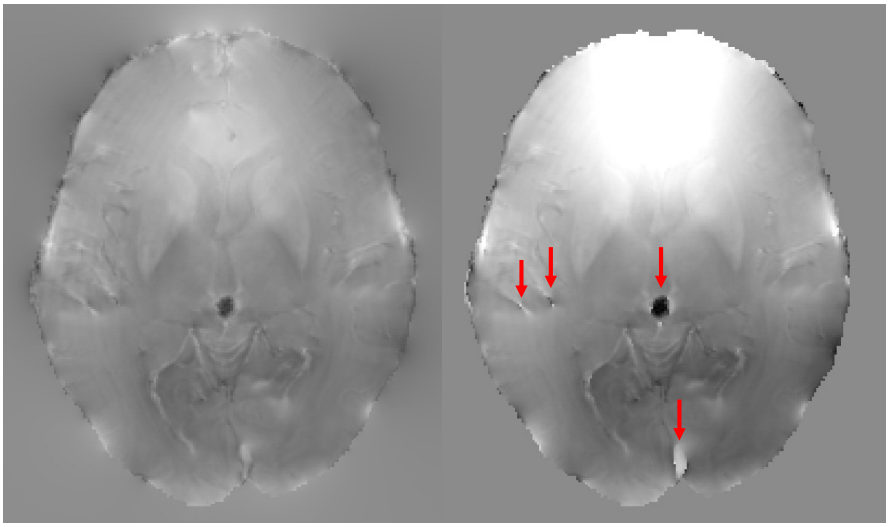


Figure 4.3 Unwrapped phase image from an example UK Biobank subject. Red arrows indicate boundaries with large phase jumps in the unwrapped phase map using PRELUDE, which are not present using the Laplacian-based algorithm.

Phase reliability masking

Due to the non-local nature of dipole inversion, voxels with unreliable phase can corrupt the entire χ estimation in their vicinity (leading to streaking artefacts) [19] and thus, should be removed from the brain mask. To address this, phase reliability maps were

estimated per subject to identify and remove these voxels. As shown in **Fig. 4.4**, regions of strong local phase variation were indicated by low intensity values on phase reliability maps, while regions with relatively homogeneous phase had intensity values close to one. Phase reliability maps are generated as follows: channel-combined phase images were first converted to complex data (i.e., combining voxel-wise phase with unit magnitude) and convolved with a 3D spherical kernel (2mm radius). This spherical kernel was normalised to account for the fraction of each voxel contained in the kernel, as can be visualised in the example kernel image in **Fig. 4.4a**, voxels at the centre of the kernel have higher intensity compared to voxels at the edge of the kernel. At brain boundaries, only the voxels within the brain mask were included in the convolution. The phase reliability map was subsequently derived by calculating the magnitude of the convolved complex data. The threshold of the phase reliability map for each echo was empirically determined after visual inspection of ~100 UK Biobank subjects. Here, two levels of thresholding were implemented: thresholds of 0.6 for first echo and 0.5 for second echo were applied to phase reliability maps to refine the brain mask used in background field removal of the two-echo combined phase data; thresholds of 0.7 for first echo and 0.6 for second echo were applied to further refine the brain mask produced in background field removal step. This further refined brain mask was used in dipole inversion step.

An additional step was applied to the refined brain mask in each thresholding level, to fill any isolated holes (in 3D) in the middle of the bran that were not connected to the sinus cavities using the MATLAB function *imfill*. This step predominantly fills back regions with crossing vessels (which lead to large local phase variance) in the centre of the brain.

This phase reliability masking procedure effectively detects region where phase varies rapidly (i.e., with large local phase variance) at brain boundaries and predominantly in the vicinity of sinus cavities due to the air/tissue interface.

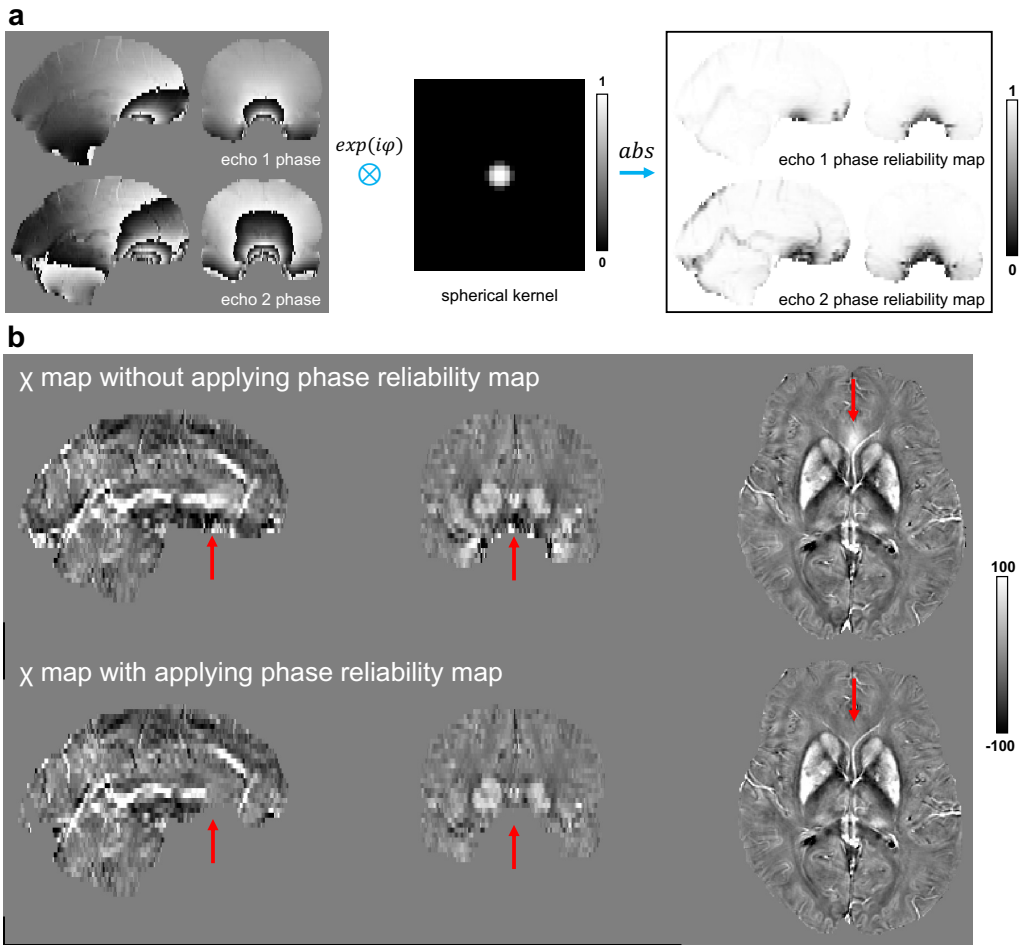


Figure 4.4 (a) Phase reliability map pipeline for each echo in a single UK Biobank subject. ⊗ represents convolution in complex space, where phase data (φ) were converted to exp ($i \cdot \varphi$). Phase reliability map was calculated as the magnitude (absolute value) of the convolved complex data **(b)** Example χ map generated without (top) and with (bottom) the phase reliability map correction. Red arrows indicate regions with strong phase variations that induced large field inhomogeneities. The phase reliability correction removes voxels with large phase variations at the brain edge, resulting in χ maps with fewer artefacts.

Background field removal and dipole inversion

Removal of background field contributions and subsequent dipole inversion are the final two steps required to generate χ maps, with a number of different algorithms proposed for each step. Here, we evaluated combinations of these algorithms based on the final χ map. These evaluations used both quantitative and qualitative metrics, including the

observation of large-scale inhomogeneities and streaking artefacts on χ maps, and cross-subject consistency of both χ maps (in standard space) and χ values in regions of interest (subcortical structures). Due to the lack of ground truth for validation, our steps for evaluation were: (1) we first looked for the presence of large-scale inhomogeneities or streaking artefacts induced by 'algorithm A', we tried to identify whether these artefacts existed in multiple subjects; (2) we then compare χ measures in ROIs generated by 'algorithm A' to results generated by 'algorithm B' that did not induce visible artefacts, if the ROI measures from 'algorithm A' did show larger variances across subjects, these variances would be likely due to artefacts, rather than true biological variances.

We compared 5 different background field removal algorithms (V-SHARP [28], PDF [31], iHARPERELLA [81], iRSHARP [82] and LBV [83]), 3 different dipole inversion algorithms (iLSQR [38], STAR-QSM [37] and MEDI [35]) and 1 single-step background field removal and dipole inversion algorithm (fast TFI [84]) resulting in the evaluation of 16 ($3 \times 5 + 1$) different combinations. Evaluations used group averaged χ maps over 50 subjects.

Figure 4.5 compares background field removal algorithms. For conciseness, we display results using iLSQR only, but evaluations were performed using all of the proposed dipole inversion algorithms. Overall, we found that V-SHARP provided the best performance, generating χ maps without observable large-scale inhomogeneities and a low cross-subject standard deviation on resulting χ maps compared to other background field removal algorithms.

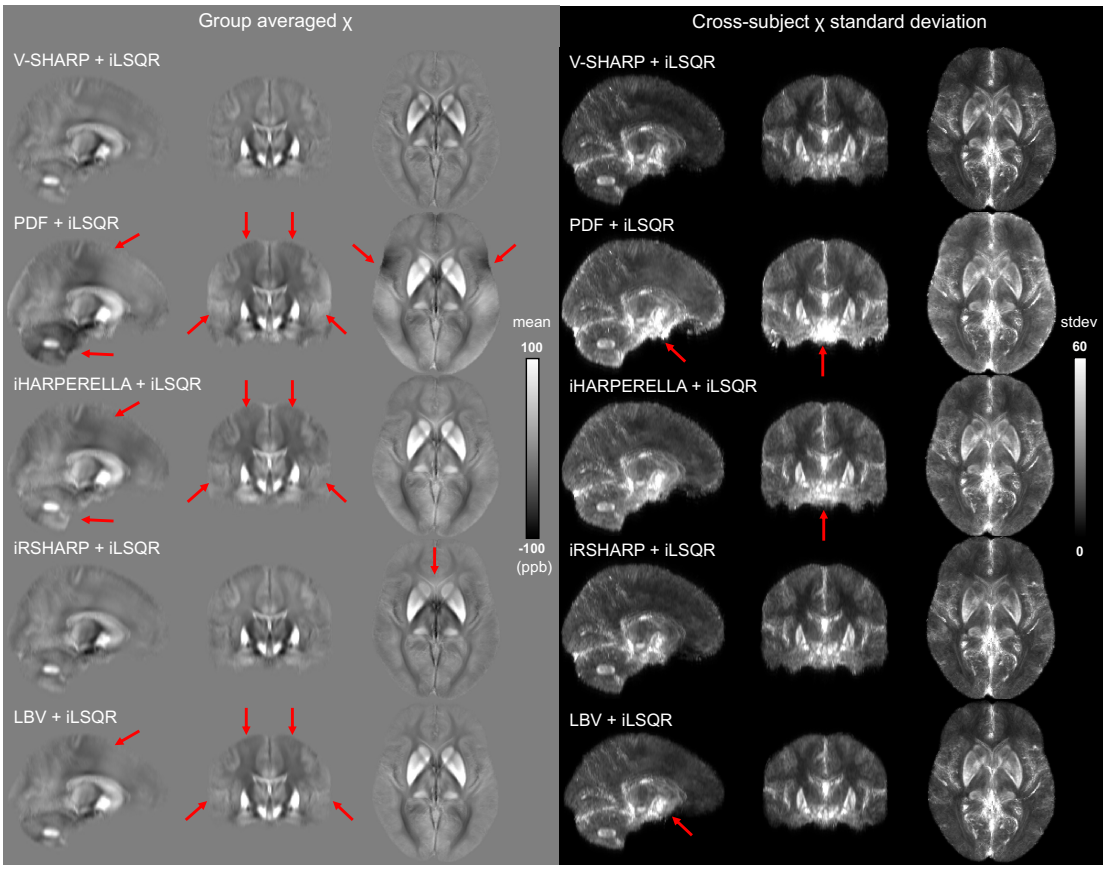


Figure 4.5 Group averaged χ maps (left) and standard deviation (stdev) maps (right) from 50 subjects. χ maps were produced using V-SHARP/PDF/iHARPERELLA/iRSHARP/LBV and iLSQR. Red arrows highlight regions of large-scale inhomogeneity (consistent across subjects) and cross-subject variation on resulting χ maps when compared to V-SHARP and iLSQR. Although iRSHARP and V-SHARP are derived from the same technique (SHARP), for UK Biobank data the V-SHARP implementation was found to remove more field inhomogeneities in brain regions in close vicinity to our regions of interest, including the caudate, putamen and pallidum.

Figure 4.6 presents evaluations of the different dipole inversion algorithms, displaying results using V-SHARP, which was the method adopted for background field removal. STAR-QSM and iLSQR produced similar appearing χ maps with better quality compared to MEDI and TFI. To further compare STAR-QSM and iLSQR, we carried out an expanded comparison, with the assumption that the phase reliability masking procedure might fail in some subjects and voxels with large field variations remain in the phase. To simulate such circumstances, phase data without the phase reliability map

masking were used for dipole inversion. **Figure 4.7** demonstrates that iLSQR outperformed STAR-QSM in such a situation.

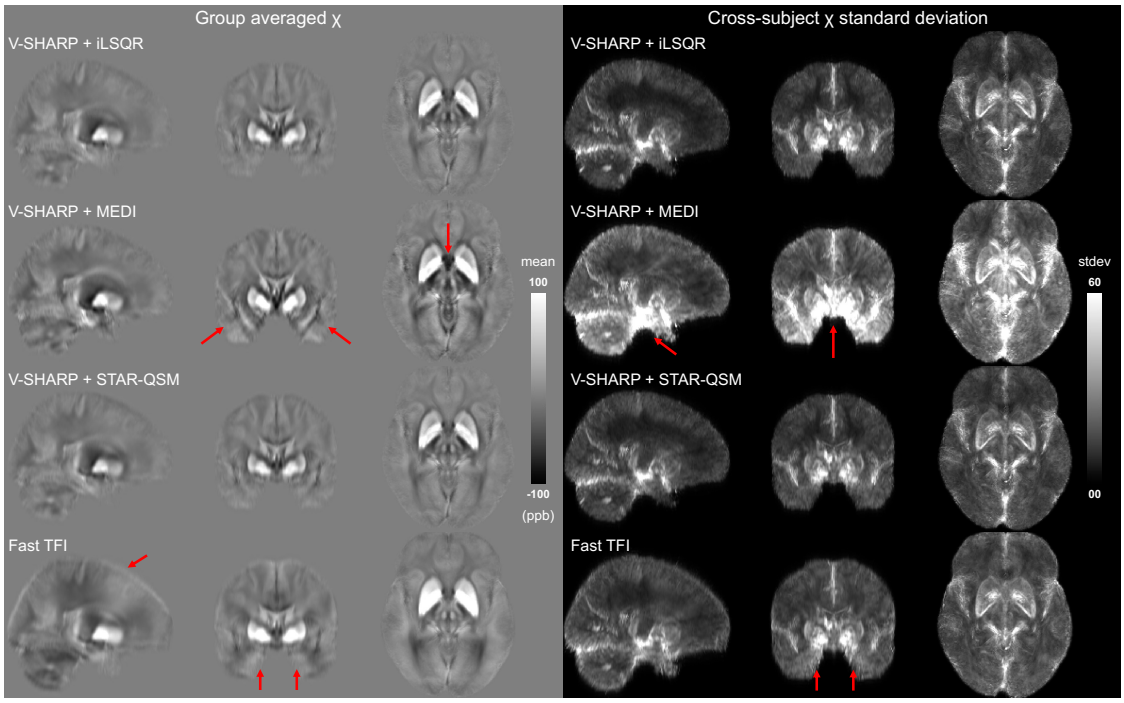


Figure 4.6 Group averaged χ maps (left) and standard deviation (stdev) maps (right) from 50 subjects. χ maps were produced using V-SHARP and iLSQR/STAR-QSM/MEDI, in addition to the single-step fast TFI algorithm. Red arrows highlight regions of large-scale inhomogeneity (consistent across subjects) and cross-subject variation on resulting χ when compared to V-SHARP and iLSQR. The group averaged χ maps using iLSQR and STAR-QSM visually appeared of very similar quality.

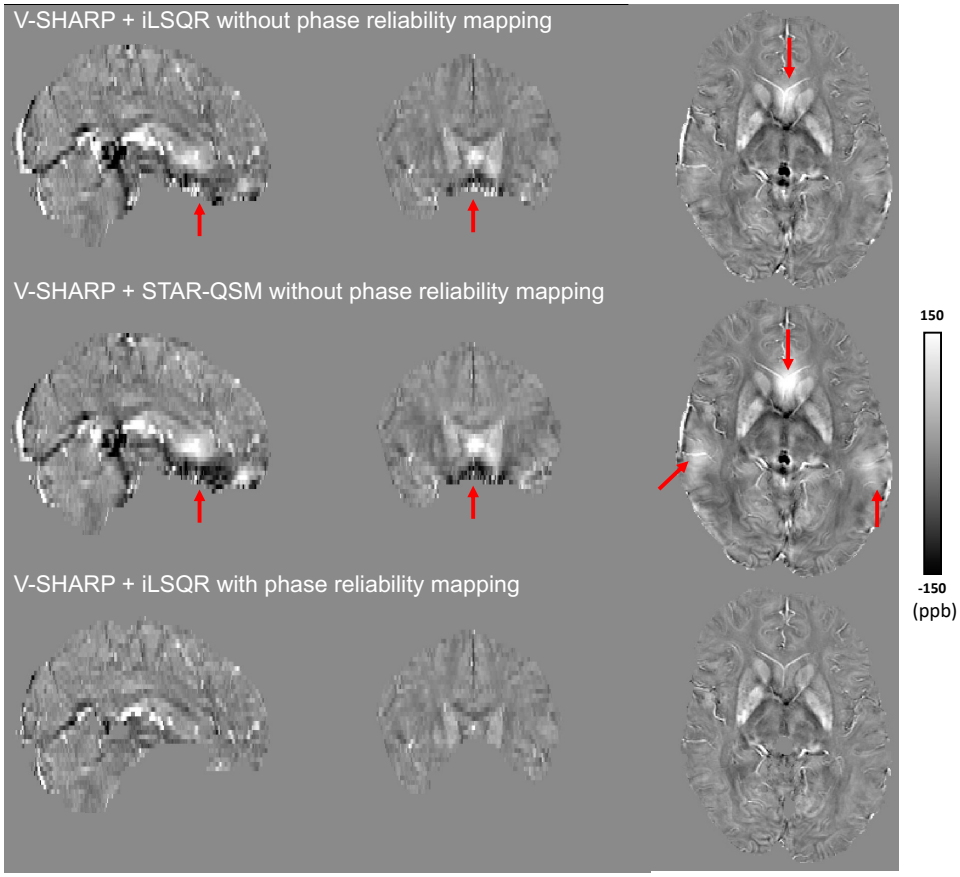


Figure 4.7 Example χ map from a single UK Biobank subject using V-SHARP and iLSQR/STAR-QSM without the phase reliability map correction. Overall, iLSQR demonstrated improved suppression of streaking artefacts and image inhomogeneities on resulting χ maps (top) verses STAR-QSM (middle), important if the phase reliability correction failed to remove all voxels with unreliable phase information. Remaining V-SHARP and iLSQR image inhomogeneities are subsequently eliminated with the phase reliability correction (bottom).

Finally, we evaluated the different background field and dipole inversion algorithms by calculating the median χ in 14 subcortical ROIs: thalamus, caudate, putamen, pallidum, hippocampus, amygdala, accumbens, with left and right separated for each region (**Fig. 4.8**). Although different combinations of algorithms showed varying degrees of artefacts on χ maps (**Figs. 4.5 and 4.6**), median χ measures in the subcortical ROIs are broadly in similar ranges. The combination of V-SHARP and iLSQR generally showed the smallest within-ROI variance.

Our comparisons determined that the combination of MCPC-3D-S coil combination, Laplacian-based phase unwrapping, masking with the phase reliability correction, V-

SHARP background field removal and iLSQR dipole inversion was the optimal pipeline for UK Biobank swMRI data.

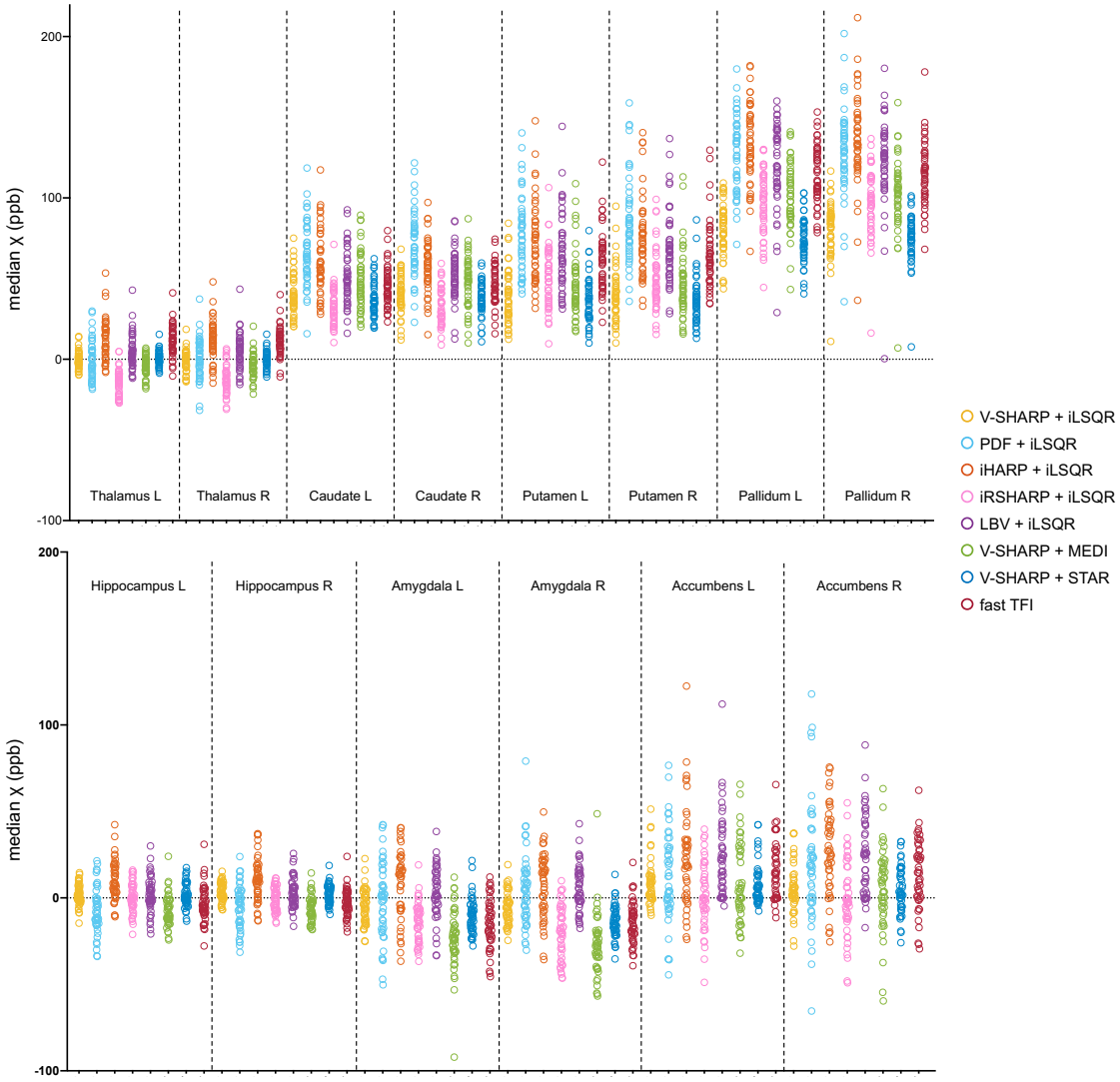


Figure 4.8 Comparison of median χ values derived from χ maps for 8 combinations of algorithms. Here, each point represents a single χ estimate from each of the 50 subjects. For each ROI, different combinations generated median χ values covering a broadly similar range. The combination of V-SHARP and iLSQR generally showed the smallest within-ROI variance.

4.2.3 Evaluations of reference region for χ maps

QSM provides a measure of relative rather than absolute χ [60]. The presence of an unknown offset in the estimated map for any individual is problematic for comparison of χ values across subjects. To address this, χ values are commonly reported as offset with respect to an internal reference region. Here, we compared the use of three widely-used

reference regions [79] (**Fig. 4.9**): mean χ across (i) the whole brain, (ii) cerebrospinal fluid (CSF) and (iii) a white matter region (forceps minor). The reason forceps minor was selected here is that (1) it is part of corpus callosum which has been widely-studied in previous literature as a reference region in QSM [79]; (2) UK Biobank provides ROI masks of forceps minor.

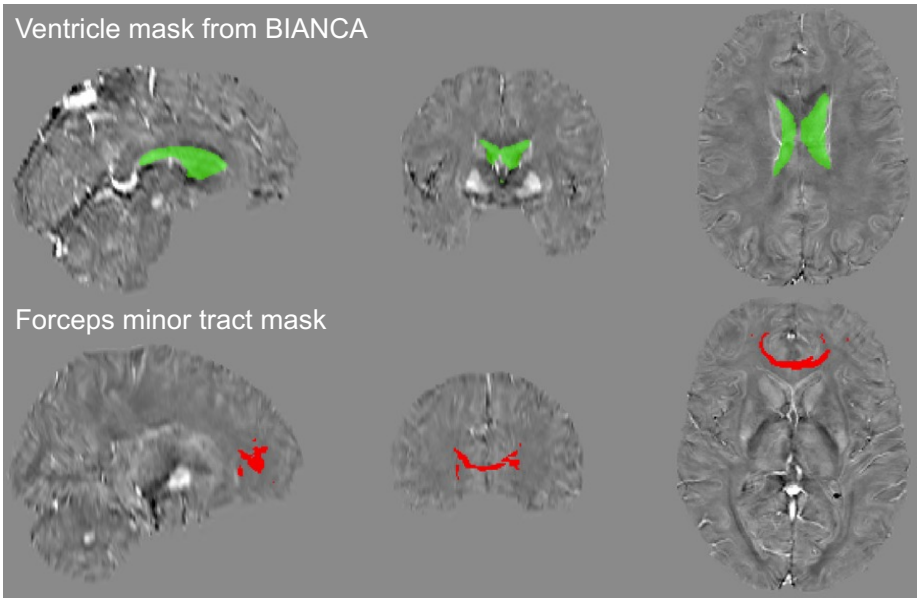


Figure 4.9 Ventricle and forceps minor tract masks used for the CSF and white matter reference, overlayed on an example χ map (single subject). Ventricle masks for each subject were previously generated as part of UK Biobank, extracted from the T2 FLAIR data using BIANCA[85]. The forceps minor tract mask was derived from the diffusion MRI data using AutoPtx[86].

The χ distribution in the ventricle mask (**Fig. 4.10**) generally revealed a bimodal (assuming to be Gaussian and inverse gamma) distribution, which likely corresponds to CSF and the choroid plexus compartments. The choroid plexus can be found in each of the brain ventricles, the main function of which is to produce CSF [87]. It is reported to be diamagnetic as it commonly contains calcification [7], thus the inverse gamma distribution (containing negative values) is considered to represent choroid plexus voxels. To extract the CSF component of this distribution, we used an in-house mixture modelling

algorithm [88]. The mean of the central Gaussian distribution was used to represent χ of CSF.

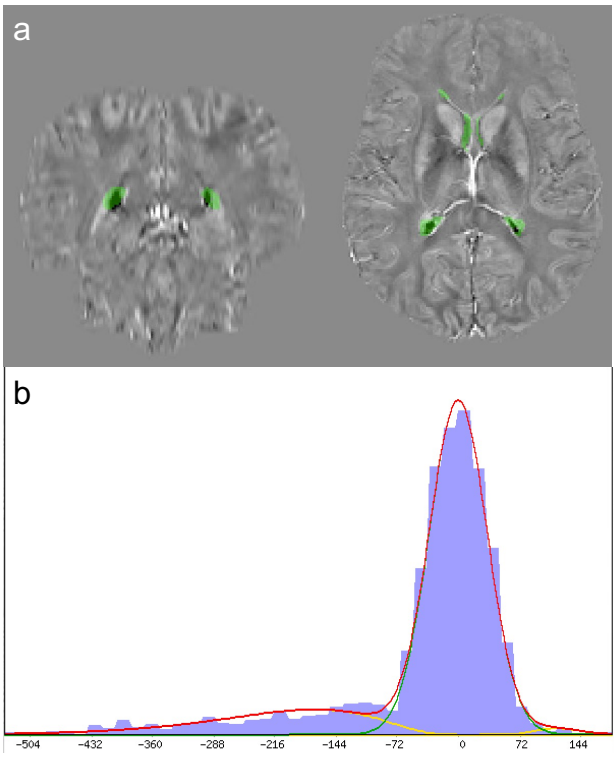


Figure 4.10 (a) Example ventricle mask overlaid on top of a χ map for a single subject. **(b)** distribution of χ in the ventricle mask. The negative voxels likely correspond to the choroid plexus, resulting in the left "tail" (negative inverse gamma) of the χ distribution. The CSF reference χ estimate was measured as the mean of the main Gaussian distribution.

Evaluation of the three reference regions were performed using UK Biobank subjects who had undergone scanning at two time points (1,447 subjects in total) with second imaging session performed approximately 2 years (2.25±0.12y) after the first imaging session. Specifically, we compared cross-scan consistency of χ estimates referenced to these three different regions. Defining χ_1 and χ_2 as the referenced χ estimates at two timepoints; $\hat{\chi}_1$ and $\hat{\chi}_2$ as the true χ at two timepoints; and ϵ_1 and ϵ_2 as the reference error at two timepoints (such that the ideal reference region corresponds to $\epsilon_1 = \epsilon_2 = 0$), the referenced χ estimates can then be written as:

$$\chi_1 = \hat{\chi}_1 + \epsilon_1$$
$$\chi_2 = \hat{\chi}_2 + \epsilon_2 \quad (4.2)$$

Here, the cross-scan consistency refers to the Pearson's correlation r between χ_1 and χ_2, which is calculated as:

$$r(\chi_1, \chi_2) = \frac{COV(\chi_1, \chi_2)}{\sigma_{\chi_1}\sigma_{\chi_2}} \quad (4.3)$$

where $COV(\chi_1, \chi_2)$ represents the covariance between χ_1 and χ_2; σ_{χ_1} and σ_{χ_2} represent the (cross-subject) standard deviations of χ_1 and χ_2.

Assuming χ and ϵ are independent (across subjects), even in the presence of large biological differences between $\hat{\chi}_1$ and $\hat{\chi}_2$, the ideal reference region would maximise $COV(\chi_1, \chi_2)$, minimise σ_{χ_1} and σ_{χ_2} (by minimising unwanted variances due to referencing), both contributing to a higher correlation r between χ_1 and χ_2. Note that this calculation is valid when the difference in error of a reference between two timepoints $(\epsilon_1 - \epsilon_2)$ and true χ changes between two time-points $(\hat{\chi}_1 - \hat{\chi}_2)$ are independent. If $(\epsilon_1 - \epsilon_2)$ and $(\hat{\chi}_1 - \hat{\chi}_2)$ are coupled (although this is unlikely), using cross-scan consistency as a metric might has the risk of favouring a reference region that $(\epsilon_1 - \epsilon_2)$ and $(\hat{\chi}_1 - \hat{\chi}_2)$ are negatively correlated (i.e., a reference region that suppresses χ difference due to biological changes between two timepoints). Such a reference would increase $COV(\chi_1, \chi_2)$, but its effect on σ_{χ_1} and σ_{χ_2} might be complicated.

In our evaluations, CSF-referenced QSM IDPs showed the highest consistency (correlation r) across two time points (**Fig. 4.11a**) and CSF in the lateral ventricles was therefore chosen as the reference region.

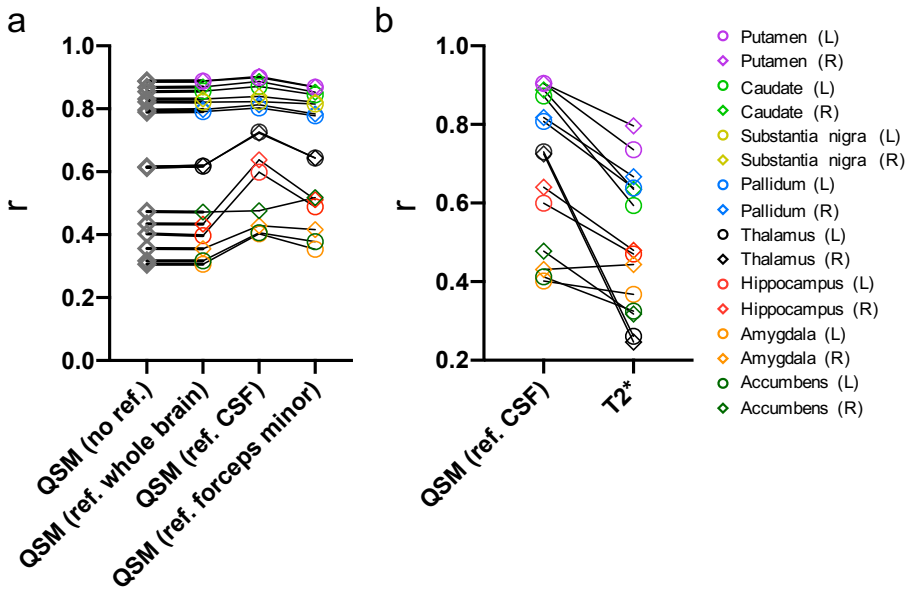


Figure 4.11 Correlation between QSM IDPs obtained at the first and second imaging visit (timepoints). (a) Overall, the CSF referenced IDPs yielded the highest r values (most evident in the thalamus and hippocampus), indicating that CSF is the most robust reference among the three regions. (b) QSM IDPs typically display higher reproducibility verses the T2* IDPs.

4.2.4 Generation of QSM-based image-derived phenotypes

In this study, CSF referenced χ map was transformed to subject's native T1 space (using FLIRT) [32,33] and MNI152 space (using FNIRT) [89], with transformation matrix and warps provided by the UK Biobank imaging processing pipeline [12]. A QSM population-average template (**Fig. 4.12a**) was produced by averaging χ maps from all available subjects, and an "aging" template (**Fig. 4.12b**) was calculated as the difference between the average χ maps for youngest (<52yo) and oldest (>75yo) subjects.

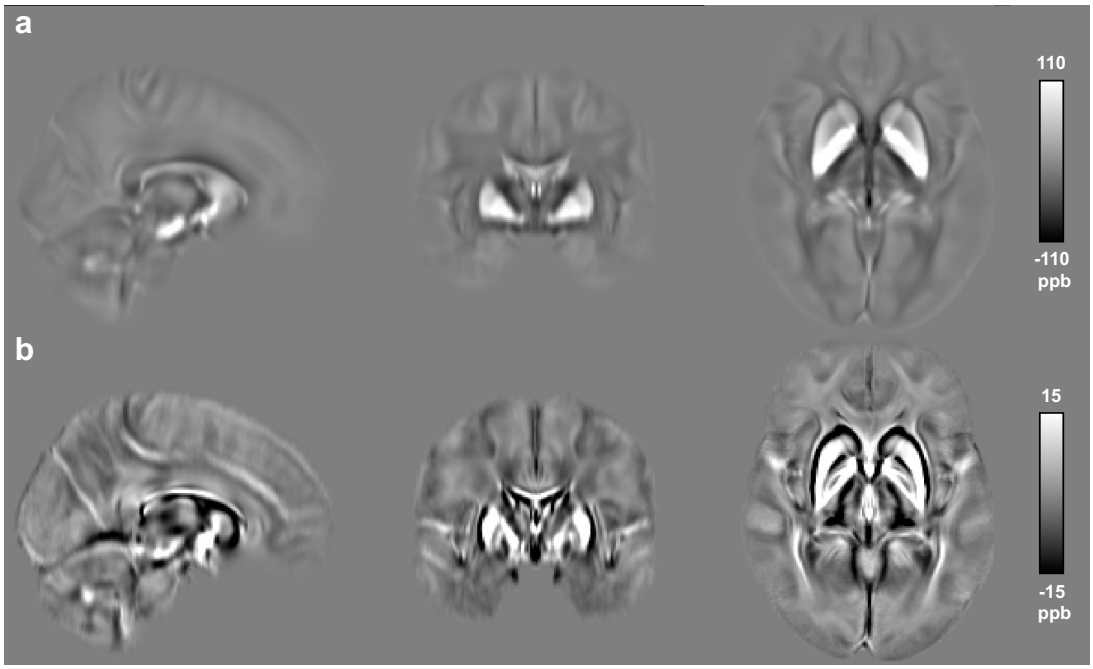


Figure 4.12 (a) QSM atlas generated by averaging χ maps (non-linearly registered to MNI152 space) from all available subjects. **(b)** QSM aging atlas, generated by taking the difference between χ maps from the youngest (< 52yo) and oldest (> 75yo) age groups. Here, differences due to aging are largely driven by atrophy. Note that atrophy-related differences would be removed with perfect non-linear registrations to MNI space, the presence of atrophy-related "edge effects" might reflect slight misalignments which could be potentially improved by multi-modal registration in future work.

Image-derived phenotypes (IDPs) of χ were generated for eight subcortical structures (accumbens, amygdala, caudate, hippocampus, pallidum, putamen, substantia nigra and thalamus, left and right), and in subject-derived regions of white matter hyperintensities (WMH). Masks for each subcortical structure in T1 space (excluding the substantia nigra) have been previously generated using FIRST (FMRIB's Integrated Registration and Segmentation Tool) [90] as part of the UK Biobank image processing pipeline. Masks for the substantia nigra used in this study were derived from a substantia nigra atlas [91] in MNI152 space. Masks for WMH lesions (derived from the BIANCA processing [8,27]) were provided to us in T1 space from the UK Biobank image processing pipeline, alongside white matter masks generated using FAST (FMRIB's Automated Segmentation Tool) [92].

FIRST-generated subcortical masks were eroded (2D 3x3 kernel) in the T1 space of each subject. The median χ-value was calculated as a separate IDP for each of the left/right subcortical regions. Given the established potential of χ in the substantia nigra as a biomarker for Parkinson's disease, the substantia nigra was selected as one of the ROIs. Unfortunately, FIRST does not produce segmentation mask for the substantia nigra, its IDPs were generated based on a substantia nigra atlas in MNI152 space which required χ maps registered to MNI152 space. However, non-linear registrations could not provide sufficiently high-quality definition of regional boundaries; and atrophy-related changes were observed on the χ "aging" template (**Fig. 4.12b**) indicating slight misalignments in non-linear registrations. Hence, applying a substantia nigra mask derived from the MNI152 atlas to χ maps in MNI152 space would inevitably include voxels outside substantia nigra. Furthermore, the amount of misalignment varied across subjects, as it was related to morphological variations of substantia nigra due to normal aging or pathology. As we were only interested in median χ across substantia nigra voxels, this unwanted variation due to morphological variations across subjects should be removed. The substantia nigra mask was refined by excluding voxels that had negative χ values, with median χ values subsequently calculated as a separate IDP for left and right substantia nigra. This refinement was based on empirical χ values and could exclude sub-regions of substantia nigra that have negative χ, but it enabled us to address the shortcomings of these MNI152 masks. In future work, a more principled and robust way of extracting substantia nigra voxels would improve the accuracy of QSM/T2* substantia nigra IDPs in UK Biobank.

For the WMH IDP, the aim was to isolate χ properties that are unique to lesions, as opposed to more global properties of white matter χ. Therefore, the difference between the estimated χ values of WMH and normal-appearing white matter was calculated as an

IDP. Here, we extracted the mean χ value from the WMH mask and the median χ value from normal-appearing white matter, defined as the intersection of FAST- and BIANCA-based white matter masks with the WMH voxels removed.

4.2.5 Generation of T2*-based image-derived phenotypes

While most of the QSM IDPs use the same spatial ROIs as existing T2* IDPs, the existing UK Biobank pipeline did not include T2* of substantia nigra or WMH. We thus generated three new T2* IDPs for (substantia nigra left and right, and WMH). This enabled a direct comparison between QSM and T2* for 18 IDPs.

Furthermore, T2* estimates are biased by the presence of macroscopic field gradients (for example, induced by air/tissue interface), particularly when imaging voxels are large (in our case, using thick slices) [93]. This confounding effect could introduce unwanted (cross-subject) variance, and potentially drive spurious associations with phenotypic or genetic measures. However, the existing UK Biobank pipeline doesn't account for this when generating T2* IDPs. Given that our QSM pipeline produces phase maps that can be used to model this effect, and that we want to compare association analyses with T2* and QSM IDPs in Chapter 5, we decided to develop a basic pipeline for deconfounding of this effect.

We first modelled the relationship between macroscopic field gradients and R2* (1/T2*) measurement errors using both simulations and UK Biobank data [93]. This produced a macroscopic field gradient confound variable specific to each subject and brain region, which was generated and regressed out from T2* IDPs. No association was found between the field gradient confounds and QSM IDPs as expected, and thus this particular confound was only applied to T2* data.

To reduce the confounding effect of field gradients on the association analyses with T2* IDPs, we generated macroscopic field gradient maps along the slice-direction (**Fig.**

4.13) for all UK Biobank subjects. Median gradient magnitude values were subsequently calculated in each subcortical ROI as a summary measure of the background field gradient. These summary measures provide an additional set of confounds when performing our association analysis. The distribution of median gradient magnitude (Gmag) for subcortical ROIs is shown in **Fig. 4.14.**

To generate the macroscopic field gradient maps, the two-echo channel-combined phase data (described in Section 4.2.2) from each subject was unwrapped using PRELUDE and two echo phase data were averaged to generate $\gamma\Delta B_{averaged}$. PRELUDE was chosen as it does not remove any background field components (as opposed to Laplacian-based methods). $\gamma\Delta B_{averaged}$ was subsequently filtered using V-SHARP, $\gamma\Delta B_{V_SHARP}$, with the macroscopic field of each subject estimated as:

$$\gamma\Delta B_{background} = \gamma\Delta B_{averaged} - \gamma\Delta B_{V_SHARP} \quad [8]$$

Gmag was calculated as the gradient magnitude (along the z-direction) of $\gamma\Delta B_{background}$ (**Fig. 4.13**). Here, given that the in-plane resolution (0.8 mm) is much higher compared to through-plane (3 mm), for the remainder of this thesis, we only calculate field gradient along the slice direction which is the predominant source of T2* measurement error.

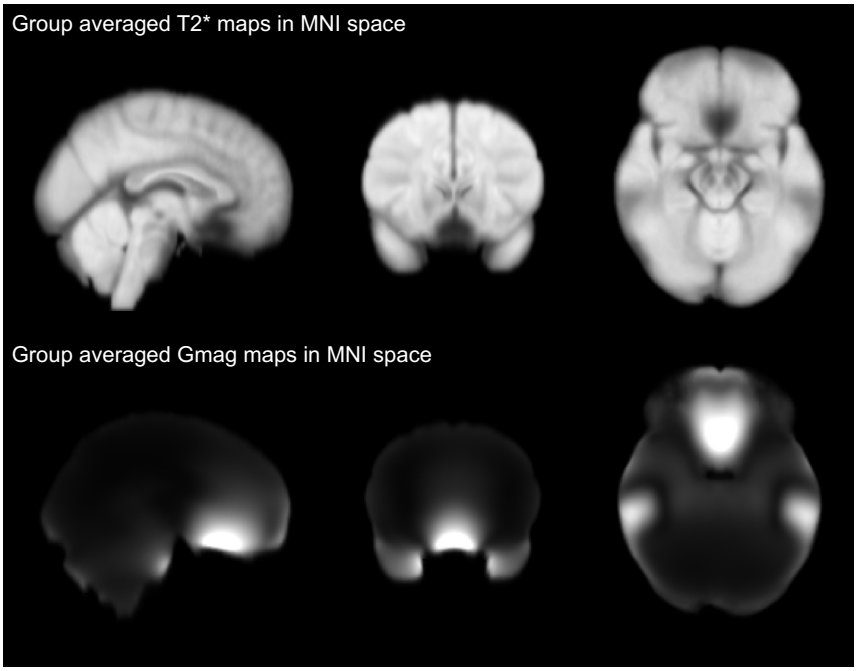


Figure 4.13 Group average T2* map (top) and Gmag (bottom) over 200 subjects. The sinus cavity and ear canals are the major sources of variations in background fields due to air/tissue interfaces. Note that voxels in the ventricles were excluded in T2* maps, but were included in the Gmag maps.

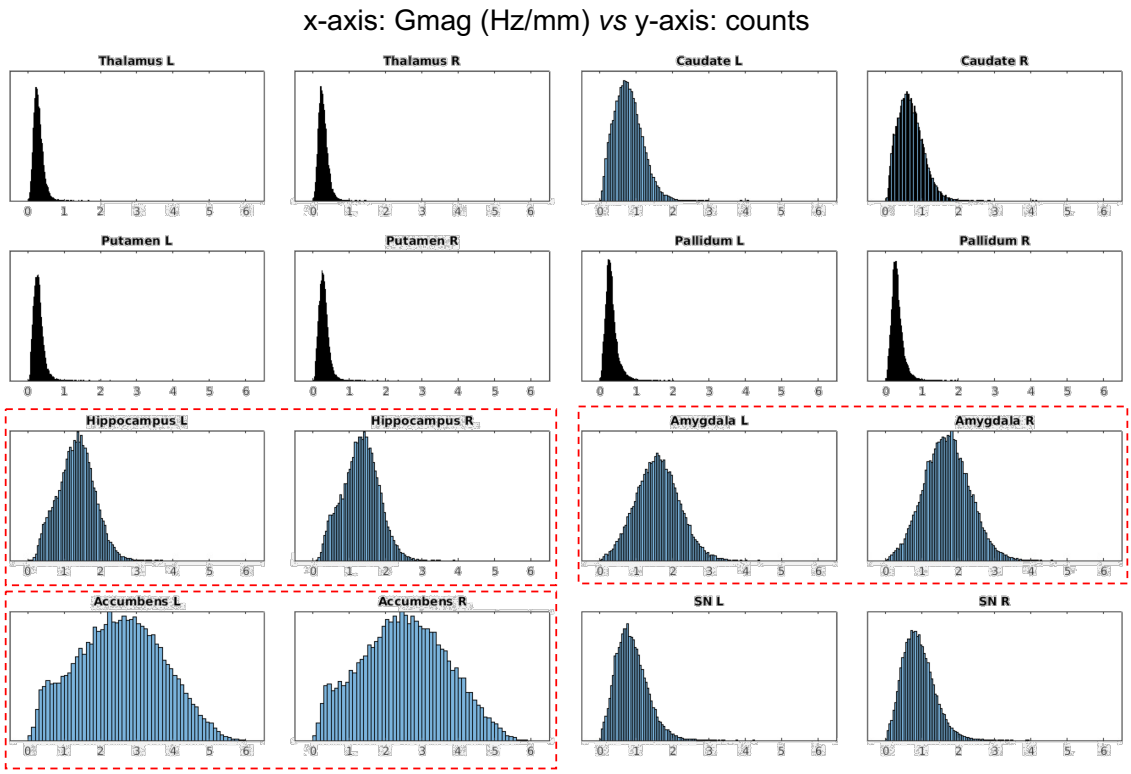


Figure 4.14 Histograms of median Gmag in 16 ROIs across all UK Biobank subjects. Only the accumbens, amygdala and hippocampus regions (highlighted by red boxes) contain a wide Gmag distribution exceeding 2 Hz/mm.

We subsequently modelled the voxel-wise relationship between macroscopic field gradients and R2* (1/T2*) (**Fig. 4.15**), to produce a set of confounds to account for the background field gradient. To achieve this, we evaluated several models to simulate the relationship between R2* and Gmag, as shown in **Fig. 4.15**. The tanh model (*A*tanh((B+x)/C)+D*) showed the best performance, defining *B*=-6.06 and *C*=1.87. We then used these fitting parameters to establish a linear relationship between the R2* and Gmag confounds, setting $Gmag_{deconf}$ = *tanh((-6.06+Gmag)/1.87)*. The deconfounding was performed at the level of IDPs, which was effectively a linear regression between R2* IDP and $Gmag_{deconf}$ to estimate *A* and *D*.

Figure 4.15 demonstrates that R2* has a dependence on field gradients where Gmag are large, but is largely independent of Gmag where they are small. From the median subcortical ROI analysis (**Fig. 4.14**), only the accumbens, amygdala and hippocampus are confounded by large macroscopic field gradients (Gmag > 2 Hz/mm). Therefore, we only performed deconfounding (linear regression) for T2* IDPs in the accumbens, amygdala and hippocampus.

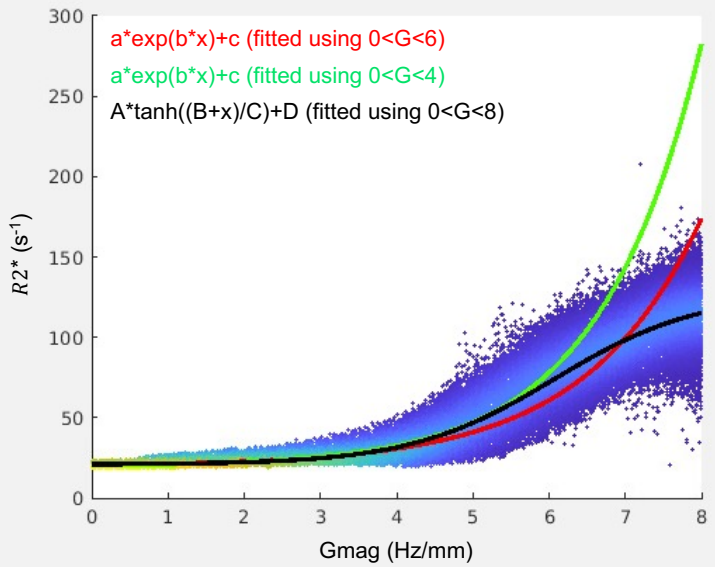


Figure 4.15 Relationship between R2* and Gmag using voxel-wise data from 150 UK Biobank subjects, fitting with an exponential and tanh model. The data scatter displays median R2* measures averaged across Gmag bins, with the colour representing the scatter density (blue – low density, green – high density). As the majority of median Gmag estimates were in the range 0<Gmag<4 Hz/mm, the exponential model (*a*exp(b*x)+c)* was fit to data in the range of 0<G<4 Hz/mm (green line) and of 0<G<6 Hz/mm (red line). The tanh function (*A*tanh((B+x)/C)+D)* (black line) showed the best performance across the whole range, particularly when Gmag > 6 Hz/mm.

No association was found between the macroscopic field gradients and QSM data (**Fig. 4.16**), which is expected as the background field removal in QSM is designed to remove the macroscopic field from phase data. Thus, this particular deconfounding was only applied to T2* IDPs.

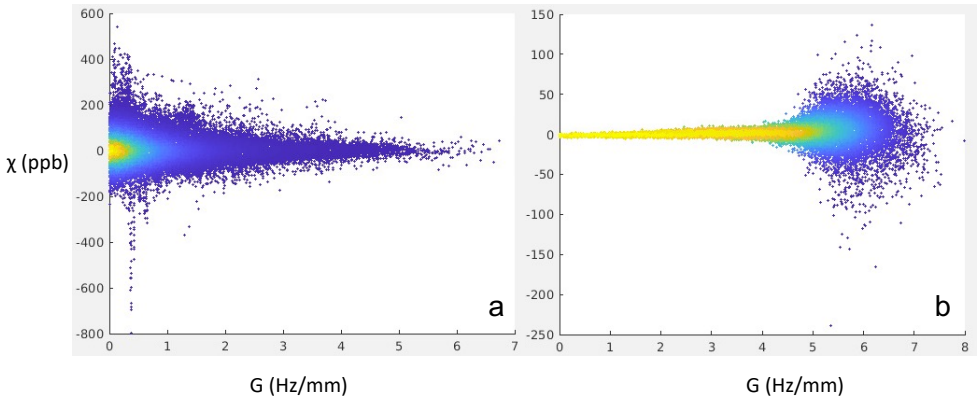


Figure 4.16 Relationship between χ measures and macroscopic field gradient Gmag. **(a)** χ vs Gmag in voxel-wise data from 150 subjects and **(b)** median value in each bin of Gmag in **(a)**.

4.2.6 Phenotypic association of T2* IDPs before and after deconfounding of macroscopic field gradients

We incorporated the confound regressors described above ($Gmag_{deconf}$), to account for biases in T2* estimates introduced by macroscopic field gradients in 3 ROIs including the accumbens, amygdala and hippocampus. As expected, the median field gradient measures correlated significantly with corresponding T2* IDPs (**Fig. 4.17,** left column) and after deconfounding (linear regression using R2* and $Gmag_{deconf}$), these correlations were dramatically reduced (**Fig. 4.17,** right column).

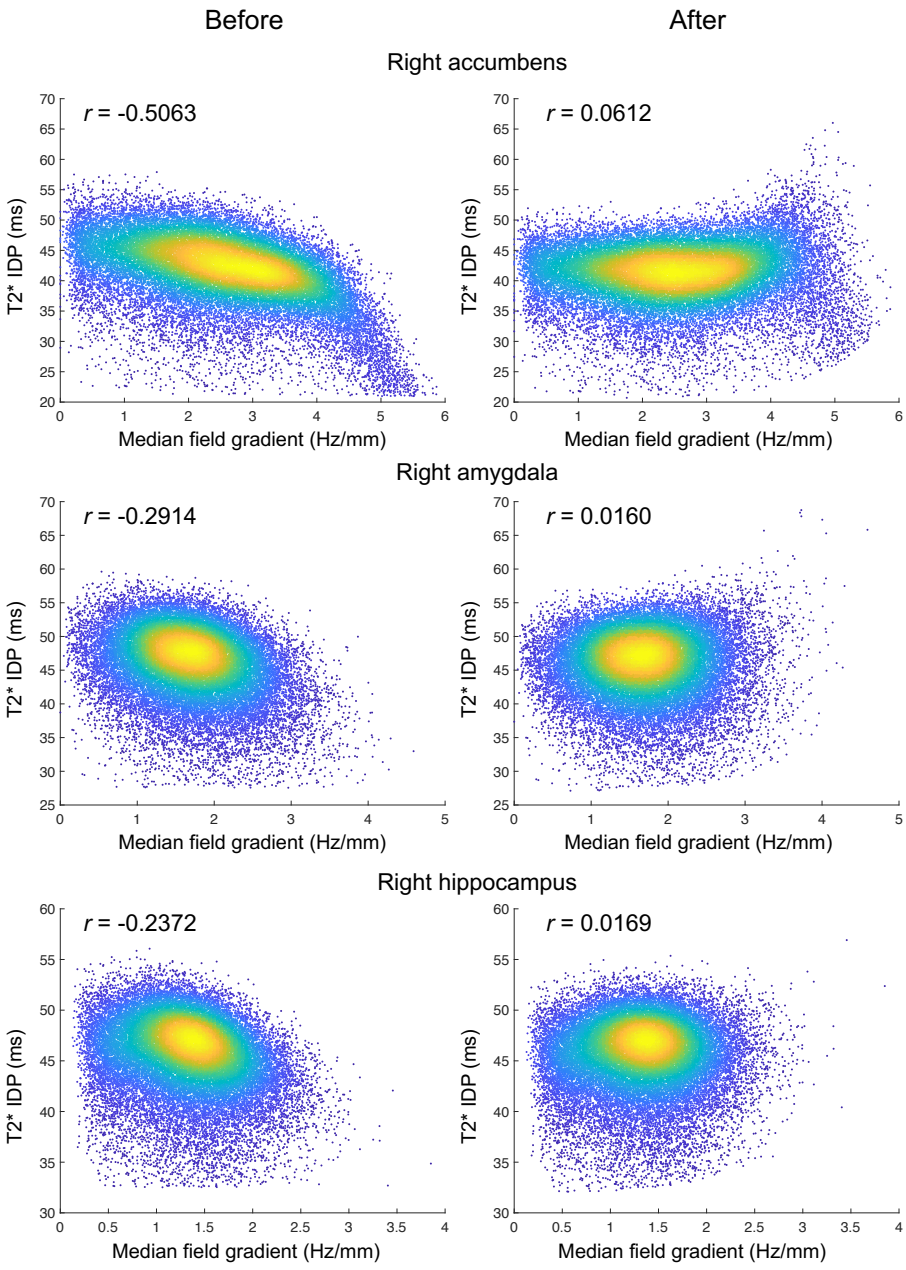
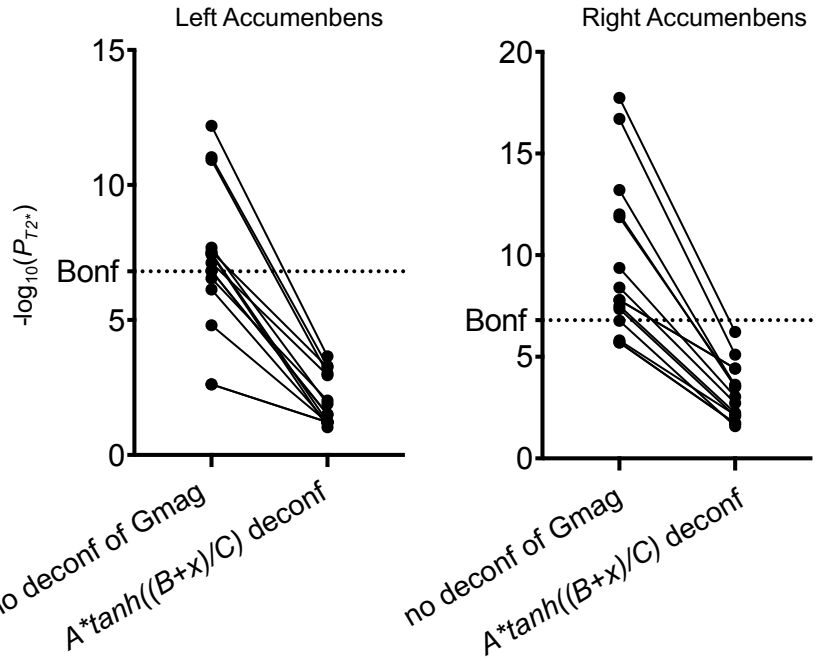


Figure 4.17 Example associations between 3 T2* IDPs (right accumbens, amygdala and hippocampus) and corresponding median field gradient measures before and after deconfounding of macroscopic field gradients based on the physical model described in Methods. As expected, T2* IDPs in these 3 regions show strong, negative correlations with field gradient measures and our proposed deconfounding was able to remove these correlations.

Before deconfounding of the macroscopic field gradient, original T2* IDPs in 3 regions (accumbens, amygdala and hippocampus) showed many spurious corelations with phenotypes related to nasal/sinus related conditions (alteration of air/tissue interface in the sinus cavity) and body size measures (alteration of overall shimming quality). For

example, the most spurious corelations were between T2* accumbens IDPs and nasal/sinus related conditions such as *nasal polyps (self-reported)*, *chronic sinusitis,* or *polypectomy of internal nose*. There have been no literature reporting links between T2* in accumbens and these nasal conditions, and the accumbens region is in the vicinity of the sinus. In addition, as shown in **Fig. 4.13,** the accumbens region is associated with extremely strong macroscopic field gradient. As expected, after deconfounding, those significant associations between T2* accumbens IDPs and nasal/sinus related phenotypes were dramatically reduced to non-significance (**Fig. 4.18**).



List of phenotypes in the plot

self-reported (1417 - nasal polyps)
secondary ICD10 (J329 - J32.9 Chronic sinusitis, unspecified)
secondary OPCS4 (E133 - E13.3 Intranasal antrostomy)
secondary OPCS4 (Y528 - Y52.8 Other specified approach to organ through other opening)
secondary OPCS4 (Y761 - Y76.1 Functional endoscopic sinus surgery)
ICD10 (J329 - J32.9 Chronic sinusitis, unspecified)
OPCS4 (E142 - E14.2 Intranasal ethmoidectomy)
OPCS4 (Y528 - Y52.8 Other specified approach to organ through other opening)
OPCS4 (Y761 - Y76.1 Functional endoscopic sinus surgery)
nasal polyp surgery / nasal polypectomy
main OPCS4 (E081 - E08.1 Polypectomy of internal nose)
main ICD10 (J339 - J33.9 Nasal polyp, unspecified)
ICD10 (J330 - J33.0 Polyp of nasal cavity)
ICD10 (J339 - J33.9 Nasal polyp, unspecified)
OPCS4 (E081 - E08.1 Polypectomy of internal nose)

Figure 4.18 Association $-\log_{10}P$ values between T2* accumbens IDPs and 15 sinus/nasal-related phenotypes. Here, each point represents one association with one unique phenotype. The list of 15 phenotypes is given below the plots. These associations are considered spurious as

accumbens regions are in the vicinity of the sinus and no previous literature has linked T2* in accumbens with sinus conditions. Two dashed horizontal lines indicate the significance threshold after Bonferroni correction ($-\log_{10}P$=7.1). Deconfounding using "tanh" model was able to dramatically reduce these associations to non-significant.

4.3 Discussion

Unlike the other brain imaging modalities in UK Biobank, which have been (or are being) collected or collated previously in thousands of subjects[39-42], QSM has previously been limited to smaller-scale studies. This UK Biobank QSM resource is approximately 2 orders of magnitude greater than the largest existing QSM dataset [98]. The number of subjects, coupled with the breadth of linked data, including genetics, extensive phenotyping and health outcomes, is expected to open up new avenues of investigation for QSM. At the time of scanning, most UK Biobank subjects are largely healthy, with the cohort age range designed to reflect a broad range of health outcomes in the coming decades. Hence, this cohort is particularly appropriate for identifying early markers of age-associated pathology. For example, in the imaged cohort, thousands of participants are expected to develop Alzheimer's and Parkinson's disease by 2030 [99]. A notable future QSM resource is the Rhineland Study, which is collecting swMRI phase images in 20,000 individuals at 3T [95]; while QSM has not yet been produced in this study, the complementary age range (≥30 years old) will ultimately enable novel investigations on its own and in combination with UK Biobank data.

Producing accurate and reproduceable χ maps for a dataset at this scale requires a robust, fully automated QSM processing pipeline [19]. We investigated available algorithms for each processing stage to identify an optimal QSM pipeline for the UK Biobank swMRI data. This includes a novel algorithm to automatically detect and exclude voxels with extremely large phase variance, a major source of imaging artefacts. Moreover, the richness of the UK Biobank imaging resource makes it an attractive target

for smaller studies to harmonise with, increasing the potential impact of our pipeline. Our QSM processing is now being incorporated into the core UK Biobank brain imaging processing pipeline [12] to be made available to researchers worldwide. To date, two ongoing COVID-19 brain imaging studies have adopted our QSM pipeline (C-MORE/PHOSP and COVID-CNS) [100] to process their brain swMRI data.

Using the two-timepoint data from 1,447 subjects (**Fig. 4.11**), we found high reproducibility (cross-scan correlations $r > 0.8$) with χ in four subcortical regions (putamen, caudate, substantia nigra and pallidum). These correlations are higher than the corresponding T2* IDPs ($0.6 < r < 0.8$). These four regions have the highest χ among all ROIs, and are reported to contain the highest iron concentrations in the brain [46,47]. χ has demonstrated a strong, positive linear relationship with iron concentration in post-mortem brain tissue [6]. These observations suggest that in structures where iron is the dominant χ source, QSM provides a reproduceable measure for tissue χ distribution.

In UK Biobank, the swMRI protocol was only allocated 2.5 minutes, placing limitations on the achievable data quality. While swMRI protocols in research studies often can acquire isotropic resolution and multiple echoes, the UK Biobank swMRI protocol was limited to two echoes with anisotropic resolution (0.8×0.8×3mm). The use of anisotropic voxels is in line with established practice for detecting cerebral microbleeds, which was the primary motivation for including swMRI in UK Biobank. The further ability to process these data for T2* and QSM is a valuable but secondary aim, for which the protocol incurs compromises. QSM involves a single-parameter fit (χ) that can be calculated from the phase at a single echo, although our pipeline explicitly uses both echoes. One limitation of the T2* estimates in UK Biobank is that they are based on the minimum of two echo times, making estimates more sensitive to noise than protocols with more echoes. The use of the thick slices in UK Biobank swMRI scans might lead to

systematic underestimation of absolute χ, compared to using thinner slices. Nevertheless, we found moderate to good reproducibility with QSM IDPs. In all but one ROI, QSM IDPs showed higher reproducibility compared to T2* IDPs.

Our reproducibility analysis showed lower cross-scan consistency for T2* IDPs compared to QSM IDPs (Fig. S10b). In previous literature [103,104], T2* data calculated using multi-echo ($\geqslant 5$) protocols showed similar reproducibility to QSM data; one possible reason for this difference is the use of a dual-echo protocol in UK Biobank. Notably, Rua et al. [103] reported that multi-echo QSM data had a significantly higher within and cross-site variability than single-echo QSM, this was hypothesized due to issues with phase unwrapping, for example, the presence of inconsistent phase accumulation across echoes that were inconsistently unwrapped. Therefore, a two-echo swMRI protocol is a major limitation in T2* estimations, but not necessarily a limitation in QSM.

Estimation of T2* is also biased by the presence of macroscopic field gradients, induced by air/tissue interfaces or poor shim quality [93]. This bias is exacerbated by the thick slices used in UK Biobank. As suggested by our association analyses of T2* IDPs (**Fig. 4.18**), spurious correlations (e.g., with nasal polyps) might be predictive of the quality of shim, as they are more likely to be driven by subject-wise variations in macroscopic field inhomogeneity rather than variations in tissue χ. As expected, background field gradients do not correlate with our χ estimates (**Fig. 4.16**) and this deconfounding is not needed for QSM IDPs.

In conclusion, following an extensive evaluation, we have developed an optimal QSM pipeline for the UK Biobank swMRI data. Dissemination of our pipeline will be crucial for harmonisation of our IDPs with data acquired in novel settings, such as clinical scanners. This will, for example, enable stratification of patients using classifiers [105]

or nomograms [106] derived from UK Biobank data. The proposed QSM pipeline was used to process phase data from 35,885 UK Biobank subjects and QSM IDPs were produced for each subject. To demonstrate the power of QSM in population neuroimaging, phenotypic and genetic association studies of QSM IDPs were carried out and are presented in the next chapter.

Chapter 5

Phenotypic and genetic associations of MR susceptibility in UK Biobank brain imaging

5.1 Introduction

Spatial maps and summary measures (i.e., IDPs) of χ were produced for each of the 35,885 UK Biobank subjects using the pipeline described in Chapter 4. In this chapter, the phenotypic and genetic associations of these χ measures are presented. This chapter (same as Chapter 4) is based on a journal paper we submitted to a journal and is under peer review, at the time of writing this thesis [14].

MRI of the brain visualises anatomical structures on the scale of millimetres, but is sensitive to microscopic tissue features. This sensitivity confers the potential to detect the earliest stages of disease for therapeutic development and disease monitoring. A common challenge to this aim is a lack of risk factors that can be used to design cohorts targeting asymptomatic early disease; a powerful alternative is to prospectively image healthy individuals at large scale and track subsequent disease. The UK Biobank study is collecting brain imaging in 100,000 participants who are predominantly healthy when scanned [11]. Participants have been deeply phenotyped and genotyped, and consent to long-term access to their health records.

**The interpretation of biological functions of genes presented in this chapter was performed by Dr Aurea B. Martins-Bach.*

UK Biobank has identified relationships between brain imaging markers and phenotypes including obesity [105], vascular disease [106] and ageing [5,6]. It has also enabled major new insights into the genetic correlates of imaging phenotypes [7,8], identifying genes with known links to psychiatric illness [9,10], vascular disease [11,12] and neurodegeneration [115].

As described in Chapter 4, we developed a QSM pipeline for UK Biobank that was run on the current release of 35,885 participants, with repeat imaging in 1,447 participants. We produced image-derived phenotypes (IDPs) of χ in a range of brain structures. In the work presented in this chapter, we focus on association analyses enabled by this new QSM resource. We carried out phenotypic associations between QSM IDPs and non-imaging phenotypes, spanning 17 categories including early life factors, lifestyle, physical/body measures, cognitive test scores, health outcomes and mental health variables. We conducted the world's first genome-wide association study (GWAS) using QSM IDPs, identifying relationships with genes with known relevance to iron, myelin and calcium, as well as less readily interpretable associations. Importantly, we found that QSM and T2* had distinct patterns of associations despite being derived from a single swMRI scan. QSM was also found to have higher heritability and two-timepoint agreement than T2* IDPs. These results demonstrate the richness of information in QSM data and the added value of QSM to the UK Biobank resource. Spatial χ maps and QSM-IDPs are being integrated into the core UK Biobank measures provided to researchers worldwide, creating potential to discover novel, non-invasive markers of brain health.

5.2 Methods

5.2.1 IDP generations, outliers and confounds removal

As described in Chapter 4 (sections 4.2.4 and 4.2.5), subcortical and white matter hyperintensity (WMH) IDPs were produced for QSM and T2* per subject. We also observed strong negative correlations between QSM/T2* WMH IDPs and the WMH volume IDP provided by UK Biobank (**Fig. 5.1**). This may indicate partial volume effects on the χ and T2* estimates within lesions. Based on this observation, QSM and T2* WMH IDPs were thus additionally processed by regressing out the WMH volume. Therefore, for each subject, we generated 16 subcortical IDPs and 2 WMH IDPs (with/without regressing out WMH volume) for QSM or T2*.

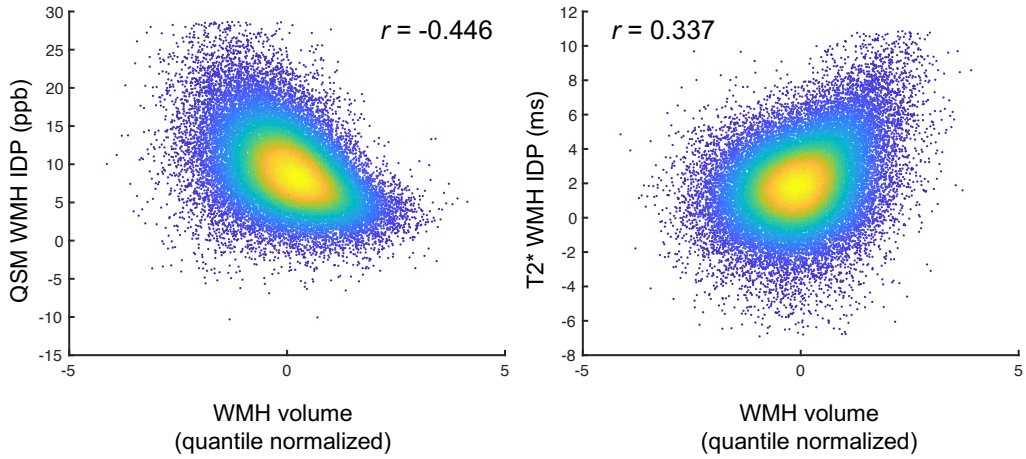


Figure 5.1 Association of WMH volume IDP with QSM WMH IDP (r = -0.446) and T2* WMH IDP (r = 0.337).

Prior to any further analyses, each IDP's $N_{subjects} \times 1$ vector first had outliers removed. Outliers were defined as being greater than 6x the median absolute deviation from the median. The remaining distribution of IDPs was then quantile normalised (Gaussianized), resulting in it being Gaussian-distributed with mean zero and standard deviation one. This Gaussianization step is to reduce effect of outliers and improve statistical robustness in association analyses, as many of the data in UK Biobank exhibits

long tails which could be problematic in association with data with a different distribution.

A recently expanded set of imaging confounds have been proposed in UK Biobank brain imaging [14,15] including age, head size, sex, head motion, scanner table position, imaging centre and scan-date-related slow drifts. Unless stated otherwise, the full set of imaging confounds were regressed out from the quantile normalised IDPs before any further analyses. This was crucial to avoid biased or spurious associations between IDPs and other non-imaging measures [2,15].

As described in Chapter 4 (section 4.2.5), T2* estimates are confounded by the presence of macroscopic field gradients (e.g., induced by air/tissue interface) [93]. To reduce such confounding effects on association analyses in UK Biobank, deconfounding for macroscopic field effects was performed to T2* IDPs. Full details of this deconfounding are described in section 4.2.5.

5.2.2 Associations between IDPs and non-imaging measures

We carried out univariate (pairwise) association analyses between 17,485 UK Biobank non-imaging phenotypes and QSM/T2* IDPs. For the remainder of this thesis, we refer to all non-imaging phenotypes as "phenotypes", to distinguish them from IDPs. Each of the 17,485 phenotypes used here had data from at least 40 subjects to ensure sufficient statistical power. These phenotypes have been grouped into 17 categories, including early life factors (such as maternal smoking around birth), lifestyle factors (such as diet, alcohol and tobacco consumption), physical body measures (such as BMI, bone density and blood assays), cognitive test scores, health outcomes (such as clinical diagnosis – ICD10 and operative procedures – OPCS4) and mental health variables (such as bipolar and major depression status). These variables were automatically curated using the FUNPACK (the FMRIB UKBiobank Normalisation, Parsing And Cleaning Kit) software to ensure that

all phenotypes variables (both quantitative and categorical) were numeric vectors and that resulting correlation coefficients were easy to interpret.

To investigate pairwise associations between IDPs and phenotypes, univariate statistics were carried out using Pearson correlation across all QSM/T2* measures (including 16 subcortical IDPs and 2 WMH IDPs) and 17,485 phenotypes (quantile normalised and fully deconfounded). As UK Biobank phenotypes have varying amounts of missing data, the full set of associations of phenotypes against IDPs had widely-varying degrees-of-freedom. Therefore, it is important to consider *P* values (and not just correlation r); *P* values were calculated and used to identify the strongest associations. Here, we follow the convention for Manhattan plots and report results using $-\log_{10}P$. The full set of 629,460 (17,485 × 18 × 2) correlations was corrected for multiple comparisons. Bonferroni correction for family-wise error (FWE) control at $P_{corrected}<0.05$ was applied, corresponding to a $-\log_{10}P_{uncorrected}$ of 7.10. Additionally, a less conservative option for multiple comparison correction is false discovery rate (FDR), which for a 5% FDR resulted in $-\log_{10}P_{uncorrected}>3.13$.

5.2.3 Associations between IDPs and genetic variants

Genome-wide association studies of IDPs

We carried out genome-wide association studies (GWASs) for all QSM and T2* IDPs, following a previously-described approach [7,8]. A GWAS of an IDP is essentially performing univariate (cross-subject) correlations between a set of genetic variants and an IDP. Here, a genetic variant is a site in DNA that varies across subject and 'genome-wide' means that it uses genetic variants located across the whole genome. In our work, GWASs were performed using the Spring 2018 UK Biobank release of over 90 million imputed genetic data.

To perform the GWASs, from all subjects with an available χ map, we selected a subset of 29,579 unrelated subjects with recent UK ancestry (to avoid confounding effects from population structure or complex cross-subject covariance). We divided this set into a discovery cohort of 19,720 subjects and a replication cohort of 9,859 subjects. We applied QC filtering to the genetic data including minor allele frequency (MAF) ≥ 0.01, imputation information score ≥ 0.3 and Hardy-Weinberg equilibrium P value $\geq 10^{-7}$, which resulted in a total of 17,103,079 genetic variants. IDPs had both imaging and genetic confounds regressed out as carried out in Elliott et al. [109], including the above-described imaging confounds and 40 population genetic principal components (supplied by UK Biobank), to avoid the confounding effects of gross population structure. IDPs were normalized (resulting in zero mean and unit variance) after the original Gaussianisation and deconfounding. GWAS was performed using the BGENIE software [117].

In total, 36 independent GWASs were performed, corresponding to the 36 IDPs being analysed per subject (18 IDPs for QSM/T2* respectively). One Manhattan plot for each GWAS was produced, plotting the $-\log_{10}P$ value (from discovery cohort) for each genetic variant. An example Manhattan plot for GWAS of QSM right thalamus IDP is shown in **Fig. 5.2**. The standard single-phenotype GWAS threshold ($-\log_{10}P = 7.5$) [7,8] as well as an additional Bonferroni multiple comparison (accounting for 36 GWASs) corrected threshold ($-\log_{10}P = 9.06$) were used. As shown in **Fig. 5.2**, significantly associated variants are normally clustered together, this is expected due to an effect known as linkage disequilibrium (LD). LD is essentially the non-random association of alleles of different genetic variants. In a region of high LD, we only report the genetic variant with the highest association, which is defined as 'peak association' (**Fig. 5.2**), because the associations in the local LD region are most likely all due to a single genetic effect

[7,8,17]. Here, peak associations with -log$_{10}$*P* value exceeding 7.5 were extracted and analysed using the method described in Elliott et al. [109].

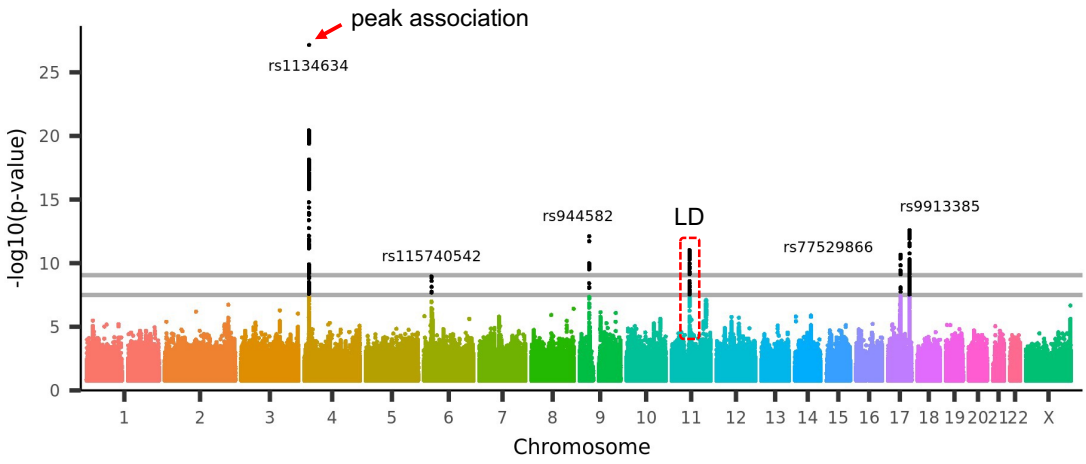


Figure 5.2 Example Manhattan plot showing GWAS result of QSM right thalamus IDP. Here, each point represents one genetic variant, the x-axis gives its location on the genome, and y-axis gives the significance of its correlation with QSM right thalamus IDP using -log$_{10}$*P*. Two horizontal grey lines indicate the standard significance threshold (lower, -log$_{10}$*P*=7.5) and after Bonferroni correction (upper, -log$_{10}$*P*=9.06). Any genetic variants that passed the standard threshold are colour coded in black. The red box is indicating a LD region on chromosome 11. The red arrow is indicating the 'peak association' of a LD region on chromosome 4. Genetic variants of peak associations are labelled with their own unique IDs.

We subsequently used Peaks software [110] (https://github.com/wnfldchen/peaks) to automatically generate clusters of peak associations between genetic variants and IDPs as previously described [7,8]. A cluster is defined as a set of IDP-variant pairs for which all genetic variants are within a 0.25-cM distance of the top variant (from IDP-variant pair with the highest -log$_{10}$*P* value) within the cluster. We classify a cluster as replicating if at least one of its IDP-variant pairs had nominal significance ($P<0.05$) in the replication cohort. Finally, we used FUMA [118] to map the genetic variants of each cluster to related genes, and to identify eQTL (expression quantitative trait loci eQTL, which seeks to identify genetic variants that affect the expression of one or more genes) for these variants.

Heritability of QSM and T2* IDPs

Following the approach described in previous studies [7],8], we use LD score regression [119] to estimate narrow sense heritability [120] (h^2) of each subcortical IDP using all available subjects (combining discovery and reproduction cohorts). Here, heritability represents the fraction of IDP variance that is explained by a linear combination of genetic variants. h^2 ranges from 0 (independent of genotype) to 1 (entirely determined by genotype).

LD scores were sourced from the European population of the 1000 Genomes Project [121]. Due to limitations in the 1000 Genome Project linkage disequilibrium score files, the X chromosome is not considered in this analysis.

5.2.4 Voxel-wise associations with phenotypes and genetic variants

We carried out voxel-wise correlations between the χ maps and non-imaging measures (both phenotypes and genetic variants) that had been identified to have significant associations with QSM-based IDPs. Interrogating χ maps at a voxel-wise level can provide further insight into the spatial localization of associations and can potentially identify additional associated areas which were not captured by the original IDPs, either because a given brain region was explicitly not included or because heterogeneity within a larger brain region diluted an association with a sub-region.

To achieve this, MNI152-space versions of the CSF referenced χ maps (registration described in Chapter 4, section 4.2.4) from all available subjects were combined into a 4D MNI152 χ matrix (of size $182 \times 218 \times 182 \times N_{subjects}$). Each of the voxel vectors in the 4D MNI152 χ matrix had outliers removed and was quantile normalised and fully deconfounded. Univariate Pearson correlations were performed between fully deconfounded χ data vectors (voxels across the 4D MNI152 χ matrix) and phenotypes or genetic variant data vectors, resulting in 3D correlation maps.

5.3 Results

5.3.1 Associations between IDPs and phenotypes

The results of associations between 18 QSM IDPs and 17,485 phenotypes are presented using Manhattan plots in **Fig. 5.3**. Here, we primarily focus on associations passing the Bonferroni-corrected threshold, according to which we identified statistically-significant associations of 251 phenotypes with QSM IDPs, and 224 phenotypes with T2* IDPs. The total number of significant associations is much larger than this, as this count pools multiple time-point measurements of the same phenotype (e.g., subject's weight measured at multiple visits), and multiple IDPs associated with the same phenotype. The full list of significant phenotypic associations is provided online at https://tinyurl.com/pheWASTable.

We compared the strength of QSM and T2* associations for each phenotype category (full results in Appendix B). Associations in some phenotype categories (e.g., *alcohol consumption*) are more specific to QSM IDPs (**Fig. 5.4a, b**) whereas other categories (e.g., *cardiac*) are more specific to T2* IDPs (**Fig. 5.4c, d**). However, the majority of phenotype categories show a mixed pattern of associations, including both common and distinct associations (e.g., *blood assays*) (**Fig. 5.4e**). This overall picture agrees with the expectation that QSM and T2* measures do not trivially recapitulate the same tissue properties, but together provide rich information from a single scan.

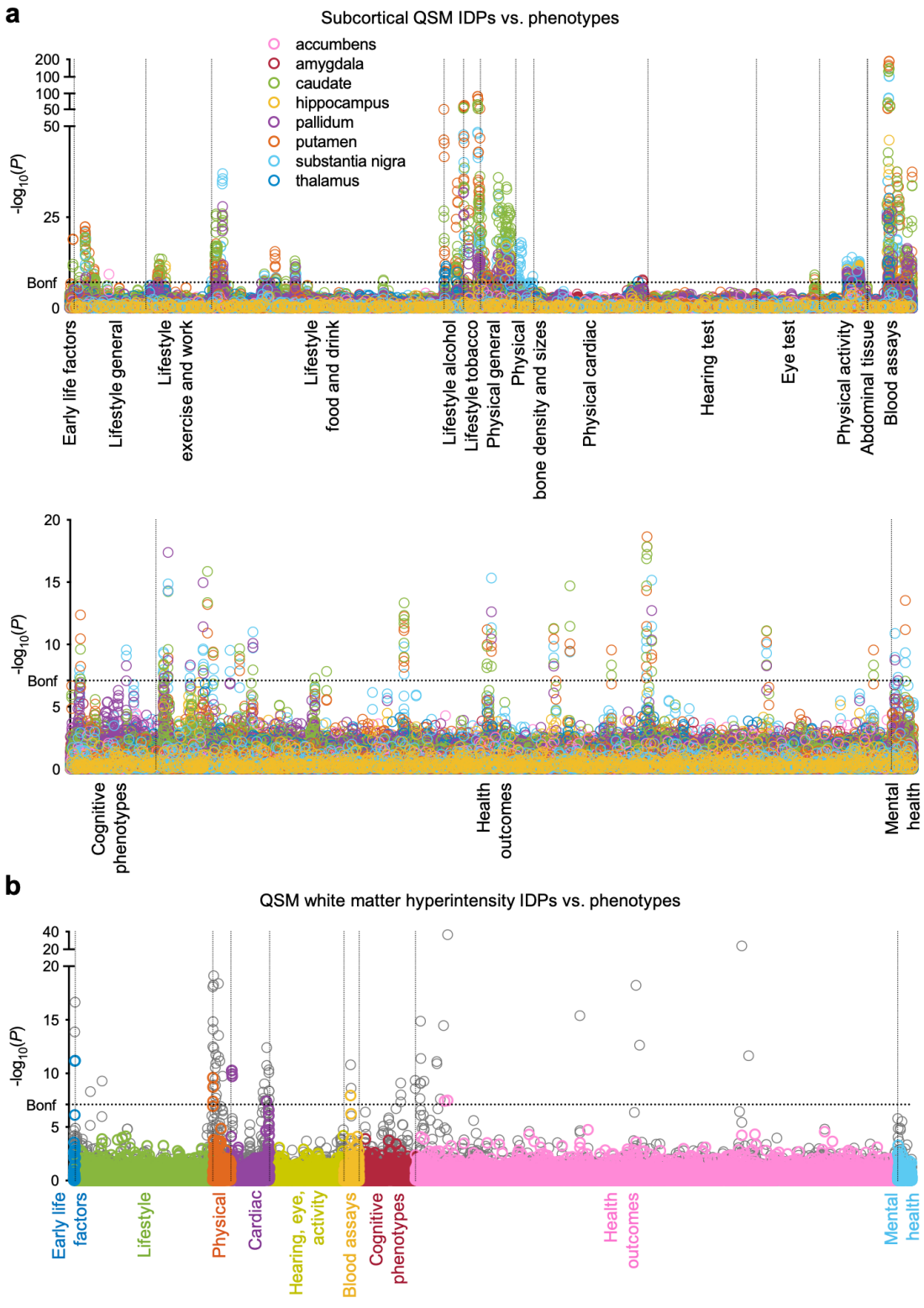


Figure 5.3 Visualization of univariate cross-subject association tests between 18 QSM IDPs and the 17,485 phenotypes in UK Biobank. Each circle represents a single IDP-phenotype association. The dashed horizontal line indicates the $-\log_{10}P$ Bonferroni threshold of 7.10. All associations above this line are considered significant. Dashed vertical lines are used to distinguish between different phenotype categories **(a)** Manhattan plot showing associations between 16 subcortical QSM IDPs and phenotypes in 17 categories. Here, different subcortical structures are coded using different colours **(b)** Manhattan plot showing associations between the QSM white matter hyperintensity (WMH) IDPs and all phenotypes (separated into 9 colour-

coded major categories). Shown behind (grey) are the associations without regressing out WMH volume. These plots clearly reveal the phenotypic association pattern of QSM IDPs. For example, phenotypes in blood assays and several lifestyle (tobacco, alcohol) categories show much stronger associations with subcortical QSM IDPs, compared to phenotypes related to hearing or eye test.

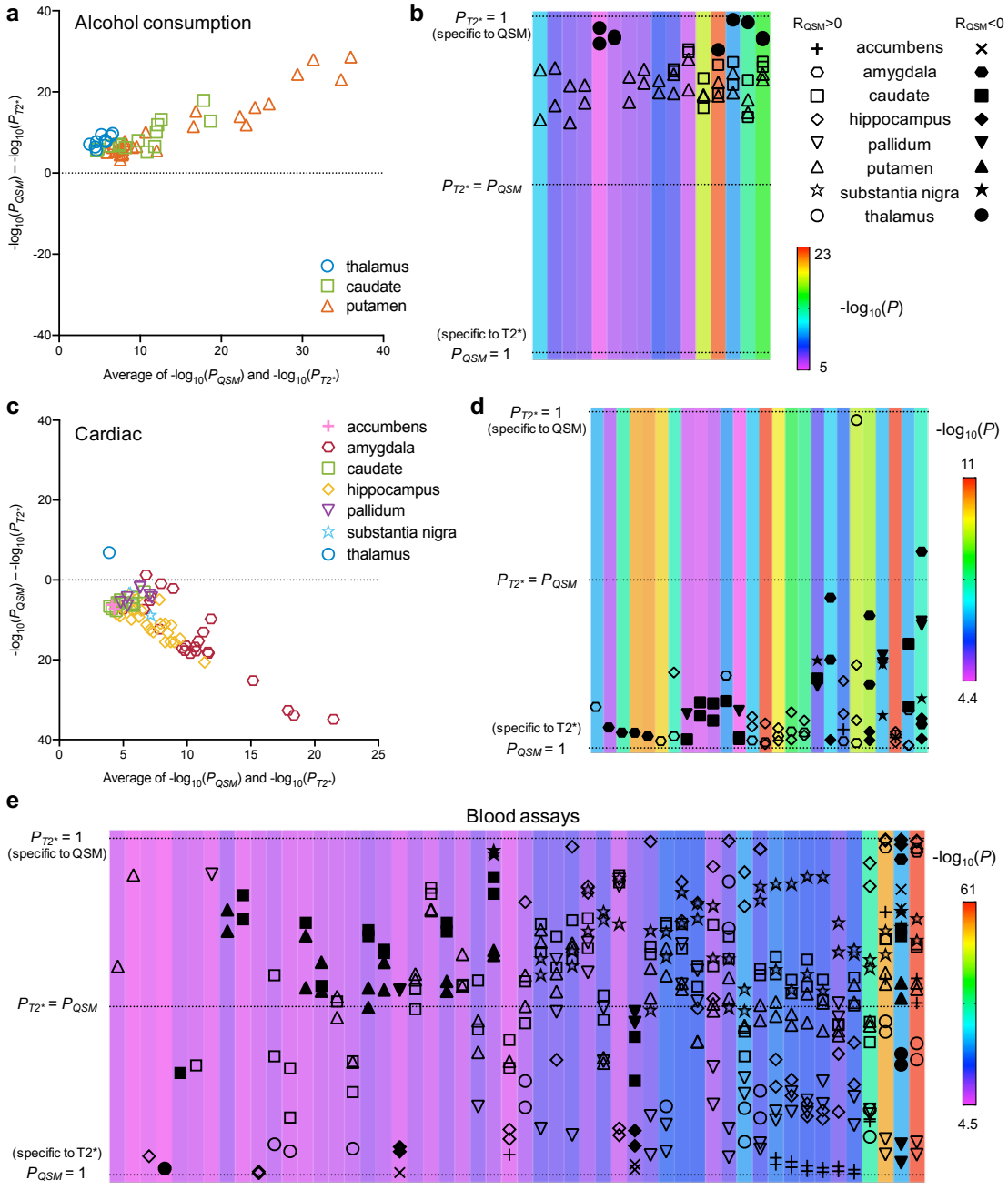


Figure 5.4 Example comparisons of phenotypic associations with QSM and T2* subcortical IDPs (ROI/phenotype pair shown if P_{QSM} or P_{T2*} passed the Bonferroni-corrected threshold). Here, we display results for **(a,b)** alcohol consumption, **(c,d)** cardiac and **(e)** blood assays categories. **(a,c)** Bland-Altman plot showing comparisons of -log$_{10}P$ values for QSM and T2* associations with (a) alcohol consumption and (c) cardiac categories. **(b,d,e)** Transformed Bland-Altman plot that aims to emphasise whether a given association is specific to QSM, T2*, or common to both. Each column represents one unique phenotype from the corresponding Bland-Altman plot, ordered from left to right by the number of associated regions. The vertical-

axis is given by the angle of each point in a Bland-Altman plot with respect to the y=0 line. Hence, datapoints at the top (or bottom) of the plot represent an association that is highly specific to QSM (or T2*), and datapoints in the middle are phenotypes that associate with both QSM and T2* in a given brain region. The background colour of each column represents the average $-\log_{10}P$ for significant associations with that phenotype. Unlike the Bland-Altman plot, this visualisation emphasises the modality specificity over the strength of correlation. For example, it is more apparent in (b) compared to (a) that thalamus-alcohol associations are highly specific to QSM. Here, the three categories reveal more QSM-specific (a,c), T2*-specific (b,d) and mixed (e) association patterns.

Having identified phenotypes that associate with QSM IDPs, we conducted voxel-wise regressions with these same phenotypes into χ maps to investigate the spatial regions driving these associations. **Figure 5.5** shows voxel-wise associations of χ with 6 representative phenotypes. Voxel-wise association maps with lead associations in each phenotype category are provided in Appendix C. In general, voxel-wise association maps are highly symmetric, including extended homogeneous regions, more focal associations with sub-regions, and associations with brain areas not included in the ROIs used to generate QSM IDPs.

We now describe associations in specific phenotype categories in more detail, focusing on associations that recapitulate previous studies or are more specific to QSM IDPs. An overview of these categories is given in **Table 5.1**.

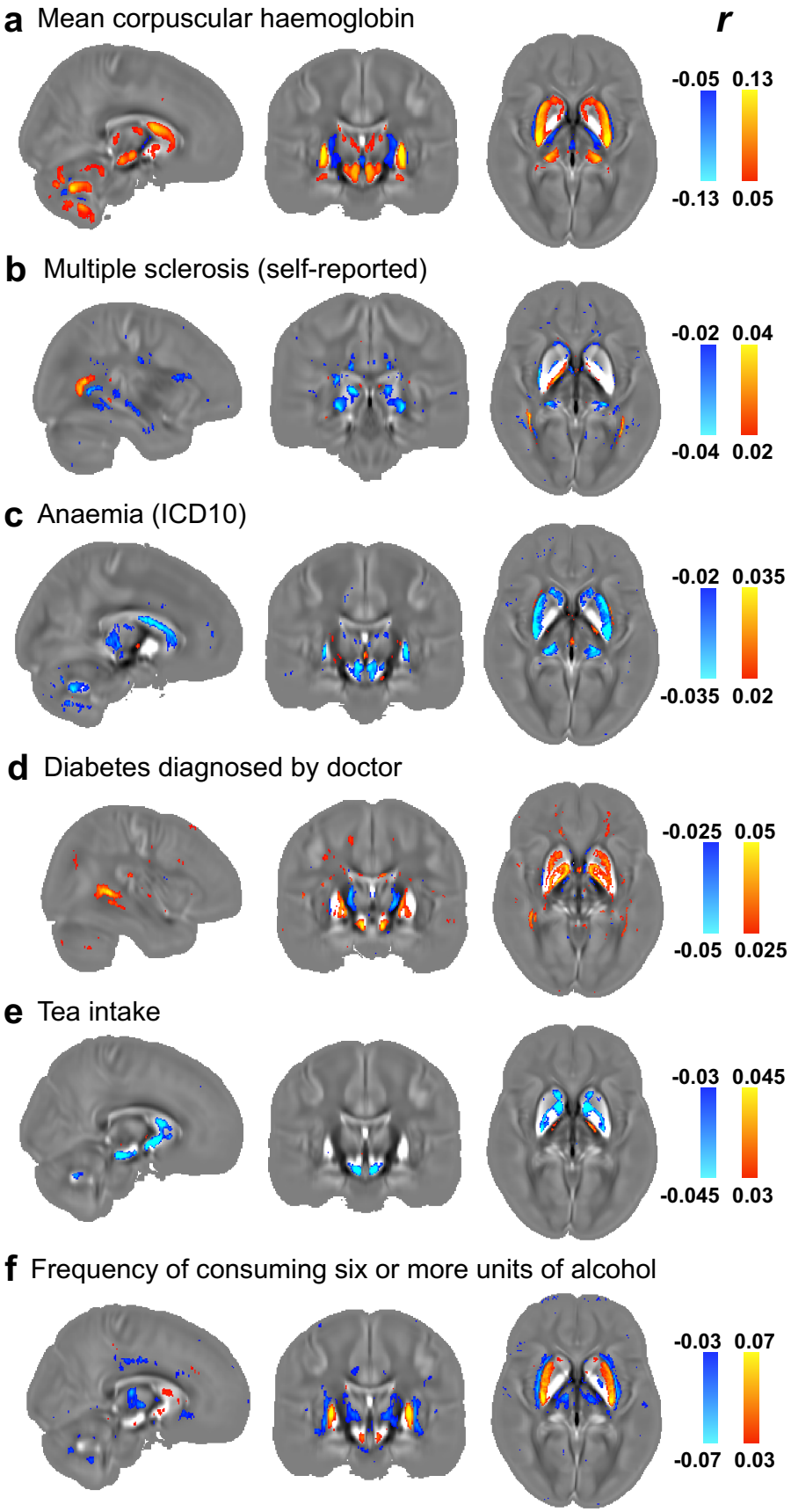


Figure 5.5 Voxel-wise association maps of 6 example phenotypes with χ maps aligned in MNI space. Pearson correlation r is shown as colour overlay (red-yellow for positive r and blue for negative r) on the population-average χ map (described in Chapter 4, section 4.2,4). **(a)** *mean*

corpuscular haemoglobin identifies all subcortical regions captured by our IDPs, as well as the red nucleus and cerebellar regions. Particularly, the putamen, caudate, substantia nigra and red nucleus exhibit homogeneous correlations across the entire region; **(b)** *multiple sclerosis (self-reported)* identifies sub-regions of thalamus (including the pulvinar nucleus and lateral geniculate nucleus), as well as focal white matter regions such as the optic radiation; **(c)** *Anaemia (ICD10)* identifies putamen, caudate, red nucleus and cerebellar regions, as well as sub-regions of substantia nigra and thalamus; **(d)** *diabetes diagnosed by doctor* identifies sub-regions of caudate, putamen, pallidum and substantia nigra, in addition to white matter regions including the splenium of the corpus callosum and optic radiations; **(e)** *tea intake* identifies sub-regions of the caudate, pallidum and substantia nigra; **(f)** *frequency of consuming six or more units of alcohol* identifies putamen and sub-regions of thalamus, caudate and substantia nigra.

Table 5.1 Summary of association results in 4 select phenotype categories

Phenotype category	**Number of phenotypes**	**Brain regions (IDPs)**	**Phenotype/IDP associations used to derive voxel-wise maps in Fig. 5.5**
Blood assays	33	all 16 subcortical regions, WMH IDPs	*mean corpuscular haemoglobin* vs χ in right putamen (r = 0.16, -$\log_{10}P$=190.37)
Health outcomes	44	***MS***: thalamus, WMH IDPs; ***anaemia***: putamen, caudate, substantia nigra; ***diabetes***: pallidum, substantia nigra, caudate, putamen	*multiple sclerosis* (*self-reported)* vs χ in right thalamus (r = −0.028, -$\log_{10}P$=6.85); *Anaemia (ICD10)* vs χ in left putamen (r = −0.048, -$\log_{10}P$=18.65); *diabetes diagnosed by doctor* vs χ in right pallidum (r = 0.047, -$\log_{10}P$=17.38)
Food and drink	22	substantia nigra, pallidum, caudate, putamen, hippocampus	*tea intake* vs χ in right substantia nigra (r = −0.069, -$\log_{10}P$=37.01)
Alcohol consumption	10	putamen, caudate, thalamus	*frequency of consuming six or more units of alcohol* vs χ in thalamus (r = −0.043, -$\log_{10}P$=9.94)

Blood assays

Phenotypic associations with blood assays include haemoglobin, cell counts, cell morphology and blood constituents. The strongest of these are haemoglobin-related phenotypes, which show strong, positive correlations with QSM IDPs (**Fig. 5.3a and** https://tinyurl.com/pheWASTable). The voxel-wise map of association with *mean corpuscular haemoglobin* (**Fig. 5.5a**) (the strongest phenotypic correlation) reveals spatially contiguous positive associations in all subcortical regions captured by our IDPs, as well as the red nucleus and cerebellar regions. Here, the putamen, caudate, substantia nigra and red nucleus exhibit homogeneous correlations across the entire region, while voxels in the pallidum, hippocampus and thalamus localise to specific sub-regions. Haemoglobin-related blood measures are used clinically as a marker for a subject's iron level [122], and the positive sign of associations with haemoglobin measures is consistent with both QSM's established relationship with iron, and the positive correlation with iron concentration from post-mortem studies [6]. Associations with QSM WMH IDPs are distinct to subcortical regions, exhibiting specificity to red blood cells and haematocrit.

Health outcomes

QSM IDPs are associated with diagnoses of multiple sclerosis (MS), anaemia and diabetes. The strongest associations in the health outcomes category are multiple sclerosis (self-reported) vs QSM WMH IDP ($r = -0.068$) and T2* WMH IDP ($r = 0.064$). Previous literature [123] reported variations of χ in MS white matter lesions (relative to normal-appearing white matter) across disease stages. Notably, our WMH IDPs were calculated in all participants irrespective of diagnosis, and thus likely represent a mixture of pathology (including MS) and normal ageing. Furthermore, previous literature reported decreased χ in the thalamus (notably in the pulvinar nucleus) for MS patients compared to healthy volunteers [124]. Associations between QSM right thalamus IDP

and *multiple sclerosis (self-reported)* ($r = -0.028$, -$\log_{10}P$=6.85) is significant at the FDR-corrected threshold (-$\log_{10}P$=3.13), but is just below the Bonferroni-corrected threshold (-$\log_{10}P$=7.1). The voxel-wise association map with *multiple sclerosis (self-reported)* (**Fig. 5.5b**) reveals spatially contiguous negative associations in sub-regions of thalamus (including the pulvinar nucleus and lateral geniculate nucleus), as well as focal white matter regions such as the optic radiation. This suggests that the sub-threshold association at the IDP level may be due to the use of ROIs covering the entire thalamus that dilute significance of results that are specific to sub-regions. Interestingly, previous literature has reported structural damage of the thalamic lateral geniculate nucleus in MS patients [125], reflecting potential damage of the visual pathway in MS.

Associations with self-reported and diagnosed anaemia are consistent with a reduction in tissue iron [6], finding negative correlations with χ and positive correlations with T2*. The voxel-wise association map with *anaemia (ICD10)* (**Fig. 5.5c**) reveals spatially contiguous negative associations in the putamen, caudate, red nucleus and cerebellar regions, as well as sub-regions of substantia nigra and thalamus.

QSM associations with diabetes include formal diagnosis, self-report, and relevant medication (insulin and metformin). The voxel-wise association map with *diabetes diagnosed by doctor* (**Fig. 5.5d**) reveals spatially contiguous positive associations in the caudate, putamen, pallidum and substantia nigra regions, in addition to white matter including the splenium of the corpus callosum and optic radiations. Body iron overload in diabetes has been frequently reported [126], with a recent brain imaging study finding increased χ in the caudate, putamen and pallidum in type 2 diabetes [127], in agreement with our results.

Finally, QSM WMH IDPs also correlated with hypertension and measures of blood pressure; vascular risk factors (including hypertension) have been reported to have an effect on MS pathology [128] which may result in changes of χ in WMH lesions.

Food and drink

QSM IDPs are associated with food and drink intake include tea, coffee, meat and carbohydrate consumptions, as well as dietary supplements (see online table at https://tinyurl.com/pheWASTable). The strongest associations relate to tea consumption, which correlates negatively with χ. Although no direct link between tea intake and χ measures have been described previously, polyphenols in both green and black tea have been reported as brain-permeable, natural iron chelators that have demonstrated neuroprotective effects [30,31]. The voxel-wise association map with *tea intake* (**Fig. 5.5e**) reveals spatially contiguous negative associations in sub-regions of the caudate, pallidum and substantia nigra. This spatial pattern of correlations is in line with a previous rodent study in which black tea extract reduced oxidative stress levels in the substantia nigra and striatum [129].

Alcohol consumption

Alcohol consumption correlated more strongly with QSM IDPs than T2* IDPs in all cases (**Fig. 5.4a, b**). Voxel-wise association map with *frequency of consuming six or more units of alcohol* (**Fig. 5.5f**) reveals spatially contiguous positive associations in the putamen and sub-regions of substantia nigra and caudate, but also negative associations in sub-regions of the thalamus. These results recapitulate a previous study finding higher χ in the putamen, caudate and substantia nigra in subjects with alcohol use disorder [131] which has been linked to abnormal body iron accumulation [33,34]. χ in the thalamus correlated with phenotypes relating to the quantity of alcohol consumption, in some cases (e.g., *frequency of consuming six or more units of alcohol*) having no significant

correlation with T2*. The thalamus is involved in the frontocerebellar circuit and Papez circuit, which are particularly affected by alcohol consumption [35,36]. Although no previous studies have linked χ in the thalamus with alcohol use disorder, neuroimaging studies have reported reductions in thalamic volume and connectivity in alcohol use disorder patients [35,36].

5.3.2 Associations between IDPs and genetic variants

Heritability of QSM and T2* IDPs

As shown in **Fig. 5.6a**, subcortical QSM and T2* IDPs were found to be highly heritable, being more than one standard error >0. In all but one IDP, QSM has higher heritability than T2*. χ in the putamen and substantia nigra showed the highest heritability (0.323-0.342), while T2* in the amygdala and accumbens showed two of the lowest heritability estimates (0.0357-0.0684). Heritability of all brain IDPs in UK Biobank were previously reported in the range of 0.000-0.405 [110]. The heritability of χ in right putamen (h^2=0.342) is >98% among UK Biobank brain IDPs, and roughly half the heritability of human height [120].

Genome-wide associations studies of IDPs

Manhattan plots for all GWASs are presented in Appendix D. The full list of peak associations is provided online at https://tinyurl.com/GWASTable. **Figure 5.6b** displays an example Manhattan plot for QSM right pallidum IDP. In total, QSM IDPs identified 292 peak associations (265 replicated), T2* IDPs identified 225 peak associations (199 replicated). **Figure 5.6c** provides a summary of peak associations from the set of GWASs. The strongest genetic association across all GWASs was found between QSM right pallium IDP and variant rs13107325, which is shown in **Fig. 5.6d**. Variant rs13107325 is related to *SLC39A8* gene which is involved in metal ion transportation and will be discussed in more detail in the following section.

Figure 5.6e provides a summary of the distribution of $-\log_{10}P$ values of all peak associations identified in GWASs. It clearly shows that QSM IDPs have a higher number of peak associations compared to T2* IDPs; and that associations with the highest $-\log_{10}P$ values are predominantly found with QSM IDPs.

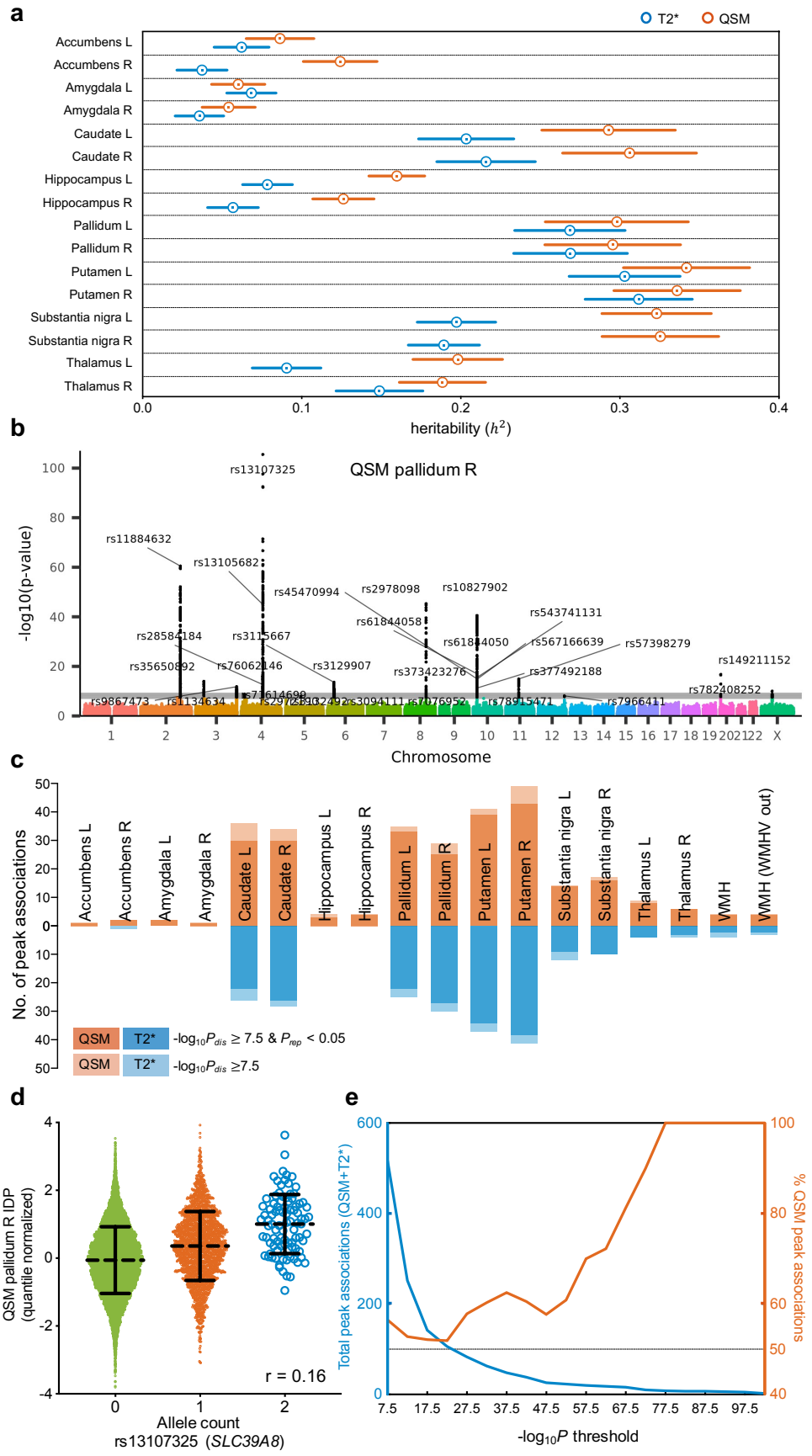


Figure 5.6 (a) Heritability estimates (h^2) for subcortical QSM and T2* IDPs grouped according to regions. Circle indicates heritability estimate and error bar indicates standard error. **(b)**

Example Manhattan plot relates to the GWAS for QSM right pallidum IDP. The lower grey horizontal line indicates the -$\log_{10}P$ threshold of 7.5 and the upper line the Bonferroni threshold of 9.06. **(c)** Stacked bar chart showing comparisons of number of peak associations identified in GWASs (passing the -$\log_{10}P$ threshold of 7.5) for QSM vs T2* IDPs. **(d)** Scatterplot showing the relationship between QSM right pallidum IDP vs allele count of rs13107325 (the strongest genetic association across all GWASs). The centre dashed line depicts the group mean χ of each allele count with error bar indicating the standard deviation. **(e)** Distribution of -$\log_{10}P$ values of all peak associations identified in GWASs. Left y axis (blue line) is showing the total number of peak associations (both QSM and T2* IDPs) with -$\log_{10}P$ greater than the thresholds (x axis). Right y axis (orange line) is showing percentage of peak associations identified with QSM IDPs.

Figure 5.7 provides a further comparison of all peak associations between QSM and T2* IDPs at corresponding positions on chromosome.

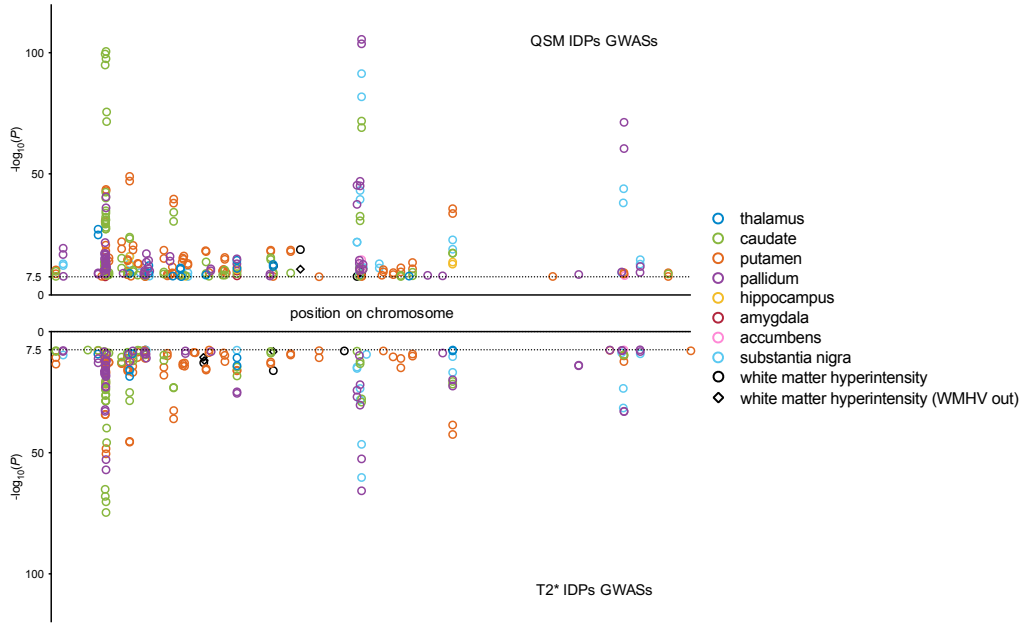


Figure 5.7 Comparison of all lead genetic associations identified in GWASs of every QSM/T2* IDP. Each circle represents an association between a IDP and a lead genetic variant where x-axis showing variant's position on chromosome and y-axis gives its -log10P in discovery cohort. QSM IDPs generally showed more genetic associations and higher -log10P values compared to T2* IDPs.

By generating clusters of peak associations, we identified 89 distinct genetic clusters, 80 of which replicated. Among the replicated clusters, 54 had associations with both QSM and T2* IDPs, 22 were unique to QSM IDPs, and 4 were unique to T2* IDPs. All clusters common to QSM and T2* IDPs replicated. Note that a cluster can include just a single genetic variant, which was the case for 11 replicated clusters. **Table 5.2** provides a summary of 19 example clusters (the full list of clusters is provided online at https://tinyurl.com/GWASTable.

Table 5.2 Details of the 19 example genetic clusters

Related function	Brain regions	Cluster #	Lead IDP	N_{pair}	rsID	MAF	Gene	Genetic function (cluster)	eQTL	$-\log_{10}P_{dis}$
Iron homeostasis	pallidum, substantia nigra, putamen, caudate, hippocampus, thalamus, amygdala, accumbens	6	QSM Pallidum (L)	15	rs11884632	0.256	*SLC40A1*	downstream, intron	*WDR75*, *SLC40A1*, *C2orf88*, *AC013439.4*	71.271
		10	T2* Putamen (L)	18	rs4428180	0.151	*TFP1:TF*	intron	*TF*	42.458
		12	QSM SN (L)	7	rs9867473	0.571	*TFRC*	UTR3	*MUC20*, *MIR570*	14.562
		27	QSM Putamen (R)	21	rs1800562	0.077	*HFE*	exon (missense)	*RP1-221C16.8*, *U91328.19*	48.973
		66	QSM Thalamus (L)	1	rs1131488	0.282	*HMBS*	exon (synonymous)	*VPS11*, *HMBS*, *RP11-110I1.14*	7.8271
Metal ion transport	caudate, putamen, pallidum, substantia nigra, accumbens, WMH	15	QSM Pallidum (R)	18	rs13107325	0.070	*SLC39A8*	exon (missense), intron	.	105.51
		47	QSM Caudate (L)	24	rs4348791	0.395	*SLC39A12*	upstream, intron	*SLC39A12*	100.55
Calcium homeostasis	caudate, pallidum, substantia nigra, putamen	49	QSM Caudate (R)	10	rs11012783	0.386	*CACNB2*	intergenic	*CACNB2*, *SLC39A12-AS1*	75.579
		60	T2* Caudate (R)	3	rs11013321	0.395	*CACNB2*	intron	.	9.0318
		68	T2* Putamen (R)	3	rs73192811	0.074	*TPCN1*	intron	*RITA1*	10.406
		70	QSM Putamen (R)	1	rs10842717	0.376	*ITPR2*	intron	.	7.7763
		16	QSM Pallidum (L)	12	rs13105682	0.057	*BANK1*	intron	.	46.911
		18	QSM Pallidum (L)	7	rs76062146	0.028	*BANK1*	intron	.	14.353
		20	QSM Pallidum (L)	2	rs71614699	0.012	*BANK1*	intron	.	10.914
Myelin and Glia	thalamus, hippocampus, pallidum, putamen	11	QSM Pallidum (L)	3	rs34457487	0.554	*MOBP*	intron	.	15.932
		74	QSM Putamen (L)	3	rs7203922	0.310	*PLLP*	upstream, intron	.	10.575
		80	QSM Thalamus (L)	4	rs1126642	0.043	*GFAP*	exon (missense)	.	11.181
Extracellular matrix	pallidum, substantia nigra, WMH	9	QSM Pallidum (L)	5	[1]	0.017	*COL3A1*	intron	.	9.5122
		25	QSM WMH	2	rs10052710	0.197	*VCAN*	intron	.	18.745

[1] 2:189666936_ATTTGACACTCCTGATTCATCAC_A

Columns **Lead IDP** and **rsID** represent the top IDP/variant pair in each group. N_{pair} indicates the number of phenotype/variant pairs included in each genetic cluster. **MAF**: minor allele frequency. The $-\log_{10}P_{dis}$ values provided are for the main discovery cohort. **Genetic function** refers to the position of the cluster's variants with regards to the corresponding gene.

Here, an exon is a coding region of a gene. A variant being a missense mutation means it will cause the substitution of a different amino acid in the resulting protein. An intron is a noncoding region of a gene. An intergenic region is located between different genes and is essentially a noncoding region. Notably, a large portion of the genetic variants associated with QSM IDPs are introns / intergenic, which are essentially 'non-coding' regions in DNA. Although the underlying mechanisms of how they regulate biological functions might be complicated and still under investigations, one possible explanation could be an intron of a gene regulates the expression of the associated gene, which leads to changes in tissue susceptibility distributions.

Most replicating clusters are associated with genes, including 10 clusters with variants in exons (6 missense). Many clusters are associated with genes involved in functions with known relevance to tissue χ, including myelination, iron and calcium. Other clusters were associated with genes whose function does not have an expected relationship to tissue χ, including transcription factors, extracellular matrix, and intracellular trafficking. Below, we describe select examples of genetic clusters in more detail.

Iron transport and homeostasis

Multiple clusters are related to genes implicated in iron transport and homeostasis. **Cluster 6** comprises eight genetic variants related to the ferroportin gene (*SLC40A1*). Voxel-wise association map with rs11884632 (*SLC40A1*, **Fig. 5.8a**) includes the pallidum, sub-regions of substantia nigra and thalamus, red nucleus and cerebellar nuclei. Ferroportin exports iron from cells, and mutations in *SLC40A1* lead to hemochromatosis [136]. Three functionally-related clusters identified associations with the transferrin gene (*TF*, **cluster 10**), the transferrin receptor gene (*TFRC*, **cluster 12**), and the homeostatic iron regulator gene (*HFE*, **cluster 27**, including a missense variant). Voxel-wise association map with rs1800562 (*HFE*, **Fig. 5.8b**) includes putamen, red nucleus,

cerebellar regions, sub-regions of caudate, substantia nigra, and thalamus. Voxel-wise association map with rs4428180 (*TF*) shows similar pattern of association to rs1800562 (*HFE*), and rs9867473 (*TFRC*) shows similar pattern of association to rs11884632 (*SLC40A1*). The TF protein delivers iron to proliferating cells via TFRC, an interaction that is modulated by the HFE protein to regulate iron absorption. Mutations in *HFE* lead to hereditary hemochromatosis, while mutations in *TF* lead to hereditary atransferrinemia [136]. The variants we identified have been previously associated with transferrin levels [137], iron biomarkers [138], and Alzheimer's disease [139]. Interestingly, associations with variants related to *SLC40A1* (iron export) and *HFE* (iron absorption) had opposite signs in corresponding regions, in line with their biological functions (**Fig. 5.8a,b**). **Cluster 66** comprises a single association of QSM in left thalamus with a potentially deleterious exonic variant (synonymous, CADD: 17.8) in the *HMBS* gene. The voxel-wise association map with this variant (rs1131488, *HMBS*) identifies sub-regions of thalamus and dispersed white matter (**Fig. 5.8c**). *HMBS* encodes an enzyme from the heme biosynthetic pathway. *HMBS* mutations are associated with acute intermittent porphyria [140] and leukoencephalopathy, which exhibit MRI anomalies in thalamus and cerebral white matter [141].

Metal ion transporters

There are also clusters associated with genes from the SLC39 family of solute-carriers, which transport divalent metal cations such as Zn^{2+} and Fe^{2+}. **Cluster 15** comprises four genetic variants associated with QSM and T2* IDPs in multiple subcortical structures and WMHs. The top variant (rs13107325) is a missense variant of *SLC39A8* (*ZIP8*). Voxel-wise association map with this variant (**Fig. 5.8d**) identifies caudate, substantia nigra and sub-regions of pallidum. *SLC39A8* encodes a transmembrane transporter protein for zinc and iron. This genetic variant has been linked to blood pressure [142], diabetes [143],

Parkinson's disease [45,46], schizophrenia [45,46], alcohol consumption [146], haemoglobin and haematocrit [147], and brain morphology [7,49,50]. **Cluster 47** comprises eleven genetic variants related to *SLC39A12* (*ZIP12*). The voxel-wise association map for the top variant (rs4348791, **Fig. 5.8e**) identifies caudate and sub-regions of putamen and pallidum. *SLC39A12* encodes a zinc/iron transmembrane transporter that is highly expressed in the brain; low expression of *SLC39A12* leads to impaired neural development [150].

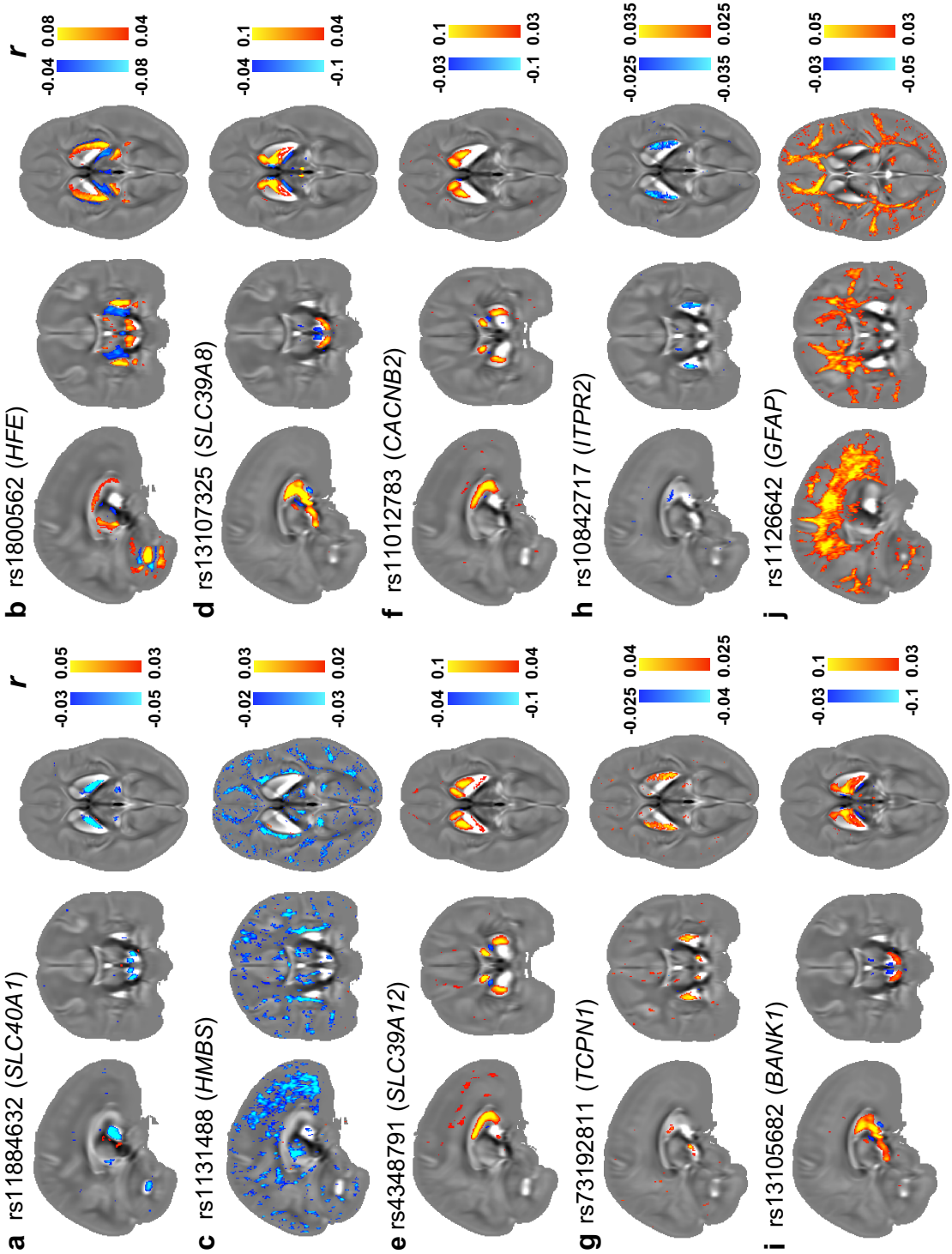


Figure 5.8 Voxel-wise association maps of top genetic variants of 10 genetic clusters with χ maps aligned in MNI space. Pearson correlation r is shown as colour overlay (red-yellow for positive r and blue for negative r) on the population-average χ map. **(a)** rs11884632 (*SLC40A1*) identifies pallidum, sub-regions of substantia nigra and thalamus, red nucleus and cerebellar nuclei; **(b)** rs1800562 (*HFE*) identifies putamen, red nucleus, cerebellar regions, sub-regions of caudate, substantia nigra, and thalamus; **(c)** rs1131488 (*HMBS*) identifies sub-regions of thalamus and dispersed white matter; **(d)** rs13107325 (*SLC39A8*) identifies caudate, substantia nigra and sub-regions of pallidum; **(e)** rs4348791 (*SLC39A12*) identifies caudate and sub-regions of putamen and pallidum; **(f)** rs11012783 (*CACNB2*) identifies caudate and sub-regions of putamen; **(g)** rs73192811 (*TPCN1*) identifies putamen and sub-regions of substantia nigra;

(h) rs10842717 (*ITPR2*) identifies putamen; **(i)** rs13105682 (*BANK1*) identifies caudate, substantia nigra and sub-regions of pallidum; **(j)** rs1126642 (*GFAP*) identifies sub-regions of thalamus and widespread white matter regions.

Calcium homeostasis

Seven clusters are related to calcium channels and regulation. **Clusters 49** and **60** contain variants related to *CACNB2*. Voxel-wise association map with rs11012783 (*CACNB2*) (**Fig. 5.8f**) identifies caudate and sub-regions of putamen. *CACNB2* encodes a subunit of voltage-gated calcium channels that regulate calcium influx from the extracellular space [151]. Variants in *CACNB2* have been associated with autism, bipolar disorder, depression and schizophrenia [53-55]. **Cluster 68** includes two intronic variants in *TPCN1* and **cluster 70** includes one genetic variant in an intron of *ITPR2*. Voxel-wise maps exhibit a similar spatial pattern in the putamen for rs73192811 (*TCPN1*, **Fig. 5.8g**) and rs10842717 (*ITPR2*, **Fig. 5.8h**), but with opposite signs. Both *TCPN1* and *ITP2* encode calcium channels that control the release of calcium from intracellular spaces. **Clusters 16**, **clusters 18** and **clusters 20** are related to *BANK1***.** Voxel-wise association map with rs13105682 (*BANK1*) (**Fig. 5.8i**) reveals spatially contiguous associations in the caudate, substantia nigra and sub-regions of pallidum. *BANK1* encodes a protein that regulates calcium mobilization from intracellular stores that is primarily related to the immune system, but is also expressed in the brain. Variants in *BANK1* have been related to working memory task-related brain activation [155].

Glia and myelin

We observed associations with genetic variants in two genes that encode structural constituents of myelin sheaths. **Cluster 74** includes genetic variants related to *PLLP*, which encodes the myelin protein plasmolipin, and **cluster 11** includes genetic variants located in an intron of *MOBP*, which encodes the myelin-associated oligodendrocyte basic protein. **Cluster 80** includes a missense variant of *GFAP*, which encodes an

intermediate filament protein that is highly specific for cells of astroglial lineage. Voxel-wise association map with rs1126642 (*GFAP*) (**Fig. 5.8j**) reveals spatially contiguous associations in sub-regions of thalamus and widespread white matter regions. Mutations in *GFAP* lead to Alexander disease, a genetic disorder characterized by fibrinoid degeneration of astrocytes, demyelination and white matter anomalies [156]. *GFAP* variations have also been associated with white matter microstructure phenotypes and Alzheimer's disease [50,58,59]. While astrocytes are present in both grey and white matter, *GFAP* expression is higher in white matter astrocytes than in grey matter astrocytes [159]. T2* in the pallidum and χ in the hippocampus were also associated with variants in the *CD82* gene, including a synonymous exonic variant (**cluster 63**, rs2303865, $-\log_{10}P$=9.03). *CD82* encodes a membrane glycoprotein highly expressed in myelinating oligodendrocytes with multiple roles, such as metastasis suppression, immune response, and in the development of oligodendrocytes and maturation of oligodendrocyte precursors. It may regulate myelin proteins gene transcription or stabilize protein levels [61,62]. This same variant has been previously associated to white matter microstructure measurements [162]. Voxel-wise association map with rs2303865 (*CD82*) (**Fig. 5.9a**) reveals spatially contiguous associations in sub-regions of pallidum, substantia nigra, red nucleus, thalamus and widespread white matter regions.

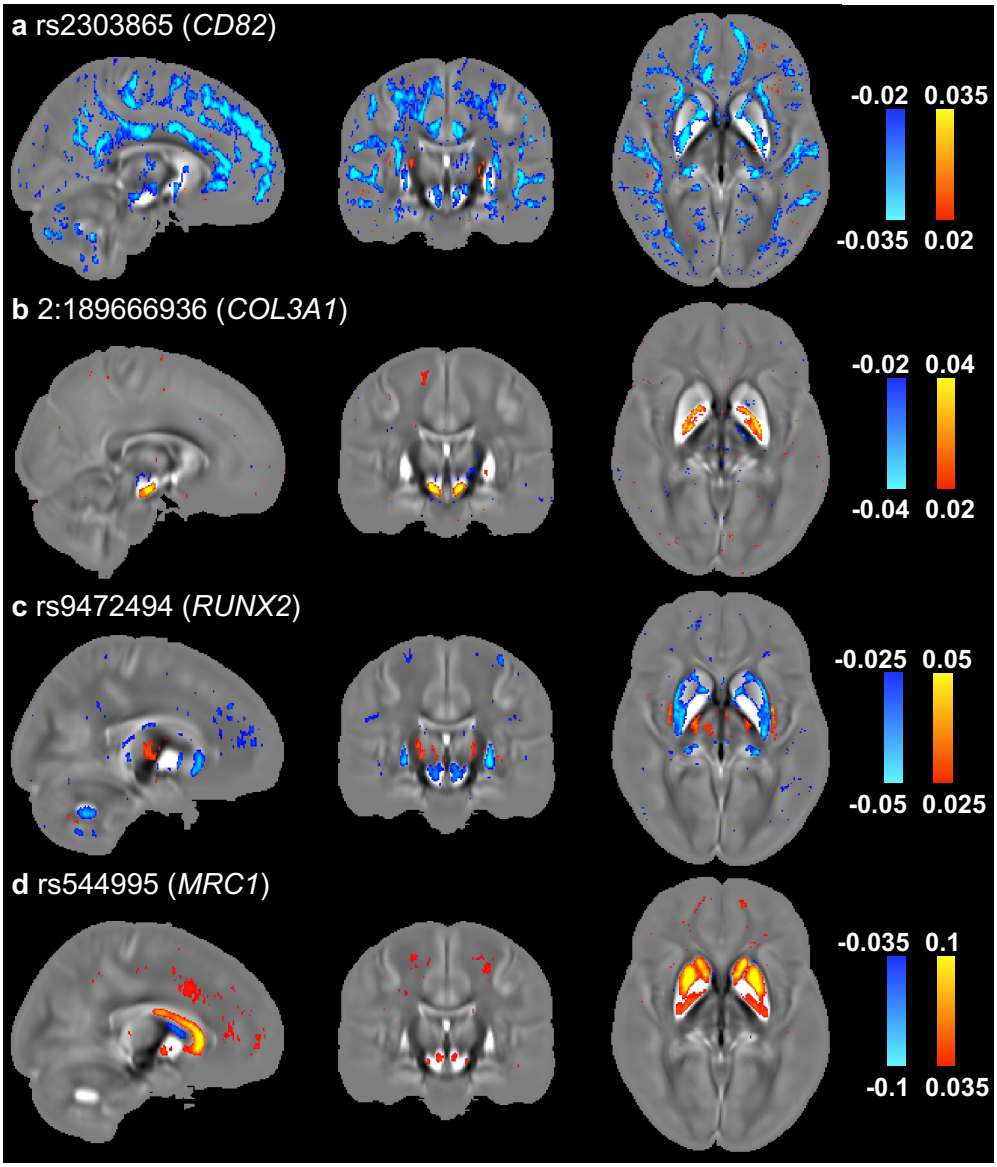


Figure 5.9 Voxel-wise association maps of top genetic variants of 4 genetic clusters with χ maps aligned in MNI space. Pearson correlation r is shown as color overlay (red-yellow for positive r and blue for negative r) on the population-average χ map. **(a)** rs2303865 (*CD82*) identifies sub-regions of pallidum, substantia nigra, red nucleus, thalamus and widespread white matter regions; **(b)** 2:189666936 (*COL3A1*) identifies pallidum and substantia nigra; **(c)** rs9472494 (*RUNX2*) identifies sub-regions of putamen, thalamus, caudate, red nucleus and substantia nigra, as well as cerebellar regions; **(d)** rs544995 (*MRC1*) identifies sub-regions of putamen, caudate, red nucleus and pallidum.

Extracellular matrix

Many genetic associations do not have an obvious, direct link to magnetic susceptibility contrast. For example, we observed associates with two genes related to the extracellular matrix, *COL3A1* and *VCAN*. **Cluster 25** includes a single genetic variant (rs10052710)

located in an intron of *VCAN* that is associated with QSM in WMHs (both with and without regressing out WMH volume). *VCAN* encodes versican, a major component of the extracellular matrix in multiple tissues including the brain, which is highly expressed in the brain during development [163]. In addition to its structural role, versican can also interact with inflammation and the immune response [164], and its expression is altered in multiple sclerosis lesions [66,67]. This and other variants in *VCAN* have been previously associated with multiple brain phenotypes, in particular to white matter microstructure metrics derived from diffusion MRI [7,50,68]. Both QSM and T2* in the globus pallidum and substantia nigra were associated with variants related to the *COL3A1* gene (**cluster 9**, peak variant 2:189666936_ATTTGACACTCCTGATTCATCAC_A, $-\log_{10}P$=9.51). *COL3A1* encodes the type III collagen, a fibrillar-forming collagen that is a major component of the extracellular matrix in a variety of organs in adults. It's also expressed throughout embryogenesis, and is considered to play a central role in cerebral cortex development. Patients with mutations in *COL3A1* have a variety of connective tissue anomalies and can also present profound brain anomalies in both grey and white matter [168]. Voxel-wise association map with 2:189666936 (*COL3A1*) (**Fig. 5.9b**) reveals spatially contiguous associations in the pallidum and substantia nigra.

Immune response and regulation of gene expression

Surprisingly, T2* and QSM IDPs are associated to many genetic variants related to transcription factors. Transcription factors regulate the transcription of DNA to RNA and can modulate the expression of multiple genes. It is challenging to anticipate how variants in transcription factors would lead to changes in T2* or χ in the brain. As an example, χ in the putamen and in substantia nigra were associated with a variant in the *RUNX2* gene (**cluster 33**, rs9472494, $-\log_{10}P$=13.00). This gene encodes a transcription factor that plays a major role in osteoblastic differentiation and skeletal morphogenesis, but that is

expressed in many tissues including the brain [169]. In the nervous system, *RUNX2* acts on its development, regeneration and repair, regulating multiple mechanisms in neurons and glia [71,72], but it can also promote ectopic vascular biomineralization [172]. Down-regulation of *RUNX2* signalling has been reported in the dorsolateral prefrontal cortex of patients with schizophrenia [173], as well as reduced expression of RUNX2 in the hippocampus of patients with bipolar disorder [174]. In our study, the association between χ and variants in *RUNX2* could be a consequence of alterations in multiple pathways, such as an increase in vascular calcifications or differences in brain development leading to changes in tissue microstructure. Voxel-wise association map with rs9472494 (*RUNX2*) (**Fig. 5.9c**) reveals spatially contiguous associations in sub-regions of putamen, thalamus, caudate, red nucleus and substantia nigra, as well as cerebellar regions.

Finally, a large number of associations were related to the gene *MRC1* (or *MRC1L1*), with 7 clusters and 78 associations being related to this gene (T2* and χ in the pallidum, caudate, putamen, as well as χ in the amygdala and WMH; strongest associations in **cluster 48**, rs544995 with QSM left caudate IDP, $-\log_{10}P$=99.50). *MRC1* encodes a molecular scavenger protein, also known as CD206, that mediates the endocytosis of glycoproteins and is primarily related to immune response. It acts by clearing harmful glycoconjugates, enzymes, hormones, cell membranes, extracellular matrix components, and micro-organisms through recognition of their carbohydrate structures [76,77]. It mediates many roles, including clearance of inflammatory molecules [176], remodelling of the extracellular matrix, immune response and cavity and scar formation after injury in the CNS [177], and is known to be expressed by astrocytes and microglia in the brain [178]. In autism spectrum disorder, *MRC1* is overexpressed in the white matter [179], and the variants rs544995 has been related to sarcoidosis, a chronic inflammatory disease

[180]. Voxel-wise association map with rs544995 (*MRC1*) (**Fig. 5.9d**) reveals spatially contiguous associations in sub-regions of putamen, caudate, red nucleus and pallidum.

How variants in the above-mentioned genes (related to immune response or regulation of gene expression) could affect tissue χ is not clear. Indirect effect via regulation of iron or calcium homeostasis, brain development, plasticity and myelination, immune response, regulation of cell cycle, scavenging of harmful molecules, that could end in the accumulation of iron and/or calcium, for example.

5.4 Discussion

5.4.1 Phenotypic and genetic associations with QSM

The results described in detail above represent approximately 5% of identified phenotypic associations, leaving a rich set of results to be explored further. Some of these phenotypes have previously-established links to χ measures in the brain (e.g., cognitive scores [82,83]), but many phenotypes lack an obvious interpretation (e.g., χ in caudate and putamen associated with *use of sun/uv protection*). In addition to the extensive literature looking at QSM in neurological conditions, there is a more limited literature in mental health conditions [84,85], such as depression and psychosis. Our results supplement this literature, identifying associations between mental health related risk factors including *seen doctor (general practitioner, GP) for nerves, anxiety, tension or depression*; *risk taking;* and *ever taken cannabis*. Voxel-wise association maps of these phenotypes are shown in Appendix C.

We described example associations for 19 of the 89 genetic clusters that have a plausible link between gene function and tissue χ. However, we also observed many associations with genetic variants related to biological functions that are not known to be directly related to tissue χ. This includes immune response, regulation of gene expression

and cell function. This rich set of associations will require additional studies to understand the genetic architecture of magnetic susceptibility in the brain.

In addition to providing insight into "true" associations, voxel-wise maps can help identify spurious associations. For example, several apparent associations at the IDP level seem to be driven by structural atrophy. While all ROI-based IDPs have the potential to be sensitive to atrophy, QSM represents an extreme of image contrast, with opposite sign of χ in grey and white matter. This causes small errors in grey-white boundaries to be amplified into detectable apparent alterations in χ. For example, QSM in substantia nigra has an apparent association with *total BMD (bone mineral density),* but the voxel-wise map exhibits thin, intense associations with a positive-negative pattern at the grey-white boundary that likely reflects atrophy (**Fig. 5.10a,b**). A similar spatial pattern of opposing positive and negative correlations exists for *body mass index (BMI)* in the primary motor and somatosensory areas (**Fig. 5.10c,d**).

5.4.2 Iron and calcium in quantitative swMRI

Overall, the most consistent and strong pattern of associations identified in our study relate swMRI to iron, both phenotypically (e.g., haemoglobin content) and genetically (e.g., iron homeostasis). Iron is involved in many fundamental biological processes in the brain including neurotransmitter production, myelin synthesis and metabolic processes [18]. Iron homoeostasis is essential to normal brain function, with elevated iron causing oxidative stress and cellular damage [18]. It remains unclear whether abnormal iron accumulation in the brain is a cause or consequence of neurodegeneration in diseases including Alzheimer's, Parkinson's and multiple sclerosis [18].

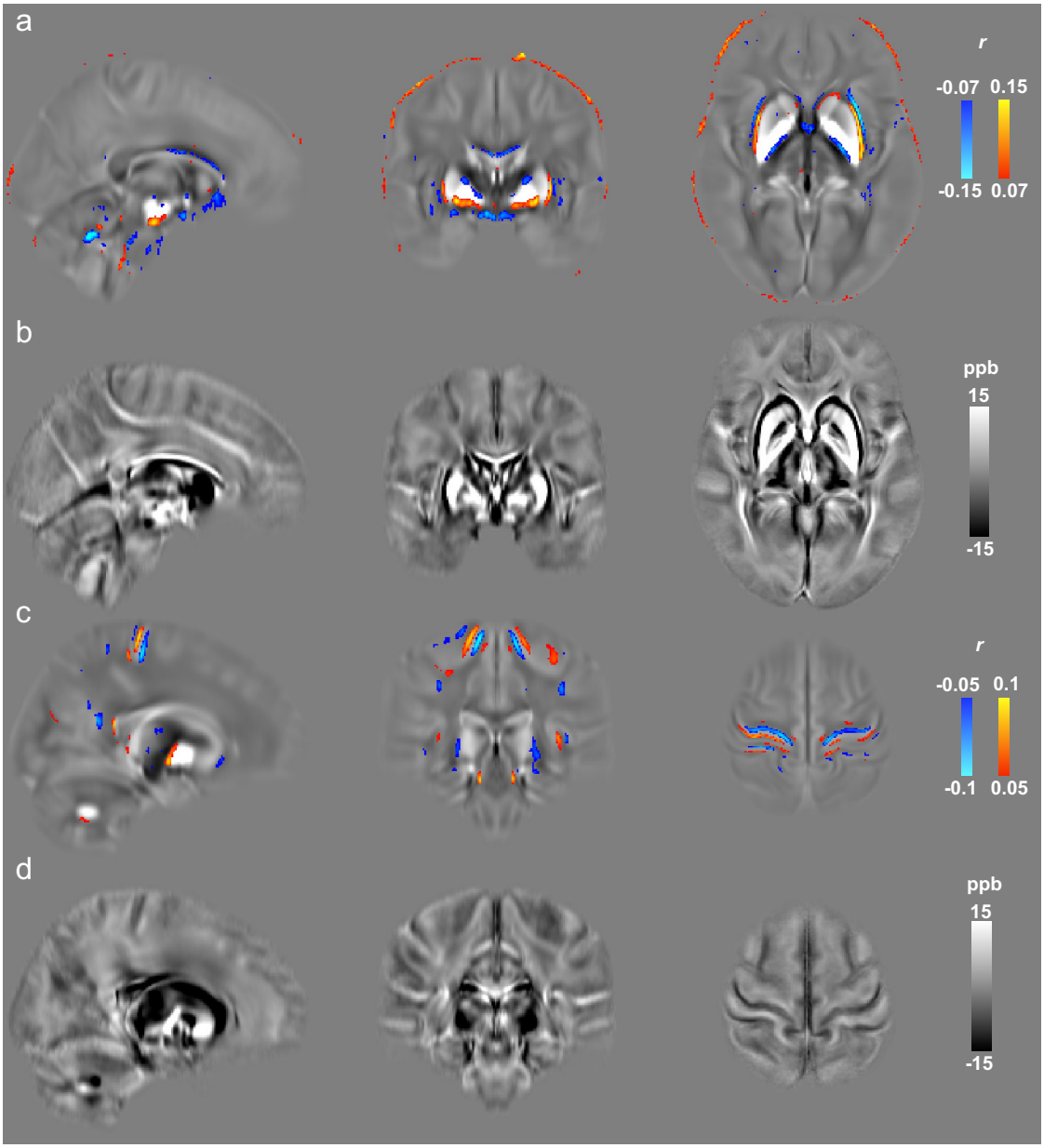


Figure 5.10 (a) Voxel-wise correlation map for *Total BMD*, with *r* values overlaid onto the susceptibility atlas. **(b)** Susceptibility aging atlas, generated by taking the difference between susceptibility maps from the youngest (< 52yo) and oldest (> 75yo) age groups in UK Biobank. Here, differences due to aging are largely driven by atrophy, displaying similar contrast to the regions of high *r* values in (a). **(c)** Voxel-wise correlations maps of *BMI* also demonstrate similar contrast to regions of brain atrophy, with **(d)** displaying the aging atlas in the same slices as (c).

We also identified multiple strong associations with variants in genes encoding calcium channels. While calcification has been shown to alter tissue χ (χ in calcified lesions have been validated using CT attenuation values [7]), little is known about the impact of other calcium forms on tissue χ. Calcium is essential for many aspects of cell

function, including division, differentiation, migration, and death [151], as well as neurotransmitter and hormone release. Perturbations in calcium homeostasis, including dysregulation of calcium channel activity, have been reported in many neurodegenerative disorders [88,89]. However, the amount of calcium in calcium channels is very limited and might not be detectable in MRI. The association between variants related to calcium channels and QSM IDPs might be driven by multiple factors or indirect links. It is unclear whether alterations of calcium channels would lead to changes in local calcium concentration and thus, changes to local susceptibility distributions; or alterations of calcium channels might be associated with changes in other tissue constituents (e.g., iron) that would drive changes in local susceptibility distributions indirectly.

In conclusion, the results presented in this chapter demonstrate the richness of information in QSM data and the added value of QSM to the UK Biobank resource. UK Biobank resource can thus play a key role in the development of QSM-based biomarkers of iron, calcium and myelin. In particular, UK Biobank has unique value for investigating early, asymptomatic disease in individuals who go on to develop neurological conditions. Furthermore, spatial χ maps and QSM-IDPs produced in this work will be provided to researchers worldwide, which will hopefully promote the use of QSM-based measures as predictive markers for preventative stratification, treatment monitoring and imaging-based screening.

Chapter 6

Summary and Future Work

6.1 Summary

The main aims of this thesis were i) to develop a pipeline for QSM reconstructions for whole, post-mortem brains, and investigate the histopathological correlates of χ measures in brains with ALS pathology; and ii) to develop a pipeline for QSM reconstructions specifically optimized for the UK Biobank swMRI data, and investigate the phenotypic and genetic associations of χ in the brain.

6.1.1 QSM pipeline considerations

QSM is essentially a multi-step image post-processing technique to reconstruct a χ distribution from the phase data collected in a GRE acquisition. Over the past decade, many algorithms have been proposed for each step of the QSM reconstruction. Thus, the selection of algorithms and combining them into a pipeline are crucial for generation of robust χ maps with minimum artefacts. In our development of QSM pipelines, we found two aspects that were particularly important: i) accurate brain masking to remove voxels with unreliable phase; and ii) selecting the optimal combination of algorithms specific for given datasets.

Accurate masking (removal of voxels with unreliable phase)

In QSM, a predominant source of artifacts arises from air/tissue interfaces. When imaging the brain *in vivo*, due to the rapid signal dephasing caused by the strong background field, voxels in the vicinity of the sinus are often corrupted and have unreliable phase values. In post-mortem imaging, brain samples are normally immersed in a susceptibility-matched liquid during scanning primarily for two aims: i) to provide a spherical shape that minimizes field distortions; and ii) to avoid a sharp transition of χ from brain tissue to air. In our work, whole brains were immersed in Fluorinert. Although care was taken to eliminate air bubbles when preparing the samples for scanning, we nevertheless observed small air bubbles on the surface of the brain. Air bubbles cause focal air/tissue interfaces, and even a small air bubble could induce strong dipole-shaped background field around the region.

In our work, we proposed two brain masking approaches to remove voxels corrupted by the air/tissue interfaces. For the post-mortem QSM pipeline presented in Chapter 3, as we directly estimated local field map using a voxel-wise fit of the phase evolution in multi-echo data, it enabled us to use the residual map from the fit to detect voxels with large residuals which were identified as having unreliable phase (predominantly voxels around air bubbles) (**Fig. 3.8)**. For the UK Biobank QSM pipeline presented in Chapter 4, we proposed a novel masking approach that utilizes phase local variance information to automatically detect voxels in the vicinity of the sinus (**Fig. 4.3**). As demonstrated in this thesis, a proper masking procedure is crucial for the generation of clean and robust χ maps.

Choice of phase processing algorithms

A numerical simulation (with known ground truth) would be a straightforward approach to compare the robustness of different algorithms, and we have created a post-mortem

brain susceptibility model for evaluations in Chapter 3. However, the performance of each algorithm also depends on properties of specific datasets. Thus, it is important to evaluate the performance of algorithms using real experimental data. In this thesis, we primarily compared combinations of different algorithms based on the quality of final χ maps in evaluations using experimental data. Both qualitative and quantitative metrics were used in these comparisons including the observation of large-scale inhomogeneities and streaking artefacts on χ maps, and cross-subject consistency of both χ maps and χ values in regions of interest. Our results, as presented in Chapters 3 and 4, demonstrated that evaluation of algorithms using experimental data is necessary to find the optimized pipeline for specific dataset.

6.1.2 Biological correlates of magnetic susceptibility in the brain

χ in grey matter

Iron

In this thesis, we primarily selected grey matter regions as ROIs, including 3 cortical grey matter regions (the primary motor, anterior cingulate and secondary visual cortices) in the post-mortem work presented in Chapter 3, and deep grey structures in the in-vivo UK Biobank work presented in Chapters 4 and 5. We found that the strongest and most consistent correlation of χ measures in our ROIs was iron, in forms of ferritin staining measures, blood haemoglobin content, and genetic variants related to iron homeostasis. Our findings are in agreement with previous literature, suggesting that in structures where iron is the dominant χ source, χ estimates could serve as surrogates of tissue iron levels.

In Chapter 3, our primary findings from the post-mortem study were: i) a statistically-significant, positive correlation between χ and ferritin stained-area-fraction (SAF) in 3 ROIs; ii) post-mortem ALS brains showing higher χ versus controls in the primary motor cortex; and iii) four post-mortem ALS brains exhibited visually apparent hyperintensities

in χ ('thin layers') within the cortical grey matter of primary motor cortex compared to the surrounding tissue.

In Chapter 5, phenotypic associations of χ identified a variety of phenotypes with direct links to iron levels (e.g., haemoglobin concentration, anaemia), as well as other phenotypes with established indirect links to iron levels (e.g., meat/tea/alcohol consumption, smoking, diabetes). The deep genetic data collected in UK Biobank enabled us to assess the genetic architecture of χ in the brain for the first time, which revealed a rich set of associations with genetic variants related to genes implicated in iron transport and homeostasis.

Myelin, glia and calcium

In addition to iron, χ estimates in the brain also have established links to myelin content and calcification. In Chapter 3, we identified a positive correlation between χ and proteolipid protein, a major constituent of myelin. This correlation is unexpected given the diamagnetic nature of myelin, which would predict a negative correlation with χ. This finding could reflect limitations of the immunohistochemistry as a semi-quantitative technique which is discussed in Section 3.4. Note that this correlation is primarily driven by regional differences between the three regions that were found to have different levels of ferritin and myelin content based on histology.

In Chapter 5, we identified multiple genetic associations with variants related to genes encoding calcium channels and metal ion transporters. Furthermore, we identified spatially contiguous associations between χ in widespread white matter regions and variants in genes related to glia. However, the amount of calcium in calcium channels is very limited and might not be detectable in MRI. The association between variants related to calcium channels and QSM IDPs might be driven by multiple factors or indirect links. It is unclear whether alterations of calcium channels would lead to changes in local

calcium concentration and thus, changes to local susceptibility distributions; or alterations of calcium channels might be associated with changes in other tissue constituents (e.g., iron) that would indirectly drive changes in local susceptibility distributions.

Other biological functions

In Chapter 5, we also identified many associations that do not have an obvious link to χ. For example, we found genetic associations related to immune response and regulation of gene expression. Whether these variants might contribute to susceptibility contrast via indirect mechanisms involving tissue iron, calcium or myelin content is currently unclear. These intriguing findings may provide new avenues for QSM research.

χ in white matter hyperintensities (WMH)

Phenotypic and genetic association analyses for χ in WMH (relative to χ of global normal-appearing whiter matter) were carried out using the UK Biobank data. We identified associations with multiple sclerosis, which is in agreement with previous literature [123]. Furthermore, we identified genetic associations with variants related to *VCAN,* which encodes a major component of the extracellular matrix and is also implicated in aspects of myelin architecture such as the nodes of Ranvier [187].

In summary, we identified a variety of biological corelates of χ that are all important to normal brain functions. We also demonstrated that altered χ are implicated in several neurological disorders. The results presented in this thesis demonstrate the potential of QSM for neuroscience research and hopefully help promote greater clinical take-up of QSM technique in the future.

6.1.3 QSM vs T2*

While derived from the same scan as T2*, QSM conveys distinct information. QSM estimates the mean χ within a voxel, reflecting bulk content of susceptibility-shifted sources like iron, whereas T2* reflects the variance of χ-induced magnetic field

fluctuations, reflecting the degree of compartmentalisation of these same sources. A consequence of this is that paramagnetic substances (e.g., iron) and diamagnetic substances (e.g., myelin) have the opposite effect on χ in QSM, but the same effect on T2* [13]. As presented in Chapter 5, our results demonstrate that QSM and T2* contribute both unique and shared information, as reflected in distinct patterns of associations. Because diamagnetic and paramagnetic constituents manifest differently in QSM and T2* data, a combination of QSM and T2* data may be able to disentangle co-occurring changes of tissue iron and myelin content in neurodegeneration [188]. In the two-timepoint analysis of QSM and T2* IDPs presented in Chapter 4, QSM-IDPs showed higher reproducibility in almost all ROIs (**Fig. 4.11b**). For example, we found higher cross-scan correlations with QSM IDPs ($r > 0.8$) in four subcortical regions (putamen, caudate, substantia nigra and pallidum), compared to corresponding T2* IDPs ($0.6 < r < 0.8$).

6.2 Future Work

In this section, I will overview a few directions that could be explored following the work presented in this thesis, including some topics that we plan to work on in the coming year.

6.2.1 Post-mortem dataset: combining QSM and R2* data with other imaging modalities and histology

As briefly mentioned in Chapter 3, my post-mortem work is part of a larger study that acquired whole-brain multi-modal MRI and regional histology (**Fig. 6.1**). Data from other modalities have been or are being processed by colleagues and ultimately, we will combine all imaging modalities and carry out MRI-histology analysis. By combining multi-modal MRI with histology, we can try to identify underlying cellular constituents

that are driving changes in different MRI modalities. Similarly, combination of different modalities could be more predictive of the underlying tissue microstructure.

Furthermore, in Chapter 3, our post-mortem MRI-histology analysis used simple summary measures of histology images, that is, the stained area fraction (SAF). SAF is only a semi-quantitative measure that does not fully exploiting the rich spatial information available in histological images. To further improve our post-mortem analyses, better histological quantifications (e.g., extracting features like cellular morphology) and registration between histology and MRI images (to enable voxel-wise rather than ROI-wise analyses) will be required. My colleagues are actively developing a registration pipeline to spatially co-register histological images with MRI [70], hence, we will be able to co-register histological images with χ maps to detect more subtle variations by performing voxel-wise analyses.

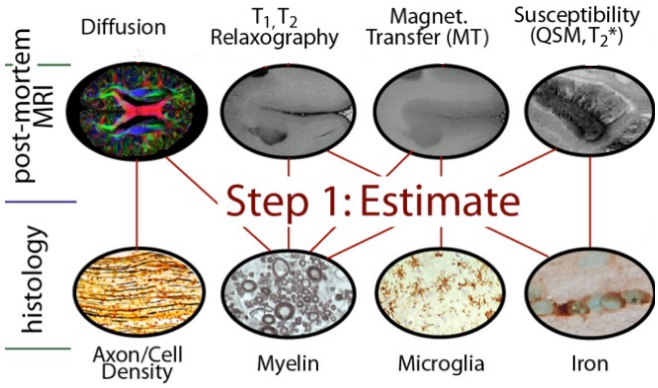


Figure 6.1 Illustration of overall plan for the post-mortem ALS study. Multi-modal post-mortem MRI consists of diffusion, T1, T2 susceptibility weighted imaging and magnetic transfer imaging. Histology will include immunohistochemistry for axon/cell density, myelin, microglia and iron. Note that the links shown here are for illustration only.

6.2.2 Voxel-wise correction for UK Biobank T2* maps

As described in Chapter 4, T2* estimates are confounded by the presence of macroscopic field gradients (for example, induced by air/tissue interface or overall shim quality) [93]. This bias is particularly problematic when imaging voxels are large. In my work, we

observed corelations between the original UK Biobank T2* IDPs (particularly in accumbens, amygdala and hippocampus) and phenotypes related to body size (which could alter shim quality) or nasal/sinus conditions (which could alter the geometry of the sinus cavity). These correlations were of concern and led to our investigation of the confounding effect of macroscopic field gradients on T2* measures. To account for potential enhancement of T2* due to significant macroscopic field variations, we performed a deconfounding of the original T2* IDPs to account for the measured field gradient magnitude (G_{mag}). However, the confounds we proposed (for macroscopic field gradients) were summary measures (median G_{mag} across voxels in each ROI), similar to the calculation of T2*/QSM IDPs. This simple deconfounding reduced the strength of various spurious associations to the point of non-significance (**Fig. 4.18**).

There is a potential limitation associated with our proposed ROI-level deconfounding. That is, median G_{mag} does not necessarily match median T2* geometrically, i.e., median G_{mag} and T2* may correspond to different voxels in a given ROI. Hence, one important direction of future work is to develop a voxel-wise correction of the measurement error induced by the presence of macroscopic field gradients for UK Biobank T2* maps. Here, I present a few details of the fundamental physical model that can be used for this correction.

As proposed in Hernando et al. [93], the presence of macroscopic field gradients introduces a signal modulation to the GRE signal characterised by the term:

$$\int_{R^3} e^{j2\pi\gamma\Delta B_0(\vec{r})TE} \cdot SRF(\vec{r}-\vec{r}_0)dr \tag{6.1}$$

Here, $SRF(\vec{r})$ refers to the spatial response function of a voxel, which depends on both the acquisition type (2D vs 3D) and the form of any filters applied by the scanner. **Figure 6.1a** shows a simulation of GRE signal modulation based on the procedure by Hernando et al. [93]. We used these simulations to model the relationship between estimated R2*

(s^{-1}) and G_z (Hz/mm) in UK Biobank swMRI data (**Fig. 6.2b**). Possible models to fit the relationship between R2* and G_z (including the '$tanh$' model we used for IDP-level deconfounding, described in Chapter 4) are shown in **Fig. 6.2c**.

Following these simulations and the methods proposed by Hernando et al. [93], we plan to develop a more sophisticated voxel-wise correction method for the UK Biobank swMRI data that will enable correction of whole brain T2* maps (i.e., not limited to ROIs) and thus, enable improved deconfounding for voxel-wise phenotypic and genetic association analyses with T2* maps. This work will be part of my post-doctoral research over the coming year.

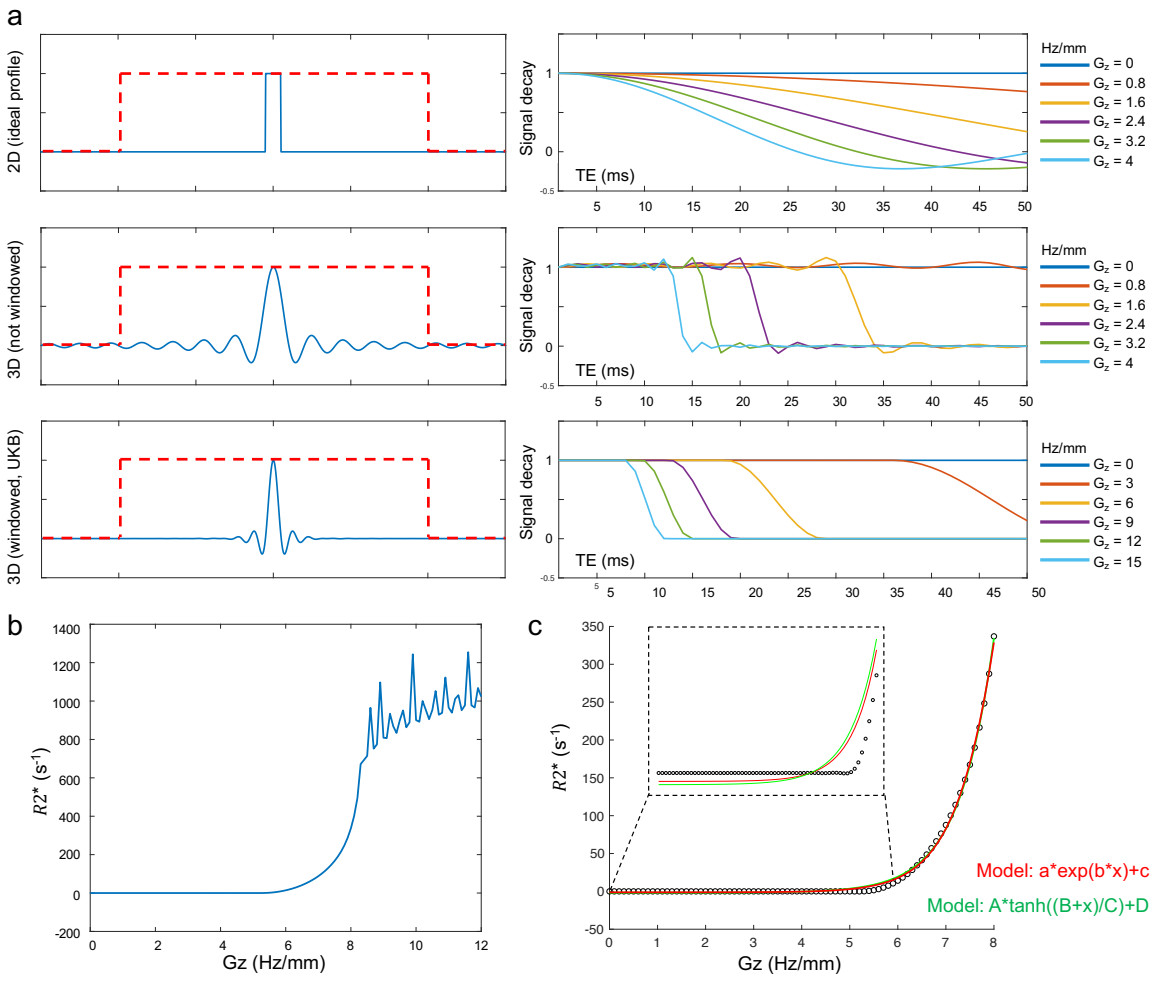


Figure 6.2 (a) Simulated signal modulation in the presence of a linearly varying macroscopic field gradient (Gz), based on the procedure proposed by Hernando et al.[93]. On the left, the signal amplitude is indicated as a boxcar function (red line, representing a large homogeneous object), and the SRF (blue line) is displayed for 3 different imaging scenarios: 2D (10 mm slice – first row), 3D (10 mm slice – second row), and the UK Biobank swMRI protocol (3D, 3mm

slice with k-space windowing – third row). One the right, the corresponding signal modulation is displayed as a function of TE and Gz. The presence of macroscopic field gradients (Gz > 0) leads to faster signal decay. **(b)** Simulated R2* estimates based on the UK Biobank protocol, as a function of Gz. The R2* estimate is dominated by noise when Gz > 8 Hz/mm, arising due to the negligible signal available for the second UK Biobank swMRI echo (20ms). **(c)** Two models were used to fit to the R2*-Gz curve over the range [0 8] Hz/m: *a*exp(b*x)+c* and *A*tanh((B+x)/C)+D*. Both models yielded similar fitted curves with $R^2 > 0.99$. Here, a = 0.0052, b = 1.384, c = -1.6924; A= 922.45, B = -9.0029, C = 1.3161, D = 921.23.

6.2.3 Future work enabled by the UK Biobank QSM resource

UK Biobank could open up major new directions for QSM as an imaging technique. While studies pre-dating UK Biobank had acquired the other neuroimaging modalities in thousands of subjects, the largest homogeneous QSM dataset we are aware of includes 336 subjects [98]. The 36,000 subjects with QSM data currently available in UK Biobank thus represent two orders of magnitude increase over any study that has come before – indeed, UK Biobank contains more subjects than all previous (approximately 455) QSM studies combined. It is also already the largest repeat imaging study, with >1400 subjects scanned at a second timepoint. Furthermore, re-imaging (i.e., second timepoint) data from over 400 subjects who have been infected with COVID-19 were collected as part of the UK Biobank COVID-19 study, which creates a unique opportunity to investigate brain-related abnormalities in COVID-19 [189].

This value is amplified by the unparalleled wealth of linked data in UK Biobank participants, including genetics, extensive phenotyping and long-term access to health outcomes. As discussed in Chapter 5, we have identified statistically-significant associations of 251 phenotypes (spanning 15 phenotype categories) and 76 genetic clusters (related to various biological functions) with QSM IDPs. This rich set of associations is expected to open up new avenues of investigation for QSM, here, I describe a few directions of future work that could be enabled by the UK Biobank QSM resource.

Brain age estimations

Iron is central to numerous biological processes in healthy brain function and progressive accumulation of iron occurs in several brain regions during healthy aging [18]. As a potential surrogate of tissue iron in the brain, QSM-based measures of χ in subcortical structures have been reported to have positive correlation with age [98]. Moreover, abnormal iron accumulation is associated with many neurodegenerative diseases that are prevalent in aging populations, including Alzheimer's and Parkinson's diseases [18]. The UK Biobank provides a unique opportunity to probe the relationship between χ and both healthy and unhealthy ageing.

One model to develop estimates of 'brain age', the apparent age of an individual's brains, is comparing their imaging data against a normative population dataset. This model is generated by forming the best possible prediction of age across a population based on neuroimaging data [190]. For any given individual's neuroimaging data, we can then calculate their brain age delta, δ, which is the difference between predicted brain age and actual chronological age (**Fig. 6.3**). Brain age delta reflects individual's deviation from the population norm: for example, positive δ indicates faster brain aging than population norm which could be due to smoking or diseases. Hence, brain age delta could be a useful measure of brain health under aging.

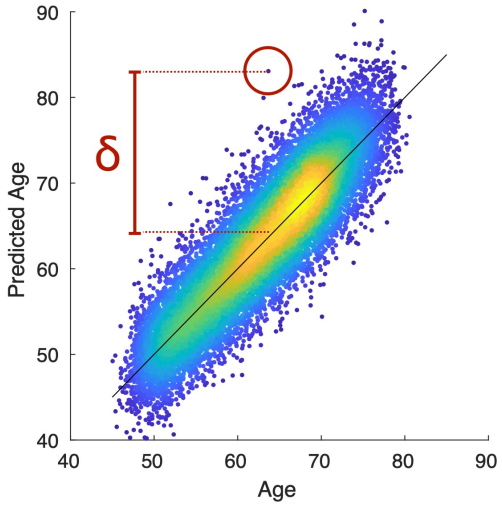


Figure 6.3 Illustration of the concept of brain age delta δ. In this plot, each data point represents one subject with x-axis represents subjects' actual chronological age and y-axis represents predicted brain age.

Motivated by QSM's age associations, we are interested in brain age estimations using QSM data. I have performed a preliminary exploration of brain age estimations using our new QSM resource, following the approach proposed in Smith et al. [190] which also used UK Biobank IDPs (excluding QSM). The correlation between our predicted brain age and the subject's actual age (r = 0.55) was lower than the correlation achieved (r = 0.74) in Smith et al. [190], indicating that our prediction is less accurate. Note that 2641 IDPs from multi-modal MRI data were used in Smith et al. [190], our 'less accurate' age predictions (possibly due to limited number of modality or data used) might mean that our predicted δ contains strong residual effects of the subject's true age.

Nevertheless, similar phenotypic and genome-wise association studies as detailed in Chapter 5 were performed using the estimated δ, which can essentially be considered as an aggregate IDP. We also calculated a voxel-wise correlation between the χ matrix and δ was carried out to identify each voxel's contribution to these δ estimates. As shown in **Fig. 6.4a**, putamen is the largest contributing region for our brain age estimations. Although the white matter fibres surrounding the subcortical regions (e.g., external capsule) were not included in the estimation, voxels in these regions show negative correlations in voxel-wise maps, which may reflect edge effects induced by atrophy. These maps would be consistent with the co-occurrence of iron accumulation (e.g., in the putamen) and volumetric changes (atrophy) in the subcortical regions. **Figure 6.4b,c** give the results of GWAS and phenotypic association results.

Here, we simply applied the approach proposed in Smith et al. [190] using QSM data, further optimization and combination with other brain imaging modalities, and/or

inclusion of more structures than the current limited set of IDPs might be possible to improve the accuracy of the brain age estimations.

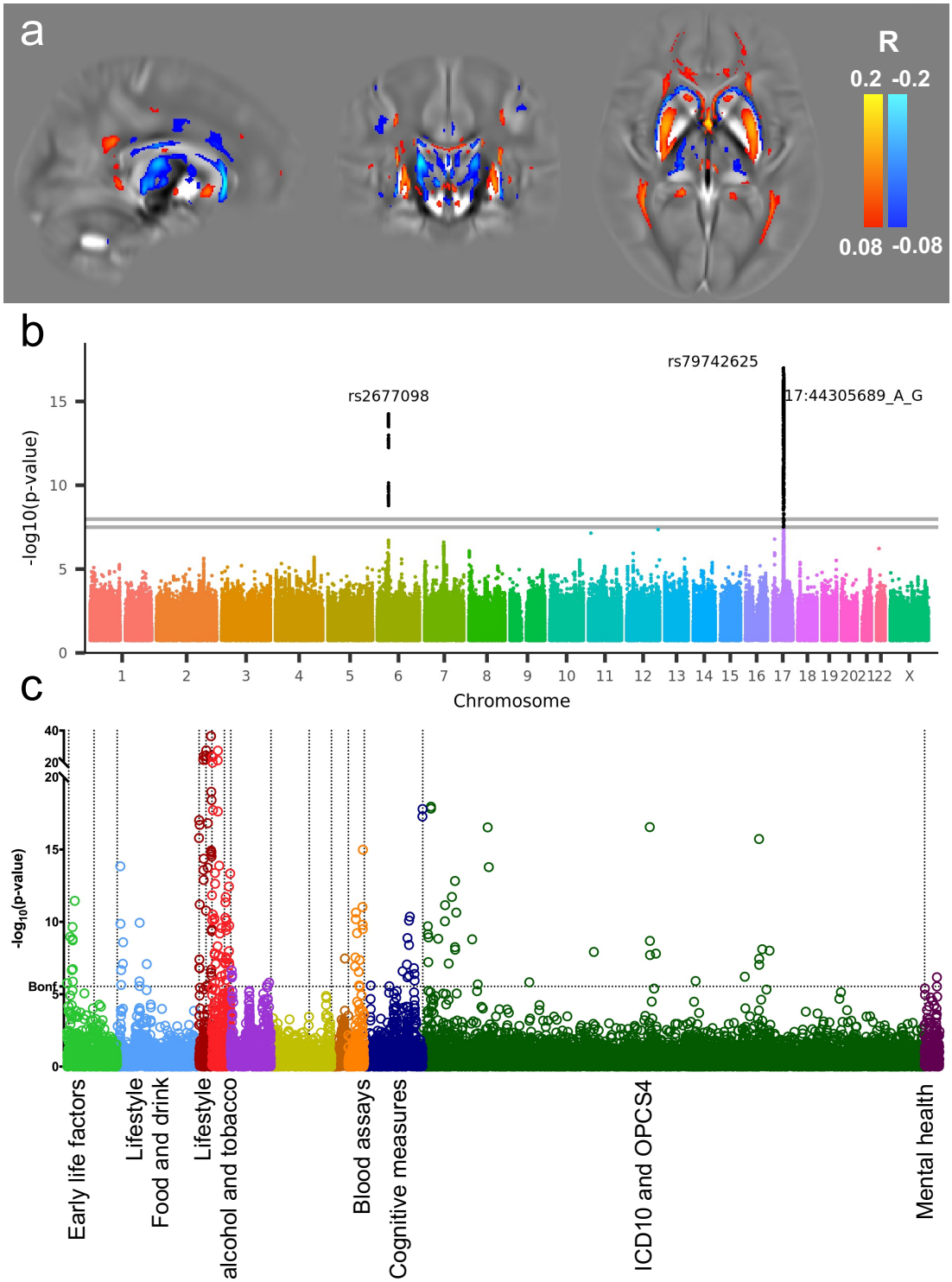


Figure 6.4 (a) Voxel-wise association maps of δ with χ maps aligned in MNI space. Pearson correlation r is shown as color overlay (red-yellow for positive r and blue for negative r) on the population-average χ map. **(b)** Manhattan plot showing GWAS results of δ. **(c)** Manhattan plot

showing phenotypic association results of δ. The most strongly associated phenotypes are *smoking status* (r = 0.05, $-\log_{10}P$=36.58), *Frequency of consuming six or more units of alcohol* (r = 0.04, $-\log_{10}P$=24.11) and *Diabetes diagnosed by doctor* (r = 0.03, $-\log_{10}P$=17.97). These 3 phenotypes show positive correlations, implying accelerated brain aging.

Studies to validate associations identified in UK Biobank

The new UK Biobank QSM resource has identified many novel associations, particularly genetic associations that need further (and more detailed) investigation. These findings are particularly interesting in two ways:

i) many genetic variants (genes) are related to iron homeostasis, but they are associated with different subcortical structures. For example, although *SLC40A1* and *TF* are both related to iron transport, variants related to *SLC40A1* are associated very strongly with χ in pallidum ($-\log_{10}P$= 71.3) and the association is weak with χ in putamen ($-\log_{10}P$= 9.2), while variants related to *TF* are associated very strongly with χ in putamen ($-\log_{10}P$= 35.6) and non-significant with χ in pallidum. Similarly, different spatial association patterns are revealed on the voxel-wise association maps. For example, although two phenotype or genetic variants are associated with the same ROI at IDP level, they may present different spatial association patterns such as homogenous across the ROI vs focal to subregions of the ROI.

ii) in addition to associations that have direct relationship with QSM (such as iron), many genetic and phenotypic associations have less obviously direct relationships with QSM, which could be further explored. For example, the association with *VCAN* was identified with a range of imaging modalities, including QSM WMH IDP, grey-white matter contrast and diffusion (in white matter) IDPs. These associations indicate the involvement of *VCAN* in myelination. Furthermore, the association between *VCAN* and QSM WMH IDP will also inform an animal study investigating rodent *Vcan* model by our colleagues.

Hence, small-cohort studies with defined characteristics (phenotypes) of participants are of interest to validate the novel phenotypic associations identified in UK Biobank data. Animal models with controlled mutation in genes or genetic variants of interest could be used to further validate the genetic correlates of χ and explore the underlying mechanisms. Furthermore, animal models could be useful to investigate the variations in spatial association patterns as well.

In addition, although UK Biobank participants are largely healthy when scanned, given the age range, participants may develop a range of neurological disorders over the coming years. In the data that we used for our analyses, serious health outcomes such as neurodegenerative disease from imaging participants are still in small numbers. Hence, the long-term access to health records enables researchers to continue using this QSM resource to study early disease markers for various neurodegenerative disease including Parkinson's disease and Alzheimer's disease.

Adapting proposed QSM pipeline to other studies similar to UK Biobank

As demonstrated throughout this thesis, we observed considerable variability of χ estimates across different combinations of background field removal and dipole inversion algorithms. Dissemination of our pipeline will facilitate harmonisation of our IDPs with data acquired in novel settings, such as clinical scanners. This will, for example, enable stratification of patients using classifiers [103] or nomograms [104] derived from UK Biobank data. To date, two ongoing COVID-19 brain imaging studies have already adopted our QSM pipeline (C-MORE/PHOSP [100] and COVID-CNS) to process their brain swMRI data collected using a protocol similar to UK Biobank. This is in addition to the UK Biobank's own COVID-19 study which is currently under review at a journal [189].

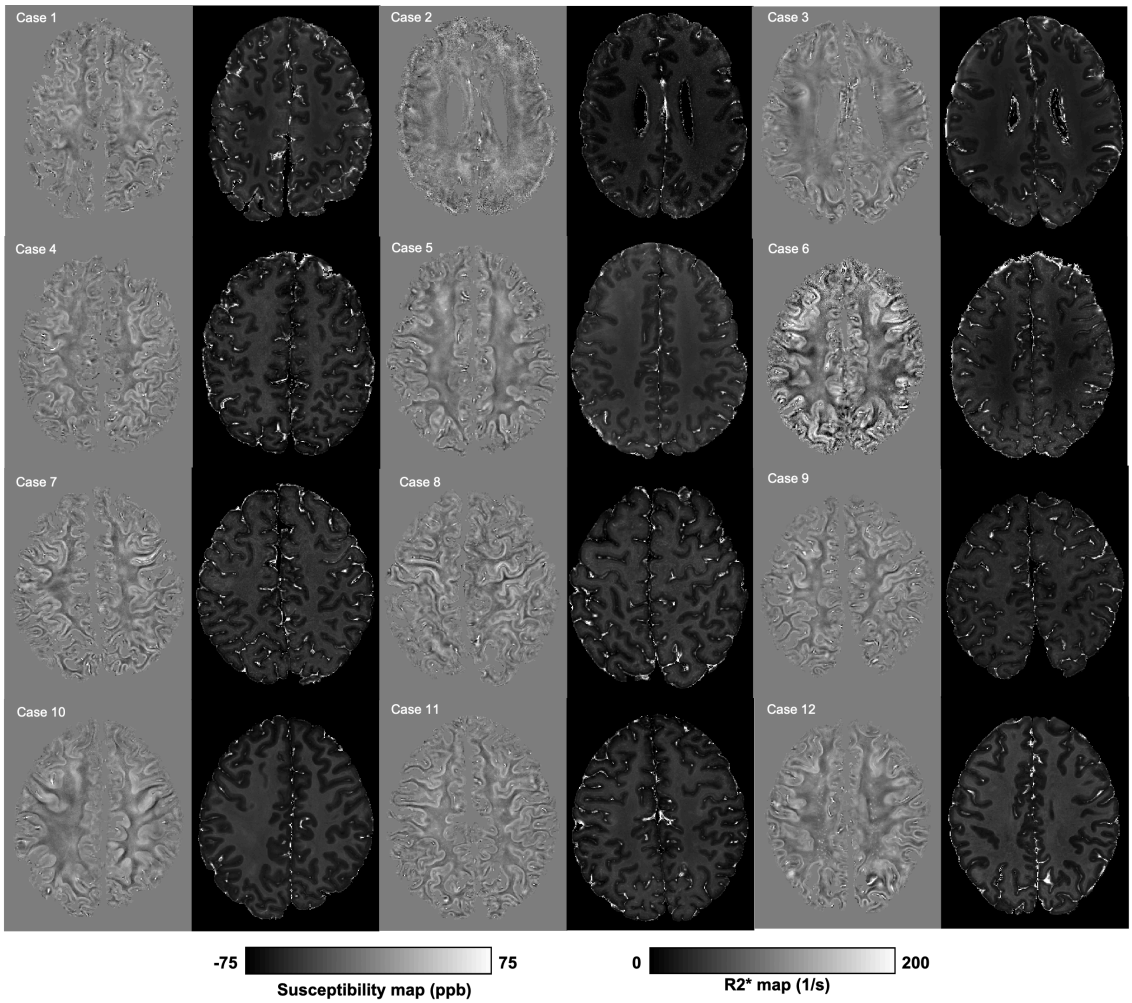
Future directions of data acquisition and postprocessing for QSM

QSM is an emerging MRI technique, due to its ability to quantify important cellular constituents (e.g., iron, myelin), a growing number of neuroimaging studies are adopting QSM in their protocols. The past decade has witnessed great progress in QSM methodology, resulting in various publicly-available toolboxes for each step of QSM processing. On the other hand, data acquisition strategy for QSM largely remains the same. A few review articles [19, 77] have proposed data acquisition strategies ranging from single-echo to multi-echo protocols. Isotropic resolution is preferred, but it is possible to perform robust QSM using data with anisotropic resolutions. Recently, in light of the development of deep learning methodology, several studies [193,194] have proposed using deep learning for QSM reconstructions and their results demonstrated the feasibility of QSM reconstruction using artificial neural networks. Therefore, there are essentially two types of QSM processing frameworks now: one is using conventional phase processing methods; another type is adopting deep learning techniques. Conventional QSM pipelines require raw (unfiltered) phase data from GRE acquisitions. Given that the performance of phase processing algorithms depends (to a non-trivial degree) on the properties of the data, there is not necessarily a single 'best' algorithm for each processing step, evaluations of different algorithms might be required to find the optimal combination of algorithms for specific datasets. Deep learning methods could be applied to various steps in QSM to replace conventional processing, for example, neural networks could be trained to solve the dipole inversion problem (input background field removed phase data) or produce χ maps from unwrapped phase data [193,194]. Raw (unfiltered) phase data are normally required, however, a recently proposed neural network is able to recovery lost information due to high-pass filtering in SWI processing [195]. With this method, filtered phase in SWI datasets might be used to produce χ maps, which will promote greater clinical take-up of QSM.

Appendices

A

R2* and quantitative susceptibility maps from all post-mortem brains.



B

Comparisons of phenotypic association between QSM and T2* IDPs

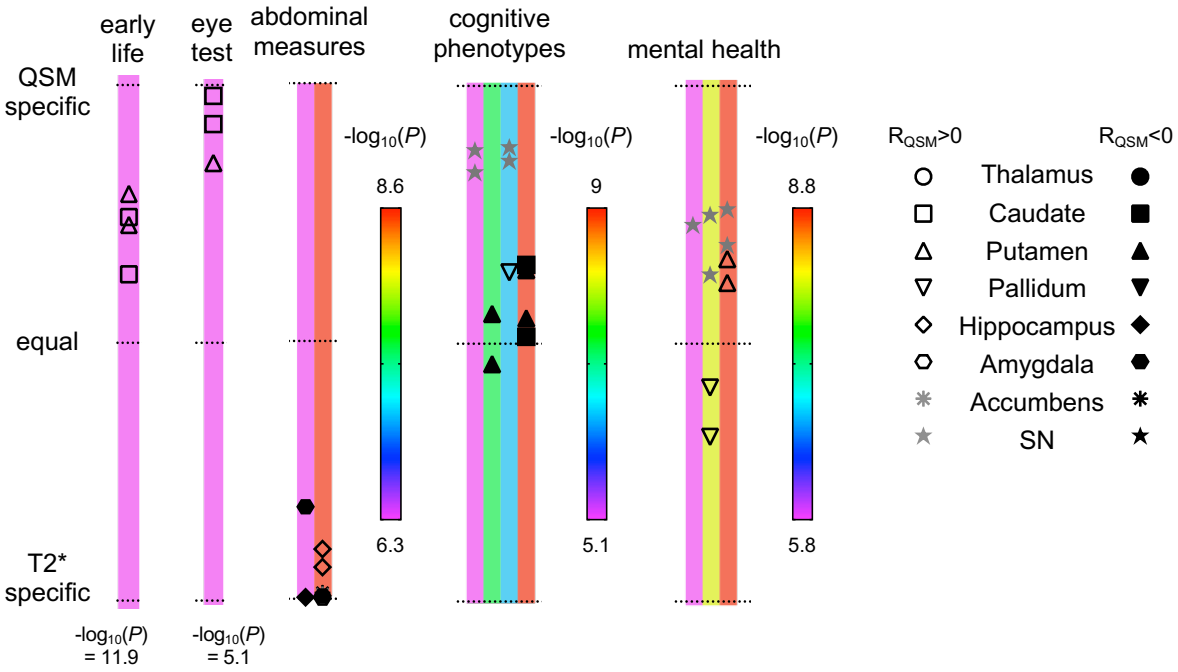


Figure B1 Transformed Bland-Altman plot for the 5 categories that showed the smallest number of associations (early life factors, eye test, abdominal measures, cognitive phenotypes and mental health).

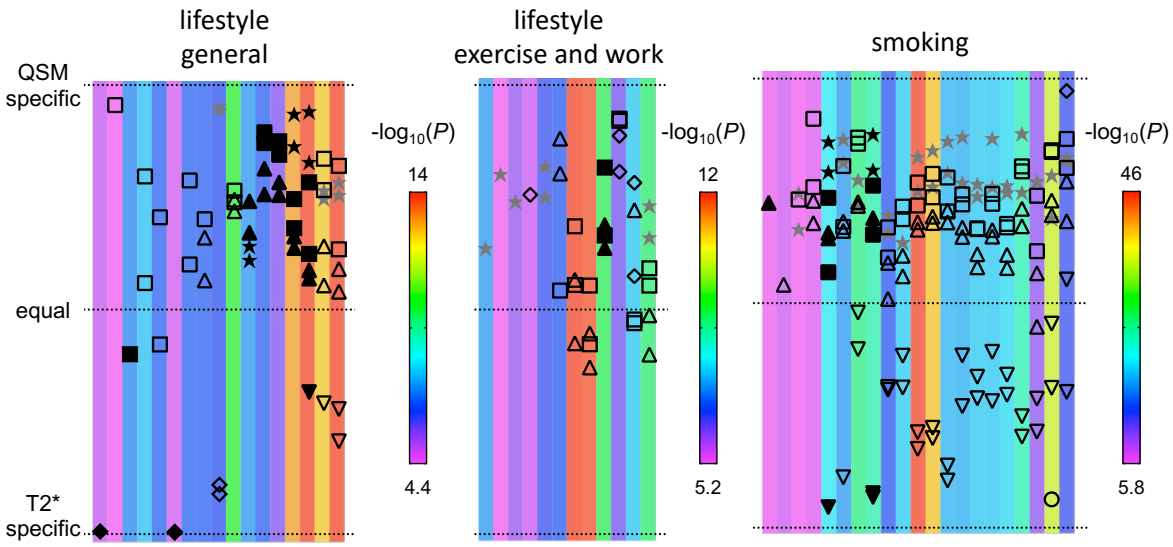


Figure B2 Transformed Bland-Altman plot for lifestyle general, lifestyle exercise and work, smoking categories.

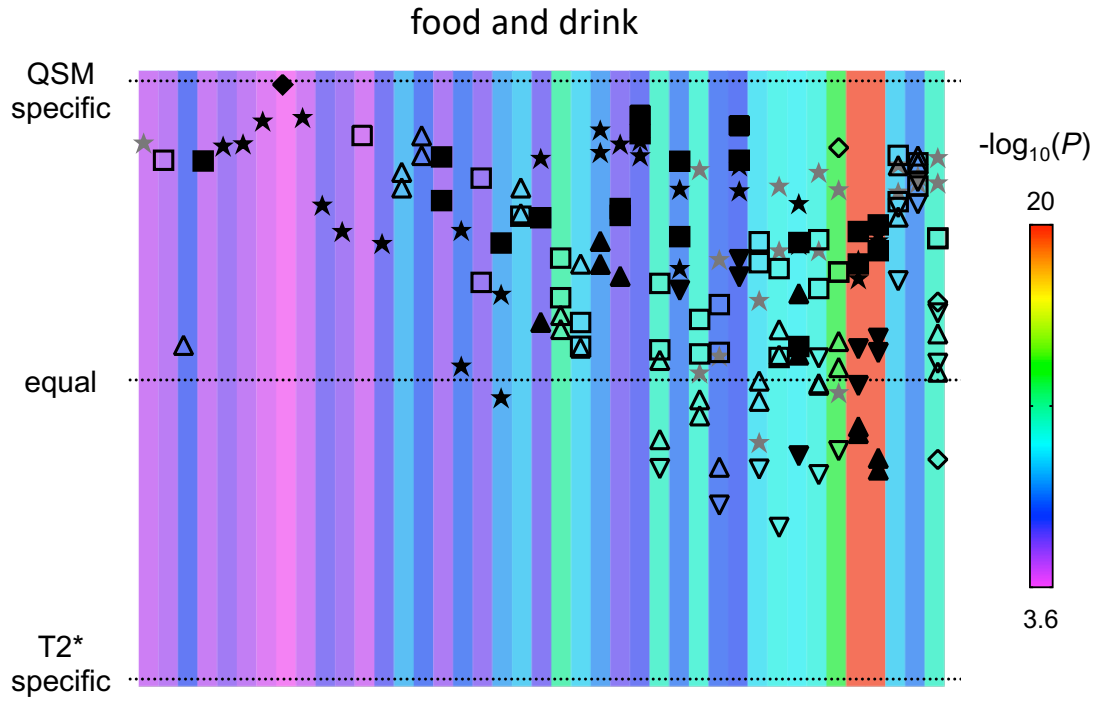


Figure B3 Transformed Bland-Altman plot for the food and drink category.

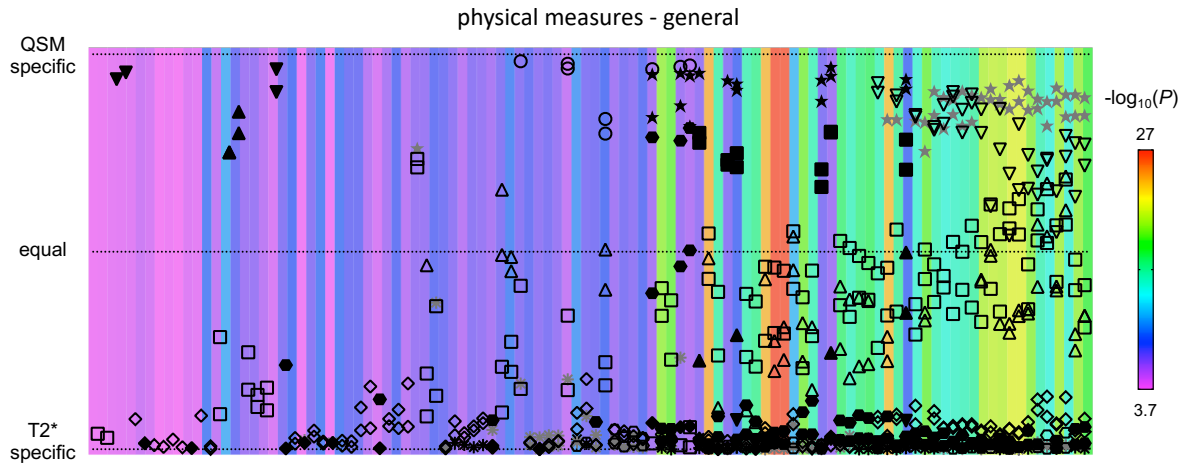


Figure B4 Transformed Bland-Altman plot for the physical measures (general) category.

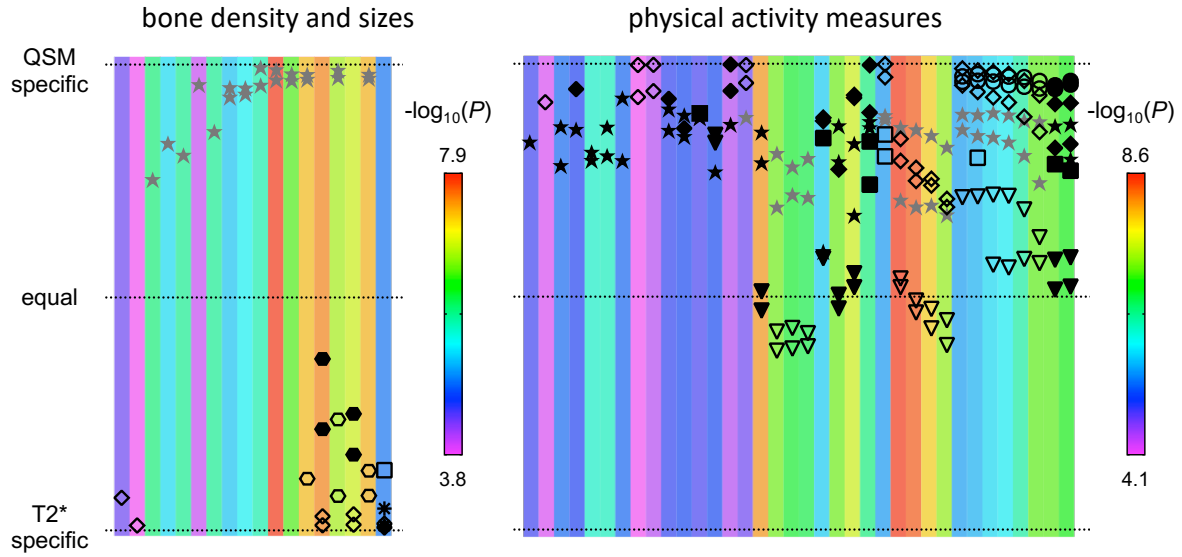


Figure B5 Transformed Bland-Altman plot for bone density and physical activity categories.

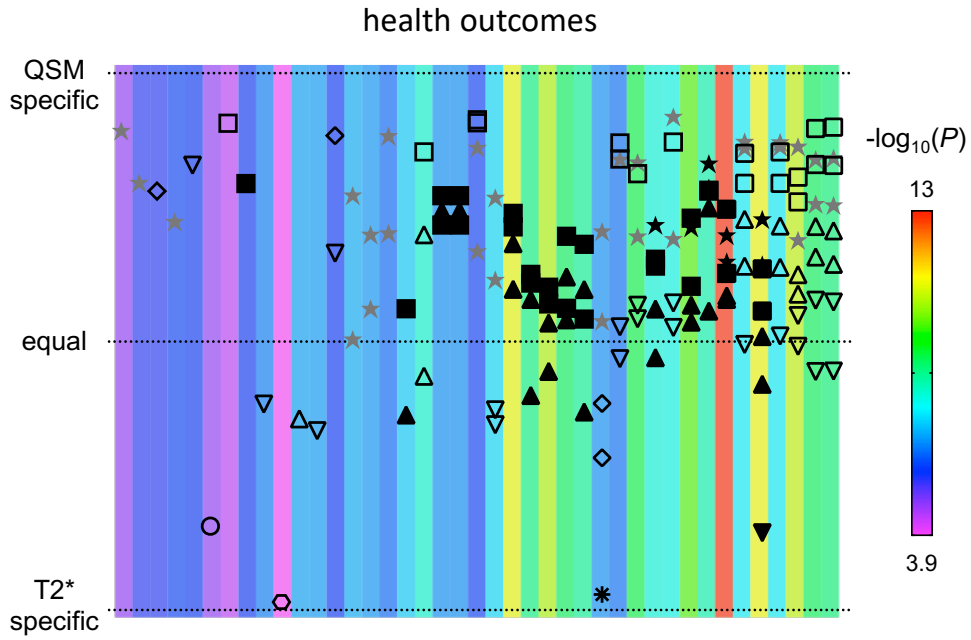
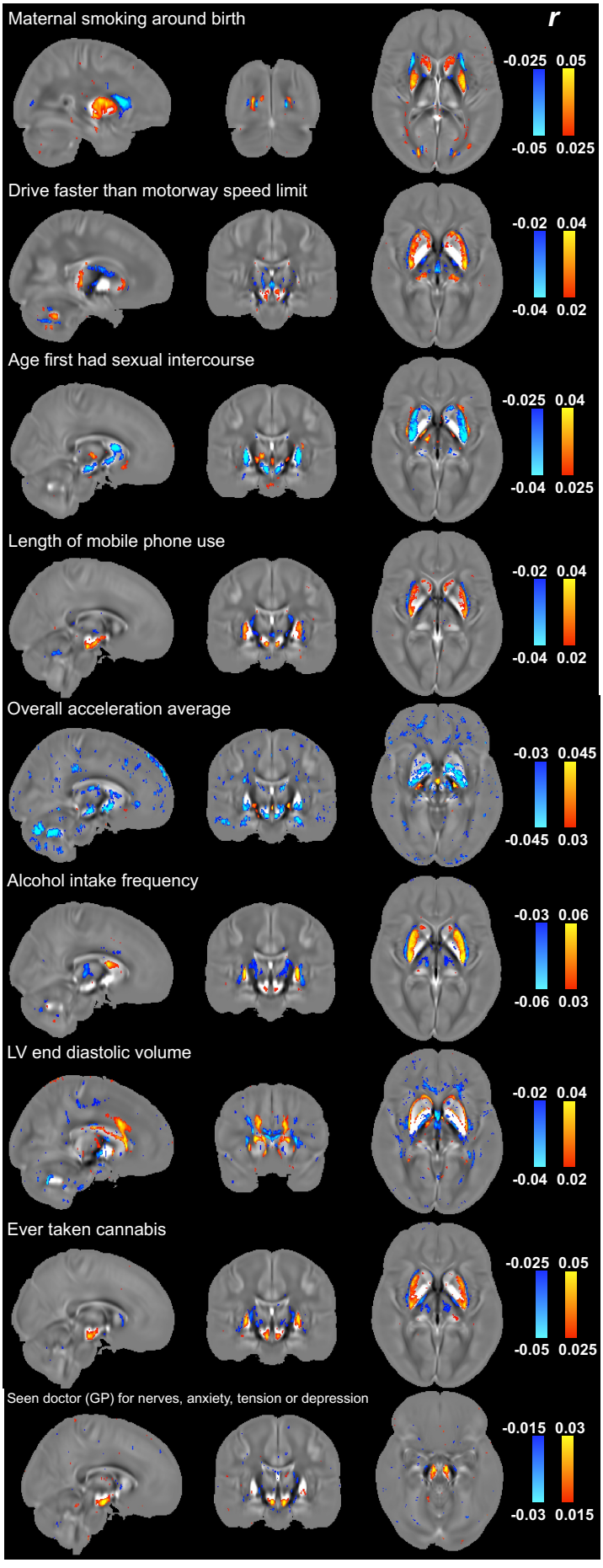


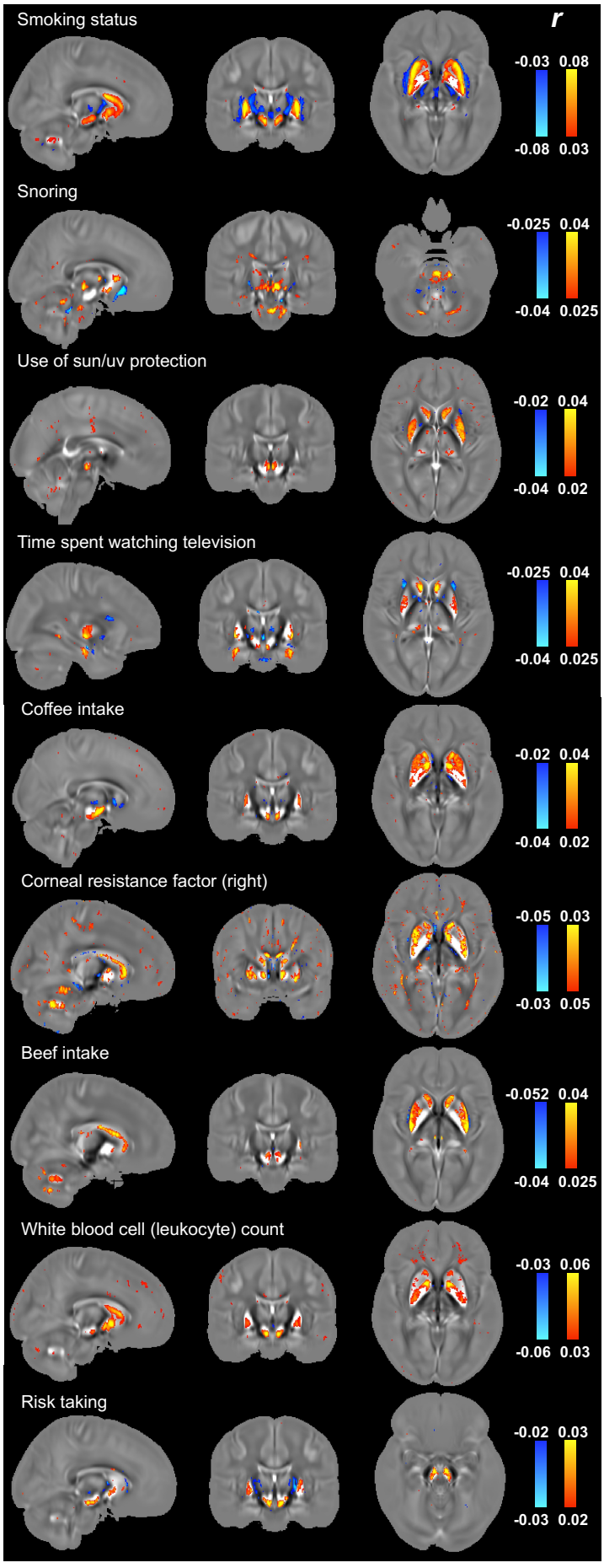
Figure B6 Transformed Bland-Altman plot for the health outcomes category.

C

Voxel-wise association maps for example associations in each phenotype category

Voxel-wise correlation maps of χ (*r* values overlaid onto the susceptibility atlas) are shown below.


Maternal smoking around birth
r
-0.025 0.05
-0.05 0.025
Drive faster than motorway speed limit
-0.02 0.04
-0.04 0.02
Age first had sexual intercourse
-0.025 0.04
-0.04 0.025
Length of mobile phone use
-0.02 0.04
-0.04 0.02
Overall acceleration average
-0.03 0.045
-0.045 0.03
Alcohol intake frequency
-0.03 0.06
-0.06 0.03
LV end diastolic volume
-0.02 0.04
-0.04 0.02
Ever taken cannabis
-0.025 0.05
-0.05 0.025
Seen doctor (GP) for nerves, anxiety, tension or depression
-0.015 0.03
-0.03 0.015

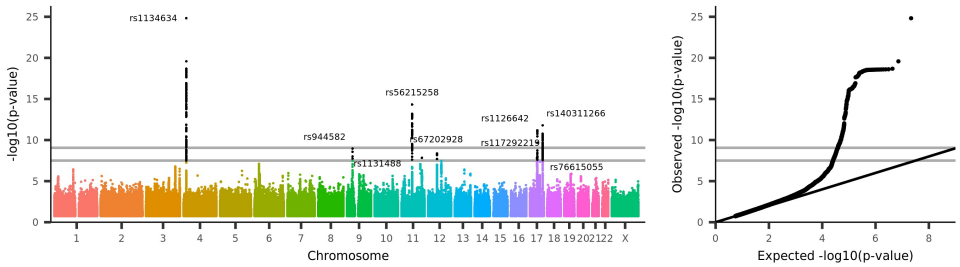

Smoking status
r
-0.03 0.08
-0.08 0.03
Snoring
-0.025 0.04
-0.04 0.025
Use of sun/uv protection
-0.02 0.04
-0.04 0.02
Time spent watching television
-0.025 0.04
-0.04 0.025
Coffee intake
-0.02 0.04
-0.04 0.02
Corneal resistance factor (right)
-0.05 0.03
-0.03 0.05
Beef intake
-0.052 0.04
-0.04 0.025
White blood cell (leukocyte) count
-0.03 0.06
-0.06 0.03
Risk taking
-0.02 0.03
-0.03 0.02

D

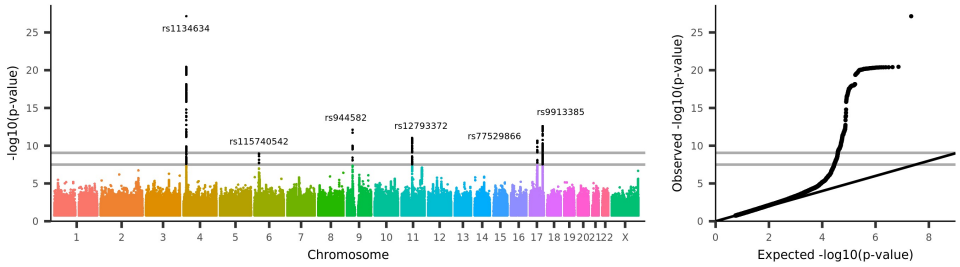
Additional GWAS results for QSM and T2* IDPs

Manhattan plots for all GWASs (QSM and T2* IDPs) are shown below.

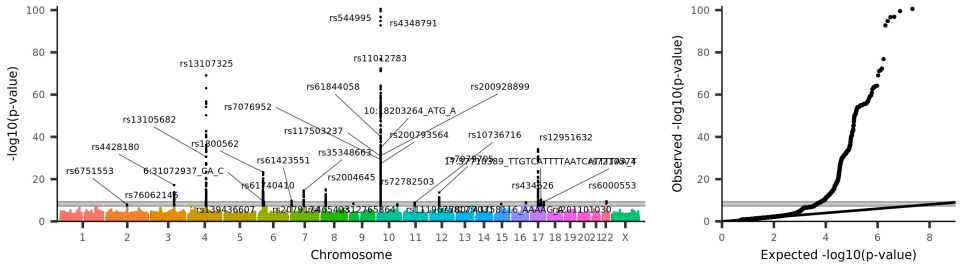
QSM left thalamus



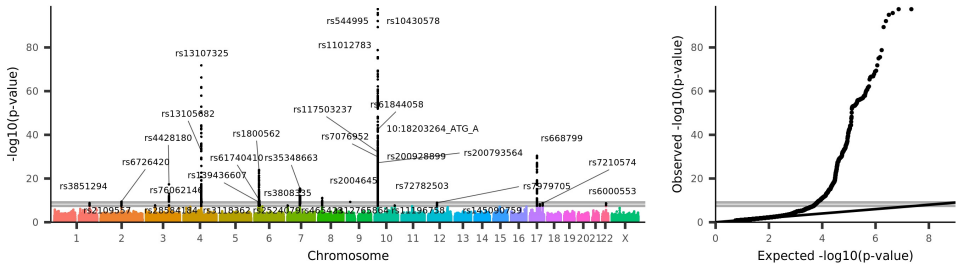
QSM right thalamus



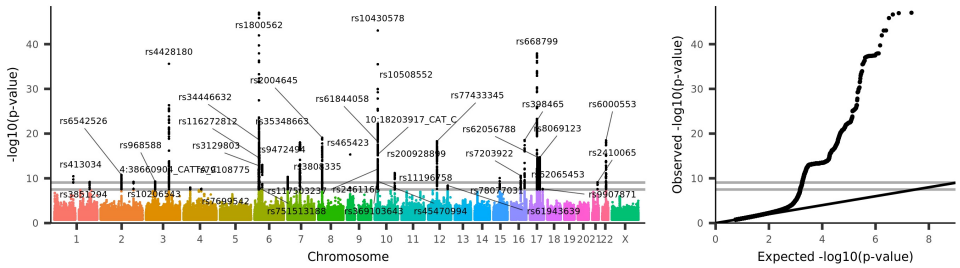
QSM left caudate



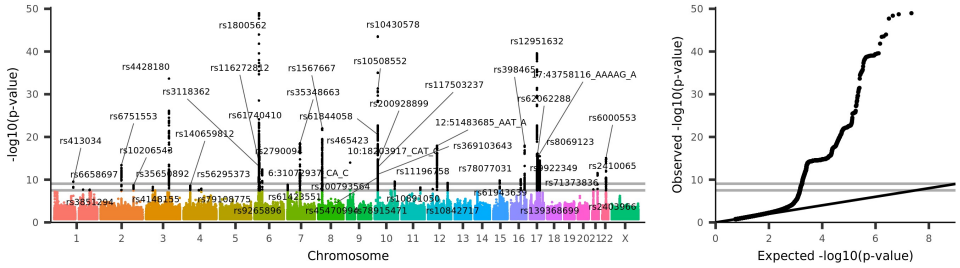
QSM right caudate



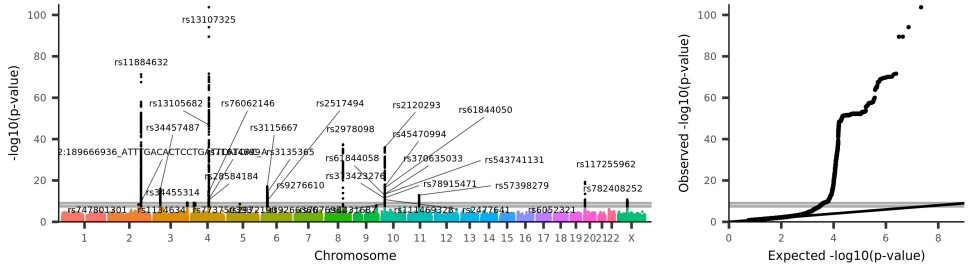
QSM left putamen



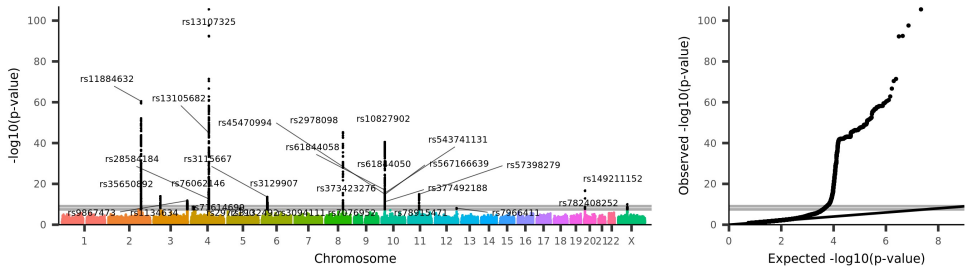
QSM right putamen



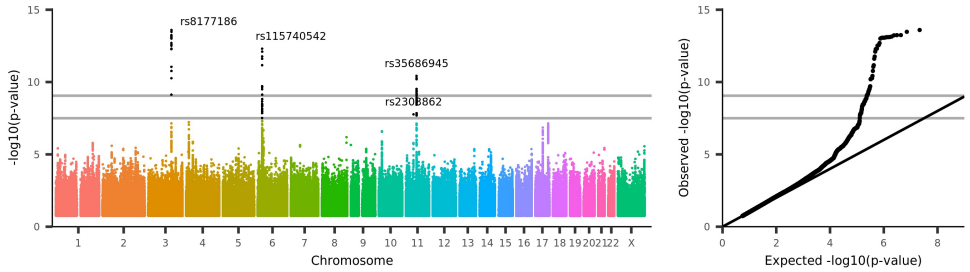
QSM left pallidum



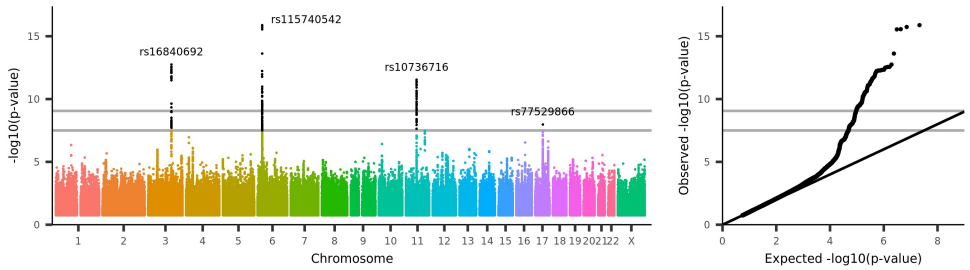
QSM right pallidum



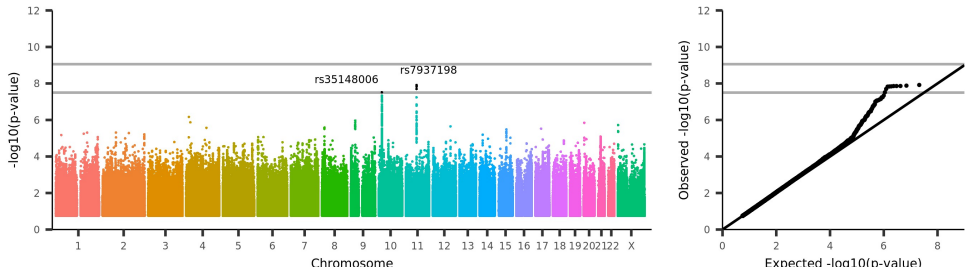
QSM left hippocampus



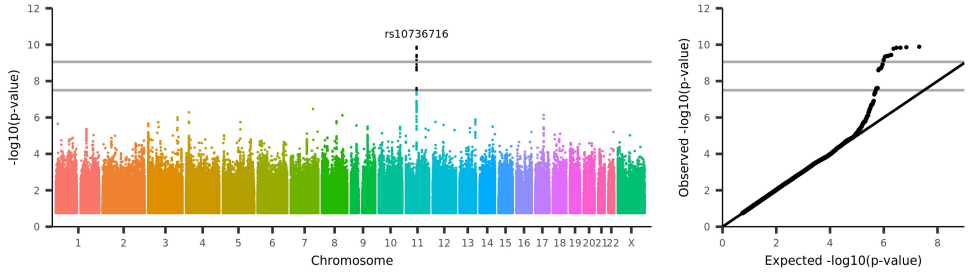
QSM right hippocampus



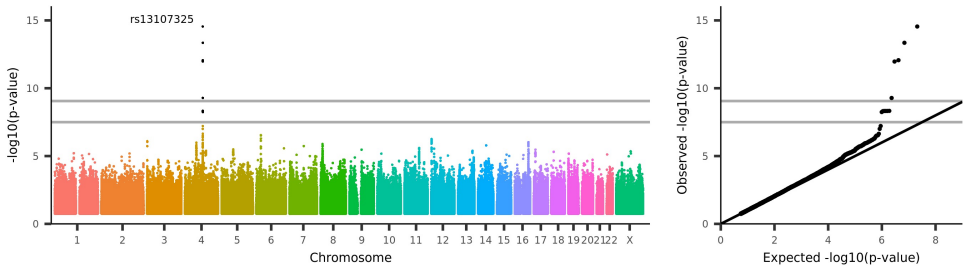
QSM left amygdala



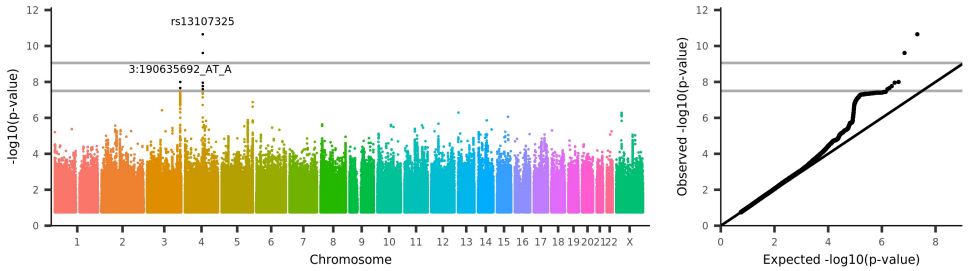
QSM right amygdala



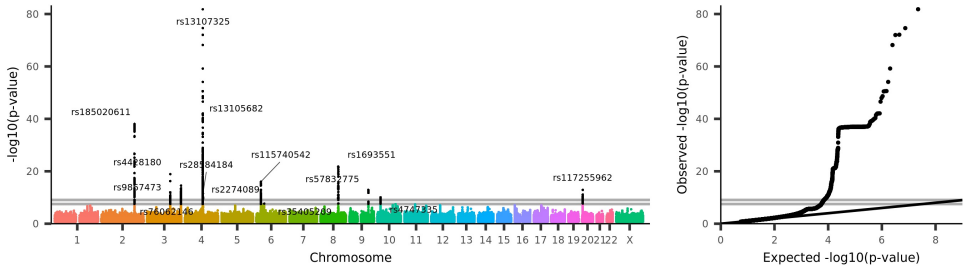
QSM left accumbens



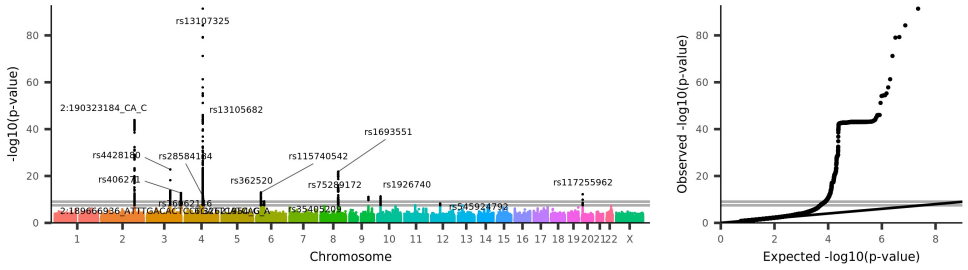
QSM right accumbens



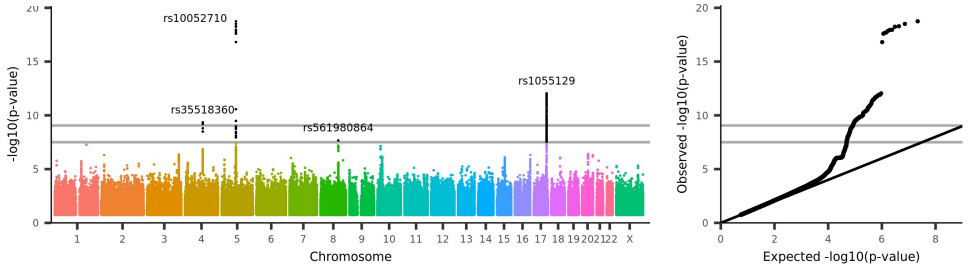
QSM left SN



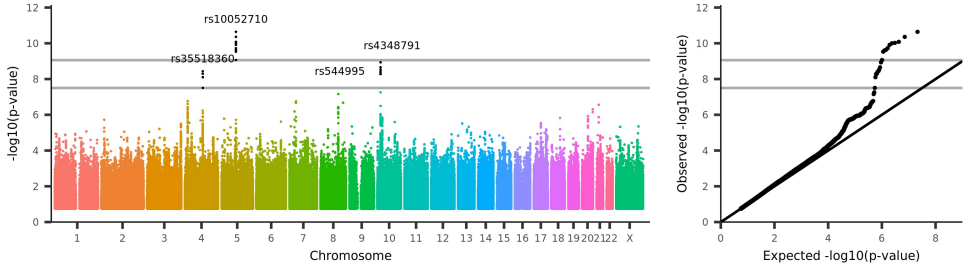
QSM right SN



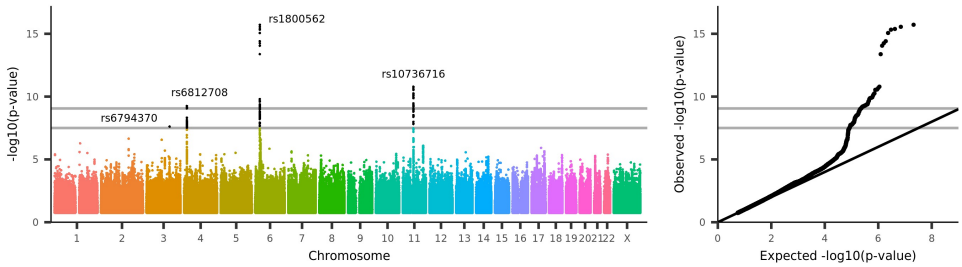
QSM WMH (without regressing out WMH volume)



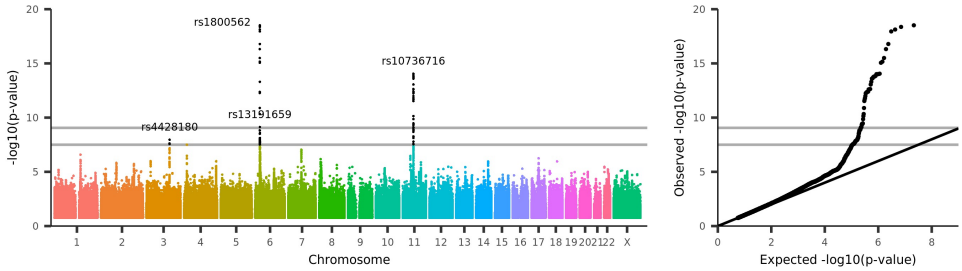
QSM WMH (after regressing out WMH volume)



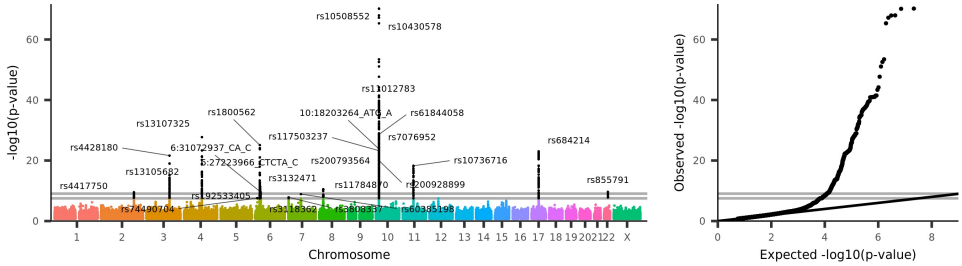
T2* left thalamus



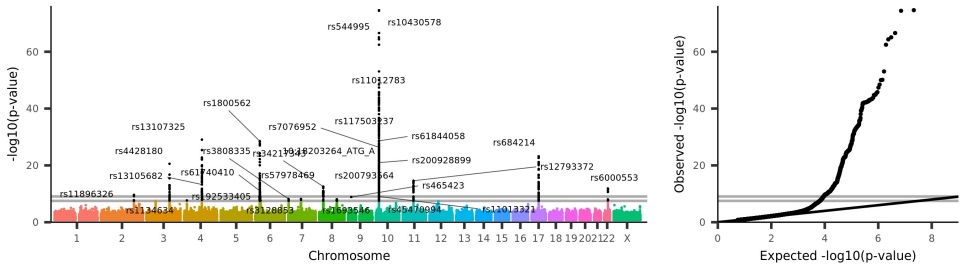
T2* right thalamus



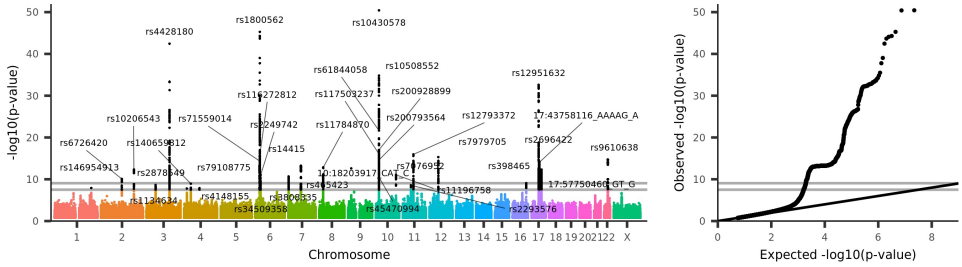
T2* left caudate



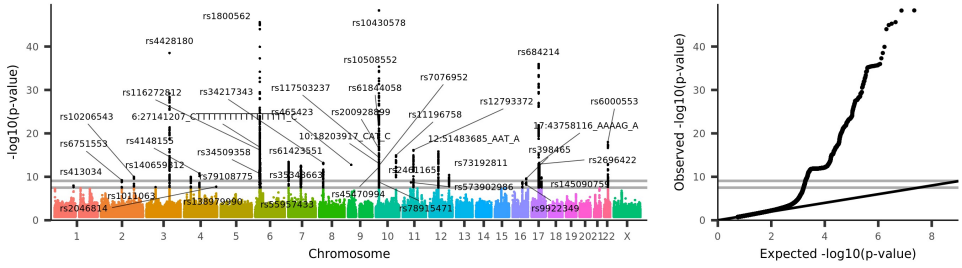
T2* right caudate



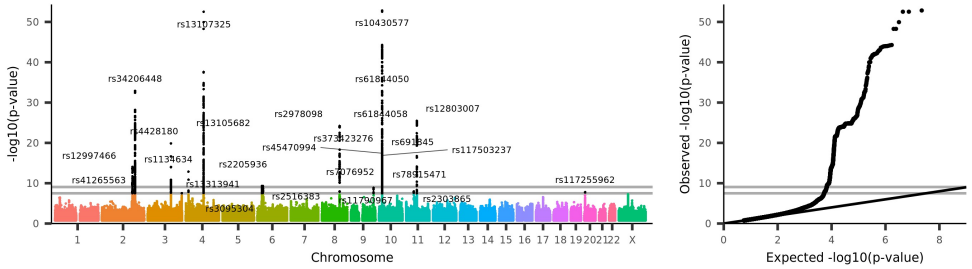
T2* left putamen



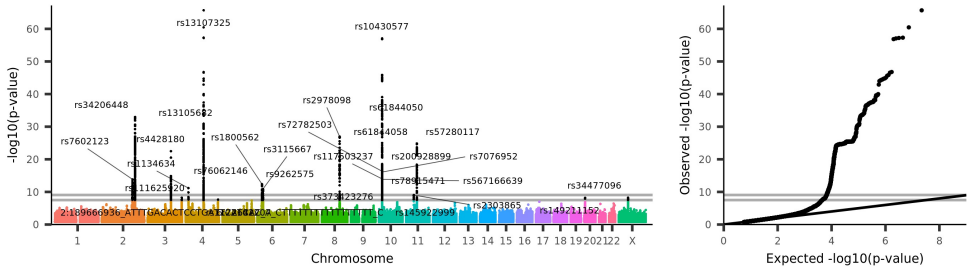
T2* right putamen



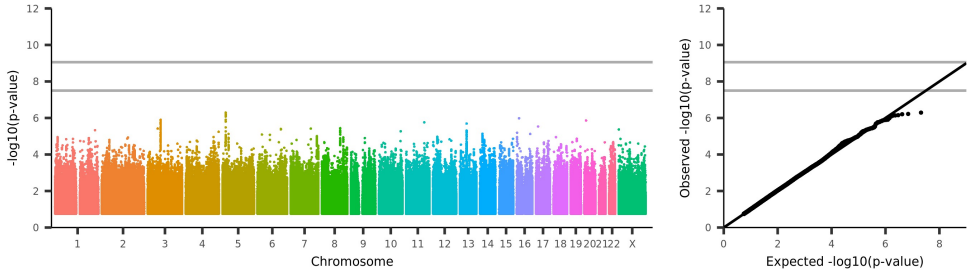
T2* left pallidum



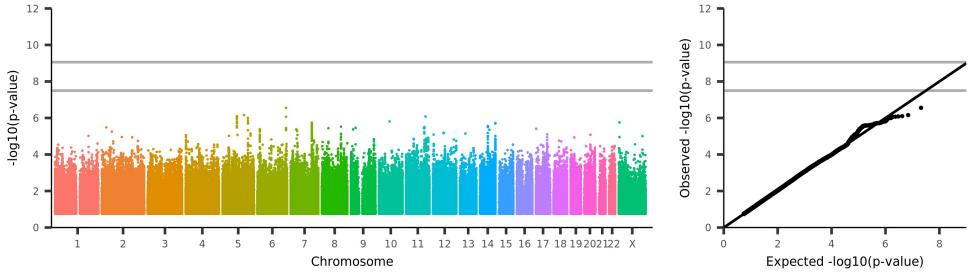
T2* right pallidum



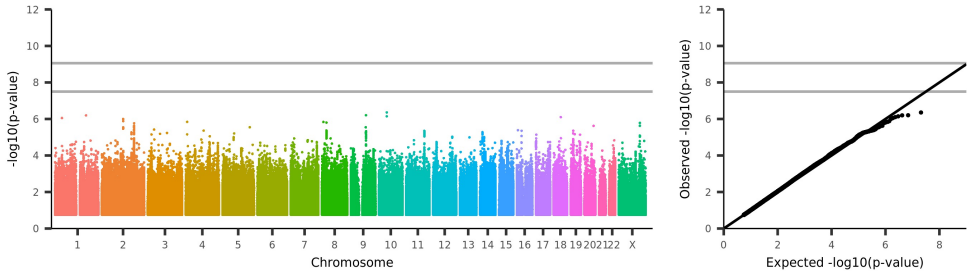
T2* left hippocampus



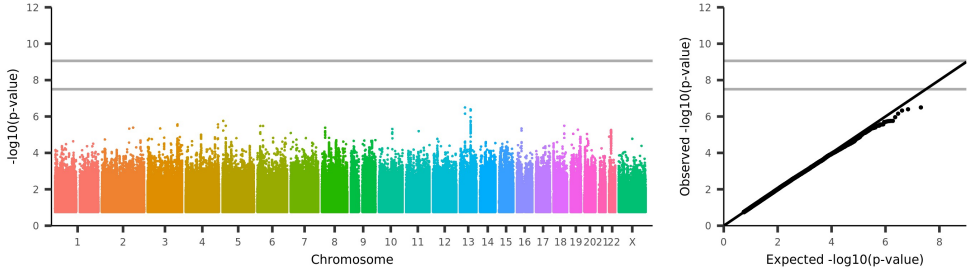
T2* right hippocampus



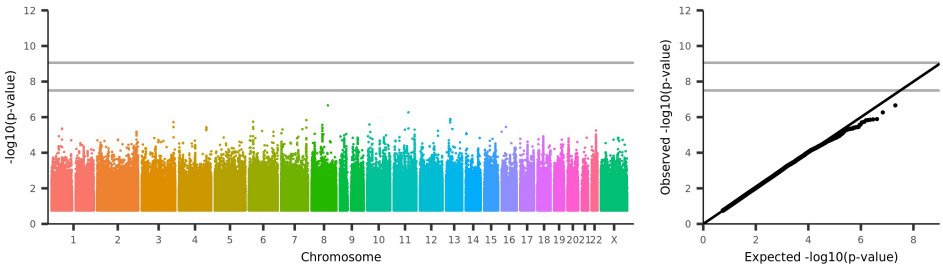
T2* left amygdala



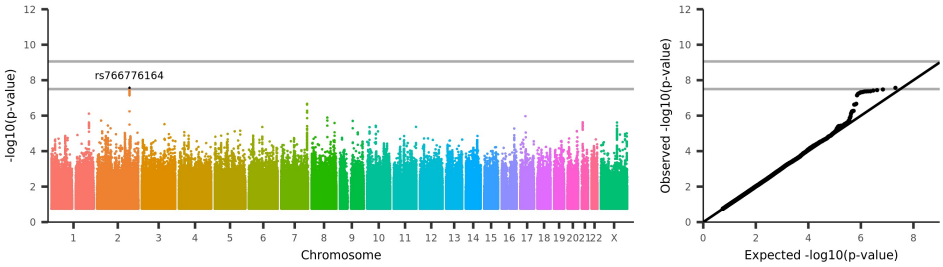
T2* right amygdala



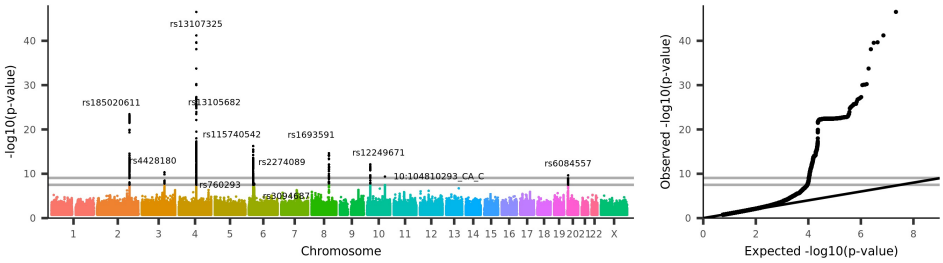
T2* left accumbens



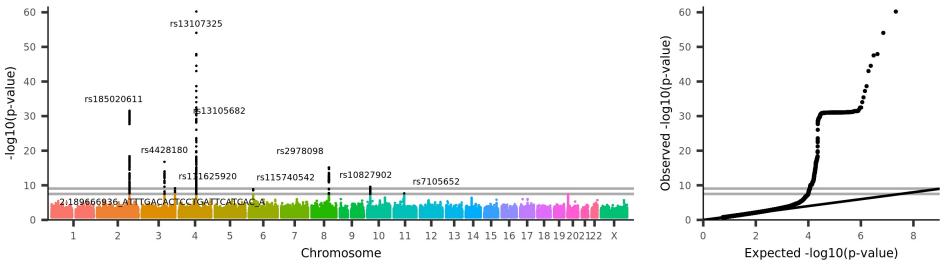
T2* right accumbens



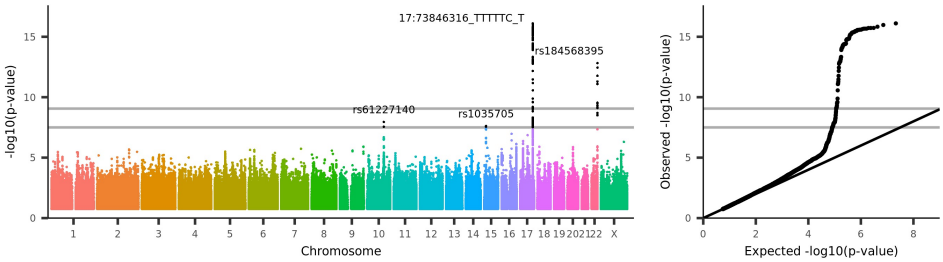
T2* left SN



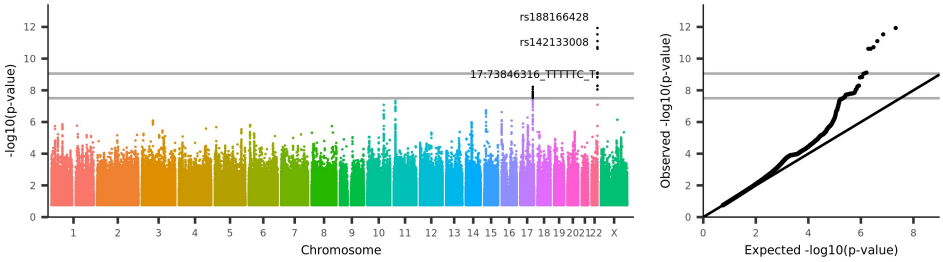
T2* right SN



T2* WMH (without regressing out WMH volume)



T2* WMH (after regressing out WMH volume)



References

[1] R. W. Brown, Y. C. N. Cheng, E. M. Haacke, M. R. Thompson, and R. Venkatesan, *Magnetic Resonance Imaging: Physical Principles and Sequence Design: Second Edition*. John Wiley & Son, 2014. doi: 10.1002/9781118633953.

[2] E. M. Haacke, Y. Xu, Y.-C. N. Cheng, and J. R. Reichenbach, "Susceptibility weighted imaging (SWI)," *Magnetic Resonance in Medicine*, vol. 52, no. 3, pp. 612–618, Sep. 2004, doi: https://doi.org/10.1002/mrm.20198.

[3] E. M. Haacke, S. Liu, S. Buch, W. Zheng, D. Wu, and Y. Ye, "Quantitative susceptibility mapping: current status and future directions," *Magnetic Resonance Imaging*, vol. 33, no. 1, pp. 1–25, Jan. 2015, doi: 10.1016/J.MRI.2014.09.004.

[4] S. Eskreis-Winkler *et al.*, "The clinical utility of QSM: disease diagnosis, medical management, and surgical planning," *NMR in Biomedicine*, vol. 30, no. 4, p. e3668, Apr. 2017, doi: https://doi.org/10.1002/nbm.3668.

[5] S. Liu *et al.*, "Susceptibility-weighted imaging: current status and future directions," *NMR in Biomedicine*, vol. 30, no. 4, p. e3552, Apr. 2017, doi: https://doi.org/10.1002/nbm.3552.

[6] C. Langkammer *et al.*, "Quantitative susceptibility mapping (QSM) as a means to measure brain iron? A post mortem validation study," *NeuroImage*, vol. 62, no. 3, pp. 1593–1599, Sep. 2012, doi: 10.1016/j.neuroimage.2012.05.049.

[7] S. Oshima *et al.*, "Brain MRI with Quantitative Susceptibility Mapping: Relationship to CT Attenuation Values," *Radiology*, vol. 294, no. 3, pp. 600–609, Jan. 2020, doi: 10.1148/radiol.2019182934.

[8] B. Bilgic, A. Pfefferbaum, T. Rohlfing, E. v. Sullivan, and E. Adalsteinsson, "MRI estimates of brain iron concentration in normal aging using quantitative susceptibility mapping," *NeuroImage*, vol. 59, no. 3, pp. 2625–2635, Feb. 2012, doi: 10.1016/J.NEUROIMAGE.2011.08.077.

[9] W. Zheng, H. Nichol, S. Liu, Y. C. N. Cheng, and E. M. Haacke, "Measuring iron in the brain using quantitative susceptibility mapping and X-ray fluorescence imaging," *NeuroImage*, vol. 78, pp. 68–74, Sep. 2013, doi: 10.1016/J.NEUROIMAGE.2013.04.022.

[10] M. Jucker and L. C. Walker, "Self-propagation of pathogenic protein aggregates in neurodegenerative diseases," *Nature*, vol. 501, no. 7465, pp. 45–51, 2013, doi: 10.1038/nature12481.

[11] K. L. Miller *et al.*, "Multimodal population brain imaging in the UK Biobank prospective epidemiological study," *Nature Neuroscience*, vol. 19, no. 11, pp. 1523–1536, 2016, doi: 10.1038/nn.4393.

[12] F. Alfaro-Almagro *et al.*, "Image processing and Quality Control for the first 10,000 brain imaging datasets from UK Biobank," *NeuroImage*, vol. 166, pp. 400–424, Feb. 2018, doi: 10.1016/j.neuroimage.2017.10.034.

[13] C. Wang *et al.*, "Methods for quantitative susceptibility and R2* mapping in whole post-mortem brains at 7T applied to amyotrophic lateral sclerosis,"

NeuroImage, vol. 222, p. 117216, Nov. 2020, doi: 10.1016/j.neuroimage.2020.117216.

[14] C. Wang *et al.*, "Phenotypic and genetic associations of quantitative magnetic susceptibility in UK Biobank brain imaging," *bioRxiv*, p. 2021.06.28.450248, Jan. 2021, doi: 10.1101/2021.06.28.450248.

[15] E. M. Haacke and J. R. Reichenbach, "Susceptibility Weighted Imaging in MRI: Basic Concepts and Clinical Applications," *Susceptibility Weighted Imaging in MRI: Basic Concepts and Clinical Applications*, Jan. 2011, doi: 10.1002/9780470905203.

[16] J. F. Schenck, "The role of magnetic susceptibility in magnetic resonance imaging: MRI magnetic compatibility of the first and second kinds," *Medical Physics*, vol. 23, no. 6, pp. 815–850, Jun. 1996, doi: https://doi.org/10.1118/1.597854.

[17] J. A. Hopkins and F. W. Wehrli, "Magnetic susceptibility measurement of insoluble solids by NMR: Magnetic susceptibility of bone.," *Magnetic Resonance in Medicine*, vol. 37, no. 4, pp. 494–500, Apr. 1997, doi: https://doi.org/10.1002/mrm.1910370404.

[18] T. A. Rouault, "Iron metabolism in the CNS: implications for neurodegenerative diseases," *Nature Reviews Neuroscience*, vol. 14, no. 8, pp. 551–564, 2013, doi: 10.1038/nrn3453.

[19] E. M. Haacke, S. Liu, S. Buch, W. Zheng, D. Wu, and Y. Ye, "Quantitative susceptibility mapping: Current status and future directions," *Magnetic Resonance Imaging*, vol. 33, no. 1. Elsevier Inc., pp. 1–25, Jan. 01, 2015. doi: 10.1016/j.mri.2014.09.004.

[20] S. D. Robinson, K. Bredies, D. Khabipova, B. Dymerska, J. P. Marques, and F. Schweser, "An illustrated comparison of processing methods for MR phase imaging and QSM: combining array coil signals and phase unwrapping," *NMR in Biomedicine*, vol. 30, no. 4, p. e3601, Apr. 2017, doi: https://doi.org/10.1002/nbm.3601.

[21] M. A. Bernstein, M. Grgic, T. J. Brosnan, and N. J. Pelc, "Reconstructions of phase contrast, phased array multicoil data," *Magnetic Resonance in Medicine*, vol. 32, no. 3, pp. 330–334, Sep. 1994, doi: https://doi.org/10.1002/mrm.1910320308.

[22] K. Eckstein *et al.*, "Computationally Efficient Combination of Multi-channel Phase Data From Multi-echo Acquisitions (ASPIRE)," *Magnetic Resonance in Medicine*, vol. 79, no. 6, pp. 2996–3006, Jun. 2018, doi: https://doi.org/10.1002/mrm.26963.

[23] S. D. Robinson *et al.*, "Combining phase images from array coils using a short echo time reference scan (COMPOSER)," *Magnetic Resonance in Medicine*, vol. 77, no. 1, pp. 318–327, Jan. 2017, doi: https://doi.org/10.1002/mrm.26093.

[24] M. Jenkinson, "Fast, automated, N-dimensional phase-unwrapping algorithm," *Magnetic Resonance in Medicine*, vol. 49, no. 1, pp. 193–197, Jan. 2003, doi: https://doi.org/10.1002/mrm.10354.

[25] M. A. Schofield and Y. Zhu, "Fast phase unwrapping algorithm for interferometric applications," *Opt. Lett.*, vol. 28, no. 14, pp. 1194–1196, Jul. 2003, doi: 10.1364/OL.28.001194.

[26] F. Schweser, S. D. Robinson, L. de Rochefort, W. Li, and K. Bredies, "An illustrated comparison of processing methods for phase MRI and QSM: removal

of background field contributions from sources outside the region of interest," *NMR in Biomedicine*, vol. 30, no. 4, p. e3604, Apr. 2017, doi: https://doi.org/10.1002/nbm.3604.

[27] S. M. Smith, "Fast robust automated brain extraction," *Human Brain Mapping*, vol. 17, no. 3, pp. 143–155, Nov. 2002, doi: https://doi.org/10.1002/hbm.10062.

[28] F. Schweser, A. Deistung, B. W. Lehr, and J. R. Reichenbach, "Quantitative imaging of intrinsic magnetic tissue properties using MRI signal phase: An approach to in vivo brain iron metabolism?," *NeuroImage*, vol. 54, no. 4, pp. 2789–2807, Feb. 2011, doi: 10.1016/j.neuroimage.2010.10.070.

[29] W. Li, B. Wu, and C. Liu, "Quantitative susceptibility mapping of human brain reflects spatial variation in tissue composition," *NeuroImage*, vol. 55, no. 4, pp. 1645–1656, Apr. 2011, doi: 10.1016/J.NEUROIMAGE.2010.11.088.

[30] H. Sun and A. H. Wilman, "Background field removal using spherical mean value filtering and Tikhonov regularization," *Magnetic Resonance in Medicine*, vol. 71, no. 3, pp. 1151–1157, Mar. 2014, doi: https://doi.org/10.1002/mrm.24765.

[31] T. Liu *et al.*, "A novel background field removal method for MRI using projection onto dipole fields (PDF)," *NMR in Biomedicine*, vol. 24, no. 9, pp. 1129–1136, Nov. 2011, doi: https://doi.org/10.1002/nbm.1670.

[32] D. Zhou, T. Liu, P. Spincemaille, and Y. Wang, "Background field removal by solving the Laplacian boundary value problem," *NMR in Biomedicine*, vol. 27, no. 3, pp. 312–319, Mar. 2014, doi: https://doi.org/10.1002/nbm.3064.

[33] W. Li, A. v Avram, B. Wu, X. Xiao, and C. Liu, "Integrated Laplacian-based phase unwrapping and background phase removal for quantitative susceptibility mapping," *NMR in Biomedicine*, vol. 27, no. 2, pp. 219–227, Feb. 2014, doi: https://doi.org/10.1002/nbm.3056.

[34] K. Shmueli, J. A. de Zwart, P. van Gelderen, T.-Q. Li, S. J. Dodd, and J. H. Duyn, "Magnetic susceptibility mapping of brain tissue in vivo using MRI phase data," *Magnetic Resonance in Medicine*, vol. 62, no. 6, pp. 1510–1522, Dec. 2009, doi: https://doi.org/10.1002/mrm.22135.

[35] J. Liu *et al.*, "Morphology enabled dipole inversion for quantitative susceptibility mapping using structural consistency between the magnitude image and the susceptibility map," *NeuroImage*, vol. 59, no. 3, pp. 2560–2568, Feb. 2012, doi: 10.1016/j.neuroimage.2011.08.082.

[36] Z. Liu, Y. Kee, D. Zhou, Y. Wang, and P. Spincemaille, "Preconditioned total field inversion (TFI) method for quantitative susceptibility mapping," *Magnetic Resonance in Medicine*, vol. 78, no. 1, pp. 303–315, Jul. 2017, doi: https://doi.org/10.1002/mrm.26331.

[37] H. Wei *et al.*, "Streaking artifact reduction for quantitative susceptibility mapping of sources with large dynamic range," *NMR in Biomedicine*, vol. 28, no. 10, pp. 1294–1303, Oct. 2015, doi: https://doi.org/10.1002/nbm.3383.

[38] W. Li *et al.*, "A method for estimating and removing streaking artifacts in quantitative susceptibility mapping," *NeuroImage*, vol. 108, pp. 111–122, Mar. 2015, doi: 10.1016/j.neuroimage.2014.12.043.

[39] T. Liu, P. Spincemaille, L. de Rochefort, B. Kressler, and Y. Wang, "Calculation of susceptibility through multiple orientation sampling (COSMOS): A method for conditioning the inverse problem from measured magnetic field map to

susceptibility source image in MRI," *Magnetic Resonance in Medicine*, vol. 61, no. 1, pp. 196–204, Jan. 2009, doi: https://doi.org/10.1002/mrm.21828.

[40] J. Yoon *et al.*, "Quantitative susceptibility mapping using deep neural network: QSMnet," *NeuroImage*, vol. 179, pp. 199–206, Oct. 2018, doi: 10.1016/J.NEUROIMAGE.2018.06.030.

[41] A. Deistung, A. Schäfer, F. Schweser, U. Biedermann, R. Turner, and J. R. Reichenbach, "Toward in vivo histology: A comparison of quantitative susceptibility mapping (QSM) with magnitude-, phase-, and R2*-imaging at ultra-high magnetic field strength," *NeuroImage*, vol. 65, pp. 299–314, Jan. 2013, doi: 10.1016/j.neuroimage.2012.09.055.

[42] C. Langkammer *et al.*, "Quantitative MR Imaging of Brain Iron: A Postmortem Validation Study," *Radiology*, vol. 257, no. 2, pp. 455–462, Nov. 2010, doi: 10.1148/radiol.10100495.

[43] S. Hametner *et al.*, "The influence of brain iron and myelin on magnetic susceptibility and effective transverse relaxation - A biochemical and histological validation study," *NeuroImage*, vol. 179, pp. 117–133, Oct. 2018, doi: 10.1016/J.NEUROIMAGE.2018.06.007.

[44] H. Sun *et al.*, "Validation of quantitative susceptibility mapping with Perls' iron staining for subcortical gray matter," *NeuroImage*, vol. 105, pp. 486–492, Jan. 2015, doi: 10.1016/J.NEUROIMAGE.2014.11.010.

[45] M. C. Kiernan *et al.*, "Amyotrophic lateral sclerosis," *The Lancet*, vol. 377, no. 9769, pp. 942–955, Mar. 2011, doi: 10.1016/S0140-6736(10)61156-7.

[46] J. Brettschneider *et al.*, "Stages of pTDP-43 pathology in amyotrophic lateral sclerosis," *Annals of Neurology*, vol. 74, no. 1, pp. 20–38, Jul. 2013, doi: https://doi.org/10.1002/ana.23937.

[47] R. H. Tan *et al.*, "TDP-43 proteinopathies: pathological identification of brain regions differentiating clinical phenotypes," *Brain*, vol. 138, no. 10, pp. 3110–3122, Oct. 2015, doi: 10.1093/brain/awv220.

[48] M. Pallebage-Gamarallage *et al.*, "Dissecting the pathobiology of altered MRI signal in amyotrophic lateral sclerosis: A post mortem whole brain sampling strategy for the integration of ultra-high-field MRI and quantitative neuropathology," *BMC Neuroscience*, vol. 19, no. 1, p. 11, 2018, doi: 10.1186/s12868-018-0416-1.

[49] J. Y. Kwan *et al.*, "Iron Accumulation in Deep Cortical Layers Accounts for MRI Signal Abnormalities in ALS: Correlating 7 Tesla MRI and Pathology," *PLOS ONE*, vol. 7, no. 4, pp. e35241-, Apr. 2012, [Online]. Available: https://doi.org/10.1371/journal.pone.0035241

[50] A. D. Schweitzer *et al.*, "Quantitative Susceptibility Mapping of the Motor Cortex in Amyotrophic Lateral Sclerosis and Primary Lateral Sclerosis," *American Journal of Roentgenology*, vol. 204, no. 5, pp. 1086–1092, Apr. 2015, doi: 10.2214/AJR.14.13459.

[51] M. Costagli *et al.*, "Magnetic susceptibility in the deep layers of the primary motor cortex in Amyotrophic Lateral Sclerosis," *NeuroImage: Clinical*, vol. 12, pp. 965–969, Feb. 2016, doi: 10.1016/J.NICL.2016.04.011.

[52] J. Acosta-Cabronero *et al.*, "Quantitative Susceptibility MRI to Detect Brain Iron in Amyotrophic Lateral Sclerosis," *Radiology*, vol. 289, no. 1, pp. 195–203, Jul. 2018, doi: 10.1148/radiol.2018180112.

[53] B. U. Foerster, D. Tomasi, and E. C. Caparelli, “Magnetic field shift due to mechanical vibration in functional magnetic resonance imaging,” *Magnetic Resonance in Medicine*, vol. 54, no. 5, pp. 1261–1267, Nov. 2005, doi: https://doi.org/10.1002/mrm.20695.

[54] K. L. Miller *et al.*, “Diffusion imaging of whole, post-mortem human brains on a clinical MRI scanner,” *NeuroImage*, vol. 57, no. 1, pp. 167–181, Jul. 2011, doi: 10.1016/J.NEUROIMAGE.2011.03.070.

[55] M. Jenkinson and S. Smith, “A global optimisation method for robust affine registration of brain images,” *Medical Image Analysis*, vol. 5, no. 2, pp. 143–156, Jun. 2001, doi: 10.1016/S1361-8415(01)00036-6.

[56] M. Jenkinson, P. Bannister, M. Brady, and S. Smith, “Improved Optimization for the Robust and Accurate Linear Registration and Motion Correction of Brain Images,” *NeuroImage*, vol. 17, no. 2, pp. 825–841, Oct. 2002, doi: 10.1006/NIMG.2002.1132.

[57] B. Kressler, L. de Rochefort, T. Liu, P. Spincemaille, Q. Jiang, and Y. Wang, “Nonlinear Regularization for Per Voxel Estimation of Magnetic Susceptibility Distributions From MRI Field Maps,” *IEEE Transactions on Medical Imaging*, vol. 29, no. 2, pp. 273–281, 2010, doi: 10.1109/TMI.2009.2023787.

[58] T. Liu, C. Wisnieff, M. Lou, W. Chen, P. Spincemaille, and Y. Wang, “Nonlinear formulation of the magnetic field to source relationship for robust quantitative susceptibility mapping,” *Magnetic Resonance in Medicine*, vol. 69, no. 2, pp. 467–476, Feb. 2013, doi: https://doi.org/10.1002/mrm.24272.

[59] B. C. Tendler and R. Bowtell, “Frequency difference mapping applied to the corpus callosum at 7T,” *Magnetic Resonance in Medicine*, vol. 81, no. 5, pp. 3017–3031, May 2019, doi: https://doi.org/10.1002/mrm.27626.

[60] J. P. Marques and R. Bowtell, “Application of a Fourier-based method for rapid calculation of field inhomogeneity due to spatial variation of magnetic susceptibility,” *Concepts in Magnetic Resonance Part B: Magnetic Resonance Engineering*, vol. 25B, no. 1, pp. 65–78, Apr. 2005, doi: https://doi.org/10.1002/cmr.b.20034.

[61] T. He, G. Smith, J.-P. Carpenter, R. Mohiaddin, D. Pennell, and D. Firmin, “A phantom study of temperature-dependent MRI T2* measurement,” *Journal of Cardiovascular Magnetic Resonance*, vol. 11, no. 1, p. P147, 2009, doi: 10.1186/1532-429X-11-S1-P147.

[62] M. F. Glasser *et al.*, “A multi-modal parcellation of human cerebral cortex,” *Nature*, vol. 536, no. 7615, pp. 171–178, 2016, doi: 10.1038/nature18933.

[63] R. Nieuwenhuys and C. A. J. Broere, “A map of the human neocortex showing the estimated overall myelin content of the individual architectonic areas based on the studies of Adolf Hopf,” *Brain Structure and Function*, vol. 222, no. 1, pp. 465–480, 2017, doi: 10.1007/s00429-016-1228-7.

[64] M. Fukunaga *et al.*, “Layer-specific variation of iron content in cerebral cortex as a source of MRI contrast,” *Proceedings of the National Academy of Sciences*, vol. 107, no. 8, p. 3834, Feb. 2010, doi: 10.1073/pnas.0911177107.

[65] S. van Duijn, R. J. A. Nabuurs, S. G. van Duinen, and R. Natté, “Comparison of Histological Techniques to Visualize Iron in Paraffin-embedded Brain Tissue of Patients with Alzheimer’s Disease,” *Journal of Histochemistry & Cytochemistry*, vol. 61, no. 11, pp. 785–792, Jul. 2013, doi: 10.1369/0022155413501325.

[66] A. Reinert, M. Morawski, J. Seeger, T. Arendt, and T. Reinert, “Iron concentrations in neurons and glial cells with estimates on ferritin concentrations,” *BMC Neuroscience*, vol. 20, no. 1, p. 25, 2019, doi: 10.1186/s12868-019-0507-7.

[67] Y. Zhang *et al.*, “Quantitative Susceptibility Mapping and R2* Measured Changes during White Matter Lesion Development in Multiple Sclerosis: Myelin Breakdown, Myelin Debris Degradation and Removal, and Iron Accumulation,” *American Journal of Neuroradiology*, vol. 37, no. 9, p. 1629, Sep. 2016, doi: 10.3174/ajnr.A4825.

[68] N. Otsu, “A Threshold Selection Method from Gray-Level Histograms,” *IEEE Transactions on Systems, Man, and Cybernetics*, vol. 9, no. 1, pp. 62–66, 1979, doi: 10.1109/TSMC.1979.4310076.

[69] M. D. Meadowcroft *et al.*, “Histological–MRI correlation in the primary motor cortex of patients with amyotrophic lateral sclerosis,” *Journal of Magnetic Resonance Imaging*, vol. 41, no. 3, pp. 665–675, Mar. 2015, doi: https://doi.org/10.1002/jmri.24582.

[70] I. N. Huszar *et al.*, “Tensor Image Registration Library: Automated Non-Linear Registration of Sparsely Sampled Histological Specimens to Post-Mortem MRI of the Whole Human Brain,” *bioRxiv*, p. 849570, Jan. 2019, doi: 10.1101/849570.

[71] R. J. Dawe, D. A. Bennett, J. A. Schneider, S. K. Vasireddi, and K. Arfanakis, “Postmortem MRI of human brain hemispheres: T2 relaxation times during formaldehyde fixation,” *Magnetic Resonance in Medicine*, vol. 61, no. 4, pp. 810–818, Apr. 2009, doi: https://doi.org/10.1002/mrm.21909.

[72] B. C. Tendler *et al.*, “A method to remove the influence of fixative concentration on postmortem T2 maps using a kinetic tensor model,” *Human Brain Mapping*, vol. n/a, no. n/a, Sep. 2021, doi: https://doi.org/10.1002/hbm.25661.

[73] P. M. Thompson *et al.*, “The ENIGMA Consortium: large-scale collaborative analyses of neuroimaging and genetic data,” *Brain Imaging and Behavior*, vol. 8, no. 2, pp. 153–182, 2014, doi: 10.1007/s11682-013-9269-5.

[74] G. N. C. (GNC) Consortium, “The German National Cohort: aims, study design and organization,” *European Journal of Epidemiology*, vol. 29, no. 5, pp. 371–382, 2014, doi: 10.1007/s10654-014-9890-7.

[75] C. Sudlow *et al.*, “UK Biobank: An Open Access Resource for Identifying the Causes of a Wide Range of Complex Diseases of Middle and Old Age,” *PLOS Medicine*, vol. 12, no. 3, pp. e1001779-, Mar. 2015, [Online]. Available: https://doi.org/10.1371/journal.pmed.1001779

[76] E. M. Haacke, Y. Xu, Y.-C. N. Cheng, and J. R. Reichenbach, “Susceptibility weighted imaging (SWI),” *Magnetic Resonance in Medicine*, vol. 52, no. 3, pp. 612–618, Sep. 2004, doi: https://doi.org/10.1002/mrm.20198.

[77] C. Liu, W. Li, K. A. Tong, K. W. Yeom, and S. Kuzminski, “Susceptibility-weighted imaging and quantitative susceptibility mapping in the brain,” *Journal of Magnetic Resonance Imaging*, vol. 42, no. 1, pp. 23–41, Jul. 2015, doi: https://doi.org/10.1002/jmri.24768.

[78] Y. Wang and T. Liu, “Quantitative susceptibility mapping (QSM): Decoding MRI data for a tissue magnetic biomarker,” *Magnetic Resonance in Medicine*, vol. 73, no. 1, pp. 82–101, Jan. 2015, doi: https://doi.org/10.1002/mrm.25358.

[79] S. Straub *et al.*, “Suitable reference tissues for quantitative susceptibility mapping of the brain,” *Magnetic Resonance in Medicine*, vol. 78, no. 1, pp. 204–214, Jul. 2017, doi: https://doi.org/10.1002/mrm.26369.

[80] B. Wu, W. Li, A. V. Avram, S. M. Gho, and C. Liu, “Fast and tissue-optimized mapping of magnetic susceptibility and T2* with multi-echo and multi-shot spirals,” *NeuroImage*, vol. 59, no. 1, pp. 297–305, Jan. 2012, doi: 10.1016/j.neuroimage.2011.07.019.

[81] W. Li, B. Wu, and C. Liu, “iHARPERELLA: an improved method for integrated 3D phase unwrapping and background phase removal,” 2015.

[82] H. Sun and A. H. Wilman, “Background field removal using spherical mean value filtering and Tikhonov regularization,” *Magnetic Resonance in Medicine*, vol. 71, no. 3, pp. 1151–1157, Mar. 2014, doi: https://doi.org/10.1002/mrm.24765.

[83] D. Zhou, T. Liu, P. Spincemaille, and Y. Wang, “Background field removal by solving the Laplacian boundary value problem,” *NMR in Biomedicine*, vol. 27, no. 3, pp. 312–319, Mar. 2014, doi: https://doi.org/10.1002/nbm.3064.

[84] L. Zhang *et al.*, “Fast quantitative susceptibility reconstruction via total field inversion with improved weighted L0 norm approximation,” *NMR in Biomedicine*, vol. 32, no. 5, p. e4067, May 2019, doi: https://doi.org/10.1002/nbm.4067.

[85] L. Griffanti *et al.*, “BIANCA (Brain Intensity AbNormality Classification Algorithm): A new tool for automated segmentation of white matter hyperintensities,” *NeuroImage*, vol. 141, pp. 191–205, Nov. 2016, doi: 10.1016/j.neuroimage.2016.07.018.

[86] M. de Groot *et al.*, “Improving alignment in Tract-based spatial statistics: Evaluation and optimization of image registration,” *NeuroImage*, vol. 76, pp. 400–411, Aug. 2013, doi: 10.1016/j.neuroimage.2013.03.015.

[87] M. P. Lun, E. S. Monuki, and M. K. Lehtinen, “Development and functions of the choroid plexus–cerebrospinal fluid system,” *Nature Reviews Neuroscience*, vol. 16, no. 8, pp. 445–457, 2015, doi: 10.1038/nrn3921.

[88] A. Llera, D. Vidaurre, R. H. R. Pruim, and C. F. Beckmann, “Variational Mixture Models with Gamma or inverse-Gamma components.” 2016. arXiv:1607.07573.

[89] M. Jenkinson, C. F. Beckmann, T. E. J. Behrens, M. W. Woolrich, and S. M. Smith, “FSL,” *NeuroImage*, vol. 62, no. 2, pp. 782–790, Aug. 2012, doi: 10.1016/J.NEUROIMAGE.2011.09.015.

[90] B. Patenaude, S. M. Smith, D. N. Kennedy, and M. Jenkinson, “A Bayesian model of shape and appearance for subcortical brain segmentation,” *NeuroImage*, vol. 56, no. 3, pp. 907–922, Jun. 2011, doi: 10.1016/j.neuroimage.2011.02.046.

[91] W. M. Pauli, A. N. Nili, and J. M. Tyszka, “A high-resolution probabilistic in vivo atlas of human subcortical brain nuclei,” *Scientific Data*, vol. 5, no. 1, p. 180063, 2018, doi: 10.1038/sdata.2018.63.

[92] Y. Zhang, M. Brady, and S. Smith, “Segmentation of brain MR images through a hidden Markov random field model and the expectation-maximization algorithm,” *IEEE Transactions on Medical Imaging*, vol. 20, no. 1, 2001, doi: 10.1109/42.906424.

[93] D. Hernando, K. K. Vigen, A. Shimakawa, and S. B. Reeder, “R mapping in the presence of macroscopic B0 field variations,” *Magnetic Resonance in Medicine*, vol. 68, no. 3, pp. 830–840, Sep. 2012, doi: https://doi.org/10.1002/mrm.23306.

[94] D. P. Hibar *et al.*, “Common genetic variants influence human subcortical brain structures,” *Nature*, vol. 520, no. 7546, pp. 224–229, 2015, doi: 10.1038/nature14101.

[95] M. M. B. Breteler, T. Stöcker, E. Pracht, D. Brenner, and R. Stirnberg, “IC-P-165: MRI IN THE RHINELAND STUDY: A NOVEL PROTOCOL FOR POPULATION NEUROIMAGING,” *Alzheimer’s & Dementia*, vol. 10, no. 4S_Part_7, pp. P92–P92, Jul. 2014, doi: https://doi.org/10.1016/j.jalz.2014.05.172.

[96] M. A. Ikram *et al.*, “The Rotterdam Scan Study: design update 2016 and main findings,” *European Journal of Epidemiology*, vol. 30, no. 12, pp. 1299–1315, 2015, doi: 10.1007/s10654-015-0105-7.

[97] S. G. Mueller *et al.*, “The Alzheimer’s Disease Neuroimaging Initiative,” *Neuroimaging Clinics of North America*, vol. 15, no. 4, pp. 869–877, Nov. 2005, doi: 10.1016/J.NIC.2005.09.008.

[98] Y. Li *et al.*, “Iron Content in Deep Gray Matter as a Function of Age Using Quantitative Susceptibility Mapping: A Multicenter Study,” *Frontiers in Neuroscience*, vol. 14, p. 1389, 2021, [Online]. Available: https://www.frontiersin.org/article/10.3389/fnins.2020.607705

[99] N. Allen *et al.*, “UK Biobank: Current status and what it means for epidemiology,” *Health Policy and Technology*, vol. 1, no. 3, pp. 123–126, Sep. 2012, doi: 10.1016/j.hlpt.2012.07.003.

[100] B. Raman *et al.*, “Medium-term effects of SARS-CoV-2 infection on multiple vital organs, exercise capacity, cognition, quality of life and mental health, post-hospital discharge,” *EClinicalMedicine*, vol. 31, p. 100683, Jan. 2021, doi: 10.1016/j.eclinm.2020.100683.

[101] P. Ramos, A. Santos, N. R. Pinto, R. Mendes, T. Magalhães, and A. Almeida, “Iron levels in the human brain: A post-mortem study of anatomical region differences and age-related changes,” *Journal of Trace Elements in Medicine and Biology*, vol. 28, no. 1, pp. 13–17, Jan. 2014, doi: 10.1016/j.jtemb.2013.08.001.

[102] E. Andrási, S. Igaz, N. Szoboszlai, É. Farkas, and Z. Ajtony, “Several methods to determine heavy metals in the human brain,” *Spectrochimica acta, Part B: Atomic spectroscopy*, vol. 54, no. 5, pp. 819–825, May 1999, doi: 10.1016/S0584-8547(99)00039-7.

[103] C. Rua *et al.*, “Multi-centre, multi-vendor reproducibility of 7T QSM and R2* in the human brain: Results from the UK7T study,” *NeuroImage*, vol. 223, p. 117358, Dec. 2020, doi: 10.1016/J.NEUROIMAGE.2020.117358.

[104] M. N. Voelker *et al.*, “The traveling heads 2.0: Multicenter reproducibility of quantitative imaging methods at 7 Tesla,” *NeuroImage*, vol. 232, p. 117910, May 2021, doi: 10.1016/J.NEUROIMAGE.2021.117910.

[105] A. Eshaghi *et al.*, “Identifying multiple sclerosis subtypes using unsupervised machine learning and MRI data,” *Nature Communications*, vol. 12, no. 1, p. 2078, 2021, doi: 10.1038/s41467-021-22265-2.

[106] L. Nobis *et al.*, “Hippocampal volume across age: Nomograms derived from over 19,700 people in UK Biobank,” *NeuroImage: Clinical*, vol. 23, p. 101904, Jan. 2019, doi: 10.1016/j.nicl.2019.101904.

[107] I. A. Dekkers, P. R. Jansen, and H. J. Lamb, “Obesity, Brain Volume, and White Matter Microstructure at MRI: A Cross-sectional UK Biobank Study,” *Radiology*, vol. 291, no. 3, pp. 763–771, Apr. 2019, doi: 10.1148/radiol.2019181012.

[108] S. R. Cox *et al.*, “Associations between vascular risk factors and brain MRI indices in UK Biobank,” *European Heart Journal*, vol. 40, no. 28, pp. 2290–2300, Jul. 2019, doi: 10.1093/eurheartj/ehz100.
[109] S. M. Smith *et al.*, “Brain aging comprises many modes of structural and functional change with distinct genetic and biophysical associations,” *eLife*, vol. 9, Mar. 2020, doi: 10.7554/eLife.52677.
[110] S. R. Cox *et al.*, “Ageing and brain white matter structure in 3,513 UK Biobank participants,” *Nature Communications*, vol. 7, no. 1, p. 13629, 2016, doi: 10.1038/ncomms13629.
[111] L. T. Elliott *et al.*, “Genome-wide association studies of brain imaging phenotypes in UK Biobank,” *Nature*, vol. 562, no. 7726, pp. 210–216, 2018, doi: 10.1038/s41586-018-0571-7.
[112] S. M. Smith *et al.*, “An expanded set of genome-wide association studies of brain imaging phenotypes in UK Biobank,” *Nature Neuroscience*, vol. 24, no. 5, pp. 737–745, May 2021, doi: 10.1038/s41593-021-00826-4.
[113] X. Shen *et al.*, “A phenome-wide association and Mendelian Randomisation study of polygenic risk for depression in UK Biobank,” *Nature Communications*, vol. 11, no. 1, p. 2301, 2020, doi: 10.1038/s41467-020-16022-0.
[114] D. Alnæs *et al.*, “Brain Heterogeneity in Schizophrenia and Its Association With Polygenic Risk,” *JAMA Psychiatry*, vol. 76, no. 7, pp. 739–748, Jul. 2019, doi: 10.1001/jamapsychiatry.2019.0257.
[115] E. Persyn, K. B. Hanscombe, J. M. M. Howson, C. M. Lewis, M. Traylor, and H. S. Markus, “Genome-wide association study of MRI markers of cerebral small vessel disease in 42,310 participants,” *Nature Communications*, vol. 11, no. 1, p. 2175, 2020, doi: 10.1038/s41467-020-15932-3.
[116] M. K. Georgakis, R. Malik, C. D. Anderson, K. G. Parhofer, J. C. Hopewell, and M. Dichgans, “Genetic determinants of blood lipids and cerebral small vessel disease: role of high-density lipoprotein cholesterol,” *Brain*, vol. 143, no. 2, pp. 597–610, Feb. 2020, doi: 10.1093/brain/awz413.
[117] D. M. Lyall *et al.*, “Association between APOE e4 and white matter hyperintensity volume, but not total brain volume or white matter integrity,” *Brain Imaging and Behavior*, vol. 14, no. 5, pp. 1468–1476, 2020, doi: 10.1007/s11682-019-00069-9.
[118] F. Alfaro-Almagro *et al.*, “Confound modelling in UK Biobank brain imaging,” *NeuroImage*, vol. 224, p. 117002, Jan. 2021, doi: 10.1016/j.neuroimage.2020.117002.
[119] C. Bycroft *et al.*, “The UK Biobank resource with deep phenotyping and genomic data,” *Nature*, vol. 562, no. 7726, pp. 203–209, 2018, doi: 10.1038/s41586-018-0579-z.
[120] K. Watanabe, E. Taskesen, A. van Bochoven, and D. Posthuma, “Functional mapping and annotation of genetic associations with FUMA,” *Nature Communications*, vol. 8, no. 1, p. 1826, 2017, doi: 10.1038/s41467-017-01261-5.
[121] B. K. Bulik-Sullivan *et al.*, “LD Score regression distinguishes confounding from polygenicity in genome-wide association studies,” *Nature Genetics*, vol. 47, no. 3, pp. 291–295, 2015, doi: 10.1038/ng.3211.

[122] J. Yang *et al.*, “Common SNPs explain a large proportion of the heritability for human height,” *Nature Genetics*, vol. 42, no. 7, pp. 565–569, 2010, doi: 10.1038/ng.608.
[123] A. Auton *et al.*, “A global reference for human genetic variation,” *Nature*, vol. 526, no. 7571, pp. 68–74, 2015, doi: 10.1038/nature15393.
[124] O. M. P. Jolobe, “Mean corpuscular haemoglobin, referenced and resurrected,” *Journal of Clinical Pathology*, vol. 64, no. 9, p. 833, Sep. 2011, doi: 10.1136/jcp.2011.090514.
[125] X. Li *et al.*, “Magnetic susceptibility contrast variations in multiple sclerosis lesions,” *Journal of Magnetic Resonance Imaging*, vol. 43, no. 2, pp. 463–473, Feb. 2016, doi: https://doi.org/10.1002/jmri.24976.
[126] F. Schweser *et al.*, “Mapping of thalamic magnetic susceptibility in multiple sclerosis indicates decreasing iron with disease duration: A proposed mechanistic relationship between inflammation and oligodendrocyte vitality,” *NeuroImage*, vol. 167, pp. 438–452, Feb. 2018, doi: 10.1016/j.neuroimage.2017.10.063.
[127] A. Papadopoulou *et al.*, “Damage of the lateral geniculate nucleus in MS,” *Neurology*, vol. 92, no. 19, p. e2240, May 2019, doi: 10.1212/WNL.0000000000007450.
[128] S. Swaminathan, V. A. Fonseca, M. G. Alam, and S. v Shah, “The Role of Iron in Diabetes and Its Complications,” *Diabetes Care*, vol. 30, no. 7, p. 1926, Jul. 2007, doi: 10.2337/dc06-2625.
[129] J. Li, Q. Zhang, N. Zhang, and L. Guo, “Increased Brain Iron Detection by Voxel-Based Quantitative Susceptibility Mapping in Type 2 Diabetes Mellitus Patients With an Executive Function Decline,” *Frontiers in Neuroscience*, vol. 14, p. 1390, 2021, [Online]. Available: https://www.frontiersin.org/article/10.3389/fnins.2020.606182
[130] R. Geraldes *et al.*, “Distinct influence of different vascular risk factors on white matter brain lesions in multiple sclerosis,” *Journal of Neurology, Neurosurgery & Psychiatry*, vol. 91, no. 4, Apr. 2020, doi: 10.1136/jnnp-2019-322369.
[131] R. K. Chaturvedi *et al.*, “Neuroprotective and neurorescue effect of black tea extract in 6-hydroxydopamine-lesioned rat model of Parkinson’s disease,” *Neurobiology of Disease*, vol. 22, no. 2, pp. 421–434, May 2006, doi: 10.1016/j.nbd.2005.12.008.
[132] S. Mandel, T. Amit, L. Reznichenko, O. Weinreb, and M. B. H. Youdim, “Green tea catechins as brain-permeable, natural iron chelators-antioxidants for the treatment of neurodegenerative disorders,” *Molecular Nutrition & Food Research*, vol. 50, no. 2, pp. 229–234, Feb. 2006, doi: https://doi.org/10.1002/mnfr.200500156.
[133] M. Juhás *et al.*, “Deep grey matter iron accumulation in alcohol use disorder,” *NeuroImage*, vol. 148, pp. 115–122, Mar. 2017, doi: 10.1016/j.neuroimage.2017.01.007.
[134] J. B. Whitfield, G. Zhu, A. C. Heath, L. W. Powell, and N. G. Martin, “Effects of Alcohol Consumption on Indices of Iron Stores and of Iron Stores on Alcohol Intake Markers,” *Alcoholism: Clinical and Experimental Research*, vol. 25, no. 7, pp. 1037–1045, Jul. 2001, doi: https://doi.org/10.1111/j.1530-0277.2001.tb02314.x.

[135] H. Rouach, P. Houzé, M. Gentil, M. T. Orfanelli, and R. Nordmann, “Changes in some pro-and antioxidants in rat cerebellum after chronic alcohol intake,” *Biochemical Pharmacology*, vol. 53, no. 4, pp. 539–545, Feb. 1997, doi: 10.1016/S0006-2952(96)00770-8.

[136] A. L. Pitel, S. H. Segobin, L. Ritz, F. Eustache, and H. Beaunieux, “Thalamic abnormalities are a cardinal feature of alcohol-related brain dysfunction,” *Neuroscience and Biobehavioral Reviews*, vol. 54, pp. 38–45, Jul. 2015, doi: 10.1016/j.neubiorev.2014.07.023.

[137] S. Segobin *et al.*, “Dissociating thalamic alterations in alcohol use disorder defines specificity of Korsakoff’s syndrome,” *Brain*, vol. 142, no. 5, pp. 1458–1470, May 2019, doi: 10.1093/brain/awz056.

[138] G. J. Anderson and E. Bardou-Jacquet, “Revisiting hemochromatosis: genetic vs. phenotypic manifestations,” *Annals of Translational Medicine*, vol. 9, no. 8, Apr. 2021, doi: 10.21037/atm-20-5512.

[139] B. Benyamin *et al.*, “Variants in TF and HFE Explain ∼40% of Genetic Variation in Serum-Transferrin Levels,” *American Journal of Human Genetics*, vol. 84, no. 1, pp. 60–65, Jan. 2009, doi: 10.1016/j.ajhg.2008.11.011.

[140] L. M. Raffield *et al.*, “Genome-wide association study of iron traits and relation to diabetes in the Hispanic Community Health Study/Study of Latinos (HCHS/SOL): potential genomic intersection of iron and glucose regulation?,” *Human Molecular Genetics*, vol. 26, no. 10, pp. 1966–1978, May 2017, doi: 10.1093/hmg/ddx082.

[141] J. S. K. Kauwe *et al.*, “Suggestive synergy between genetic variants in TF and HFE as risk factors for Alzheimer’s disease,” *American Journal of Medical Genetics Part B: Neuropsychiatric Genetics*, vol. 153B, no. 4, pp. 955–959, Jun. 2010, doi: https://doi.org/10.1002/ajmg.b.31053.

[142] L. Ma, Y. Tian, C. Peng, Y. Zhang, and S. Zhang, “Recent advances in the epidemiology and genetics of acute intermittent porphyria,” *Intractable & Rare Diseases Research*, vol. advpub, p., 2020, doi: 10.5582/irdr.2020.03082.

[143] S. H. Kevelam, R. A. Neeleman, Q. Waisfisz, E. C. H. Friesema, J. G. Langendonk, and M. S. van der Knaap, “Acute intermittent porphyria-related leukoencephalopathy,” *Neurology*, vol. 87, no. 12, p. 1258, Sep. 2016, doi: 10.1212/WNL.0000000000003129.

[144] G. B. Ehret *et al.*, “Genetic variants in novel pathways influence blood pressure and cardiovascular disease risk,” *Nature*, vol. 478, no. 7367, pp. 103–109, 2011, doi: 10.1038/nature10405.

[145] L. Lind, “Genome-Wide Association Study of the Metabolic Syndrome in UK Biobank,” *Metabolic Syndrome and Related Disorders*, vol. 17, no. 10, pp. 505–511, Oct. 2019, doi: 10.1089/met.2019.0070.

[146] N. Carrera *et al.*, “Association study of nonsynonymous single nucleotide polymorphisms in schizophrenia,” *Biological Psychiatry*, vol. 71, no. 2, pp. 169–177, Jan. 2012, doi: 10.1016/j.biopsych.2011.09.032.

[147] O. B. Smeland *et al.*, “Genome-wide Association Analysis of Parkinson’s Disease and Schizophrenia Reveals Shared Genetic Architecture and Identifies Novel Risk Loci,” *Biological Psychiatry*, vol. 89, no. 3, pp. 227–235, Feb. 2021, doi: 10.1016/j.biopsych.2020.01.026.

[148] A. Thompson *et al.*, “Functional validity, role, and implications of heavy alcohol consumption genetic loci,” *Science Advances*, vol. 6, no. 3, p. eaay5034, Jan. 2020, doi: 10.1126/sciadv.aay5034.

[149] M. H. Chen *et al.*, “Trans-ethnic and Ancestry-Specific Blood-Cell Genetics in 746,667 Individuals from 5 Global Populations,” *Cell*, vol. 182, no. 5, pp. 1198-1213.e14, Sep. 2020, doi: 10.1016/j.cell.2020.06.045.

[150] Q. Luo *et al.*, “Association of a Schizophrenia-Risk Nonsynonymous Variant With Putamen Volume in Adolescents: A Voxelwise and Genome-Wide Association Study,” *JAMA Psychiatry*, vol. 76, no. 4, pp. 435–445, Apr. 2019, doi: 10.1001/jamapsychiatry.2018.4126.

[151] B. Zhao *et al.*, “Large-scale GWAS reveals genetic architecture of brain white matter microstructure and genetic overlap with cognitive and mental health traits (n = 17,706),” *Molecular Psychiatry*, 2019, doi: 10.1038/s41380-019-0569-z.

[152] W. Chowanadisai, D. M. Graham, C. L. Keen, R. B. Rucker, and M. A. Messerli, “Neurulation and neurite extension require the zinc transporter ZIP12 (slc39a12),” *Proceedings of the National Academy of Sciences*, vol. 110, no. 24, p. 9903, Jun. 2013, doi: 10.1073/pnas.1222142110.

[153] Z. Buraei and J. Yang, “The β Subunit of Voltage-Gated Ca2+ Channels,” *Physiological Reviews*, vol. 90, no. 4, pp. 1461–1506, Oct. 2010, doi: 10.1152/physrev.00057.2009.

[154] E. K. Green *et al.*, “The bipolar disorder risk allele at CACNA1C also confers risk of recurrent major depression and of schizophrenia,” *Molecular Psychiatry*, vol. 15, no. 10, pp. 1016–1022, 2010, doi: 10.1038/mp.2009.49.

[155] X. Liao and Y. Li, “Genetic associations between voltage-gated calcium channels and autism spectrum disorder: a systematic review,” *Molecular Brain*, vol. 13, no. 1, p. 96, 2020, doi: 10.1186/s13041-020-00634-0.

[156] J. W. Smoller *et al.*, “Identification of risk loci with shared effects on five major psychiatric disorders: A genome-wide analysis,” *The Lancet*, vol. 381, no. 9875, pp. 1371–1379, Apr. 2013, doi: 10.1016/S0140-6736(12)62129-1.

[157] G. A. M. Blokland *et al.*, “Genome-wide association study of working memory brain activation,” *International Journal of Psychophysiology*, vol. 115, pp. 98–111, May 2017, doi: 10.1016/j.ijpsycho.2016.09.010.

[158] M. Brenner, A. B. Johnson, O. Boespflug-Tanguy, D. Rodriguez, J. E. Goldman, and A. Messing, “Mutations in GFAP, encoding glial fibrillary acidic protein, are associated with Alexander disease,” *Nature Genetics*, vol. 27, no. 1, pp. 117–120, 2001, doi: 10.1038/83679.

[159] B. M. Bettcher *et al.*, “Astrogliosis and episodic memory in late life: higher GFAP is related to worse memory and white matter microstructure in healthy aging and Alzheimer’s disease,” *Neurobiology of Aging*, vol. 103, pp. 68–77, Jul. 2021, doi: 10.1016/j.neurobiolaging.2021.02.012.

[160] B. Bellaver *et al.*, “Astrocyte Biomarkers in Alzheimer Disease,” *Neurology*, vol. 96, no. 24, p. e2944, Jun. 2021, doi: 10.1212/WNL.0000000000012109.

[161] S. Goursaud, E. N. Kozlova, J.-M. Maloteaux, and E. Hermans, “Cultured astrocytes derived from corpus callosum or cortical grey matter show distinct glutamate handling properties,” *Journal of Neurochemistry*, vol. 108, no. 6, pp. 1442–1452, Mar. 2009, doi: https://doi.org/10.1111/j.1471-4159.2009.05889.x.

[162] A. Mela and J. E. Goldman, “CD82 Blocks cMet Activation and Overcomes Hepatocyte Growth Factor Effects on Oligodendrocyte Precursor Differentiation,” *Journal of Neuroscience*, vol. 33, no. 18, pp. 7952–7960, May 2013, doi: 10.1523/JNEUROSCI.5836-12.2013.

[163] A. Mela and J. E. Goldman, “The Tetraspanin KAI1/CD82 Is Expressed by Late-Lineage Oligodendrocyte Precursors and May Function to Restrict Precursor Migration and Promote Oligodendrocyte Differentiation and Myelination,” *Journal of Neuroscience*, vol. 29, no. 36, pp. 11172–11181, Sep. 2009, doi: 10.1523/JNEUROSCI.3075-09.2009.

[164] B. Zhao *et al.*, “Large-scale GWAS reveals genetic architecture of brain white matter microstructure and genetic overlap with cognitive and mental health traits (n = 17,706),” *Molecular Psychiatry*, 2019, doi: 10.1038/s41380-019-0569-z.

[165] S. Islam and H. Watanabe, “Versican: A Dynamic Regulator of the Extracellular Matrix,” *Journal of Histochemistry & Cytochemistry*, vol. 68, no. 11, pp. 763–775, Sep. 2020, doi: 10.1369/0022155420953922.

[166] T. N. Wight, I. Kang, and M. J. Merrilees, “Versican and the control of inflammation,” *Matrix Biology*, vol. 35, pp. 152–161, Apr. 2014, doi: 10.1016/j.matbio.2014.01.015.

[167] R. A. Sobel, “The extracellular matrix in multiple sclerosis: an update,” *Brazilian Journal of Medical and Biological Research*, vol. 34, no. 5, May 2001, doi: 10.1590/S0100-879X2001000500007.

[168] J. M. de Jong, P. Wang, M. Oomkens, and W. Baron, “Remodeling of the interstitial extracellular matrix in white matter multiple sclerosis lesions: Implications for remyelination (failure),” *Journal of Neuroscience Research*, vol. 98, no. 7, pp. 1370–1397, Jul. 2020, doi: https://doi.org/10.1002/jnr.24582.

[169] L. C. A. Rutten-Jacobs *et al.*, “Genetic Study of White Matter Integrity in UK Biobank (N=8448) and the Overlap With Stroke, Depression, and Dementia,” *Stroke*, vol. 49, no. 6, pp. 1340–1347, Jun. 2018, doi: 10.1161/STROKEAHA.118.020811.

[170] D. Horn *et al.*, “Biallelic COL3A1 mutations result in a clinical spectrum of specific structural brain anomalies and connective tissue abnormalities,” *American Journal of Medical Genetics Part A*, vol. 173, no. 9, pp. 2534–2538, Sep. 2017, doi: 10.1002/ajmg.a.38345.

[171] J. H. Jeong *et al.*, “Expression of runx2 transcription factor in non-skeletal tissues, sperm and brain,” *Journal of Cellular Physiology*, vol. 217, no. 2, pp. 511–517, 2008, doi: 10.1002/jcp.21524.

[172] J. W. Wang and S. Stifani, “Roles of Runx Genes in Nervous System Development,” in *RUNX Proteins in Development and Cancer*, Y. Groner, Y. Ito, P. Liu, J. C. Neil, N. A. Speck, and A. van Wijnen, Eds. Singapore: Springer Singapore, 2017, pp. 103–116. doi: 10.1007/978-981-10-3233-2_8.

[173] A. Benítez-Burraco and C. Boeckx, “Possible functional links among brain- and skull-related genes selected in modern humans,” *Frontiers in Psychology*, vol. 6, no. June, pp. 1–19, Jun. 2015, doi: 10.3389/fpsyg.2015.00794.

[174] A. M. Cobb *et al.*, “Runx2 (Runt-Related Transcription Factor 2) Links the DNA Damage Response to Osteogenic Reprogramming and Apoptosis of Vascular

Smooth Muscle Cells," *Arteriosclerosis, Thrombosis, and Vascular Biology*, vol. 41, no. 4, pp. 1339–1357, Apr. 2021, doi: 10.1161/ATVBAHA.120.315206.

[175] P. Karpiński, J. Samochowiec, M. M. Sąsiadek, Ł. Łaczmański, and B. Misiak, "Analysis of global gene expression at seven brain regions of patients with schizophrenia," *Schizophrenia Research*, vol. 223, pp. 119–127, 2020, doi: 10.1016/j.schres.2020.06.032.

[176] F. M. Benes, B. Lim, D. Matzilevich, J. P. Walsh, S. Subburaju, and M. Minns, "Regulation of the GABA cell phenotype in hippocampus of schizophrenics and bipolars," *Proceedings of the National Academy of Sciences of the United States of America*, vol. 104, no. 24, pp. 10164–10169, 2007, doi: 10.1073/pnas.0703806104.

[177] C. E. Napper, K. Drickamer, and M. E. Taylor, "Collagen binding by the mannose receptor mediated through the fibronectin type II domain," *Biochemical Journal*, vol. 395, no. 3, pp. 579–586, May 2006, doi: 10.1042/BJ20052027.

[178] P. Allavena, M. Chieppa, P. Monti, and L. Piemonti, "From Pattern Recognition Receptor to Regulator of Homeostasis: The Double-Faced Macrophage Mannose Receptor," *Critical Reviews in Immunology*, vol. 24, no. 3, pp. 179–192, 2004, doi: 10.1615/CritRevImmunol.v24.i3.20.

[179] M. T. Fitch, C. Doller, C. K. Combs, G. E. Landreth, and J. Silver, "Cellular and molecular mechanisms of glial scarring and progressive cavitation: in vivo and in vitro analysis of inflammation-induced secondary injury after CNS trauma.," *The Journal of neuroscience : the official journal of the Society for Neuroscience*, vol. 19, no. 19, pp. 8182–98, Oct. 1999, doi: 10.1523/jneurosci.19-19-08182.1999.

[180] E. M. E. Burudi, S. Riese, P. D. Stahl, and A. R□gnier-Vigouroux, "Identification and functional characterization of the mannose receptor in astrocytes," *Glia*, vol. 25, no. 1, pp. 44–55, Jan. 1999, doi: 10.1002/(SICI)1098-1136(19990101)25:1<44::AID-GLIA5>3.0.CO;2-C.

[181] A. N. Sciara *et al.*, "Neuroinflammatory Gene Expression Alterations in Anterior Cingulate Cortical White and Gray Matter of Males With Autism Spectrum Disorder," *Autism Research*, vol. 13, no. 6, pp. 870–884, 2020, doi: 10.1002/aur.2284.

[182] T. Hattori *et al.*, "Genetic variants in mannose receptor gene (MRC1) confer susceptibility to increased risk of sarcoidosis," *BMC Medical Genetics*, vol. 11, no. 1, p. 151, 2010, doi: 10.1186/1471-2350-11-151.

[183] L. Chen *et al.*, "Quantitative Susceptibility Mapping of Brain Iron and β-Amyloid in MRI and PET Relating to Cognitive Performance in Cognitively Normal Older Adults," *Radiology*, vol. 298, no. 2, pp. 353–362, Nov. 2020, doi: 10.1148/radiol.2020201603.

[184] S. Ayton *et al.*, "Cerebral quantitative susceptibility mapping predicts amyloid-β-related cognitive decline," *Brain*, vol. 140, no. 8, pp. 2112–2119, Aug. 2017, doi: 10.1093/brain/awx137.

[185] S. Yao *et al.*, "Quantitative Susceptibility Mapping Reveals an Association between Brain Iron Load and Depression Severity," *Frontiers in Human Neuroscience*, vol. 11, p. 442, 2017, [Online]. Available: https://www.frontiersin.org/article/10.3389/fnhum.2017.00442

[186] M. Xu *et al.*, “Brain iron assessment in patients with First-episode schizophrenia using quantitative susceptibility mapping,” *NeuroImage: Clinical*, vol. 31, p. 102736, Jan. 2021, doi: 10.1016/J.NICL.2021.102736.

[187] P. Marambaud, U. Dreses-Werringloer, and V. Vingtdeux, “Calcium signaling in neurodegeneration,” *Molecular Neurodegeneration*, vol. 4, no. 1, p. 20, 2009, doi: 10.1186/1750-1326-4-20.

[188] E. Pchitskaya, E. Popugaeva, and I. Bezprozvanny, “Calcium signaling and molecular mechanisms underlying neurodegenerative diseases,” *Cell Calcium*, vol. 70. Elsevier Ltd, pp. 87–94, Mar. 01, 2018. doi: 10.1016/j.ceca.2017.06.008.

[189] S. Islam and H. Watanabe, “Versican: A Dynamic Regulator of the Extracellular Matrix,” *Journal of Histochemistry and Cytochemistry*, vol. 68, no. 11, pp. 763–775, 2020, doi: 10.1369/0022155420953922.

[190] H.-G. Shin *et al.*, “χ-separation: Magnetic susceptibility source separation toward iron and myelin mapping in the brain,” *bioRxiv*, p. 2020.11.07.363796, Jan. 2021, doi: 10.1101/2020.11.07.363796.

[191] G. Douaud *et al.*, “Brain imaging before and after COVID-19 in UK Biobank,” *medRxiv*, p. 2021.06.11.21258690, Jan. 2021, doi: 10.1101/2021.06.11.21258690.

[192] S. M. Smith, D. Vidaurre, F. Alfaro-Almagro, T. E. Nichols, and K. L. Miller, “Estimation of brain age delta from brain imaging,” *NeuroImage*, vol. 200, pp. 528–539, Oct. 2019, doi: 10.1016/J.NEUROIMAGE.2019.06.017.

[193] W. Jung, S. Bollmann, and J. Lee, “Overview of quantitative susceptibility mapping using deep learning: Current status, challenges and opportunities,” *NMR in Biomedicine*, vol. n/a, no. n/a, p. e4292, Mar. 2020, doi: https://doi.org/10.1002/nbm.4292.

[194] J. Yoon *et al.*, “Quantitative susceptibility mapping using deep neural network: QSMnet,” *NeuroImage*, vol. 179, pp. 199–206, Oct. 2018, doi: 10.1016/J.NEUROIMAGE.2018.06.030.

[195] C. Kames, J. Doucette, C. Birkl, and A. Rauscher, “Recovering SWI-filtered phase data using deep learning,” *Magnetic Resonance in Medicine*, vol. 87, no. 2, pp. 948–959, Feb. 2022, doi: https://doi.org/10.1002/mrm.29013.